Instytut Fizyki Jądrowej
im. Henryka Niewodniczańskiego
Polskiej Akademii Nauk
ul. Radzikowskiego 152, 31-342 Kraków
www.ifj.edu.pl/badania/publikacje
Kraków, March 2019

Production of light neutral mesons in the ALICE experiment at the LHC

Adam Matyja

Habilitation Thesis

Wydano nakładem Instytutu Fizyki Jądrowej im. Henryka Niewodniczańskiego
Polskiej Akademii Nauk
Kraków 2019

Recenzent: Prof. dr hab. Jan Figiel
ISBN 978-83-63542-05-4

Mojej żonie Justynie
oraz moim dzieciom Emilowi i Milenie

"Os iusti
Meditabitur sapientiam
Et lingua eius
Loquetur iudicium

Beatus vir qui
Suffert tentationem
Quoniam cum probates fuerit
Accipiet coronam vitae

Kyrie, fons bonitatis
Kyrie, Ignis Divine, eleison. (...)"

Lilium, *Elfen Lied*

"The mouth of the just one
Will prepare itself for wisdom
And his tongue
Is telling a judgement

Blessed is the one
Who bears a temptation
Since after being tested,
He will receive the crown of life

Lord, the source of good-heartedness
Lord, the divine fire, be gracious (...)"

English translation - *The lily*, *Elfen Lied*

"Sprawiedliwe usta
Rozważą mądrość,
A język
Wypowie osąd.

Błogosławiony człowiek,
Co oparł się pokusie,
Której niegdyś spróbował,
Bowiem on otrzyma koronę żywota.

O Panie, zródło dobroci serca,
Odwieczny Ogniu, miej miłosierdzie. (...)"

Polish translation - *Lilia*, *Elfia pieśń*

ABSTRACT

Light pseudo-scalar neutral mesons have been studied in e^+e^-, hadron-hadron, hadron-nucleus and nuclear collisions for decades. The results associated with neutral mesons provide information that is as good as that which comes from charged pions or hadrons. However, they have the advantage that they are not affected by Coulomb forces as charged pions. Due to the fact that the differential cross-section can be factorized into short distance (perturbative) and long distance (non-perturbative) terms when sufficiently large momentum transfer occurs, the measurement of neutral meson spectra provides a chance to test NLO or NNLO pQCD calculations or to constrain parton distribution and fragmentation functions.

The existence of the Quark-Gluon Plasma (QGP) state was postulated in seventies of the last century. The QGP is a highly dense and hot QCD medium in thermal equilibrium where quarks and gluons are almost free. The strongly interacting QGP state has been discovered at RHIC experiments in heavy-ion collisions and is also formed in nuclear collisions at the LHC. The QGP properties can be probed with neutral mesons. Hard (high p_{T}) partons are produced in hard scatterings at the early stage of a collision. Hard partons interact with the dense QGP medium, lose energy, and emerge as quenched jets in the final state after hadronization. Modification of a jet energy results also in reduction of the energy of leading hadrons and in particular neutral mesons. This phenomenon, known as jet quenching, can be quantified via the nuclear modification factor which shows a large suppression of hadron yields at high p_{T} in the most central AA collisions compared to pp collisions scaled by the number of nucleon-nucleon binary collisions. Thus, the measurement of neutral meson spectra constrains mechanisms of parton energy loss in dense systems via studies of the nuclear modification factor.

The ALICE experiment has been designed to study the Quark-Gluon Plasma. However, not only heavy-ion collisions but also pp and pA collisions can be studied there. The π^0 and η mesons are reconstructed in ALICE mainly via their photonic decays. Photons can be directly measured in ALICE electromagnetic calorimeters, EMCal and PHOS or reconstructed from e^+e^- pairs which come from photon conversion in the central barrel detectors' material. Calibration of detectors in which photons and electrons are identified plays a very important role. In this context, calibration of two detectors, the Time Projection Chamber (TPC) and the Electromagnetic Calorimeter (EMCal), of the ALICE detector is explained.

The overview of the world results for many hadron-hadron, nucleus-nucleus and hadron-nucleus collisions collected in a very wide range of center-of-mass collision energy, from few GeV to few TeV, is given in the paper. Thanks to the LHC accelerator which provided pp collisions in the energy range $\sqrt{s} = 0.9$ to 13 TeV, p-Pb collisions at $\sqrt{s_{\mathrm{NN}}} = 5.02$ and 8.16 TeV, as well as Pb-Pb collisions at $\sqrt{s_{\mathrm{NN}}} = 2.76$ and 5.02 TeV, the ALICE experiment could extend neutral meson mea-

surements to new energies unavailable before the LHC era. Inclusive π^0 and η meson production spectra have been measured in a wide p_T range at mid-rapidity. The nuclear modification factor shows the large suppression in the central Pb-Pb collisions. The existence of strongly interacting QGP state of matter is confirmed. No suppression is observed in p-Pb collisions, which supports the thesis that suppression is a final state effect. The measured η/π^0 ratio shows universal behaviour among systems and energies. However, deviation from m_T scaling in very low p_T range is indicated. The results from the ALICE experiment give new constraints on various models in both perturbative and non-perturbative regimes.

Data collected by ALICE in pp collisions at $\sqrt{s} = 13$ TeV can provide very precise measurement of neutral meson spectra and information about jet fragmentation. Future measurements of neutral meson production spectra and isolated photon - jet correlations in pp collisions at $\sqrt{s} = 13$ TeV are discussed.

TABLE OF CONTENTS

CHAPTER I

INTRODUCTION

Multiparticle production dynamics at high energies have been studied via an inclusive approach. The inclusive differential cross-section was formulated for the first time in 1967 [1]. The process of interest is the inclusive production of hadrons

$$h_1 h_2 \to hX \tag{I.1}$$

where h_1 and h_2 are initial state colliding hadrons (or nuclei), h is the subject of studies and X means any other produced particle in the final state. This has been studied in many experiments since that time. It helped to constrain predictions from Quantum Chromodynamics (QCD) [2]. QCD is the theory of strong interactions with a running coupling constant α_s. The strong coupling constant depends on the momentum Q^2 transferred in the interaction. The running constant shows logarithmic dependence on Q^2

$$\alpha_s(Q^2) \sim \frac{1}{\ln(Q^2/\Lambda^2)} \tag{I.2}$$

where Λ defines the scale. A typical value of the scale is $\Lambda \approx 200$ MeV. For large values of Q^2 (the so called hard collision regime) one can use perturbative methods (the strong coupling constant is much less than unity), while for small Q^2 values (the so called soft collision regime, where the strong coupling constant is of order of one) one can only use very complicated numerical methods on lattice (for the first time used by Wilson in 1974 [3]).

The QCD potential between a quark and an anti-quark can be written as a function of a separation distance

$$V(r) = -\frac{\alpha}{r} + \sigma r \tag{I.3}$$

where α is a Coulomb-like term factor and σ is an "elastic" term factor. The larger a distance r the stronger the attractive force. In a result quarks cannot be separated. This feature is called confinement. For several decades of different system collisions studies we have found out that colored quarks and gluons are bound inside hadrons. From the other hand quarks behave as free particles on very short distances. It is known as the asymptotic freedom. It was postulated the emergence of free colored particles in a dense state of matter [4, 5] at the time. These free colored objects were expected to be quarks or gluons rather than hadrons. A dense state of matter has been called the quark-gluon plasma (QGP) [6]. Such a state could arise in the fraction of the first second

of the existence of the universe. Because the plasma state is a state of high energy density and high temperature, one can get it by colliding heavy nuclei accelerated to high energies.

Both fixed target and collider experiments using ion beams have been carried out since the early eighties. Starting from Bevelac at Lawrence Berkeley Laboratory (LBL), where different ion species were accelerated, through experiments at the Alternating Gradient Synchrotron (AGS) at the Brookhaven National Laboratory (BNL), the Super Proton Synchrotron (SPS) at CERN, the Relativistic Heavy Ion Collider (RHIC) at BNL and the Large Hadron Collider (LHC) at CERN researches have been conducted to find a new state of matter. The per nucleon pair energy in the center-of-mass system, $\sqrt{s_{\rm NN}} = 200$ GeV and 5 TeV was achieved for RHIC and LHC in the present experiments, respectively. The different heavy nuclei such as sulphur ^{32}S, silicon ^{28}Si, gold ^{197}Au or lead ^{208}Pb and many others were collided in the mentioned accelerators.

Lattice QCD predicts a phase transition from hadron gas to plasma of deconfined quarks and gluons, which induces gluon radiation from the scattered parton and diminish production of high-$p_{\rm T}$ hadrons (known as a jet quenching) [7, 8]. A milestone for QGP searches was the discovery of an extremely dense and hot state of matter, which was called the strongly interacting quark-gluon plasma (sQGP). All four RHIC experiments (STAR [9], PHENIX [10], PHOBOS [11] and BRAHMS [12]) have observed the unique state via reduction of hadron yields in central nuclear collisions in comparison to binary proton-proton collisions (called suppression of hadron yields), as predicted [13, 14].

The LHC experiments have opened the new energy regime. Besides binary proton-proton (pp) collisions, proton-lead (p-Pb), lead-lead (Pb-Pb) and ksenon-ksenon (Xe-Xe) collisions have been carried out. The center-of-mass collision energy spans the energy range between $\sqrt{s} = 0.9$ and 13 TeV for pp and reaches 8 and 5 TeV for p-Pb and Pb-Pb, respectively. Thus, it is ~ 25 time more than at RHIC. The similar state like found at RHIC has been observed in heavy-ion collisions in the ALICE experiment, however hotter, the energy density is larger and suppression in plasma is larger.

Neutral mesons and photons, which have been studied at the ALICE experiment, are independent and complementary probes of the hot and cold QCD matter in comparison to charged hadrons. The measurement of transverse momentum spectra of these neutral probes in binary collisions helps to constrain QCD in both perturbative (NLO, NNLO calculations) and non-perturbative (parton density functions or fragmentation functions) regimes.

Meson production in nuclear collisions allows studying several effects. Neutral hadrons are subjected to quenching as charged hadrons. One can study collective effects, modification of nucleon parton density function in nuclei, energy loss mechanisms and other effects accompanying the dense matter. In particular, the difference in quark content of π^0 and η mesons can lead to a difference in suppression pattern. Moreover, a comparison of light neutral mesons with heavier hadrons may provide input for comparisons of energy loss by different partons.

Neutral mesons are also the major background to other processes like direct photon production. It is of particular importance because of photons which do not interact strongly and serve as a thermometer of the dense matter. Additionally, the η/π^0 cross-section ratio helps to test $m_{\rm T}$ scaling which is used to estimate not measured contributions to photon spectra coming from background particle decays.

The experimental summary of neutral meson results coming from the ALICE collaboration is

presented in this paper. Photons which are identified as clusters in two ALICE electromagnetic calorimeters EMCal and PHOS or reconstructed from electron-positon pairs in the inner tracking detectors ITS (Inner Tracking System) and TPC (Time Projection Chamber) are combined into neutral mesons. The π^0 and η meson spectra have been measured in proton-proton collisions at $\sqrt{s} = 0.9$, 2.76, 5.02, 7 and 8 TeV and $\sqrt{s} = 0.9$, 2.76, 7 and 8 TeV, respectively. ALICE has also measured neutral meson spectra in p-Pb collisions at $\sqrt{s_{\rm NN}} = 5.02$ TeV and in several centrality classes in Pb-Pb collisions at $\sqrt{s_{\rm NN}} = 2.76$ and 5.02 TeV. The η/π^0 cross-section ratio has been shown for every collision system and energy where η meson spectrum was accessible. The nuclear modification factor is presented for p-Pb and Pb-Pb collision systems. Results are compared to various models and pQCD calculations.

Due to the fact that EMCal and TPC are extensively used in the analyses their calibration have been also described.

Moreover, two potentially interesting measurements (like precise measurement of neutral meson spectra and direct photon correlated with jet analysis in pp collisions at $\sqrt{s} = 13$ TeV) which are possible in ALICE are investigated.

I.1 Author's contribution

The work presented in this manuscript is based on experimental data coming from the ALICE experiment at the LHC. The ALICE experiment is a large collaboration of over thousand people coming from different laboratories spread all over the world. The very high quality of the experimental results is possible thanks to a technical, software and data analysis effort of many collaborators. It is justified to express the role of the author in the complex process of releasing results. The role can be quantified as follows:

- On the technical level, I have been ALICE responsible for the gain calibration of the Time Projection Chamber with radioactive krypton gas [15, 16]. I implemented the software and developed the gain calibration method of TPC. Both the calibration software and the method belong to the official ALICE analysis framework. Since the TPC is the major tracking device of the ALICE detector its calibration is crucial in order to obtain the optimal charged particle identification (PID) via specific energy loss ($\mathrm{d}E/\mathrm{d}x$), very close to analytical curves. The krypton calibration underlies all the analyses relying on identified particles in ALICE. The method of krypton calibration is described in Sec. **IV.14**.

- The method of the krypton calibration used in ALICE, which differs from original NA49 method [17], was transferred back by me to NA49 collaboration and used there for optimal particle identification. Later on, when I joined NA61/SHINE collaboration in 2015, the method was successfully applied in NA61/SHINE collaboration, under my supervision[1].

- On the technical level, I have been ALICE responsible for the time calibration of the Electromagnetic Calorimeter (EMCal) since 2015. I developed the method of the time calibration which is a part of the official ALICE analysis software. The time calibration is one of the

[1] Work done together with N. Davis and A. Rybicki (INP PAN, Kraków).

major calibrations of the EMCal detector. All the results concerning photons, electrons and neutral mesons which use EMCal information need properly calibrated detector and in particular timing information. Section **IV.15** is dedicated to this issue.

- On both technical and physics analysis level, I was involved in the EMCal super-modules assembly and I was involved in the photon and neutral meson analyses in the EMCal. It resulted in the EMCal cluster finder (called unfolding) which disentangle overlapped electromagnetic showers. The clusterizer became a part of the official ALICE analysis software. The first results on neutral pion spectra with the unfolding clusterizer have been shown [18]. Besides neutral meson measurement in pp at $\sqrt{s} = 7$ TeV the clusterizer has been used in many analyses as a cross-check in systematic studies. A description of the clusterizer can be found in Sec. **V.3**. Perspectives for the neutral meson measurement at $\sqrt{s} = 13$ TeV are shown in Sec. **VI.1**.

- I was also extensively involved in the analyses of neutral pion production, in particular, in pp collisions at $\sqrt{s} = 5$ TeV with EMCal, where I am the main author [19]. This measurement will serve as a baseline for the nuclear modification factor analysis in p-Pb and Pb-Pb collisions, where systematic uncertainties are strongly reduced, when both spectra are measured in the same experiment. Chapter **V** is devoted to neutral meson analyses in ALICE.

- Also on the experimental side I was involved in the photon-jet correlation studies, where expectations for ALICE Run II were shown [20]. Perspectives for the measurement are shown in Sec. **VI.2**.

- Finally, as a member of the ALICE collaboration, I participated in experimental data taking as a TPC and ECS (experiment control system) shifter as well as Shift Leader since 2007. I became the Expert ECS shifter after the LHC long shutdown I (LS1) in 2015.

The various results on both calibrations and neutral mesons or photon-jet correlations have been published or shown at international conferences.

I.2 Outline of the paper

The main goal of the paper is to overview neutral meson production and to show technical issues standing behind the analyses. As one can see, neutral mesons can also be used to study properties of the QGP.

This paper is organized in the following way. The basic introduction to the high energy hadron physics and heavy ion physics is discussed in Chapter **II**. The experimental overview and remarks coming from measurements are presented in Chapter **III**. The experimental apparatus together with very important TPC and EMCal calibrations are described in Chapter **IV**. Chapter **V** is devoted to neutral meson analyses together with the physics motivation in the ALICE experiment. A perspective of few interesting analyses where both the EMCal and the TPC are involved in, which haven't been possible in the ALICE experiment until the end of data taking in LHC run II are mentioned in Chapter **VI**. The paper is concluded in Chapter **VII**.

CHAPTER II

SELECTED TOPICS FROM HIGH ENERGY AND NUCLEAR PHYSICS

The basic theoretical concepts and important experimental results related to the neutral meson analysis of both pp and heavy ion collisions are discussed in this chapter. Section **II.1** is devoted to factorization in simple hadronic systems and more complicated nuclear collisions. The QCD phase diagram and concept of the quark-gluon plasma is discussed in Sec. **II.2**. Then the current understanding how the evolution of nuclear collision looks like is discussed in Sec. **II.3**. The quark-gluon plasma searches and the discovery made at RHIC is described in Sec. **II.4**. Then, a very important observable, nuclear modification factor is introduced in Sec. **II.5**. The parton distribution function and fragmentation function are expounded in Sec. **II.6**. The last Section of the chapter is dedicated to Monte Carlo generators.

II.1 Factorization

Both experimental and theoretical developments allow us to study and understanding inclusive particle production of a broad range of collision energy up to large transverse momentum, p_{T}. In high energy proton-proton (pp) collisions large transverse momentum hadrons originate mainly from fragmentation of quarks and gluons created in hard collisions. It is well described within the perturbative quantum chromodynamics (pQCD) framework [21]. Due to the large four-momentum transfer, Q^2, which occurs in sufficiently high-p_{T} regime, the cross-section may be factorized (see e.i. collinear factorization [22]) into convolutions of short-distance and long-distance parts. The short distance part describes the hard interaction of partons and depends explicitly on the large scales related to the large four-momentum transfer, Q^2. It can be evaluated via pQCD. There are two main ingredients of long distance parts. The first one represents the inner structure of the initial state hadrons. The kinematic distributions of quarks and gluons within the hadron are described by parton distribution functions (PDFs). The second one represents the probability of fragmentation of a final state quark or gluon into the observed particle of interest. Such probabilities are described by fragmentation functions (FFs). The very important feature of the long distance parts is that they are universal - the same in any inelastic reaction. However, they are nonperturbative and need to be experimentally validated. The differential cross-section of single inclusive particle production

in hadronic collisions can be written as follows:

$$E\frac{\mathrm{d}^3\sigma^h}{\mathrm{d}p^3} = \sum_{a,b,c} f_{a/h_1}(x_1,\mu_{FI}^2) \times f_{b/h_2}(x_2,\mu_{FI}^2) \times D_{h/c}(z_c,\mu_{FF}^2) \times \mathrm{d}\widehat{\sigma}_{ab\to cX}(x_1,x_2,\mu_R^2), \qquad \textbf{(II.1)}$$

where $f_{i/h}(x,\mu_{FI}^2)$ denotes the hadron h PDF of parton i carrying a fraction x of hadron's longitudinal momentum, and $D_{h/i}(z_i,\mu_{FF}^2)$ the FF of parton i into a hadron h carrying a fraction z_i of the parton's momentum. The sum runs over all partonic sub-processes $ab \to cX$ with $\mathrm{d}\widehat{\sigma}_{ab\to cX}(x_1,x_2,\mu^2)$ the inclusive cross-section of partons a and b into c. μ_{FI}, μ_{FF} and μ_R are initial and final state factorization and renormalization scales, respectively. Usually factorization and renormalization scales are set to a value of transverse momentum: $\mu_{FI} = \mu_{FF} = \mu_R = p_{\mathrm{T}}$. For systematic studies scales are checked for a half and double of p_{T}.

The description of soft part of interactions in collision, which populate mostly low-p_{T} regime of particle spectra is more demanding. There are complicated interactions between valence quarks, gluons and see quark-antiquark pairs where no obvious large Q^2-scale is present. The absence of the large scale prevents the perturbative treatment. Besides the numerical lattice approach only phenomenological models with certain assumptions about parton dynamics are able to mimic observations (for example Lund model [23]). One needs to say that before QCD times the Regge theory [24] had commonly been used to describe data.

When collisions of two nuclei are considered similar factorization like in Eq. **II.1** can be applied, but incidental hadrons need to be substituted by nuclei, so that $f_{i/A}(x,\mu_{FI}^2)$ is the PDF, which tells us about the probability of finding parton i with a momentum fraction $x = p_{\mathrm{parton}}/p_{\mathrm{nucleus}}$ inside the nucleus with a mass number A. One can treat each interacting nucleus as a collection of free partons since partons are effectively "frozen" during the hard scattering (characteristic time of the parton-parton interaction is much smaller than any long-distance interaction). Thus, the parton densities in a nucleus are expected to be a superposition of A independent nucleons N (protons or neutrons) in the high-p_{T} production limit:

$$f_{i/A}(x,\mu_{FI}^2) = A \cdot f_{i/N}(x,\mu_{FI}^2). \qquad \textbf{(II.2)}$$

We can measure inclusive differential production cross-sections of a hadron in the experiment and compare it to theoretical model predictions or Monte Carlo generators. Usually, it is given by formula:

$$E\frac{\mathrm{d}^3\sigma}{\mathrm{d}p^3} = \frac{1}{2\pi p_{\mathrm{T}}}\frac{1}{\mathcal{L}}\frac{1}{BR}\frac{1}{\varepsilon}\frac{N(\Delta p_{\mathrm{T}},\Delta y)}{\Delta p_{\mathrm{T}}\Delta y}, \qquad \textbf{(II.3)}$$

where the luminosity $\mathcal{L} = \frac{N_{\mathrm{evt}}}{\sigma}$ is expressed in terms of the trigger cross-section σ and the number of events N_{evt}, BR is the branching ratio of a hadron in a given decay channel, ε is the effective efficiency correction, $N(\Delta p_{\mathrm{T}},\Delta y)$ is a number of reconstructed mesons in given Δp_{T} and Δy interval.

II.2 QCD phase diagram

There are two very important properties of QCD coming from hadron structure, the asymptotic freedom and the quark confinement. The deconfined phase should also exist somewhere at very

high temperature. The QCD phase diagram [25] on the baryon chemical potential (μ_B) and temperature (T) plane is shown in Fig. **II-1**. The baryon chemical potential tells about the energy needed to

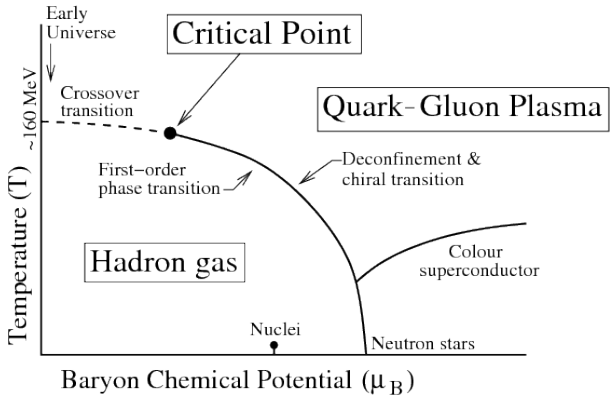

FIGURE II-1: QCD phase diagram [25].

create yet another baryon. It is related to the baryon density and can be defined as $\mu_B = (n_q - n_{\bar{q}})/3$, where n_q and $n_{\bar{q}}$ are the quark and antiquark number densities, respectively.

The most important remark is that the QCD phase diagram is not well known experimentally and the picture is only schematic. The ordinary nuclear matter exists at low temperature and $\mu_B \simeq 0.9$ GeV. The vacuum is considered in a region where $T = \mu_B = 0$. There are two regions of special interest in the phase diagram. The first one is called hadronic gas, the other is QGP region. They are separated by a line of the first order phase transition (as a function of temperature and finite μ_B), which ends at the critical point with co-existence of both phases where second order phase transition occurs, and the region of crossover phase transition (at low μ_B and high temperature). The crossover transition is predicted by lattice QCD [26] at small or vanishing μ_B and temperature around the critical temperature $T_C \sim 150 - 170$ MeV. There is also another region at low T and large μ_B of the astrophysical interest where colored superconductivity appears. However, boundaries on the phase diagram are not established.

As mentioned before lattice QCD predicts a transition from the hadron gas to the plasma state. The temperature scan around critical temperature shows a step in the energy density ε [27] like shown in Fig. **II-2**. The energy density is related to the number of degrees of freedom (dof). There are 3 dof for pure pion hadron gas and 37 dof for two flavor QGP. The difference is more than 10 times.

II.3 Heavy ion collision

To create quark gluon plasma one needs to collide heavy ions at large energies to obtain the energy density large enough. Although, experimentally it is relatively easy (techniques for receiving electron-donated heavy ions and their acceleration are well known), the theoretical description is not trivial. One needs to separate a heavy ion collision (HIC) into several stages [28]. The schematic picture of a heavy ion collision is shown in Fig. **II-3**. There are two Lorentz contracted incoming

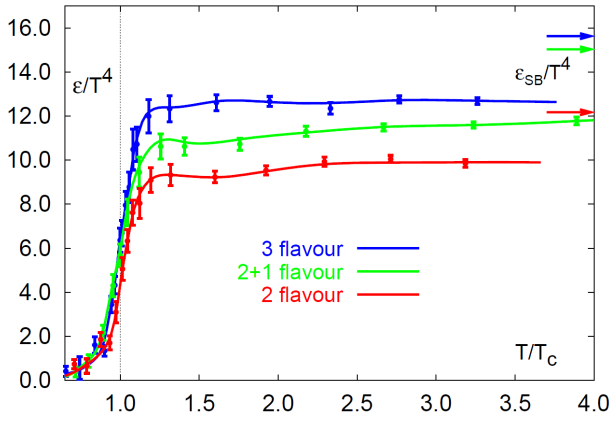

FIGURE II-2: Energy density as a function of temperature for different number of degenerated flavors scenarios. Arrows show the Stefan-Boltzmann limit for an ideal quark-gluon gas [27].

ions of size ~ 1 fm [30] (due to wee partons caused by wee fluctuations). The next phase is a pre-equilibrium state where hard scattering occurs. Next, there are soft collisions and dense matter is created (potentially QGP when energy density is sufficient) which expands hydrodynamically. The dense matter cools down and hadronize. The last step is hadron freeze-out. A space time dia-

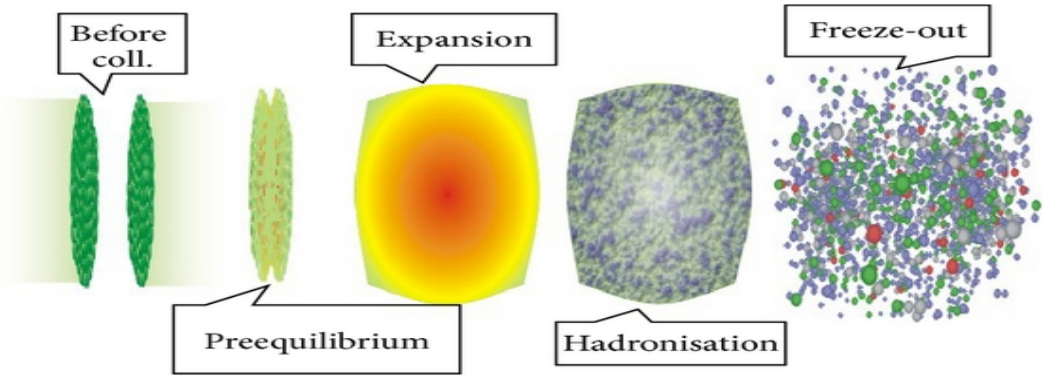

FIGURE II-3: Simplified picture of the heavy ion collision [29].

gram for the time evolution of the colliding system with and without QGP formation is shown in Fig. **II-4**. For collisions without QGP formation, QGP stage and mixed stage can be omitted. The case when QGP is formed is described below. There are two highly relativistic heavy nuclei A and B incoming, whose description need to be properly done. They were usually described by Glauber Model [31] but recently Color Glass Condensate (CGC) [32] description is considered. Two nuclei move along the light cone, until they collide in the centre at time $t = 0$. The energy density of nuclear matter is $\varepsilon \sim 0.17$ GeV/fm^3. Up to time $t < \tau_0 \sim 1\text{fm}/c \sim 3 \times 10^{-24}$ s one can identify **pre-equilibrium stage**. During this stage partons scatter among each other. High p_T particles are

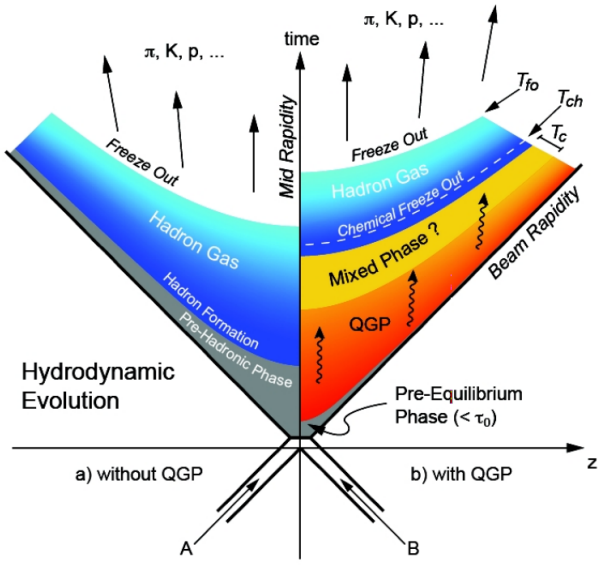

FIGURE II-4: Space time evolution of the collision for two scenarios when QGP is formed or not.

produced in hard processes at this phase. The system is not in equilibrium, but constituents want to establish the local statistical equilibrium. The time τ_0 after which the QGP is formed is then called the thermalization time. This time should be less than 1 fm/c after the collision (look i.e. at [33]) and should be at least as long as the crossing time of colliding nuclei. The near thermalization state forces the evolution of the created matter according to relativistic perfect fluid dynamics. In the **hydrodynamic expansion stage** driven by large pressure gradients, the temperature exceeds critical temperature T_C. The energy density of such medium can be calculated according to the Bjorken formula [28]:

$$\varepsilon = \frac{1}{\tau_0 A_{\mathrm{T}}} \frac{\mathrm{d}E_{\mathrm{T}}}{\mathrm{d}y}, \tag{II.4}$$

where $\mathrm{d}E_{\mathrm{T}}/\mathrm{d}y$ is rapidity transverse energy density, A_{T} is a transverse overlap area of colliding nuclei. The system expands, energy density is decreasing and the system cools down. At the end of this stage ($t \sim 1-10$ fm/c) when critical temperature is reached and phase transition is supported system begins to convert into hadron gas and remains in the mixed phase. This is time of **hadronization stage**. In this stage over very small temperature interval entropy density will decrease very fast. The total entropy must be conserved, so system expands rapidly, but temperature remains more or less constant. Hadrons continue to collide elastically and inelastically among themselves. Hadrons changes energy and momentum as well as alter abundances of species. The chemical **freeze-out** occurs when inelastic collisions die out, so flavor composition is fixed. The temperature related to the chemical freeze-out T_{ch} can still be very high, equal or slightly lower than T_C. The local equilibrium can still be maintained via elastic collisions. When elastic scattering stops kinetic freeze-out occurs. Hydrodynamic description is breaking down and one needs to use relativistic kinetic theory framework. Hadrons decouple from the system after $t \sim 10-15$ fm/c and then can be observed in surrounding detectors. The overview of the collision modelling and

experimental results can be found in [25, 29, 34, 35, 36].

II.4 QGP at RHIC

The searches of quark-gluon plasma started in late '70 in Bevalac at Berkeley with up to 2 GeV/A of energy beam of different ion species was shot at the fixed target. Many other experiments were carried out since that time. Some hints of QGP had been reported at SPS experiments [37]. The discovery of a new state came at RHIC era and was a surprise. The QGP had expected to be an ideal gas turned out to be almost ideal fluid and was called strongly interacting quark-gluon plasma (sQGP) [38, 39]. The interaction strength could be understood in terms of Coulomb coupling parameter Γ [40] which take values $\Gamma < 1$ for gaseous plasma and $1 < \Gamma < 10$ for liquid plasma.

One of the effects which accompanied sQGP is jet quenching. The first jets, collimated sprays of particles, were observed in the electron-positron (e^+e^-) collisions in 1975 [41]. Jet is created as a result of fragmentation of high momentum color parton produced at the early stage of collision (production time $t \sim 1/p_{\mathrm{T}}$) in the hard interaction into colorless hadrons. It is a perfect tool to probe a dense medium. The jet production rate is calculable in perturbative QCD. In a dense medium this high momentum parton interacts with surrounding matter and loses energy.

When hadronization time comes the available energy is smaller than the initial energy of the parton what results in lower energy jet or total disappearance of the jet. The first observation of jet quenching was not with jets but with high-p_{T} jet fragments. The effect was observed by comparing the spectra of azimuth correlation of high-p_{T} charged hadrons originating from pp collisions with collisions of heavy nuclei (see Fig. **II-5** [42]) or the comparison of central and peripheral nuclear collisions (see Fig. **II-6** [43]) at different intervals of the transverse momentum, p_{T} of the leading 'trigger' particles ($p_{\mathrm{T}}^{\mathrm{trig}}$) and associated particles ($p_{\mathrm{T}}^{\mathrm{assoc}}$). There are two maxima at near side ($\Delta\varphi = 0$) and away side ($\Delta\varphi = \pi$) coming from hadrons inside jets for pp and d-Au collisions. However, there is a lack of maximum at $\Delta\varphi = \pi$ for the central Au-Au collisions like seen in Fig. **II-5** or suppression of maximum when comparing central and semi-central Au-Au collisions especially visible in the bottom row of Fig. **II-6**. The energy of the away side parton in the central Au-Au collisions is not gone. It is dissipated in the medium thereby producing soft particles. The away side peak reappears when all the particles are taken into account.

There are several mechanisms of energy loss in a dense medium. There is collisional energy loss via elastic scatterings and radiative energy loss via inelastic soft gluon radiation. The first one dominate at low momenta, the second one at high momenta. The energy loss ΔE per unit path length L depends on properties of the medium (transport coefficient $\hat{q}$, gluon rapidity density $\mathrm{d}N^g/\mathrm{d}y$, temperature T) as well as properties of parton (parton species, energy E). For collisional energy loss mechanisms $\Delta E \sim L$, for radiative $\Delta E \sim L^2$. Even stronger $\Delta E \sim L^3$ dependence [44] is suggested through virtual gluons emitted into the medium as described by Anti-de-Sitter/Conformal-Field-Theory (AdS/CFT) correspondence. For recent reviews of jet quenching see e.g. [45, 46, 47, 48, 49].

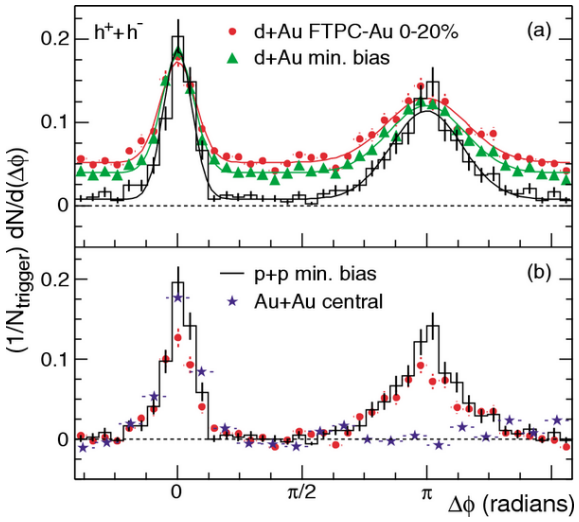

FIGURE II-5: Two-particle azimuth distributions for (a) minimum bias (green triangles) and central (red dots) d-Au collisions, and for pp (black line) collisions for the center-of-mass energy $\sqrt{s_{\rm NN}} = 200$. (b) Comparison of two-particle azimuth distributions for central d-Au collisions (blue stars) to those seen in pp and central Au-Au collisions for the same collision energy [42].

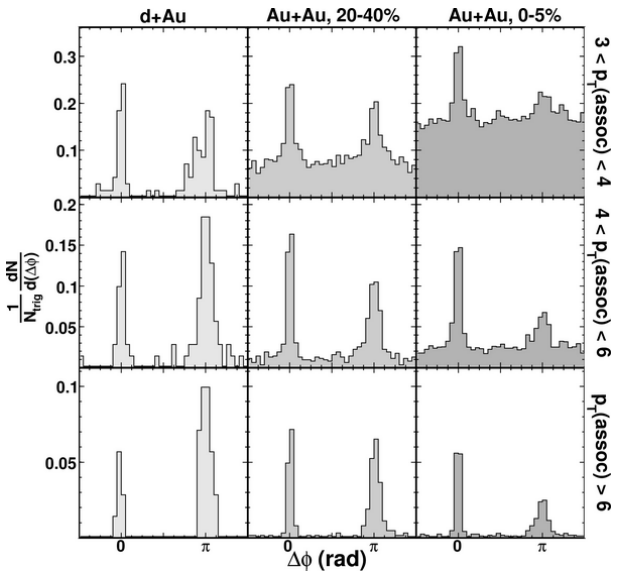

FIGURE II-6: Azimuth correlation of high $p_{\rm T}$ charged hadrons for $8 < p_{\rm T}^{\rm trig} < 15$ GeV/c, for d-Au, $20-40\%$ Au-Au and $0-5\%$ Au+Au events at the center-of-mass energy $\sqrt{s_{\rm NN}} = 200$ GeV (left to right). $p_{\rm T}^{\rm assoc}$ increases from top to bottom [43].

II.5 Nuclear modification factor

To understand pp collisions is very crucial from the perspective of heavy ion collisions which are very challenging. Simple binary collisions, like pp collisions, serve as a baseline for phenomena occurring in HIC. To quantify effect in HIC nuclear modification factor is introduced,

$$R_{\mathrm{AA}} = \frac{1}{N_{\mathrm{coll}}^{AA}} \frac{\mathrm{d}^2 N^{AA}/\mathrm{d}y\mathrm{d}p_{\mathrm{T}}}{\mathrm{d}^2 N^{pp}/\mathrm{d}y\mathrm{d}p_{\mathrm{T}}}, \tag{II.5}$$

where the yield in rapidity and transverse momentum intervals for nuclear collisions is in the nominator and scaled by number of binary collisions N_{coll}^{AA} the yield in pp collisions in the denominator. N_{coll}^{AA} is mean number of nucleon-nucleon collisions occurring in a single nucleus-nucleus (AA) collision and usually is obtained within the Glauber model [31]. Sometimes N_{coll}^{AA} can be substituted by

$$N_{\mathrm{coll}}^{AA} = T_{AA} \times \sigma_{\mathrm{INEL}}^{pp}, \tag{II.6}$$

where T_{AA} is the nuclear overlap function and $\sigma_{\mathrm{INEL}}^{pp}$ is the total inelastic cross-section. The example R_{AA} distribution for π^0 and η mesons as well as for direct photons at RHIC is shown in Fig. **II-7**. The example R_{AA} distribution for charged hadrons at LHC is shown in Fig. **II-8**.

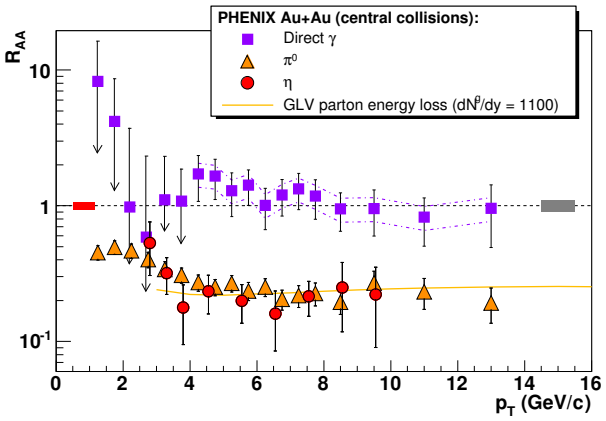

FIGURE II-7: Nuclear modification factor R_{AA} as a function of p_{T} for π^0 (triangles) and η (circles) mesons, and for direct photons (squares) produced in central Au-Au collisions at the center-of-mass energy $\sqrt{s_{\mathrm{NN}}} = 200$ GeV. Solid yellow line represents jet quenching calculations for leading pions in medium with initial gluon density $\mathrm{d}N^g/\mathrm{d}y = 1100$. Dash-dotted lines denotes NLO pQCD calculation for direct photon R_{AA}. The color bands at unity are normalization uncertainties [50].

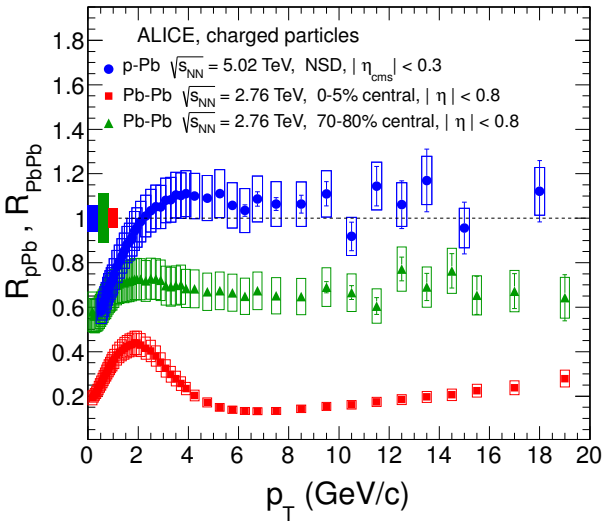

FIGURE II-8: Nuclear modification factor as a function of p_{T} for $0-5\%$ central (red squares) and $70-80\%$ central (green triangles) Pb-Pb collisions at $\sqrt{s_{\mathrm{NN}}} = 2.76$ TeV and for p-Pb collisions (blue dots) at $\sqrt{s_{\mathrm{NN}}} = 5.02$ TeV. The color bands at unity are normalization uncertainties [51].

Nuclear modification factor illustrates the medium effect (initial state effects like Cronin or nuclear shadowing and final state effects: collisional and radiative energy loss). However, one needs to remember that there are two regimes in p_{T}. There is a soft processes' region (below $p_{\mathrm{T}} \simeq 2$) where particle production scales with number of participants (N_{part}) and hard processes' region (above $p_{\mathrm{T}} \simeq 2$) where particle production scales with number of binary collisions (N_{coll}). $R_{\mathrm{AA}} = 1$ means no nuclear effects (like for direct photons which interact electromagnetically shown in Fig. **II-7** or for p-Pb collisions in Fig. **II-8**, where no modification is expected). $R_{\mathrm{AA}} < 1$ shows nuclear medium effect (the example of jet quenching in dense nuclear matter is shown in Fig. **II-7** or in Fig. **II-8** for central Au-Au collisions or for central Pb-Pb collisions, respectively). Finally, $R_{\mathrm{AA}} > 1$ means enhancement. Cronin effect plays a role here (for d-Au collisions at RHIC or at SPS energies). Cronin effect is most probably caused by multiple low-momentum parton scattering on target nucleons in the initial phase before hard scattering.

Similarly to R_{AA}, the central to peripheral collisions appropriately scaled nuclear modification factor R_{CP} is defined:

$$R_{\mathrm{CP}} = \frac{N^P_{\mathrm{coll}}}{N^C_{\mathrm{coll}}} \frac{\mathrm{d}^2N^C/\mathrm{d}y\mathrm{d}p_{\mathrm{T}}}{\mathrm{d}^2N^P/\mathrm{d}y\mathrm{d}p_{\mathrm{T}}}, \tag{II.7}$$

here $C(P)$ stands for central (peripheral) heavy ion collisions and $N^{C,P}_{\mathrm{coll}}$ are corresponding scaling factors. R_{CP} is useful when no reference spectrum is available and we don't want to relay on extrapolations. Some systematic uncertainties are cancelled out and also effects like Cronin are minimized.

II.6 Parton distribution and fragmentation functions

After the factorization of the differential cross-section according to Eq. **II.1** one needs to determine non-perturbative terms:

- Parton distribution functions, $f_{i/h}(x,\mu^2_{FI})$,
- Fragmentation functions, $D_{h/i}(z_i,\mu^2_{FF})$.

PDFs comprise the probability of finding parton of flavor i and longitudinal momentum fraction $x = p_L^{\mathrm{parton}}/p_L^{\mathrm{hadron}}$ (the Bjorken x variable) inside a hadron h. μ_{FI} is the initial state factorization scale. It is very important to know the inner structure of proton because it is of interest of many ongoing and future experiments. Protons are commonly used for experiments at the LHC. The uncertainties on PDF plays an important role in Higgs boson couplings, beyond standard model analyses or particle production spectra.

The dependence of the PDFs on Bjorken x is driven by non-perturbative dynamics and cannot be calculated perturbatively. The μ^2_{FI} dependence can be computed in pQCD up to any given order and is governed by the Dokshitzer-Gribov-Lipatov-Altarelli-Parisi (DGLAP) evolution equations [52, 53, 54, 55] in the generic form:

$$\mu^2_{FI}\frac{\partial}{\partial\mu^2_{FI}} f_{i/h}(x,\mu^2_{FI}) = \sum_j P_{ij}(x,\alpha_s(\mu^2_{FI})) \otimes f_{j/h}(x,\mu^2_{FI}), \tag{II.8}$$

where $P_{ij}(x,\alpha_s(\mu_{FI}^2))$ are the Altarelli-Parisi splitting functions (they have an interpretation as probabilities of splitting parton i to parton j) which can be computed within pQCD and $\otimes$ symbol denotes convolution. In order to illustrate the impact of the DGLAP evolution on the PDFs comparison of the MSTW PDFs [56] at a low scale of $\mu_{FI}^2 = Q^2 = 10$ GeV^2 with the PDFs evolved to a typical LHC scale of $Q^2 = 10^4$ GeV^2 is shown in left or right hand side of Fig. **II-9**, respectively. PDFs are shown together with one standard deviation uncertainty band in this plot. The effect of

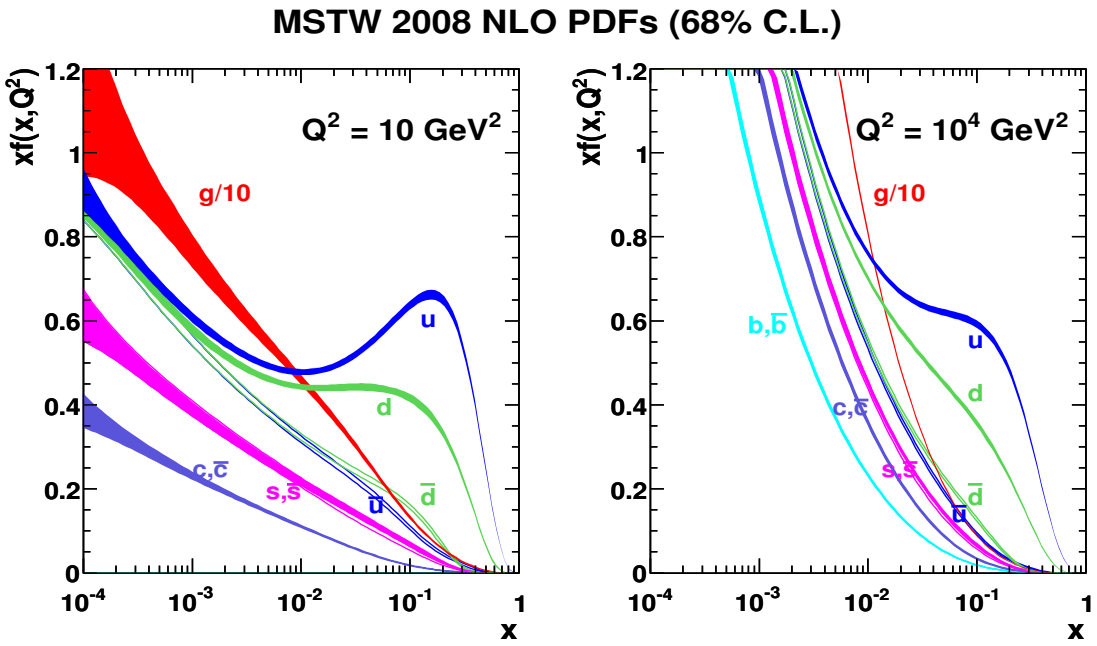

FIGURE II-9: MSTW 2008 NLO PDFs at $Q^2 = 10$ GeV^2 (left) and $Q^2 = 10^4$ GeV^2 (right) [56].

the evolution is dramatic - a very steep rise of gluons and see quarks. Also, a new "b-channel" is opened at the LHC energy. One can see a characteristic bump of u and d quarks at $x \approx 1/3$ due to valence composition of proton. The relative amount of valence quarks is limited by proton valence quark content (uud) as a consequence of the valence quark sum rules:

$$\begin{aligned} \int_0^1 dx[f_u(x) - f_{\bar{u}}(x)] &= 2, \\ \int_0^1 dx[f_d(x) - f_{\bar{d}}(x)] &= 1, \\ \int_0^1 dx[f_s(x) - f_{\bar{s}}(x)] = \int_0^1 dx[f_c(x) - f_{\bar{c}}(x)] &= 0. \end{aligned} \tag{II.9}$$

The other constraints like energy-momentum conservation (total momentum of proton must be equal to the sum of momenta of its constituents):

$$\sum_{i=q,\bar{q},g} \int_0^1 dx\, x f_i(x) = 1, \tag{II.10}$$

and number of quark flavors must be satisfied for the PDF that have the assumed parameterization which can be written in a general form:

$$xf(x,\mu^2_{FI,0}) = A_f x^{a_f}(1-x)^{b_f} I_f(x), \tag{II.11}$$

where A_f, a_f, b_f are parameters and $I_f(x)$ - interpolation function takes a complicated functional form at initial low scale $\mu^2_{FI,0}$. The major problem with PDFs is that cannot be calculated, but they can be parameterized using experimental data at some scale as an input and evaluated to high energy via DGLAP equations.

To determine proton PDFs several clear processes types are used like Deep Inelastic Scattering (DIS) (eg.: $e^- p \to e^- X$), Drell-Yan lepton pair production (DY) (eg.: $pp \to \mu^+\mu^- X$) or others. For DIS or DY the characteristic scale can be associated to virtuality of the exchanged gauge boson. Many processes from fixed target experiments and collider experiments at HERA, Tevatron and LHC have been used to determine PDFs. A number of collaborations provide regular updates on their PDF sets. One can bring here:

- CTEQ [57] (CT14),
- MMHT [58] (MMHT14, the successor of MSTW08 [56]),
- NNPDF [59] (NNPDF3.0),
- ABMP [60] (ABMP16),
- CJ (CTEQ-Jefferson Lab) [61] (CJ15),
- HERAPDF [62] (HERAPDF2.0),

and others. The differences between groups are coming from values of cut-offs, different data-sets taken into the fits, parameterizations and others. Mostly the recent PDF sets go to NNLO in the strong coupling. The recent PDF review can be found in [63].

There are also a variety of heavy-ion experiments where not single free proton PDFs are needed but bounded within a nucleus with a mass number A and an atomic number Z. There are additional effects which need to be taken into account considering nucleus like shadowing, anti-shadowing, Fermi-motion or EMC-effect [64]. There are several assumptions underlying the nuclear PDFs. The bound proton PDFs have the same sum rules and evolution equations as the free proton PDFs, and any contribution from $x > 1$ region is neglected (the other nucleons can impact bounded proton causing this effect). In addition, the isospin symmetry is assumed to connect neutrons (n) and protons (p) in nucleus ($f_u^{n/A}(x) = f_d^{p/A}(x)$ and $f_d^{n/A}(x) = f_u^{p/A}(x)$). Having these assumptions one can build nucleus PDFs as:

$$f_i^{(A,Z)}(x,\mu^2_{FI}) = \frac{Z}{A} f_i^{p/A}(x,\mu^2_{FI}) + \frac{A-Z}{A} f_i^{n/A}(x,\mu^2_{FI}). \tag{II.12}$$

Contrary to free proton PDFs there is much fewer data to be taken into the nPDFs constraints spanning the x and Q^2 space. However, in this area several groups show their results:

- nCTEQ15 [65],
- EPS09 [66],
- EPPS16 [67],

- HKN [68],
- DSSZ [69],
- KT16 [70].

All the mentioned nPDFs are NLO and even KT16 is NNLO. The nCTEQ15, EPS09 and EPPS16 use the most recent proton baseline PDFs (CTEQ6.1-like, CTEQ6.1 and CT14NLO, respectively) and data from RHIC π^0 measurements. In addition, the EPPS16 uses the recent LHC data. Nuclear PDFs suffer from limited amount of data what is reflected in particular in constraints on gluon and strange parton density functions.

Fragmentation function $D_{h/i}(z_i, \mu^2_{FF})$, describes the probability that the outgoing parton i fragments into the observed hadron h with fractional momentum $z_i = p_{\text{hadron}}/p_{\text{parton i}}$ and μ_{FF} is a fragmentation scale. The FF dependence on the scale is driven, similarly to PDFs, by DGLAP time-like scale evolution equations (with positive four-momentum transfer) which are known to NLO accuracy [71, 72, 73, 74]. The functional form of FFs is analogous to PDF in Eq. **II.11**. Also the momentum sum rule is imposed. Moreover, having constrained, for example charged pion fragmentation function $D_{i/\pi^+}(x, \mu^2_{FF,0})$ at some initial scale $\mu^2_{FF,0}$ additional conditions must be imposed, like for example isospin symmetry for unflavored FFs of light see quarks ($D_{\bar{u}/\pi^+} = D_{d/\pi^+}$).

To determine pion FFs, again, some clear process must be taken from available pool of results, like single-inclusive hadron production in e^-e^+ annihilation (SIA) and pp collisions or semi-inclusive deep-inelastic lepton-nucleon scattering (SIDIS). There are several groups which are calculating FFs. The most commonly used sets of parton-to-charged-hadron parameterizations with the NLO accuracy:

- Kretzer [75],
- KKP [76],
- BFGW [77],
- HKNS [78],
- AKK05 [79],
- DSS [80, 81],
- AKK08 [82].

The comparison between them can be found in [83]. Different groups use different parameterization and differing data sets. The result of any calculation overshoots the data in general by a factor of $1-2$. A major problem could come from the gluon fragmentation function which is not well determined from e^+e^- experiments (enters at NLO only). The change of the gluon fragmentation function may affect the slope of the p_{T} distributions. The most recent parton-to-pion FF [84] uses as an input ALICE measurement on the inclusive π^0 mesons and results from BELLE and BABAR which makes the agreement between data and pQCD calculations much better. Usually, the analyses of FFs comprise pions, kaons, protons and lambdas as final state hadrons. Based on η meson production in SIA at various collision energies and in pp collisions at RHIC the AESSS FF [85] has been calculated.

II.7 Monte Carlo generators

Monte Carlo event generator is a tool used in experimental physics to simulate events with features of signal and background processes. Usually an event generator is a complex routine which combines the known or calculable phenomena and sometimes unconfirmed models which we believe to work or to have the best description of data in the range which is non-perturbative. Because an event generator is a computer program it should be structural. Therefore, we can "factorize" it into components like:

- Hard process,
- Parton shower,
- Hadronization,
- Multiparticle interactions,
- Decay of unstable hadrons.

A typical hadron collider event is shown in Fig. **II-10**. There are two incidental hadrons (grey

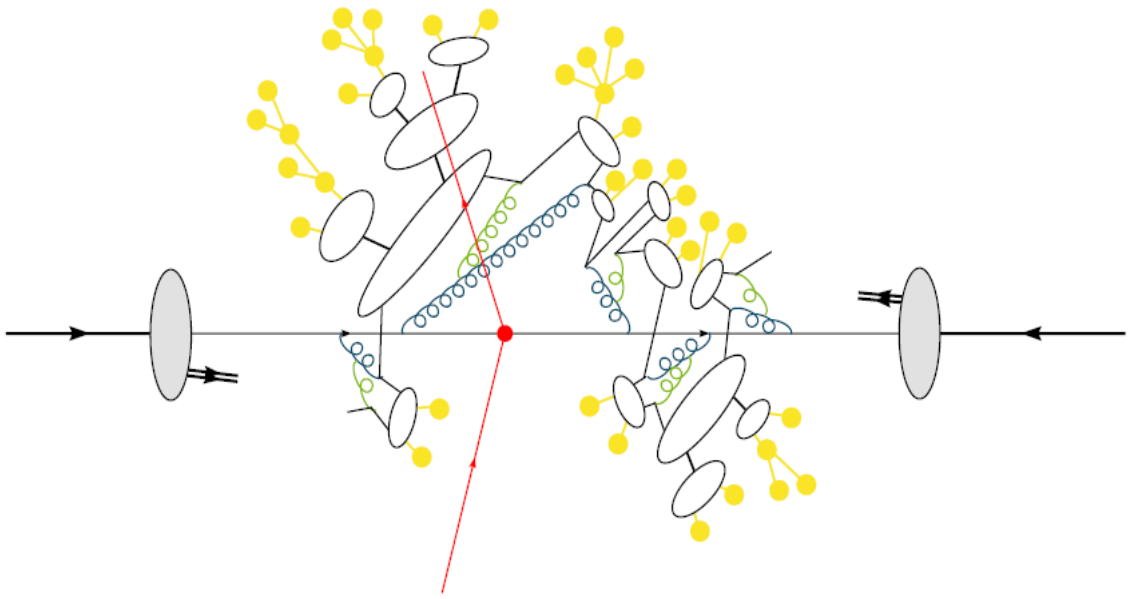

FIGURE II-10: Sketch of the simulation of a typical hadron collider event. Figure taken from [86].

ellipses) from which one parton interact in a hard scattering event (red blob). Then parton showers evolve (blue and green springs). It is the interconnection between the hard scale Q (where pQCD works) and a small scale $Q_0 \sim 1$ GeV (where pQCD starts to break down). During this stage all the colored particles emit mostly collinear and soft gluons. Partonic degrees of freedom are converted into hadrons (yellow circles) via hadronization model. The hadronization stage (white blobs) goes through cluster hadronization in this case. Due to the fact that many hadrons formed in

the hadronization stage are not stable they decay. Last but not least, there may be additional hard process called multiple partonic interactions (MPI, not illustrated in the sketch).

All the steps are here briefly discussed. The more detailed summary can be found in [86, 87, 88]. The simulation of hard processes in the leading order is straightforward in generators like PYTHIA [89, 90], HERWIG(++) [91, 92] or SHERPA [93, 94]. Basically each event generator works in the tree level. Some generators developed methods to incorporate next-to-leading order corrections, which are merged with parton showers. There are several methods of showering used in different generators. The transverse momentum ordered parton showers interleaved with MPI are used in PYTHIA. Angular ordered parton showers are used in HERWIG++, while SHERPA uses Catani-Seymour dipole factorization formalism. There are much more showering methods used in MC generators. Finally, one needs to use hadronization to get colorless hadrons. There are two main models of hadronization. The Lund string fragmentation model [95] is used in PYTHIA, while Cluster model [96] is used in SHERPA and HERWIG.

The LUND model assumes the potential energy of color sources like e.i. a quark and an antiquark (the endpoints of string spanned among them) which are separated by a large distance. The energy increases linearly with the separation distance. When a distance is much larger than ~ 1 fm the string breaks down and a new pair of quark and antiquark is created. In that picture a kink in a string is associated to a gluon.

A cluster hadronization model is based on preconfinement of parton showers. The clusters which are parton combinations, namely gluons, are treated as excited prehadronic states. They split into quark-antiquark pairs (or diquark-antidiquark pairs). Clusters are formed from color-connected pairs. In most cases clusters decay sequentially quasi two body in the phase space.

At the end of generation chain stands the treatment of hadronic decays. They play an important role because the output of hadronization are not always stable and detectable particles, but excited resonance states which decay down to stable particles. There are sophisticated models with proper treatment of matrix elements for decays modes, spin correlations or radiative returns which describe decays.

The recent searches indicate the importance of MPI. They are much softer than major hard process, but are still hard processes, and can be interleaved with parton showers, etc coming from major hard scattering. These processes also produce additional particles in the available phase space in the final state. There are different applications of MPI in different generators. As an example a mechanism in HERWIG++ is based on color reconnection model [97] (a similar mechanism had been included to PYTHIA). The color reconnection means that partons can be color-connected when they are close in phase space and they can emerge from different partonic interactions. The measure of distance is done via the partons invariant mass in such a way that a distance is small when the invariant mass of partons cluster is small.

On top of that MC generators provide sets of (nuclear) parton density functions and fragmentation functions we can change and tune.

There are much more generators which are stand-alone projects (like heavy ion collision generator EPOS [98, 99] which is based on Gribov-Regge theory) or base on already written components (e.i. base on PYTHIA showering) and change only few parts of them (like multi purpose generator HIJING [100] which do heavy ion collision generation with mini-jet production or nuclear shadowing).

CHAPTER III

INTRODUCTION TO NEUTRAL MESONS

The π mesons were proposed in the 1935 by Hideki Yukawa as exchange particles carrying the strong nuclear force [101]. The charged pions were discovered in 1947 by C. F. Powell et al. in the photographic emulsion based cosmic experiment [102]. Neutral pions are electrically neutral and do not leave any track. They existence was first deduced from its decay products. The final confirmation came from cyclotron results [103] in 1950 where π^0 meson was identified via double photonic decay.

Charged and neutral pions have nearly identical masses. The charged and neutral pion mass is 139.57061 ± 0.00024 MeV/c^2 [104] and 134.9770 ± 0.0005 MeV/c^2 [104][1], respectively. The mass difference is therefore $m_{\pi^\pm} - m_{\pi^0} = 4.5936 \pm 0.0005$ MeV/c^2 [104]. Almost the same mass imply that a symmetry is involved. Pions are assigned to the triplet representation (or adjoint representation **3**) of $SU(2)$ flavor symmetry (or isospin I symmetry) Lie group.

The η meson was discovered in 1961 in the $\pi^+\pi^-\pi^0$ decay mode [105] at the Bevatron accelerator [106] in Lawrence Berkeley National Laboratory in US. Currently, the η meson mass is known to be 547.862 ± 0.017 MeV/c^2 [104].

When more and more particles were discovered Gell-Mann presented The Eightfold Way [107, 108] in 1961 to classify hadrons and, among the others, predicted existence of missing η' resonance. Gell-Mann [109], independently to Zweig [110, 111] presented the quark model later on in 1964. The model considered only three types of fundamental objects (currently known as u, d and s quarks) and their anti-partners. According to Gell-Mann composite particles like pions, etas and kaons are arranged in the pseudo-scalar mesons nonet in the electric charge Q and strangeness S space, like shown in Fig. **III-1**. The pseudo-scalar meson means that they have total spin $J = 0$ and odd P-parity. In addition, π^0 and η mesons have even C-parity. Usually, it is noted as $J^{PC} = 0^{-+}$ [104]. They both have no strangeness, neither charm nor bottomness, $S = C = B = 0$. Very important is quark content of these two neutral mesons. The π^0 meson is a combination of quark and antiquark states:

$$\pi^0 = \frac{1}{\sqrt{2}}(u\bar{u} - d\bar{d}). \qquad \textbf{(III.1)}$$

The η meson quark content is a linear combination of η_1 and η_8 $SU(3)$ states of strong forces. The

[1] Currently the π^0 meson mass is calculated from the charged pion mass and the mass difference between charged and neutral pion.

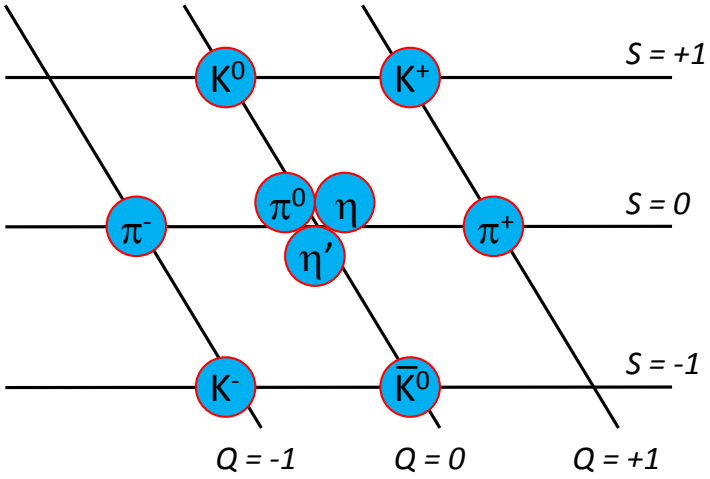

FIGURE III-1: The pseudo-scalar mesons nonet.

η_1 is a singlet state and η_8 is a part of an octet state of SU(3) symmetry. They quark content state can be written as:

$$\eta_1 = \frac{1}{\sqrt{3}}(u\bar{u} + d\bar{d} + s\bar{s}) \qquad \textbf{(III.2)}$$

and

$$\eta_8 = \frac{1}{\sqrt{6}}(u\bar{u} + d\bar{d} - 2s\bar{s}). \qquad \textbf{(III.3)}$$

One needs to notice that π^0, η_1 and η_8 are mutually orthogonal linear combinations of the quark pairs $u\bar{u}$, $d\bar{d}$ and $s\bar{s}$. Due to the electroweak mixing one gets:

$$\begin{pmatrix} \eta \\ \eta' \end{pmatrix} = \begin{pmatrix} \cos\theta_P & -\sin\theta_P \\ \sin\theta_P & \cos\theta_P \end{pmatrix} \begin{pmatrix} \eta_8 \\ \eta_1 \end{pmatrix}, \qquad \textbf{(III.4)}$$

where $\theta_P = -11.5^\circ$ is a pseudo-scalar singlet-octet mixing angle [104], and η or η' are real observed particles.

The π^0 and η mesons are well known particles. They have been observed in plenty of experiments and their decay modes have been studied. After the short introduction we are going to concentrate on the production spectra of π^0 and η mesons and their ratios in the remaining part of this chapter. Some aspects of neutral meson studies like so called "seagull" effect, Bubble Chamber measurements which were based on photons (but not reconstructed invariant mass of two photons) or the single spin asymmetries results coming from polarized beams will be not discussed.

The first transverse momentum spectra measurements of π^0 and η mesons together with further measurements are mentioned and tabularized in Sec. **III.1**. The important conclusions coming from the results of extensively studied neutral mesons are discussed in Sec. **III.2**. The spectra were mostly used to constrain parton distribution functions of many incidental projectiles as well

as to constrain neutral pion and η meson fragmentation functions. The common parameterization of spectra for the broad range of energy has been investigated among decades. In particular, η/π^0 cross-section ratio and commonly used m_{T} scaling are discussed in Sec. **III.3** in this context. Section **III.4** presents the view on the neutral meson production in hadronic collisions from the perspective of theoretical rather than empirical description. The results concerning neutral meson which have been studied in both cold and hot nuclear matter formed in nuclear collisions are summarized in Sec. **III.5**.

III.1 Previous measurements

The transverse momentum spectra of neutral mesons, like π^0 or η, have been measured in the variety of experiments. The first results for the intermediate meson transverse momentum range coming from the accelerator experiment were carried out at the Intersecting Storage Ring (ISR) at CERN in 70's. The ISR provided pp collisions at five center-of-mass collision energies $\sqrt{s} = 23.5$, 30.6, 44.8, 52.7 and 62.4 GeV. The invariant cross-section ($E\frac{\mathrm{d}^3\sigma}{\mathrm{d}p^3}$) spectra of the π^0 meson have been measured in the central region (polar angle $\theta = 90^\circ$) in a wide transverse momentum range $2.5 < p_{\mathrm{T}} < 9$ GeV/c [112, 113, 114]. The π^0 meson was reconstructed in double photonic channel. Results were first confirmed by experiments which measured photons and assumed that every photon is coming from π^0 decay. We can recall here the experiment [115] at the energies available at the ISR and fix target experiments [116, 117, 118] at Fermi National Accelerator Laboratory (FNAL) in US. Later, the confirmation of results with π^0 reconstructed in double photonic decay mode came with the other ISR experiment [119]. The π^0 production spectra have been measured in pp collisions at the center-of-mass energies $\sqrt{s} = 23.6$, 30.8, 45.1, 53.2 and 62.9 GeV at angles $\theta = 90^\circ$ and $\theta = 53^\circ$ in a range covering $0.5 < p_{\mathrm{T}} < 8$ GeV/c.

The η meson production spectra have also been measured by [113, 114] in pp collisions at $\sqrt{s} =$ 30.6, 44.8, 52.7 and 62.4 GeV in the range $3 < p_{\mathrm{T}} < 5.6$ GeV/c [2]. The η meson was reconstructed from two photons with $BR(\eta \to \gamma\gamma) = 0.38$, which is slightly lower than currently known [104]. The ratio of production cross-section η/π^0 was found to be 0.55 ± 0.10 above $p_{\mathrm{T}} = 3$ GeV/c. This result has been confirmed by the other ISR experiment [119] where η production spectrum coming from pp collisions at $\sqrt{s} = 53.2$ GeV has been measured in the range $3 < p_{\mathrm{T}} < 4.5$ GeV/c and η to π^0 cross-section ratio was about 0.5.

Further, π^0 or η meson production cross-section spectra as well as the ratio of cross-sections η/π^0 have been measured in various systems (pp, $\pi^{\pm}p$, $\mathrm{K}^{\pm}\mathrm{p}$, $\mathrm{p\bar{p}}$) for many polar angle θ (or pseudo-rapidity $\eta = -\ln[\tan(\theta/2)]$) ranges in many experiments at ANL (bubble chamber experiments) [120, 121, 122, 123], ISR [124, 125, 126, 127, 128, 129, 130, 131, 132, 133, 134, 135, 136, 137, 138, 139, 140, 141, 142], experiments of Carey [143, 144], M2 [145, 146, 147, 148, 149, 150, 151, 152, 153], bubble chamber experiment [154], E704 [155], E706 [156, 157, 158, 159, 160] at FNAL, bubble chamber experiments [161, 162, 163, 164, 165, 166, 167, 168] at CERN, NA24 [169], UA2 [170, 171], ACCMOR [172], WA69 [173, 174], WA70 [175, 176, 177] and UA6 collaboration [178, 179], NA27 [180, 181] at SPS, CDF [182] collaboration at Tevatron,

[2] Only production spectrum for the collision energy $\sqrt{s} = 52.7$ is shown in both papers [113, 114].

PHENIX [50, 183, 184, 185, 186, 187, 188, 189] and STAR [190, 191, 192, 193, 194] collaboration at RHIC. The collection of experiments with the published π^0 meson production cross-section is shown in Table **III-1**, where the collision system, the approximate p_T range and the center-of-mass collision energy $\sqrt{s}$ [3] (p_{lab} in case of a fix target experiment) are indicated. The collection of experiments with the published η meson production cross-section or the η/π^0 cross-section ratio is shown in Table **III-2**, where the collision system, the approximate p_T range and the center-of-mass collision energy $\sqrt{s}$ (p_{lab} in case of a fix target experiment) and the cross-section ratio η/π^0 are indicated.

Although the inclusive production spectra of pions in proton-deuteron collisions were studied in FNAL [195] they had measured charged pion spectra first. The neutral pion spectra in pd as well as in deuteron-deuteron collisions were measured at ISR [196] for the first time. The p_T range of π^0 meson production spectra measured in pd collisions at $\sqrt{s_{NN}} = 37.2$ and 44.1 GeV and in dd collisions at $\sqrt{s_{NN}} = 26.3$ and 31.6 GeV is $2.3 < p_T < 4.5$ GeV/c.

The other hadron-nuclei collision experiments were carried out at FNAL [197, 198, 199, 200, 159], KEK [201], by Karabarbounis [202], and in BCMOR [137] at ISR, in NA3 [203], in HELIOS [204], in TAPS/CERES [205], in WA80 [206, 207, 208], WA98 [209] at SPS, in PINOT [210] at SATURNE in Saclay, in PHENIX [211, 50, 185] at RHIC, in HADES [212] at GSI. The collection of experiments with the published π^0 or η meson production cross-section or the η/π^0 cross-section ratio in hadron-nucleus collisions is shown in Table **III-3** or Table **III-4**, respectively. Nuclei-nuclei collisions have been studied by Karabarbounis [202] at ISR, WA80 [206, 207, 208, 213, 214, 215], WA98 [216, 217, 218, 219] at SPS, TAPS [220, 221, 222, 223, 224, 225] at SIS in GSI and at RHIC in PHENIX [50, 226, 227, 228, 229, 230, 231, 232, 233, 234, 235, 236, 237, 238, 239] and STAR [240, 241]. The collection of experiments with the published π^0 or η meson production cross-section or the η/π^0 cross-section ratio in nuclear collisions is shown in Table **III-5** or Table **III-6**, respectively. Results from other experiments after the first ALICE neutral meson publication are given for completeness.

[3] The center-of-mass energy is calculated according to the formula $\sqrt{s} = E^{CMS} = \sqrt{m_1^2 + m_2^2 + 2p_{lab}m_2}$, where m_1 is a beam particle mass and m_2 is a fix target particle mass.

Experiment (Author/Year)	System	$\sqrt{s}$ (GeV)	p_{lab} (Gev/c)	p_{T} range	Ref.
ISR (Büsser 73, 74, 75)	pp	23.5, 30.6, 44.8		2.5 – 9	[112, 113, 114]
ISR (Büsser 73, 74, 75)	pp	52.7, 62.4		2.5 – 9	[112, 113, 114]
ANL (Campbell 73)	pp	5.	12.4	0 – 0.6	[120]
ANL (Swanson 74)	pp	5.	12.4	0 – 0.6	[121]
ANL (Jaeger 75)	pp	5.	12.4	0 – 0.6	[122]
ISR (Eggert 75)	pp	23.6, 30.8, 45.1		1.5 – 8	[119]
ISR (Eggert 75)	pp	53.2, 62.9		1.5 – 8	[119]
FNAL (Carey 76)	pp	9.7 – 27.5	50 – 400	0.3 – 4	[144]
FNAL M2 (Donaldson 76)	$\pi^{\pm}$p, pp	13.8, 19.4	100, 200	1 – 5	[145]
ISR (Darriulat 76)	pp	45, 53		1.6 – 3.8	[124, 125]
ISR (Clark 78)	pp	53, 63		5.25 – 16.5	[126]
ISR (Angelis 78)	pp	30.7, 53.1, 62.4		3.5 – 14	[127]
ISR (Clark 78)	pp	52.7		2.69 – 5.09	[196]
ISR (Amaldi 79)	pp	53.2		2.1 – 5.1	[128]
ISR (Kourkoumelis 79)	pp	30.6, 52.7, 62.4		3 – 6	[130]
ISR (Kourkoumelis 79)	pp	52.7, 62.4		7 – 15	[131]
ISR (Kourkoumelis 80)	pp	30.6, 44.8, 52.7, 62.8		3 – 16	[133]
ISR (Lloyd Owen 80)	pp	23, 53		1 – 4.25	[134]
PS (Ajinenko 80)	K^+p	7.8	32	0 – 1	[163]
SPS (Poiret 81)	$\bar{\mathrm{p}}$p	7.9	32	0 – 0.75	[164]
ISR (Anassontzis 82)	pp	63		3 – 12	[135]
ISR (Angelis 82)	p$\bar{\mathrm{p}}$, pp	52.7		1.25 – 5	[136]
UA2 (Banner 82)	p$\bar{\mathrm{p}}$	540		1.5 – 4.5	[170]
ISR AFS (Akesson 83)	pp	63		1 – 4	[138]
BCGMNS (Barth 84)	K^+p	11.5	70	0 – 1.34	[165]
ISR AFS (Akesson 85)	p$\bar{\mathrm{p}}$, pp	53		2 – 6	[139]
UA2 (Banner 85)	p$\bar{\mathrm{p}}$	540		6.25 – 40	[171]
ACCMOR (Pauss 85)	π^-p, K^-p	10.5	58	0 – 0.8	[172]
ISR (Angelis 86)	p$\bar{\mathrm{p}}$, pp	52.7		1.25 – 10	[142]
BCMOR (Angelis 87)	pp	31		3 – 9	[137]
NA24 (87)	$\pi^{\pm}$p, pp	23.8	300	1.25 – 7	[169]
UA6 (87)	p$\bar{\mathrm{p}}$, pp	24.3		2.5 – 5.1	[178]
WA70 (87)	$\pi^{\pm}$p	23	280	4 – 7	[175]
FNAL M2 (Kennett 87)	π^-p	13.8 – 19.4	100 – 200	0 – 2.24	[153]
NA22 (87)	π^+p, K^+p, pp	21.7	250	0 – 1.6	[168]
NA27 (87)	π^-p	26	360	0 – 4	[180]
WA70 (88)	pp	23	280	4 – 6.5	[176]
ISR AFS (Akesson 90)	pp	63		4.5 – 11	[141]
NA27 (91)	pp	27.5	400	0.2 – 1.6	[181]
WA69 (91)	πp, Kp	12.3 – 16.2	80 – 140	0 – 2.4	[173]
E704 (94)	p$\bar{\mathrm{p}}$, pp	19.4	200	1 – 4.5	[155]
UA6 (98)	p$\bar{\mathrm{p}}$, pp	24.3		4.1 – 7.7	[179]
E706 (03)	pp	31.6	530	1 – 9	[159]
E706 (03)	pp	38.8	800	1 – 12	[159]
PHENIX (03, 06, 07)	pp	200		1 – 20	[183, 185, 184]
E706 (04)	π^-p	31.1	515	1 – 10	[160]
STAR (04)	pp	200		1.5 – 2.2	[190]
PHENIX (09)	pp	62.4		1 – 7	[186]
STAR (09,10)	pp	200		1 – 17	[241, 192]
STAR (14)	pp	200		5 – 16	[194]
PHENIX (16)	pp	510		1 – 30	[189]

TABLE III-1: Hadron-hadron collisions with a published π^0 production cross-section. For each experiment the collision system, the center-of-mass energy $\sqrt{s}$ (p_{lab} in case of fixed-target energy), the p_{T} range is quoted. The publications below the line came after the first ALICE neutral meson publication.

Experiment (Author/Year)	System	$\sqrt{s}$ (GeV)	p_{lab} (Gev/c)	p_{T} range	η/π^0 ratio	Ref.
ISR (Büsser 75, 76)	pp	52.7		$3-5$	0.55 ± 0.10	[113, 114]
ISR (Eggert 75)	pp	53.2		$3-4.5$	~ 0.5	[119]
PS (Borg 76)	K^+p	5.3	14.3	$0-1.4$	0.18 ± 0.07	[161]
PS (Bartke 77)	π^+p	5.6	16	$0-1.4$	–	[162]
FNAL M2 (Donaldson 78)	$\pi^\pm$p, pp	13.8, 19.4, 23.8	100, 200, 300	$1.6-4$	0.44 ± 0.05	[146]
FNAL M2 (Donaldson 78)	$K^\pm$p	13.8, 19.4, 23.8	100, 200, 300	$1.6-4$	0.74 ± 0.12	[146]
FNAL (Kass 79)	pp	27.5	400	low-p_{T}	<0.05	[154]
ISR (Amaldi 79)	pp	30.6		$0.9-3$	–	[129]
ISR (Amaldi 79)	pp	53.2		$3-5$	0.5 ± 0.07	[129]
ISR (Kourkoumelis 79)	pp	31, 53, 62		$3-11$	0.55 ± 0.07	[132]
ANL (Levman 80)	$\bar{\mathrm{p}}$p	<1.8	<0.7	low-p_{T}	<0.11	[123]
ISR AFS (Akesson 83)	pp	63		$2-4$	0.46 ± 0.07	[138]
EHS-RCBC (Bailly 84)	pp	26	360	$0-2$	~ 0.22	[166]
BEBC (Chakrabarti 85)	p$\bar{\mathrm{p}}$	4.9	12	<1	0.25 ± 0.15	[167]
ISR AFS (Akesson 85)	p$\bar{\mathrm{p}}$, pp	53		$2-6$	0.55 ± 0.04	[139]
UA2 (Banner 85)	p$\bar{\mathrm{p}}$	540		$3-6$	$0.60\pm0.04\pm0.15$	[171]
ISR AFS (Akesson 86)	pp	63		$0.2-1.5$	0.07 ± 0.055	[140]
UA6 (Antille 87)	p$\bar{\mathrm{p}}$	24.3		$2.5-4$	0.458 ± 0.046	[178]
UA6 (Antille 87)	pp	24.3		$2.5-4$	0.482 ± 0.040	[178]
NA27 (87)	π^-p	26	360	$0-4$	0.34 ± 0.06	[180]
WA70 (89)	pp	23	28 0	$4-7$	$0.45\pm0.02\pm0.04$	[177]
WA70 (89)	π^+p	23	280	$4-7$	$0.44\pm0.03\pm0.04$	[177]
WA70 (89)	π^-p	23	280	$4-7$	$0.48\pm0.02\pm0.04$	[177]
NA27 (91)	pp	27.5	400	$0.2-1.6$	-	[181]
WA69 (92)	πp, Kp	$12.3-16.2$	$80-140$	$0-1.8$	$0.1-0.45$	[174]
CDF (93)	$\bar{\mathrm{p}}$p	1800		12.0	$1.05\pm0.15\pm0.23$	[182]
UA6 (98)	$\bar{\mathrm{p}}$p	24.3		$4.1-7.7$	0.52 ± 0.02	[179]
UA6 (98)	pp	24.3		$4.1-7.7$	0.48 ± 0.02	[179]
E706 (03)	pp	31.6	530	$3-8$	0.41 ± 0.03	[159]
E706 (03)	pp	38.8	800	$3-10$	0.44 ± 0.03	[159]
E706 (04)	π^-p	31.1	515	$3-8$	0.41 ± 0.05	[160]
PHENIX (06)	pp	200		$2-12$	0.48 ± 0.03	[50, 185]
PHENIX (10)	pp	200		$2-20$	0.51 ± 0.01	[187]
STAR (10)	pp	200		$1-14$	0.46 ± 0.05	[192]
PHENIX (14)	p$^\uparrow$p	200		$0.5-5$	–	[188]

TABLE III-2: Hadron-hadron collisions with a published η production cross-section or an η/π^0 ratio. For each experiment the collision system, the center-of-mass energy $\sqrt{s}$ (p_{lab} in case of fixed-target energy), the p_{T} range, the η/π^0 ratio is quoted. If two uncertainties are given, the first one is statistical, the second one is systematic. The publications below the line came after the first ALICE neutral meson publication.

Experiment (Author/Year)	System	$\sqrt{s_{\rm NN}}$ (GeV)	$p_{\rm lab}$ (Gev/c)	$p_{\rm T}$ range	Ref.
ISR (Clark 78)	pd	37.2		2.1 – 4.47	[196]
ISR (Clark 78)	pd	44.1		2.1 – 4.9	[196]
FNAL (Baltrusaitis 80)	pBe	19.4, 23.8, 27.5	200, 300, 400	1.5 – 6	[197]
KEK (Kanzaki 81)	pBe	5.1	12	1 – 2.1	[201]
ISR (Karabarbounis 81)	αp	44		2 – 5.5	[202]
E629 (Povlis 83)	pBe, π^+Be	19.4	200	2.15 – 3.80	[199]
E629 (Povlis 83)	pC, π^+C	19.4	200	2.15 – 4.75	[199]
E629 (Povlis 83)	pAl, π^+Al	19.4	200	2.15 – 4.25	[199]
E515 (Delchamps 85)	pBe	23.8	300	2.5 – 5	[200]
ISR NA3 (86)	pC, $\pi^\pm$C, (KC)	19.4	200	2.9 – 6	[203]
E706 (92, 93)	π^-Be, π^-Cu	30.6	500	3 – 10	[156, 157]
E706 (92, 93)	pBe, pCu	30.6	500	4 – 10	[156, 157]
HELIOS (95)	pBe	29.1	450	0 – 1.5	[204]
TAPS/CERES (98)	pBe, pAu	29.1	450	0.02 – 1.3	[205]
E706 (98)	π^-Be	31.6	515	3 – 12	[158]
E706 (03)	pBe	31.6	530	1 – 10	[158, 159]
E706 (03)	pBe	38.8	800	1 – 12	[158, 159]
E706 (04)	π^-Be	31.1	515	1 – 12	[160]
WA80 (88)	pAu	10.7	60	0.4 – 2	[206, 208]
WA80 (88, 90, 91)	pAu	19.4	200	0.4 – 2.8	[206, 207, 208]
PHENIX (03, 07)	dAu	200		1 – 18	[211, 185]
WA98 (08)	pC, pPb	17.4	160	0.7 – 3.5	[209]
STAR (10)	dAu	200		1 – 17	[192]
HADES (13)	pNb	3.18	3.5	0.25 – 1.5	[212]

TABLE III-3: Hadron-nucleus collisions with a published π^0 production cross-section. For each experiment the collision system, the center-of-mass energy $\sqrt{s}$ ($p_{\rm lab}$ in case of fixed-target energy), the $p_{\rm T}$ range is quoted. For the KEK result, instead of one average result the range is quoted. The publications below the line came after the first ALICE neutral meson publication.

III.2 Parameterizations

During last fifty years π^0 and η mesons have been studied a lot. There are few remarks coming from the past analyses. The inclusive production cross-section spectra have been measured in a broad range of the collision energy spanning three orders of magnitude ($\sqrt{s_{\rm NN}} = 3 - 1800$ GeV). Neutral mesons were produced mostly in central region, however there are also measurements for other rapidity, y (polar angle, θ) regions. The π^0 meson production spectra have been measured mostly in soft and intermediate $p_{\rm T}$ range. However, there is one result where transverse momentum range was extended up to $p_{\rm T} = 40$ GeV/c. The η meson production spectrum has been measured up to $p_{\rm T} = 12$ GeV/c. The $x_{\rm T} = 2p_{\rm T}/\sqrt{s_{\rm NN}}$ range probed was in the range $0.01 < x_{\rm T} < 0.5$.

Neutral meson production has been studied in simple e^+e^- or hadron-hadron systems (not only in pp collisions but also in p$\bar{\rm p}$, $\pi^\pm$p and Kp) and variety of more complex hadron-nucleus and nucleus-nucleus collisions. The neutral meson production in variety of experiments where e^+e^- beams were collided are not described here. Although, the tremendous outcome from them was to constrain fragmentation functions (see [50] for summary and [84, 85] for the latest sets of

Experiment (Author/Year)	System	$\sqrt{s_{\rm NN}}$ (GeV)	$p_{\rm lab}$ (GeV/c)	$p_{\rm T}$ range	η/π^0 ratio	Ref.
FNAL (Baltrusaitis 79)	pBe	19.4, 23.8, 27.5	200, 300, 400	$2.5-5$	0.47 ± 0.10	[198]
KEK (Kanzaki 81)	pBe	5.1	12	$0.7-1.5$	$0.119-0.226$	[201]
ISR (Karabarbounis 81)	αp	44		$2.5-3$	0.51 ± 0.15	[202]
E629 (Povlis 83)	pBe	19.4	200	$2.4-3.70$	–	[199]
E629 (Povlis 83)	pC	19.4	200	$2.4-4.5$	0.53 ± 0.03	[199]
E629 (Povlis 83)	pAl	19.4	200	$2.4-2.85$	–	[199]
E629 (Povlis 83)	π^+C	19.4	200	$2.4-3.2$	–	[199]
E515 (Delchamps 85)	pBe	23.8	300	$2.5-5$	0.47 ± 0.03	[200]
E706 (93)	π^-Be	30.6	500	$4-8$	$0.44\pm0.05\pm0.05$	[157]
E706 (93)	pBe	30.6	500	$4.5-7$	$0.44\pm0.06\pm0.05$	[157]
HELIOS (95)	pBe	29.1	450	$0-1.5$	0.057 ± 0.007	[204]
TAPS/CERES (98)	pBe	29.1	450	$0.02-2.7$	$6.9\pm0.5\%$	[205]
TAPS/CERES (98)	pAu	29.1	450	$0.02-2.7$	$8.8\pm1.1\%$	[205]
E706 (03)	pBe	31.6	530	$3-9$	0.45 ± 0.01	[159]
E706 (03)	pBe	38.8	800	$3-12$	0.42 ± 0.01	[159]
E706 (04)	π^-Be	31.1	515	$3-10$	0.48 ± 0.01	[160]
PHENIX (06, 07)	dAu	200		$2-12$	0.47 ± 0.03	[50, 185]
STAR (10)	dAu	200		$1-14$	0.44 ± 0.08	[192]
HADES (13)	pNb	3.18	3.5	$0-1.5$	–	[212]

TABLE III-4: Hadron-nucleus collisions with a published η production cross-section or an η/π^0 ratio. For each experiment the collision system, the center-of-mass energy $\sqrt{s}$ ($p_{\rm lab}$ in case of fixed-target energy), the $p_{\rm T}$ range, the η/π^0 ratio is quoted. The publications below the line came after the first ALICE neutral meson publication.

fragmentation functions which contain BELLE and BABAR results as well as coming from RHIC and LHC). One also needs to remember that HERA data brought very valuable measurements on parton density functions in DIS and photo-production (for the recent review see [242, 243, 244]).

The data normalization sometimes do not agree and direct comparison between experiments is not possible or not accurate. Ratios where normalization is cancelled are more adequate.

Based on the isospin symmetry [245] the π^0 differential cross-section is the half of the differential cross-section of charged pions in pp interactions,

$$\frac{{\rm d}\sigma}{{\rm d}p}(\pi^0) = \frac{1}{2}\left[\frac{{\rm d}\sigma}{{\rm d}p}(\pi^+) + \frac{{\rm d}\sigma}{{\rm d}p}(\pi^-)\right] \qquad \textbf{(III.5)}$$

It was shown by ANL experiment [122] and confirmed also in others.

The studies of structure functions for different particles have been carried out via π^0 production from different beams [147]. The cross-section ratio

$$R(A/B) = \frac{E{\rm d}\sigma(Ap\to\pi^0X)/{\rm d}p^3}{E{\rm d}\sigma(Bp\to\pi^0X)/{\rm d}p^3}, \qquad \textbf{(III.6)}$$

where A and B are $\pi^\pm$, K^-, p, $\bar{\rm p}$, has been measured for few incident angles and range $1 < p_{\rm T} < 4$ GeV/c. It was noticed that pion and kaon have a similar structure function (the ratio $R(\pi/K)$

Experiment (Author/Year)	System	$\sqrt{s_{\mathrm{NN}}}$ (GeV)	p_{lab} (Gev/c)	p_{T} range	Ref.
ISR (Clark 78)	dd	26.3		2.1 – 4.68	[196]
ISR (Clark 78)	dd	31.6		2.3 – 4.66	[196]
ISR (Karabarbounis 81)	αα	30.6		2 – 4.5	[202]
BCMOR (Angelis 87)	dd, αα	31		3.5 – 9	[137]
WA80 (88)	OAu	10.7	60	0.4 – 2.6	[206, 208]
WA80 (88)	OAu	19.4	200	0.4 – 3	[206, 207, 208]
WA80 (88)	OC	10.7	60	0.4 – 2.4	[206]
WA80 (88)	OC	19.4	200	0.4 – 2.4	[206, 208]
TAPS (91, 94)	ArCa	1.9	1.0	0 – 0.9	[220, 222, 223]
TAPS (91)	NeAl	1.6	0.35	0 – 0.2	[220]
TAPS (93)	XeAu	1.4	0.044	0.005 – 0.1	[221]
TAPS (94)	KrZr	1.9	1.0	0 – 1.05	[222]
TAPS (94)	AuAu	1.9	1.0	0 – 0.95	[222]
TAPS (94)	ArCa	2.1	1.5	0 – 1.25	[223]
TAPS (97)	CC	1.8, 1.9	0.8, 1	0 – 0.9	[224]
TAPS (97)	CC	2.7	2	0 – 1.4	[224]
TAPS (97)	CAu	1.8	0.8	0 – 0.7	[224]
WA80 (94, 95)	SS	19.4	200	0.3 – 3	[213, 214, 215]
WA80 (94, 95)	SAu	19.4	200	0.3 – 4	[213, 214, 215]
WA98 (96, 98, 00, 02)	PbPb	17.3	158	0.3 – 4.1	[216, 217, 218, 219]
WA98 (01)	PbNb	17.3	158	0.3 – 3.1	[219]
PHENIX (02)	AuAu	130		1 – 4	[226]
TAPS (03)	NiNi	2.7	1.9	0 – 1	[225]
TAPS (03)	CaCa	2.7	20	0 – 1	[225]
PHENIX (03, 08, 12)	AuAu	200		1 – 20	[227, 229, 231, 236]
STAR (04)	AuAu	130		0.5 – 3	[240]
PHENIX (08)	CuCu	22.4		1 – 5	[230]
PHENIX (08)	CuCu	62.4		1 – 8	[230]
PHENIX (08)	CuCu	200		1 – 18	[230]
STAR (09)	AuAu	200		1 – 12	[241]
PHENIX (12)	AuAu	39		1 – 8	[236]
PHENIX (12)	AuAu	62.4		1 – 10	[236]
PHENIX (18)	CuAu	200		1 – 20	[238]
PHENIX (18)	UU	192		1 – 18	[239]

TABLE III-5: Nucleus-nucleus collisions with a published π^0 production cross-section. For each experiment the collision system, the center-of-mass energy $\sqrt{s_{\mathrm{NN}}}$ (p_{lab} in case of fixed-target energy), the p_{T} range is quoted. The publications below the line came after the first ALICE neutral meson publication.

is constant and has different value for different energies), however different from the proton one (the ratio $R(p/\pi)$ is falling with increasing p_{T}). The similar dependence was confirmed in hadron-nucleus experiment [203], where different particles were collided with Carbon target. The studies with neutral pions are mentioned here, but this subject was extensively studied for charged hadrons (see [246, 247]).

There was also a strong angular dependence observed. Spectra are the least steep in the central region ($y \sim 0$ or $\theta \sim 90^{\circ}$). Moving towards larger $|y|$ they become steeper and steeper (see i.e. [147]

Experiment (Year)	System	$\sqrt{s_{\rm NN}}$ (GeV)	$p_{\rm lab}$ (Gev/c)	$p_{\rm T}$ range	η/π^0 ratio	Ref.
ISR (Karabarbounis 81)	$\alpha\alpha$	30.6		$2.5-3$	1.0 ± 0.3	[202]
WA80 (88)	OC	19.4	200	$0.4-2.8$	$0.2-0.5$	[208]
TAPS (94)	ArCa	2.1	1.5	$0-0.9$	$(2.2\pm0.4)\%$	[223]
TAPS (94)	KrZr	1.9	1.0	$0-0.8$	$(1.3\pm0.6)\%$	[223]
TAPS (94)	AuAu	1.9	1.0	$0-0.8$	$(1.4\pm0.6)\%$	[223]
TAPS (94)	ArCa	1.9	1.0	$0-0.8$	$(1.9\pm1.2)\%$	[223]
WA80 (95)	SS	19.4	200	$0.5-1.5$	0.42 ± 0.13	[213, 214]
WA80 (95)	SAu	19.4	200	$0.5-3.5$	0.55 ± 0.07	[213, 214]
TAPS (97)	CC	1.8	0.8	$0-0.5$	$(3.1\pm1.1)\times10^{-}3$	[224]
TAPS (97)	CC	1.9	1	$0-0.5$	$(5.7\pm1.4)\times10^{-}3$	[224]
TAPS (97)	CC	2.7	2	$0-1.4$	$(36\pm4)\times10^{-}3$	[224]
WA80 (88)	OAu	19.4	200	$2-2.4$	0.61 ± 0.20	[208]
WA98 (00)	PbPb	17.3	158	$0.6-2.6$	$0.486\pm0.077\pm0.097$	[218]
TAPS (03)	NiNi	2.7	1.9	$0-0.7$	-	[225]
TAPS (03)	CaCa	2.7	20	$0-0.7$	-	[225]
PHENIX (06)	AuAu	200		$2-12$	0.40 ± 0.04	[50, 228]
PHENIX (10)	AuAu	200		$5-20$	-	[234]
PHENIX (13)	AuAu	200		$5-18$	0.45 ± 0.01	[237]
PHENIX (18)	CuAu	200		$2-20$	$0.5\pm0.01\pm0.02$	[238]
PHENIX (18)	UU	192		$2-14$	-	[239]

TABLE III-6: Nucleus-nucleus collisions with a published η production cross-section or an η/π^0 ratio. For each experiment the collision system, the center-of-mass energy $\sqrt{s}$ ($p_{\rm lab}$ in case of fixed-target energy), the $p_{\rm T}$ range, the η/π^0 ratio is quoted. If two uncertainties are given, the first one is statistical, the second one is systematic. The publications below the line came after the first ALICE neutral meson publication.

or [138]).

Based on [142], where pp and $\rm p\bar{p}$ collisions have been studied, the measured $\rm p\bar{p}/pp$ cross-section ratio versus $p_{\rm T}$ is around unity for the range $1.25 < p_{\rm T} < 10$ GeV/c (although there was a deviation from unity at large $p_{\rm T}$ in previous measurements [136]). The π^0 mesons are mostly the fragmentation product of gluons [248] and contribution from valence quark annihilation diagram is not dominant. The difference between the gluon structure function of the proton and antiproton is not expected.

The η/π^0 ratio depends on the colliding system because of a different quark content. It is similar for $\pi^{\pm}$p and pp collisions (~ 0.44) and differs for $K^{\pm}$p collisions (~ 0.74) [146]. The value of the ratio comes from a simple counting the relevant $q\bar{q}$ combinations taking into account up, down and strange quarks or antiquarks [249]. Besides parton fragmentation the direct production of π^0 and η mesons is expected (so called Higher Twist correction) [250]. The correction is of order of 10% but do not change the ratio by a large factor and gives the similar values.

It was found that π^0 production spectra, in the same way as charged particle production spectra, show less steep behaviour than extrapolated from low $p_{\rm T}$ ($p_{\rm T} < 1$ GeV/c) data (which show $\sim$

$\exp(-6p_{\mathrm{T}})$ behaviour) and the inclusive pion cross-section should follow the form

$$E\frac{\mathrm{d}^3\sigma}{\mathrm{d}p^3} = Ap_{\mathrm{T}}^{-n}\exp(-bx_{\mathrm{T}}), \tag{III.7}$$

where $x_{\mathrm{T}} = 2p_{\mathrm{T}}/\sqrt{s}$ is the scaling variable and A, n, b are fit parameters. The significant deviation from the purely exponential behaviour, suggests an increased contribution due to hard scattering of partons. It has been studied in parton models [251, 252, 253, 254, 255, 256, 257, 258, 259, 260, 261, 262], where power-law spectra are modified by fragmentation function. The low center-of-mass energy spectra were suggested to follow the radial scaling [263]. The empirical formula related to the radial scaling variable $x_{\mathrm{R}} = 2p/\sqrt{s}$ is following:

$$E\frac{\mathrm{d}^3\sigma}{\mathrm{d}p^3} = A(p_{\mathrm{T}}^2 + m^2)^N(1-x_{\mathrm{R}})^M, \tag{III.8}$$

where A, N, M are fit parameters.

Hagedorn [264] proposed a different empirical function:

$$E\frac{\mathrm{d}^3\sigma}{\mathrm{d}p^3} = Af(p_{\mathrm{T}}) = A\left(\frac{p_0}{p_{\mathrm{T}}+p_0}\right)^n, \tag{III.9}$$

where A, n, p_0 are fit parameters. This functional form has the following features at extrema:

$$f(p_{\mathrm{T}}) \to \begin{cases} 1-\frac{n}{p_0}p_{\mathrm{T}} \approx \exp(-\frac{n}{p_0}p_{\mathrm{T}}) & \text{for } p_{\mathrm{T}} \to 0, \\ \left(\frac{p_0}{p_{\mathrm{T}}}\right)^n & \text{for } p_{\mathrm{T}} \to \infty. \end{cases} \tag{III.10}$$

It has the exponential behaviour for low p_{T} and power-law for large p_{T}. However, the function is not unique when we consider experimental uncertainties. Data points can be parameterized by function with slightly modified fit parameters.

III.3 m_{T} scaling

The other parameterization which was used to describe data is so called the m_{T} scaling, which also comes from an empirical observation [265]. It assumes that the differential cross-section of a hadron h with a mass m_{h} as a function of the transverse mass of the produced particle $m_{\mathrm{T}} = \sqrt{m_{\mathrm{h}}^2 + p_{\mathrm{T}}^2}$ has the same shape $f(m_{\mathrm{T}})$ for all hadrons. The only difference is coming from the normalization factor C_{h} for various hadrons:

$$E\frac{\mathrm{d}^3\sigma}{\mathrm{d}p^3}(h) = C_{\mathrm{h}}f(m_{\mathrm{T}}). \tag{III.11}$$

The functional form which describes data in the broad range $0.2 < m_{\mathrm{T}} < 14$ GeV/c^2 can be written as:

$$f(m_{\mathrm{T}}) = (m_{\mathrm{T}}+a)^{-n}, \tag{III.12}$$

with parameters $a = 1.2$ and $n = 10$ [50]. The cross-section ratio of η and π^0 mesons can be written:

$$R_{\eta/\pi^0}(p_T) = E\frac{d^3\sigma}{dp^3}(\eta)/E\frac{d^3\sigma}{dp^3}(\pi^0) = R_{\eta/\pi^0} \cdot \left(\frac{a+\sqrt{m_\eta^2+p_T^2}}{a+\sqrt{m_{\pi^0}^2+p_T^2}}\right)^n, \qquad \textbf{(III.13)}$$

where $R_{\eta/\pi^0} = C_\eta/C_{\pi^0}$ is the asymptotic value of the η/π^0 ratio for large p_T.

The η/π^0 ratios coming from various experiments at various center-of-mass energies are plotted in Fig. **III-2**, **III-3**, **III-4** for hadron-hadron, hadron-nucleus and nucleus-nucleus collisions, respectively. The η/π^0 cross-section ratio in hh, hA and AA collisions, where h=p, $\bar{p}$, $\pi^\pm$ and

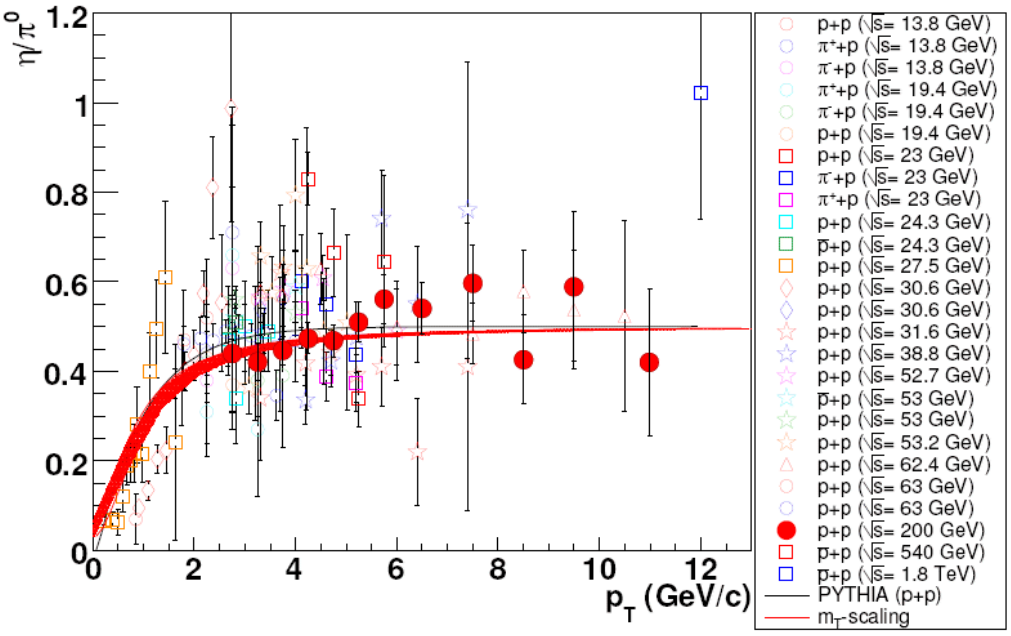

FIGURE III-2: The η/π^0 ratio as a function of transverse momentum, p_T measured in the hadron-hadron collisions. The black curve represents PYTHIA 6 [266] prediction for pp collisions at $\sqrt{s} =$ 200 GeV. The red band comes from m_T scaling prediction with parameters $a = 1.2$, $n = 10-14$, $R_{\eta/\pi^0} = 0.5$. Figure taken from [50].

A stands for nucleus, is rising rapidly with increasing p_T and then levels off at value 0.5 around $p_T \approx 3$ GeV/c.

It is very interesting that PYTHIA 6 [266] Monte Carlo (black solid line) generated for pp collisions at $\sqrt{s} = 200$ GeV describes the data points for every system and energy. It is an indication that the cross-section ratio is independent of the characteristics of the initial collision process, but depends on the ratio of η and π^0 meson fragmentation functions.

The red band in figures comes from m_T scaling prediction (Eq. **III.13**) with parameters $a = 1.2$, $n = 10-14$ and asymptotic value $R_{\eta/\pi^0} = 0.5$. It seems that m_T scaling shape is universal among energies and systems. The high-p_T part ($p_T > 3$ GeV/c) is well reproduced by many experiments,

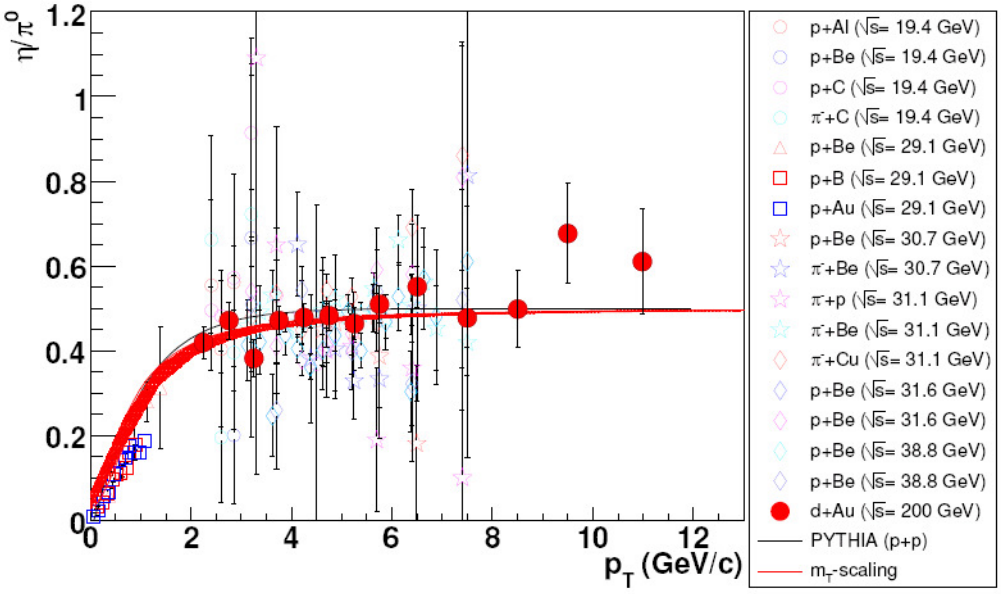

FIGURE III-3: The η/π^0 ratio as a function of transverse momentum, p_{T} measured in the hadron-nucleus collisions. The black curve represents PYTHIA 6 [266] prediction for pp collisions at $\sqrt{s} = 200$ GeV. The red band comes from m_{T} scaling prediction with parameters $a = 1.2$, $n = 10 - 14$, $R_{\eta/\pi^0} = 0.5$. Figure taken from [50].

although error bars are large. It is worth mentioning that in the low-p_{T} regime ($p_{\mathrm{T}} < 1$ GeV/c) the data description by m_{T} scaling is not very good. The π^0 yield at very low $m_{\mathrm{T}} < 0.4$ GeV/c^2 has plenty of contributions coming from resonance decays and the spectral shape is better described by Hagedorn parameterization (Eq. **III.9**) than by m_{T} scaling formula.

There were plenty of experiments which had measured η/π^0 ratio before the LHC era. However, their precision was not sufficient to probe m_{T} scaling with high statistics. Two experiments, NA27 (pp collisions at $\sqrt{s} = 27.5$ GeV) and PHENIX (pp collisions at $\sqrt{s} = 200$ GeV) provide the η/π^0 ratio with the highest accuracy at low-p_{T} ($p_{\mathrm{T}} < 1.6$ GeV/c) and high-p_{T} ($p_{\mathrm{T}} > 2.25$ GeV/c), respectively. PHENIX does not apply correction on secondary π^0 coming from weak decays which is used in ALICE. The correction is also not mentioned in the NA27 case. However, it does not change the final conclusions. Although the measurement provides world's most precise data points at low-p_{T} for the η/π^0 ratio it is not conclusive concerning m_{T} scaling violation. For $p_{\mathrm{T}} < 1$ GeV/c results show deviation from m_{T} scaling lying below the m_{T} scaling expectation curve (marked in the red color), however higher p_{T} points burdened with larger uncertainty lay above the expectation curve. In contrary to low energy experiment, the confirmation of scaling is observed for many particle species, such as kaons, ϕ and other in collisions at $\sqrt{s_{\mathrm{NN}}} = 200$ GeV [267]. The m_{T} scaling or violation magnitude and possibly the collision energy dependence can be clarified in future analysis at experiments at LHC.

Additional phenomena present in heavy ion collisions like strong collective radial flow observed at RHIC [268] can modify single particle spectra at low-p_{T}. Based on hydrodynamic flow

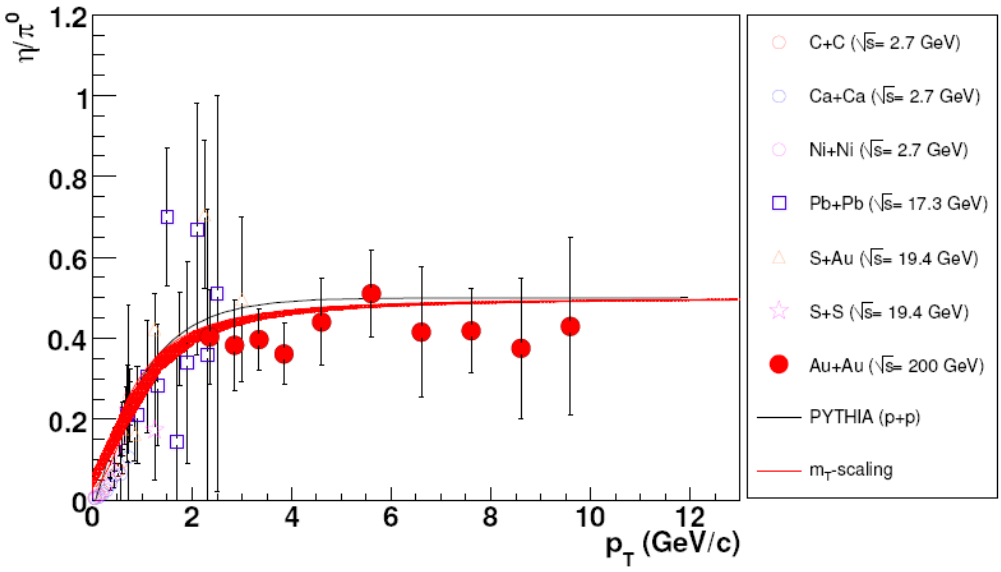

FIGURE III-4: The η/π^0 ratio as a function of transverse momentum, p_{T} measured in the nucleus-nucleus collisions. The black curve represents PYTHIA 6 [266] prediction for pp collisions at $\sqrt{s} =$ 200 GeV. The red band comes from m_{T} scaling prediction with parameters $a = 1.2$, $n = 10 - 14$, $R_{\eta/\pi^0} = 0.5$. Figure taken from [50].

one expects a larger boost for heavier particles and in consequence larger η/π^0 ratio in HIC in comparison to hadron-hadron collisions. Since the η meson is more than three times heavier than π^0 meson it can imply m_{T} scaling violation in the range of $p_{\mathrm{T}} < 2$ GeV/c [269]. The η/π^0 ratio can also serve as a discriminator of different parton recombination scenarios in hadron production in HIC [270].

The prediction of ratio coming from m_{T} scaling and PYTHIA 6 are very close to each other. The reason is that standard PYTHIA 6 uses Lund string fragmentation function [95]:

$$f(z) \sim z^{-1}(1-z)^{a} \exp\left(-b m_{\mathrm{T}}^2/z\right), \tag{III.14}$$

where a and b are free parameters adjusted to LEP results. The explicit dependence on m_{T} is visible.

III.4 Neutral mesons in hadron-hadron collisions

Having used the factorization theorem from Eq. **II.1** the differential cross-section of the inclusive production of neutral mesons can be described theoretically. The central piece of the description lies in the perturbative part of partonic hard scattering cross-section evaluation. The leading-order (LO) description [271, 272] and the next-to-leading order (NLO) corrections [273] have been calculated. Additionally, NLO corrections for polarized pp beams [274, 275] have been computed. The theoretical description of experimental data was satisfactory for high center-of-mass energy collider data. However, the low center-of-mass energy fixed target and also low center-of-mass

energy collider results were underpredicted [276, 277, 278] and there was increasing discrepancy towards larger rapidities. It forced to take a definite step of the re-summation to next-to-leading logarithmic accuracy [21], which made the theory to data agreement at low and high center-of-mass energies much better. However, RHIC data were overestimated at high-p_{T} values. It needed a further investigation in pQCD formalism or better choice or tuning of fragmentation functions. It has also been noticed that the agreement between theory and experiment depends on the choice of the factorization and renormalization scale μ.Although, at the time of first experiments which measured neutral meson production the discrepancy between data and theoretical description was significant, the pQCD calculations describes well the large increase of the observed cross-section from ISR through SpS and Sp$\bar{\mathrm{p}}$S to RHIC energies. The agreement between theory and data have been evaluated for several times (see i.e. [279]).

RHIC started to look into collisions with polarized proton beams (see for example [186, 189, 190, 193, 194, 280, 281, 282, 283, 284]) before and during LHC time what brought new constraints on gluon PDF in the Bjorken x range $0.01 < x_B < 0.4$, the fragmentation functions and the transverse momentum dependence (TMD) correlations.

III.5 Neutral mesons in pA and heavy ion collisions

Both spectra and nuclear modification factors of neutral pion and η mesons in different centrality classes have been measured in the wide range of energies spanning $\sqrt{s_{\mathrm{NN}}} \sim 5$ to 200 GeV. The Cronin effect has a large impact on heavy ion collisions at SPS and lower energies (see eg. $\alpha-\alpha$ collisions at $\sqrt{s_{\mathrm{NN}}} = 31$ GeV [137]). On the other side, there is a strong suppression visible at high RHIC energies (see eg. central Au-Au collisions at $\sqrt{s_{\mathrm{NN}}} = 130$ GeV [226]). The onset of suppression starts somewhere before $\sqrt{s_{\mathrm{NN}}} = 39$ GeV for Au-Au collisions [236] (see Fig. **III-5**) and between $\sqrt{s_{\mathrm{NN}}} = 22.4$ and 62.4 GeV for Cu-Cu collisions [230] (see Fig. **III-6**)). The suppression of π^0 mesons have been noticed later on by WA98 experiment [209] in the most central $0-13\%$ Pb-Pb collisions at $\sqrt{s_{\mathrm{NN}}} = 17.3$ GeV.

The RHIC data provided very strong evidence of jet quenching. The detailed studies of π^0 [231, 233] and η [234] meson R_{AA} could also confirm that phenomenon. Both STAR and in particular PHENIX presented precise measurements of neutral meson spectra and the nuclear modification factor in several centrality classes in the range $1 < p_{\mathrm{T}} < 20$ GeV/c (see Fig. **III-7**). The common suppression pattern (by factor of ~ 5) of π^0 and η mesons has been observed at high p_{T}. It was not confirmed that after the range with a strong suppression seen in R_{AA} for pions at p_{T} of $6-10$ GeV/c there is a slow rise of R_{AA} (like predicted in models [287, 288]) or it remains constant. This had been an open question before LHC era, solved in neutral meson analyses in ALICE. The angular dependence ($\Delta\varphi$) of R_{AA} and path length dependence of energy loss was also studied by PHENIX [229].

The RHIC results populated in plenty of models (review of model basics can be found in [45, 44, 46, 47, 48, 49].). PHENIX and STAR presented comparisons of π^0 meson yield suppression in Au-Au at $\sqrt{s_{\mathrm{NN}}} = 200$ GeV [232, 241] to various models constraining parameters (the medium transport coefficient $\hat{q}$, the initial color-charge density dN^g/dy or the initial energy loss parameter ε_0) of these models, like the Parton Quenching Model [289, 290] (PQM), the Gyulassy-Levai-

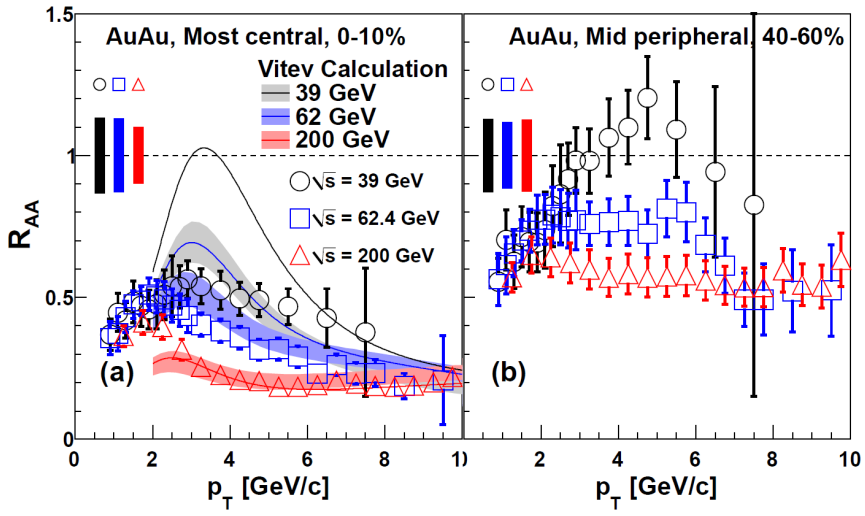

FIGURE III-5: Nuclear modification factor (R_{AA}) of π^0 mesons as a function of p_{T} for a) most central $0-10\%$ and mid-peripheral $40-60\%$ Au-Au collisions at $\sqrt{s_{\mathrm{NN}}} = 39$ (circles), 62 (squares) and 200 GeV (triangles) measured by PHENIX [236] compared to pQCD calculations [285] with regular (solid lines) and reduced (corresponding to larger initial-state parton mean free paths) (bands) Cronin effect. Boxes around unity represent scale uncertainty.

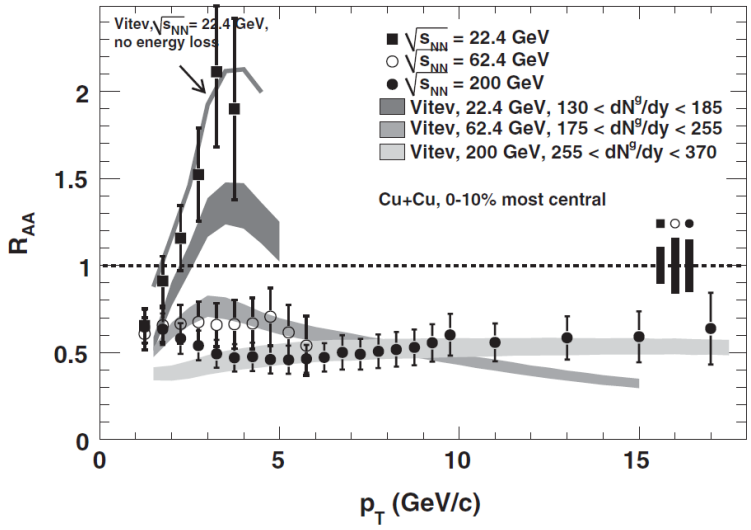

FIGURE III-6: R_{AA} of π^0 mesons as a function of p_{T} for the most central $0-10\%$ Cu-Cu collisions at $\sqrt{s_{\mathrm{NN}}} = 22.4$ (squares), 62.4 (open dots) and 200 GeV (full dots) measured by PHENIX [230] and compared to jet quenching theory calculations [286]. The bands for the calculations correspond to the assumed initial gluon density parameter (dN^g/dy) range. The solid line represents calculations without parton-energy loss for the central Cu-Cu collisions at lowest energy. Boxes around unity represent scale uncertainty.

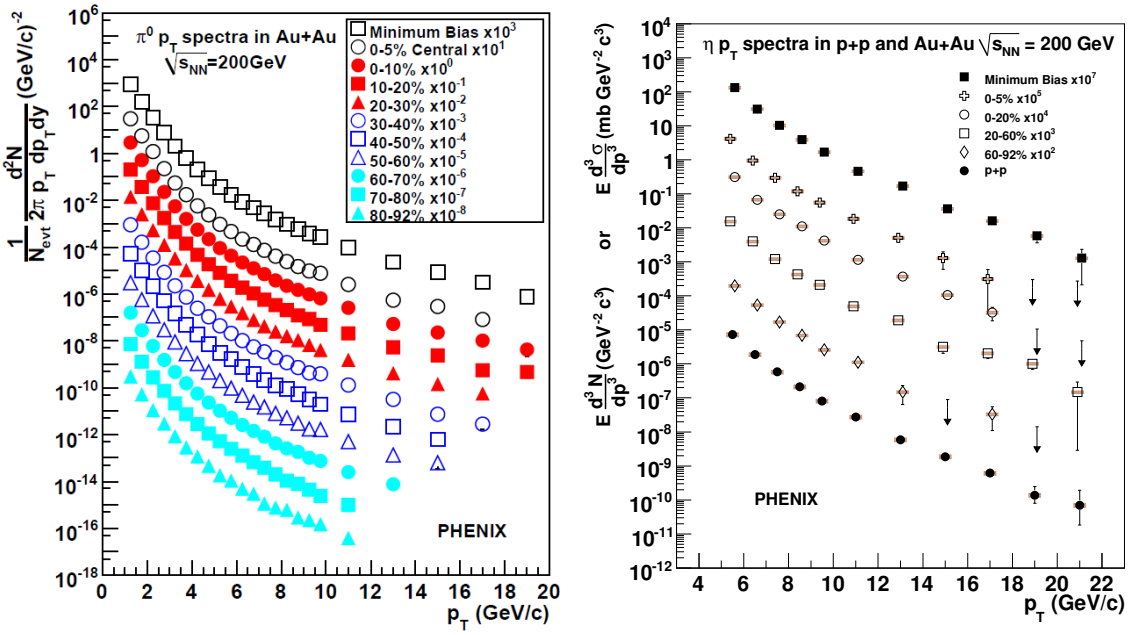

FIGURE III-7: π^0 [231] (left) and η [234] (right) invariant cross-section in pp or invariant yield in Au-Au collisions of various centralities measured with PHENIX at $\sqrt{s_{\rm NN}} = 200$ GeV.

Vitev [291] (GLV) model, the Wicks-Horowitz-Djordjevic-Gyulassy[292, 293] (WHDG) model or the Zhang-Owens-Wang-Wang [294] (ZOWW) model. Models differs in energy loss mechanisms and treatment of initial state multiple scattering or modified nPDFs.

Looking into theoretical description of RHIC data one can have an impression that data are well described. It is true when looking into just one variable and energy. The broader view shows some discrepancies [235, 237]. In particular, data collected at lower than $\sqrt{s_{\rm NN}} = 200$ GeV energies are not so well described by theoretical predictions [236] (see Fig. **III-5**). Also looking in parallel into elliptic flow (v_2) and $R_{\rm AA}$ models have troubles to describe data simultaneously.

New results obtained for π^0 meson spectra and $R_{\rm AA}$ in Au-Au collisions at $\sqrt{s_{\rm NN}} = 200$ GeV increased the range and precision of the measurement at PHENIX [235, 237]. It allowed for more detailed studies of energy loss mechanisms in dense matter giving new constraints to pQCD inspired models like Arnold-Moore-Yaffe [295, 296] (AMY), higher-twist approach [297] (HT), Arnesto-Salgado-Wiedemann [298] (ASW) or ASW AdS/CFT inspired model [44]. In the first three models (AMY, HT, ASW) the energy loss is proportional to the path length in medium squared (L^2). The dominant mechanism is through radiative energy loss. In the last approach (ASW AdS/CFT), the energy loss is proportional to L^3. The AMY, HT, ASW describe $R_{\rm AA}$ well and it is not possible to distinguish between them without more precise results. However, they have problems when describing the in-plane or out-of-plane dependence. The last AdS/CFT inspired models as more adequate to describe data. The other approach (JW model [299, 300]) which took into account geometrical effects due to fluctuations or CGC effects also described data reasonably well (see Fig. **III-8**).

Neutral mesons in d-Au collisions at $\sqrt{s_{\rm NN}} = 200$ GeV show no suppression at high $p_{\rm T}$ [211,

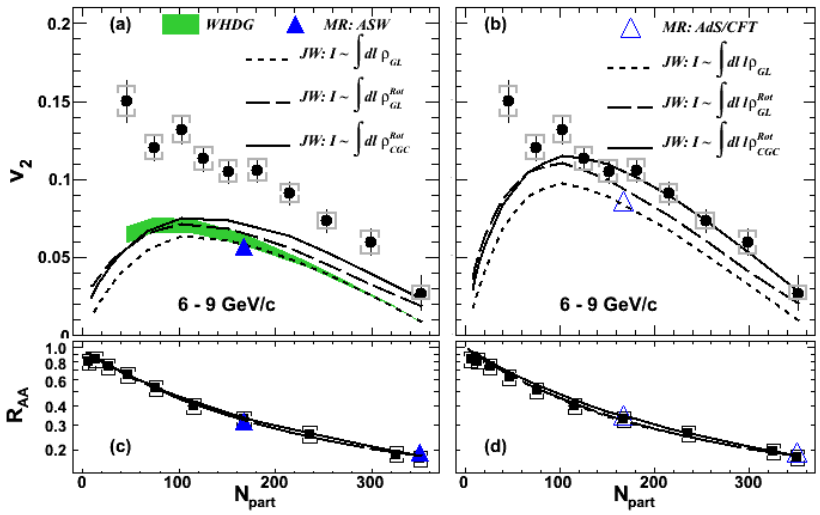

FIGURE III-8: a), b) Elliptic flow (v_2) and c), d) nuclear modification factor (R_{AA}) as a function of number of participants (N_{part}) for different models: WHDG (shaded bands), ASW MR (full triangle), AdS/SFT MR (open triangle) and three versions of JW model (solid, long and short dashed lines) with a), c) quadratic path length (l) dependence or b), d) cubic l dependence compared to PHENIX Au-Au at $\sqrt{s_{NN}} = 200$ GeV data [235] (full dots).

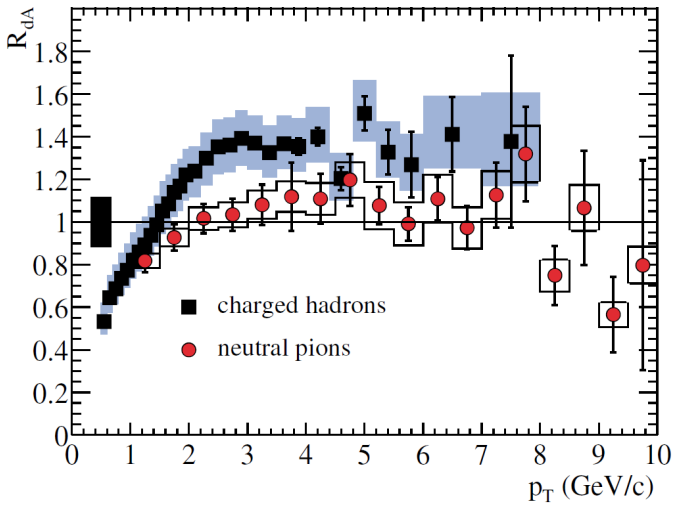

FIGURE III-9: Comparison of nuclear modification factor for charged hadrons (squares) and neutral pions (dots) measured by PHENIX in d-Au collisions at $\sqrt{s_{NN}} = 200$ GeV [211].

185, 192] within uncertainties. Data suggest a little enhancement but not as large as for charged hadrons which consist of baryons and mesons together (see Fig. **III-9**). No suppression but enhancement supports the thesis that suppression in the central Au-Au collisions is not an initial state effect nor arise from modification in nPDFs, but is the final state effect.

CHAPTER IV

EXPERIMENTAL APPARATUS

The ALICE experiment [301] is a dedicated heavy-ion experiment at the LHC [302]. It contains detectors made in almost all known technics. The beam pipe is surrounded by the Inner Tracking System (ITS). Then there is the large volume gaseous Time Projection Chamber (TPC) which is the main tracking device of ALICE. There are additional detectors which are used for a particle identification in the central barrel region like Transition Radiation Detector (TRD), Time Of Flight (TOF) and High Momentum Particle Identification Detector (HMPID). There are two calorimeters installed in ALICE. One of them is Photon Spectrometer (PHOS) with Charged-Particle Veto (CPV), the other one is Electromagnetic Calorimeter (EMCal) together with its extension called Dijet Calorimeter (DCal). All these detectors are surrounded by a large solenoid with weak field $B = 0.5$ T. The ALICE Cosmic Ray Detector (ACORDE) is located on top of the magnet. One arm of ALICE is devoted to muon detection. It consists of an Absorber, a Muon Trigger and a Muon Tracker as well as a Dipole Magnet. It covers pseudo-rapidity in the range $-4 < \eta < -2.5$. There are also forward detectors which are V0, T0 detectors and Forward Multiplicity Detector (FMD) which are located on both sides of the ITS as well as Photon Multiplicity Detector (PMD) which is installed on the magnet gates or Zero Degree Calorimeter (ZDC) and ALICE Diffractive (AD) which are away from the interaction point by a large distance of order of 100 m. The scheme of the ALICE detector is shown in Fig. **IV-1**. The most important detectors which are used in the analyses are described at first in Sections **IV.1**-**IV.4**. Then detectors used for the centrality determination are discussed in Sec. **IV.5**-**IV.6**. All the remaining detectors which are used as trigger inputs are mentioned in Sec. **IV.7**-**IV.11**. The triggers used in the analysis are explained in Sec. **IV.12**. The determination of centrality classes is shown in Sec. **IV.13**. The calibration of TPC and EMCal detectors is summarized in Sec. **IV.14** and Sec. **IV.15**, respectively. Finally, Sec. **IV.16** is devoted to the performance of the ALICE detector.

IV.1 Inner Tracking System

The 6 cm outer diameter beam pipe made of beryllium, copper and stainless steel is surrounded by the Inner Tracking System which is a six layer silicon vertex detector and provides information about the primary vertex with a resolution better than 100 μm. Every two layers are made in a different technology. The first two layers (located at radii 3.9 and 7.6 cm, respectively) have been

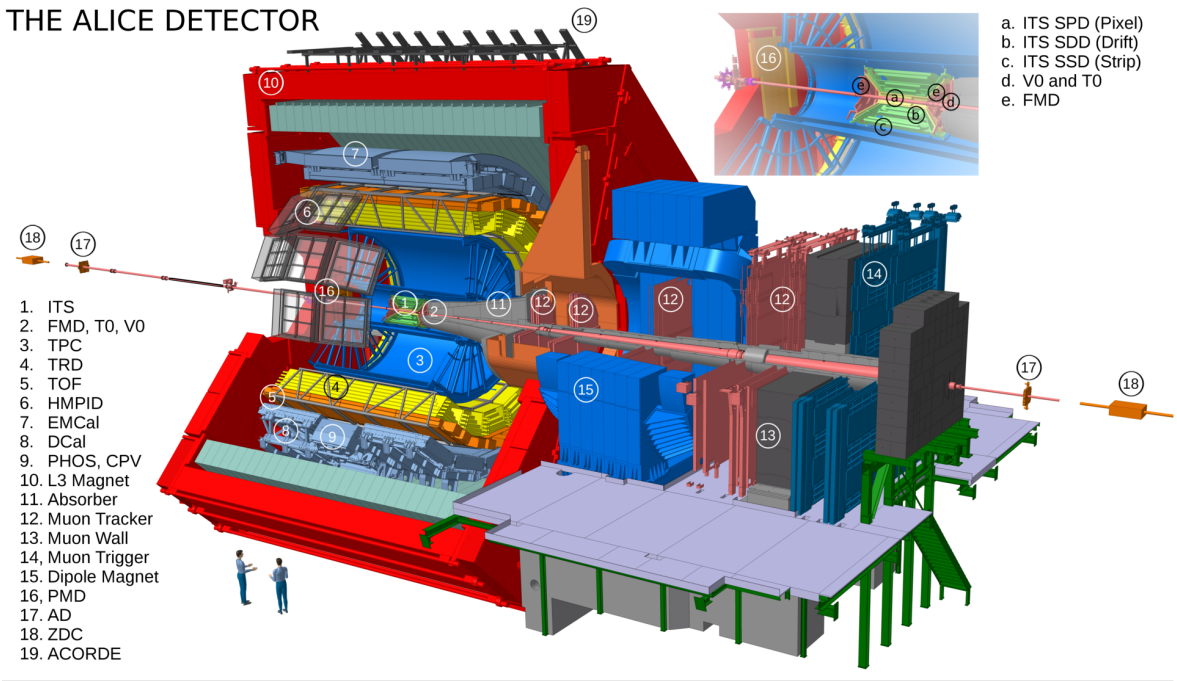

FIGURE IV-1: The sketch of the ALICE detector in Run II. Figure based on Ref. [303]

done as the Silicon Pixel Detector (SPD) to cope with the high particle density expected in heavy ion collisions (HIC). The middle two layers (located at radii 15 and 23.9 cm, respectively) form Silicon Drift Detector (SDD) and outer two layers (located at radii 38 and 43 cm, respectively), where the track density is not so large, are equipped with double-sided Silicon Strip Detectors (SSD). The ITS covers the pseudo-rapidity[1] range $|\eta| < 0.9$. Six layers have all together 12 571 648 readout channels. The ITS is responsible for $\sim 8\%$ of radiation length. The relative momentum resolution based only on ITS is better than 2% for pions with transverse momentum $0.1 < p_{\mathrm{T}} < 3$ GeV/c. The layout of the ITS detector is shown in Fig. **IV-2**.

IV.2 Time Projection Chamber

The main tracking device of the ALICE detector is the Time Projection Chamber (TPC) [15]. The TPC has been designed to cope with the highest charged particle multiplicities per rapidity unit in the central region, $\mathrm{d}N_{\mathrm{ch}}/\mathrm{d}\eta = 8000$. The TPC is a 5 m diameter cylinder with a length of 5 m. The central electrode with voltage of 100 kV allows operating with a drift field of 400 V/cm, divides the drift volume (90 m^3) on two readout parts. The readout chambers (ROC) are installed at the two endplates of the cylinder. The TPC readout is divided into 18 sectors. Each sector consists of inner and outer chamber (IROC and OROC, respectively). The operation is based on the multiwire proportional chamber technique with pad readout. There are 557568 readout pads

[1] Pseudo-rapidity is defined as $\eta = -\ln \tan(\theta/2)$ with the polar angle θ.

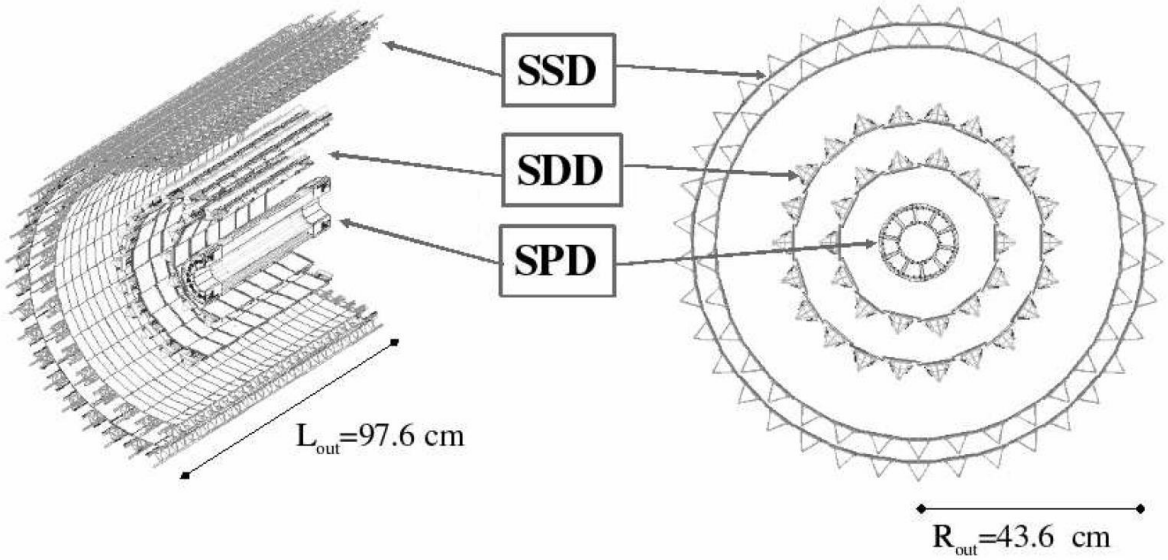

FIGURE IV-2: Layout of the ITS [301].

with three different sizes (4 mm × 7.5 mm for IROC and 6 mm × 10 mm or 6 mm × 15 mm for OROC) allocated on 72 ROCs. The schematic view of the TPC is shown in Fig. **IV-3**. The example IROC is shown in Fig. **IV-4**. The cold gas mixture $Ne-CO_2-N_2$ $(85.7-9.5-4.8\%)$[2] requires temperature stability and less than 0.1 K homogeneity within the whole TPC volume. This is caused by the non-saturated drift velocity (2.7 cm/μs). The TPC is responsible for $\sim 3.5\%$ of material budget (including gas).

IV.3 Photon Spectrometer

The PHOton Spectrometer (PHOS) [304] is a high granularity detector made from the array of lead-tungstate, $PbW0_4$ (PWO) crystal scintillators (see Fig. **IV-5** on the left hand side). Each detection cell consists of crystal of dimensions 2.2 cm ×2.2 cm ×18 cm coupled to the Avalanche Photo Diode (APD) followed by a low-noise preamplifier. This ensures 20 radiation lengths. Each PHOS module (see Fig. **IV-5** on the right hand side) consists of 3584 cells arranged into 56×64 cells array, what gives 1.2×1.4 m^2 size of one module in total. There are three and a half modules (see Fig. **IV-6**) positioned at the bottom of the ALICE detector at a distance of 460 cm from the interaction point. The PHOS covers small region at mid-pseudo-rapidity, $|\eta| < 0.13$ and 70° in an azimuth ($250^\circ < \varphi < 320^\circ$). A temperature stability is crucial to increase the crystal light yield. PHOS modules are operated at temperature of -25° C stabilized with a precision of 0.3° C. The

[2]The gas mixture was a subject to change in order to optimize stability of TPC or its performance. The TPC was also operating with $Ar-CO_2$ $(90-10\%)$ or $Ne-CO_2$ $(90-10\%)$ gas mixture.

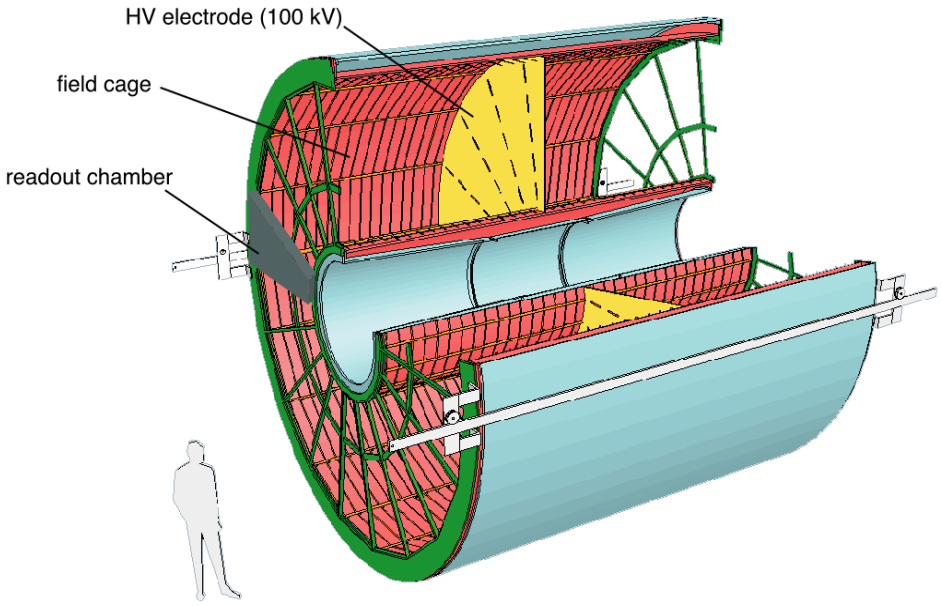

FIGURE IV-3: The view of the TPC field cage. The high voltage electrode is located in the middle of the drift volume. The example readout chamber is also shown.

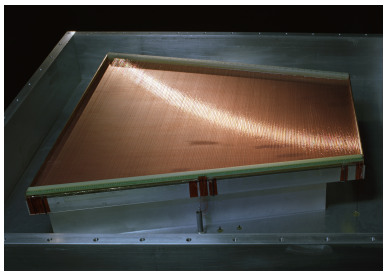

FIGURE IV-4: The Inner Read Out Chamber of TPC.

energy resolution of PHOS calorimeter is very high [305]:

$$\frac{\sigma_E}{E} = \sqrt{\left(\frac{0.018 \pm 0.0007}{E}\right)^2 + \left(\frac{0.033 \pm 0.0007}{\sqrt{E}}\right)^2 + (0.011 \pm 0.003)^2}, \qquad \textbf{(IV.1)}$$

with energy E in GeV.

The Charged-Particle Veto detector is placed on top of one half PHOS module at a distance of 5 mm. CPV is a multi wire proportional chamber with pad readout. The cathode plane is segmented into 3584 pads of size 22 mm $\times$10.5 mm. The active volume of 14 mm thickness is filled with $Ar - CO_2$ (80 – 20%) gas mixture. It gives less than 5% of the material budget.

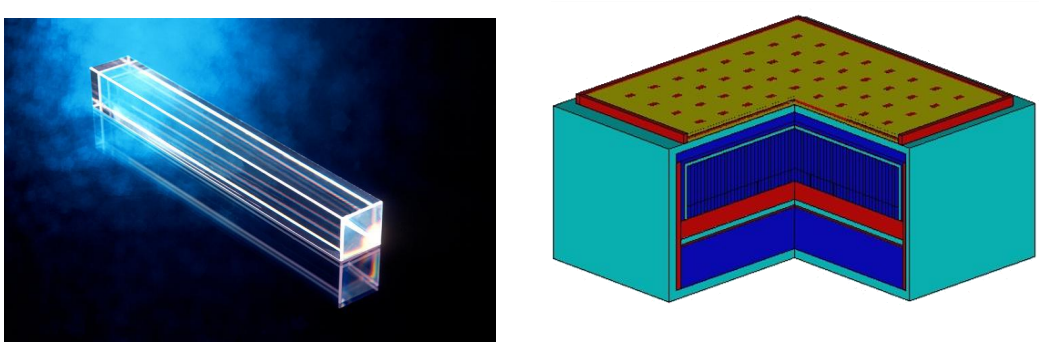

FIGURE IV-5: Left: A photography of a PHOS crystal. Right: Schematic view of the PHOS module. The thermal insulation is in cyan-blue color, a common base (in red) for blue crystals on top of it. CPV (in yellow) is located on top of the module. Cooling plates are located in the bottom and marked as a blue area.

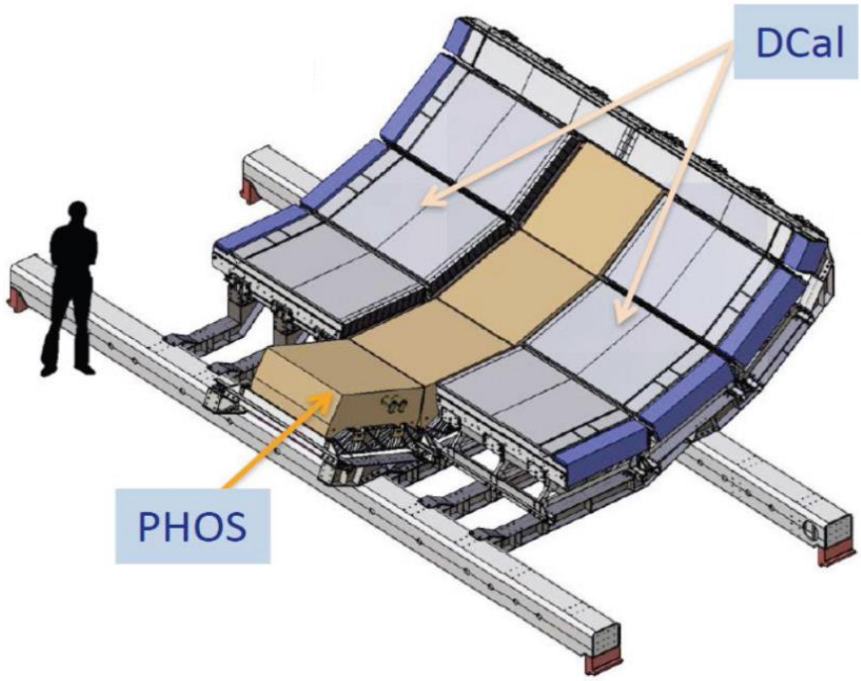

FIGURE IV-6: A view of PHOS super modules surrounded by DCal super modules on the common support frame.

IV.4 Electromagnetic Calorimeter

The EMCal detector [306] and its extension (called DCal) [307] is built in the Shish-kebab technology. It covers 107° in azimuth direction ($80° < \varphi < 187°$) on the top of ALICE and 67° in

azimuth ($260^\circ < \varphi < 327^\circ$) on the bottom of ALICE. Longitudinal length is ∼700 cm, covering $|\eta| < 0.67$ (with a gap for the PHOS on the bottom, $0.22 < |\eta| < 0.67$). The detector is segmented in 17664 towers. Each tower consists of a stack of 78 scintillators of polystyrene (1.76 mm thick) interleaved with 77 lead tiles (1.44 mm thick). Each tower is a pyramidal frustum directed approximately to collision point with 6 cm × 6 cm front face area and height 24.6 cm. Four towers (2 × 2) form a module. A global view of the module is available in Fig. **IV-7** on the left hand side. Each module has a fixed width in the φ direction and a tapered width in the η direction with a full taper of 1.5°. There are 12 (12 × 1) modules in each strip module. Each Super Module (SM) is assembled from 24 strip modules (see Fig. **IV-7** on the right hand side). The whole EMCal comprises

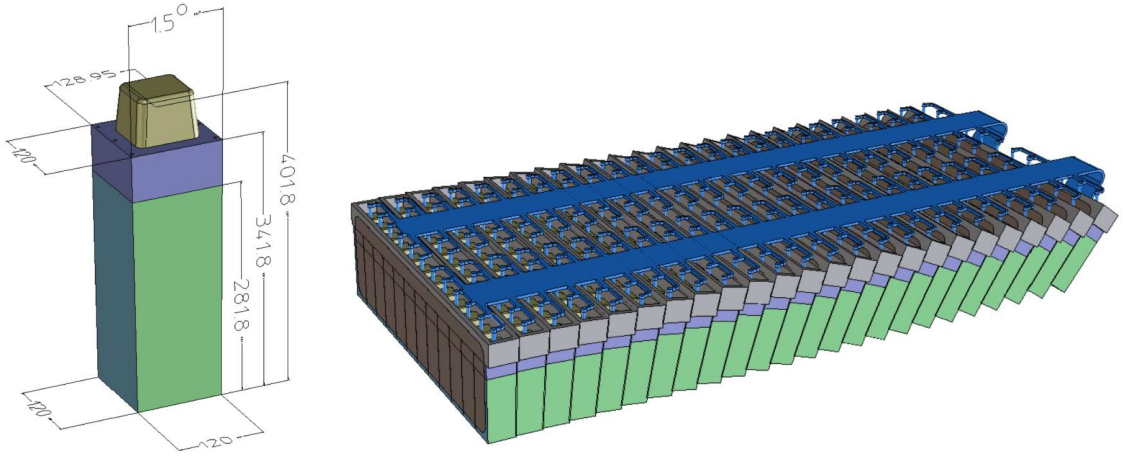

FIGURE IV-7: Left: A single taper module with the dimensions shown in mm. Right: ALICE EMCal super module.

20 Super Modules (10 full and 2 ×1/3 SM for the main part and 6 ×2/3 SM and ×1/3 SM for the extension) (see Fig. **IV-8** for EMCal and Fig. **IV-6** for DCal)[3] which are 428 cm far from the interaction point. The active volume density is ∼5.68 g/cm^3. This results in 19.5 radiation lengths. The energy resolution of the calorimeter is [308]:

$$\frac{\sigma_E}{E} = \sqrt{\left(\frac{0.048 \pm 0.008}{E}\right)^2 + \left(\frac{0.113 \pm 0.005}{\sqrt{E}}\right)^2 + (0.017 \pm 0.003)^2}, \qquad \textbf{(IV.2)}$$

with energy E in GeV.

IV.5 V0 detector

The V0 detector is used as a trigger detector and for centrality determination. The V0 detector is a small angle hodoscope made of two arrays of scintillator counters, V0A and V0C. V0A is

[3]The EMCal geometry has been changed since the first operation of the ALICE experiment. Only four SMs had been installed at first. Eight SMs were installed in 2010. DCal modules were installed during long shutdown LS1 and 20 SMs are fully operational since 2015.

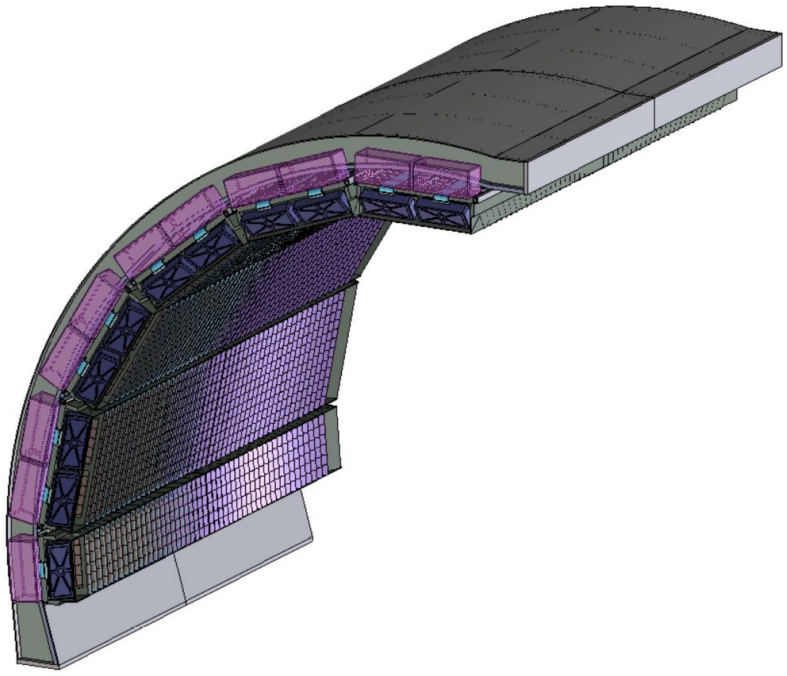

FIGURE IV-8: Layout of the array of EMCal super modules on the support frame.

installed 3.4 m away from the nominal interaction point (IP), while V0C is fixed to the front face of the hadronic absorber, 0.9 m from IP. V0A and V0C cover different pseudo-rapidity ranges: $2.8 < \eta < 5.1$ and $-3.7 < \eta < -1.7$, respectively. Each V0 side is segmented into 32 counters distributed in four rings eight 45° sectors each. The time resolution of individual counter is better than 1 ns.

IV.6 Zero Degree Calorimeter

The ZDC measures energy in forward direction carried by spectator nucleons in heavy ion collisions. The energy is related to number of participants which is related to centrality of the collision. The centrality information delivered by ZDC is used for triggering. ZDC consists of two hadronic ZDCs (one for detecting neutrons, called ZN, and one for protons, called ZP) located at ~ 112.5 m[4] away from IP on each side and electromagnetic calorimeters (ZEM) placed ~ 7 m away from IP. The role of the ZEM is to measure electromagnetic fraction (mostly photons generated by π^0 decays) coming from the collision and to help in the centrality determination (mostly peripheral collisions).

The hadronic component of ZDC are quartz fibres sampling calorimeters. The shower which is generated in a passive material of the absorber produces Cherenkov radiation in quartz fibres which is collected by photomultiplier tubes (PMT). The absorber is made of tungsten or brass for

[4]The ZDC were moved from $|z| \approx 114$ m to $|z| \approx 112.5$ m during the winter shutdown 2011/2012.

ZN or ZP, respectively. It results in 251 and 100 radiation lengths, respectively. Calorimeters have an elongated shape $7.04 \times 7.04 \times 100$ cm^3 and $12 \times 22.4 \times 150$ cm^3 for ZN and ZP, respectively. ZN covers $|\eta| > 8.8$, ZP covers $6.5 < |\eta| < 7.5$ and ZEM covers $4.8 < |\eta| < 5.7$.

IV.7 T0 detector

The T0 detector was designed to generate start time for the TOF detector and to measure the vertex position for each interaction giving the trigger signal when the position is within desirable range. The T0 can generate minimum bias and multiplicity trigger in addition.

The detector was assembled from two arrays of Cherenkov counters. There are 12 counters coupled with PMT in each array. Detectors are located on either side of IP. T0C and T0A are placed 72.7 cm and 375 cm away from IP, respectively. T0C and T0A cover the pseudo-rapidity range $-3.28 < \eta < -2.97$ and $4.61 < \eta < 4.92$, respectively. Detector parts on both sides are placed 6.5 cm away the beam axis in radial direction to maximize triggering efficiency, which is $\sim 50\%$ for pp collisions and $\sim 100\%$ in Pb-Pb collisions.

IV.8 Time Of Flight

The TOF detector supports a particle identification in the intermediate momentum range (below $p = 2.5$ GeV/c for pions and kaons and below 4 GeV/c for protons). TOF is constructed in the Multi-gap Resistive-Plate Chamber (MRPC) technology. It is divided into 18 sectors of 20° in azimuth and 5 segments of different size in z direction covering pseudo-rapidity range $|\eta| < 0.9$. Each module consists of 15 or 19 MRPC strips. One 10-gap double-stack MRPC strip is 122 cm long and 13 cm wide. Each strip has two rows of 48 pads. There are 157248 pads in total placed on 1638 strips. The strips are placed inside gas-tight modules. The chosen gas mixture is $C_2H_2F_4-$i-$C_4H_{10}-SF_6$ $(90-5-5\%)$. The TOF is responsible for 29.5% radial thickness. The TOF is localized on the radius between $3.7 < r < 3.99$ m. Three central modules in front of PHOS have not been installed in order to reduce material budget.

IV.9 Transition Radiation Detector

The main purpose of the TRD is to identify electrons with momentum above 1 GeV/c. The detector is segmented into 18 super modules covering azimuth $\varphi = 20°$ each. Each super module consists 30 modules arranged in six radial layers containing five stacks. Each trapezoidal shape super module has 7.8 m length. It is translated to $|\eta| < 0.84$ pseudo-rapidity coverage. Each module is a multi wire proportional chamber with pad readout. There are 1.18×10^6 pads in total. The detector operating gas mixture is $Xe - CO_2$ $(85-15\%)$. The total gas volume is 27.2 m^3. The TRD drift field is relatively small in comparison to TPC and is 0.7 kV/cm. The total material budget of detector is 23.4%. TRD is located on the radius between $2.9 < r < 3.68$ m.

IV.10 ALICE Cosmic Ray Detector

The main purpose of the ALICE COsmic Ray DEtector (ACORDE) is to provide trigger signal for alignment, calibration and commissioning of some other detectors and study cosmic rays. The ACORDE is an array of 60 modules (30 in $\varphi \times 2$ in z direction) located on top of the ALICE magnet ($r = 8.5$ m). Each module consists of two scintillator counters of size 190×20 cm^2 on top of each other. The ACORDE covers pseudo-rapidity $|\eta| < 1.3$ and azimuth $|\varphi| < 60^\circ$. The radial detector thickness is 4.7%.

IV.11 Muon Spectrometer

Muon arm has been designed to reconstruct muons in the forward region of pseudo-rapidity $-4 < \eta < -2.5$. The spectrometer consists of a carbon-concrete-steel absorber (~ 60 radiation length) to absorb hadrons or photons, 5 tracking stations (ST) of two planes each, a dipole magnet and two trigger stations of two planes each. Five tracking stations form the Muon Chamber (MCH). Two STs are located before the dipole, one ST inside the dipole and two remaining after the dipole at a distance $z = -5.357,\ -6.86,\ -9.83,\ -12.92,\ -14.221$ m, respectively. Every tracking station consists of two planes. Each plane has two cathode planes, which are both read-out to provide two dimensional spatial information. There are 9 types of pad sizes. The larger pads are used at larger radii. There are around 1 million readout pads in total. The gas mixture used in stations is $Ar - CO_2$ ($80 - 20\%$). The spatial resolution achieved is $\sim 70\ \mu$m. Two trigger stations form Muon Trigger (MTR). Two station are build as Resistive Plate Chambers (RPC). Each station contains two planes which contains 18 RPC modules with a typical size of 0.7 m $\times$3 m. The RPC electrodes are made of low-resistivity Bakelite. The gas inside RPCs is a mixture of Ar-$C_2H_2F_4$-i-buthane-SF_6 ($50.4 - 41.3 - 7.2 - 1\%$). Two trigger stations are located at distance to the nominal interaction point $z = -16.12$ and -17.12 m.

IV.12 Trigger

ALICE has used several detectors for a triggering purpose over several years during running time. ALICE trigger logic is based on SPD, TOF, PHOS, EMCal, ACORDE, V0, T0, MTR, ZDC and TRD inputs. Trigger detectors have different functions. They are listed below [303]:

- SPD: L0 - hit-multiplicity and hit-topology based trigger,
- PHOS: L0 - photon trigger,
- EMCal: L0/L1 - photon and neutral jet trigger,
- V0: L0 - minimum-bias interaction coincidence trigger and centrality trigger,
- T0: L0 - event vertex selection and interaction trigger,
- ZDC: L1 - minimum-bias interaction and electromagnetic trigger in Pb-Pb,
- TRD: L1 - electron, high-p_{T} particle and charged jet trigger,
- TOF: L0 - multiplicity, topology and cosmic-ray trigger,

- ACORDE: L0 - cosmic-ray trigger,
- MTR: L0 - muon trigger.

The trigger was optimised to run in different modes: ions, pA and pp having different counting rates. It is divided into several levels. A Level 0 (L0) signal is delivered to detectors at 1.2 μs. However, it is to fast to receive all trigger inputs. A Level 1 (L1) signal is based on the all input detector signals and it takes 6.2 μs to deliver the proper information to detectors. The important remark is that the ALICE Central Trigger Processor makes a decision in 100 ns. The remaining time latency is coming from a signal propagation in cables (ZDC) and the computation time for the trigger input signals (TRD, EMCal). The Level 2 (L2) trigger is much slower. The information is coming to detectors after $\sim$ 100 μs. The reason of large latency is that high multiplicity events (for example in Pb-Pb collisions) need to be reconstructed when several events are waiting in the reconstruction pipeline. The time is directly related to the maximum TPC drift time. The most important triggers which are used in the analyses are shown in Table **IV-1**. The MB_{OR} trigger was

Trigger	Description	Condition
MB_{OR}	minimum bias	signal in V0 and SPD
MB_{AND}	minimum bias	signal in V0A and V0C
MBZ	minimum bias	MB and signals in both ZDCs
CENT	central	V0 based centrality trigger for Pb-Pb $(0-10\%)$
SEMI	semi-central	V0 based semi-central trigger for Pb-Pb $(0-50\%)$
EMC1	EMCal L0	EMCal L0 shower trigger in coincidence with MB
EG1	photon/electron	EMCal L1 photon algorithm following EMCal L0
EG2	photon/electron	like EG1 but with lower threshold than EG1
PHI7	photon by PHOS	PHOS energy deposit in coincidence with MB

TABLE IV-1: Selected ALICE triggers [303].

used at low luminosity runs while MB_{AND} one at runs with higher background in pp data taking. Additionally, these minimum bias triggers were used in Pb-Pb collisions in 2010, 2015 and 2018 and p-Pb periods in 2013 and 2016. MBZ minimum bias trigger was used in 2011 Pb-Pb period in order to suppress the electromagnetic interactions between the lead ions. Additionally, data with CENT and SEMI centrality triggers were taken. Starting with 2012 rare EMCal and PHOS triggers were taken into account. The PHI7 and EMC1 triggers required an energy deposit within 4×4 cells above a given threshold. The EG1 triggers have larger threshold than EMC1 trigger.

IV.13 Centrality determination

Nuclei are not dimensionless objects. The volume of their interaction depends on the impact parameter, b, of the collision. The impact parameter is the distance between the centres of the two colliding nuclei in a plane transverse to the beam axis. The centrality of the collisions is directly related to the impact parameter. The centrality c of nuclear collisions is customary expressed in

terms of percentage of the total hadronic interaction cross-section σ_{AA},

$$c(b) = \frac{\int_0^b \frac{d\sigma}{db'} db'}{\int_0^\infty \frac{d\sigma}{db'} db'} = \frac{1}{\sigma_{AA}} \int_0^b \frac{d\sigma}{db'} db'. \tag{IV.3}$$

The centrality in Pb-Pb collisions is estimated by the energy deposited in the zero-degree calorimeter (E_{ZDC}) or by particle multiplicity (N_{ch}) in the experiment [309]. It is valid under assumption of monotonic correlation between centrality and a given estimator (for example E_{ZDC} can be used in $0-30\%$ centrality). The cross-section can be replaced by the total number of events observed, N_{ev}, that

$$c \approx \frac{1}{N_{ev}} \int_{N_{ch}}^\infty \frac{dn}{dN'_{ch}} dN'_{ch} \approx \frac{1}{N_{ev}} \int_0^{E_{ZDC}} \frac{dn}{dE'_{ZDC}} dE'_{ZDC}. \tag{IV.4}$$

The centrality determination via the particle multiplicity in the V0 detector is shown in Fig. **IV-9**. The V0 particle multiplicity is compared to the model based on a Glauber description of nuclear

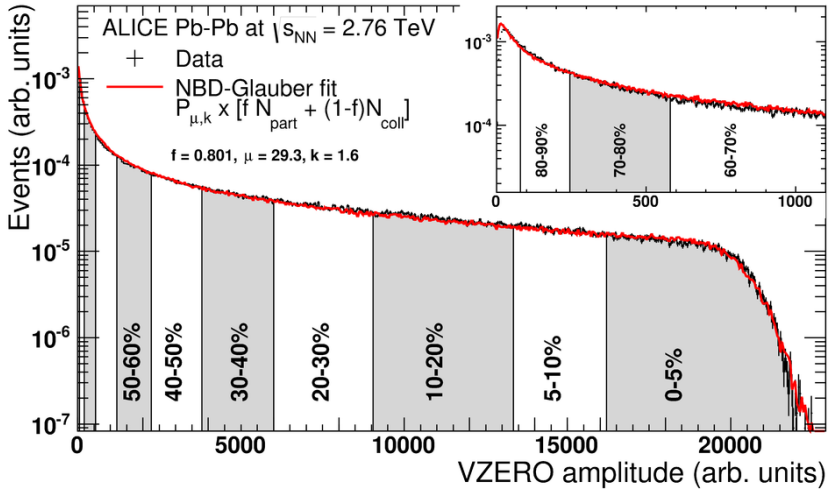

FIGURE IV-9: Distribution of the V0 amplitude (sum of V0A and V0C) for Pb-Pb collisions at the center-of-mass energy $\sqrt{s_{NN}} = 2.76$ TeV. Centrality bins are defined according to Eq. **IV.4**. The absolute scale is defined by the fit to the model. The inset shows the magnified version of the most peripheral region. Figure taken from [309].

collisions [31] with the modified Woods-Saxon distribution of the nuclear density function. A nuclear collision is treated as a superposition of binary nucleon-nucleon interactions in the model. The volume of the overlap region is proportional to the number of participant nucleons, N_{part}. The number of spectators is given by $N_{spec} = 2A - N_{part}$, where A is a mass number of the nucleus. The number of participants and the number of binary collisions, N_{coll} are calculated for a given value of the impact parameter. The number of particle sources is given by

$$N_{ancestors} = f \times N_{part} + (1-f) \times N_{coll}, \tag{IV.5}$$

where f represents number of soft interactions and $1-f$ - number of hard collisions. Each particle source follows the negative binomial distribution with parameters μ (mean multiplicity) and k (width of the distribution), to produce particles and to give the final particle multiplicity spectrum. Values of f, μ and k taken from the fit are following: $f = 0.801$, $\mu = 29.3$ and $k = 1.6$. Fit describes 88% of total hadronic cross-section.

The other estimator of Pb-Pb centrality - energy deposited by spectators in ZDC - can be used in a limited regime due to the fact that some spectator nucleons are bound into light nuclear fragments. They travel together with a beam in the beam-pipe and become undetected by the hadronic ZDC. This effect is intensified for peripheral events and monotonic behaviour between number of participants and energy deposit is broken (naive relation $N_{\text{part}} = 2A - E_{\text{ZDC}}/E_{\text{A}}$, with the mass number of Pb $A = 208$ and E_{A} - the beam energy per nucleon, does not occur). An information from ZEM is necessary to correct hadronic ZDC information. The correlation between the hadronic ZDC energy and the ZEM amplitude is shown in Fig. **IV-10**. Centrality classes are

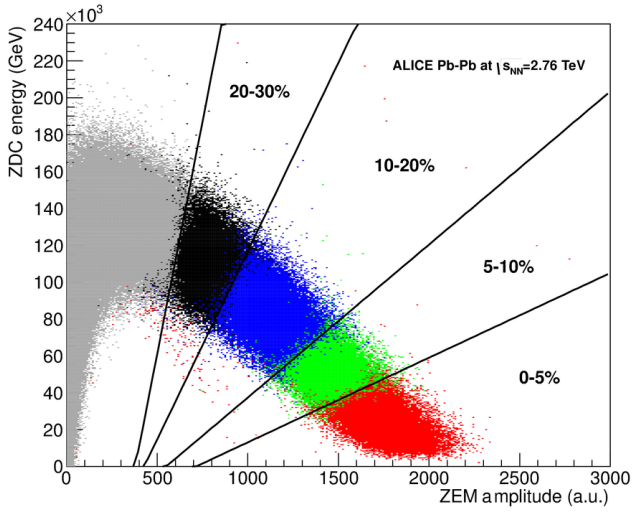

FIGURE IV-10: Spectator energy deposited in the hadronic calorimeter ZDC as a function of ZEM amplitude for Pb-Pb collisions at the center-of-mass energy at $\sqrt{s_{\text{NN}}} = 2.76$ TeV. Events with the same color belong to the same centrality class selected by V0 amplitudes. The lines represent the fit to the boundaries of centrality classes. Figure taken from [309].

defined by cuts on the two dimensional ZDC hadronic energy-ZEM amplitude plane. At first V0 amplitude is used to determine centrality regions, then they are refitted with linear functions with a common intersection. The ZDC information can be used to determine centrality only in central $0-30\%$ collisions.

Five different centrality estimators are use in p-Pb collisions [310] to determine centrality:

- CL1: the number of clusters in the outer layer of SPD,
- V0A: the amplitude measured by the V0A detector (the Pb-going side in the p-Pb collision),
- V0C: the amplitude measured by the V0A detector (the p-going side in the p-Pb collision),
- V0M: the sum of the amplitudes coming from both V0A and V0C,

- ZNA: the energy deposited in the neutron calorimeter on the A-side (the Pb-going side in the p-Pb collision).

Distribution of the V0A amplitude in Pb-going direction, together with centrality classes is shown in Fig. **IV-11**. The similar model like for Pb-Pb collisions has been fitted. The parameters obtained from fit are following: $\mu = 11$, $k = 0.44$. The similar distributions and fits have been performed for V0M and CL1 estimators (and V0C as a cross-check). They belong to the same abstract class and give similar results. One remark is very important here that events with the same number of participants belong to a different centrality class so we cannot use the phrase centrality class anymore. Instead V0A multiplicity intervals will be used. The last estimator, which is based on the ZDC energy is not sensitive on multiplicity bias. The slow nucleon emission model describes the data very well [310] like shown in Fig. **IV-12**.

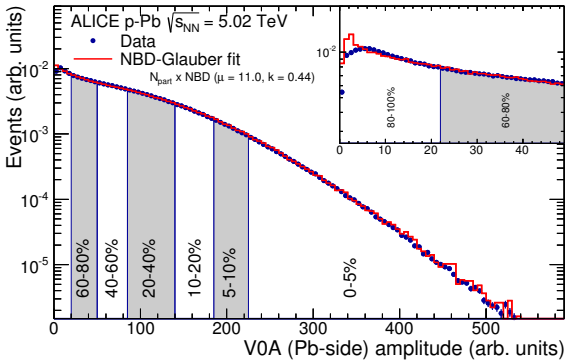

FIGURE IV-11: Distribution of the V0A amplitude in Pb-going direction for p-Pb collisions at the center-of-mass energy $\sqrt{s_{\mathrm{NN}}} = 5.02$ TeV together with the fit (red line). Centrality classes are marked by vertical lines. The inset shows a zoom-in of the most peripheral events. Figure taken from [310].

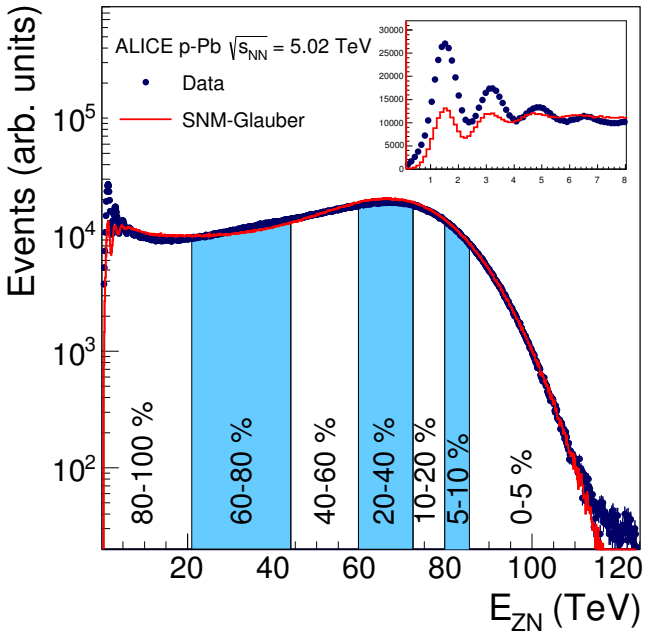

FIGURE IV-12: Distribution of the neutron energy measured by ZN in the Pb-going direction for p-Pb collisions at the center-of-mass energy $\sqrt{s_{\mathrm{NN}}} = 5.02$ TeV together with the fit (red line). Centrality classes are marked by vertical lines. The inset shows a zoom-in of the most peripheral events. Figure taken from [310].

IV.14 TPC calibration

The main goal of the calibration is to provide the information needed for reconstruction software. Each detector has its own calibration procedures. However, the calibration of the TPC will be de-

scribed hereafter as one of two most important for the further analyses. The second most important one, the EMCal calibration is described in the next section.

There are four major run types used for different calibration in the ALICE TPC [15]:

- Pedestal runs,
- Calibration pulser runs,
- Laser runs,
- Krypton runs.

Pedestal runs are used to determine the electronics baseline (pedestal) and its width (noise) for every readout channel. During these runs the zero suppression (ZS) is switched off. The typical pedestal of one electronic channel is shown in Fig. **IV-13** while the noise distribution for all channels and for each pad type is shown in Fig. **IV-14**. The measured mean noise level achieved 0.7

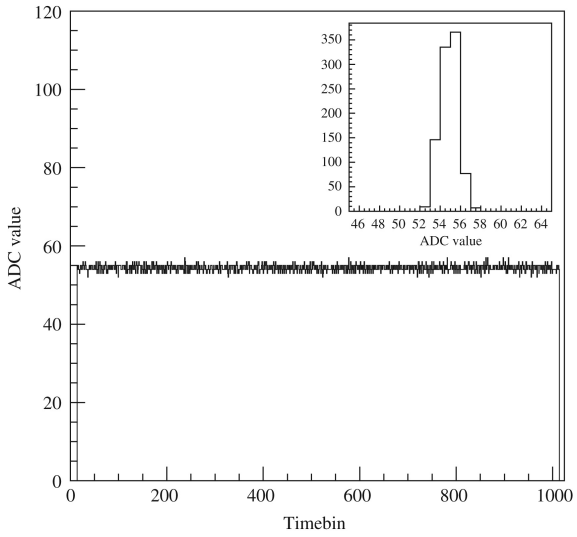

FIGURE IV-13: Typical baseline of one channel with inset showing its distribution [15].

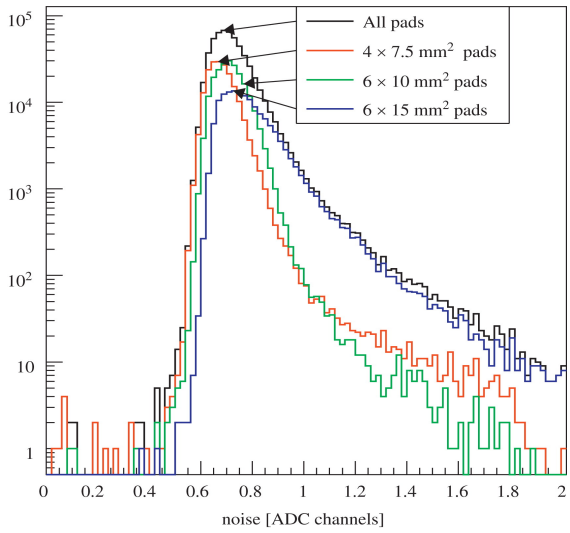

FIGURE IV-14: The noise distribution for all TPC pads (black) and different pad sizes: short pads (red), medium pads (green) and long pads (blue) [15].

ADC count (700 e^-) and exceeded expectations of 1 ADC count (1000 e^-). The extracted values of pedestal and noise become a baseline for the zero suppression with the Front-End Electronics (FEE) to cope with huge amount of data. The data volume was reduced from $\sim$ 700 MB/event without ZS to less than 70 kB/event with ZS for empty events. It allowed for data rates up to 1 kHz for p-p and a few 100 Hz for Pb-Pb collisions at LHC energies. Pedestal runs are executed before data taking for every LHC fill.

Calibration pulser system is used to calibrate drift-time and calibrate timing of all readout channels. The system also helps to identify dead channels and floating wires. During pulser runs the cathode wire grids of the Read-Out Chambers are pulsed and signal is induced on pads without

gas amplification. Figure **IV-15** shows the distribution of timing variation in the whole TPC. The RMS of the distribution corresponds to 5.2 ns, what can be translated as a shift causing additional systematic uncertainty of cluster position resolution of about 140 μm, which is the second order effect. The calibration pulser runs are executed similarly to pedestal runs before data taking for every LHC fill.

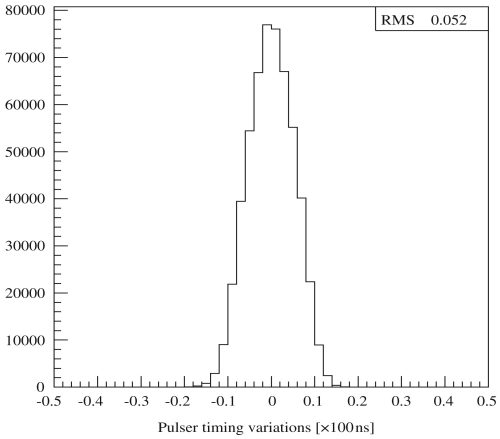

FIGURE IV-15: Distribution of pulser timing variations of all pads [15].

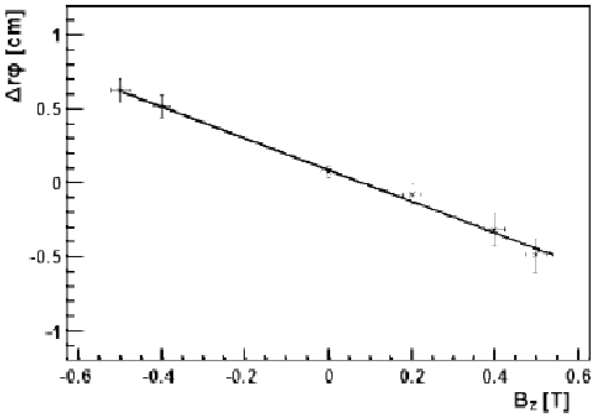

FIGURE IV-16: A deviation of the electron drift from the ideal path caused by the $E \times B$ effect as a function of the magnetic field.

Laser system uses 336 narrow ultraviolet laser beams to calibrate drift field parameters in time. Since TPC is the very big cylindrical detector any mechanical distortion as well as any electrical imperfection in the field cage or readout chambers can cause non-uniform electron drift. The electron drift can be also unsettled by relative misalignment of the magnetic and electric field ($E \times B$ effect), variation of temperature or atmospheric pressure and local variation of the electric field from moving charges (space charge distortion). Temperature and pressure are measured with a high quality sensors. The laser system provides straight tracks to measure the drift velocity, to correct drift velocity for $E \times B$ effect, and test alignment of readout chambers and central electrode. For each laser beam and several magnetic field settings the deviation of the electron drift $\Delta r\varphi$ from the ideal path is measured as shown in Fig. **IV-16**. The $E \times B$ effect is as large as 7 mm for the longest drift and nominal field. It corresponds to the designed precision of the correction less than 1%. The mentioned drift velocity is crucial for track matching with other detectors. It can be measured via matching laser tracks and mirror positions [5]. The laser shots every half hour interspersed between physics events.

Krypton runs have been taken to calibrate the detector response (gain). One of the main purposes of the ALICE TPC detector is a precise $\mathrm{d}E/\mathrm{d}x$ measurement. The good knowledge of the detector gain is crucial. The method applied by ALICE collaboration removes both a gas and

[5] The drift velocity can be also measured via matching tracks from two halves of the TPC using cosmic tracks (from cosmic runs) or via matching of the TPC primary vertices from two halves of the TPC (regular pp collision runs) or via matching of TPC and ITS tracks (regular pp collision runs).

an electronics response fluctuations. The gas gain calibration of readout modules is based on the radioactive decay of the ^{83}Kr isotope. The method has been developed by ALEPH [311] and DELPHI [312] collaborations. It has also been used with success by the NA49 collaboration [313, 17][6], STAR collaboration [314] and later on in NA61 collaboration[7]. It consists in connecting a radioactive $^{83}_{37}$Rb source with the gas recirculating system of the ALICE TPC. The radioactive $^{83}_{36}$Kr isotope gas obtained from the source is injected into a detector volume of the chamber. The isotope is excited and unstable. The excitation energy of the krypton is 41.6 keV (half-life time is 1.9 hr). It decays down to the ground state through an intermediate state with an energy of 9.4 keV (half-life is 147 ns). It indicates that there are two transitions with a defined energy: 32.2 keV and 9.4 keV. A result of the first transition is a number of electrons coming from internal conversion or Auger emission with a total energy not exceeding 32.2 keV. One X-ray photon with an energy from range 12.6 to 14.3 keV can also be emitted. The second transition outcome is manifested by a couple of electrons or a single 9.4 keV photon. Electrons interact with a detector gas in a place where they were created while photons escape. Their radiation length is of an order of 30 cm. Photons interact with gas molecules via photo-electric effect. All the electrons coming from the krypton decay directly or from the photo-electric effect ionise gas molecules. The resulting clusters coming from the ionisation are registered by the TPC readout chambers. The characteristic energy spectrum of the krypton isotope decay is well known (see Fig. **IV-17**). It results in an adequate charge deposit spectrum so the response of TPC is possible to investigate. The comparison of the characteristic spectra of deposited charge in various parts of TPC chambers allows to study the local gain variation. Due to this the registered spectra have different x scales in different TPC chambers and on different pads. If the gain is higher (lower), the spectrum is wider (narrower). Having collected enough statistics of krypton data a pad-by-pad calibration is possible. Krypton campaign was performed in 2008, 2009, 2011, 2012, 2015 and 2018 for one week each time. Data with 1 kHz random trigger were taken for different high voltage and magnetic field settings as well as for different gas compositions over these years.

The procedure of the krypton analysis bases on several steps:

1. Installation and injection of the krypton source.
2. Krypton cluster reconstruction.
3. Characteristic spectrum preparation.
4. Spectrum fitting.
5. Corrections of bad channels.
6. Gain map and calibration constants extraction.

The first step is purely technical and well described in [15]. **The dedicated cluster finder algorithm** is necessary in the krypton analysis. The reason lies behind the topology of a typical krypton cluster in comparison to the cluster coming from physics data (i.e. from charged particles passing through the sensitive volume of the chamber). Particle clusters are always defined as collected on

[6] Author was responsible for the gain calibration via radioactive Krypton of NA49 TPC in 2011. The method was developed by author on the purpose of the ALICE TPC calibration. The method is different from previously used in NA49 collaboration.

[7] Author is also a member of the NA61/SHINE collaboration and was responsible for the gain calibration of TPC via radioactive Krypton in 2015.

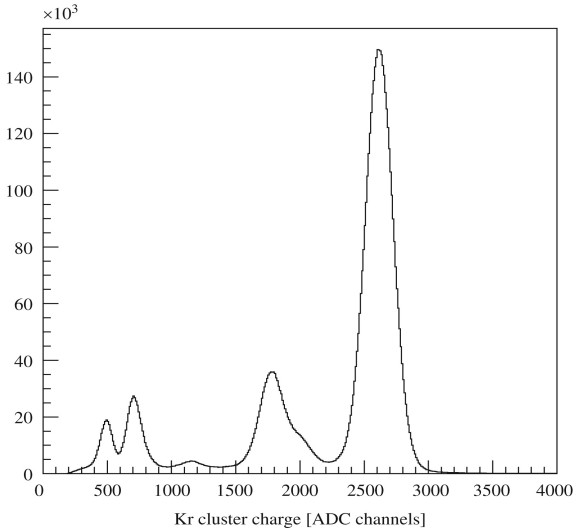

FIGURE IV-17: The characteristic radioactive krypton decay from OROCs [15].

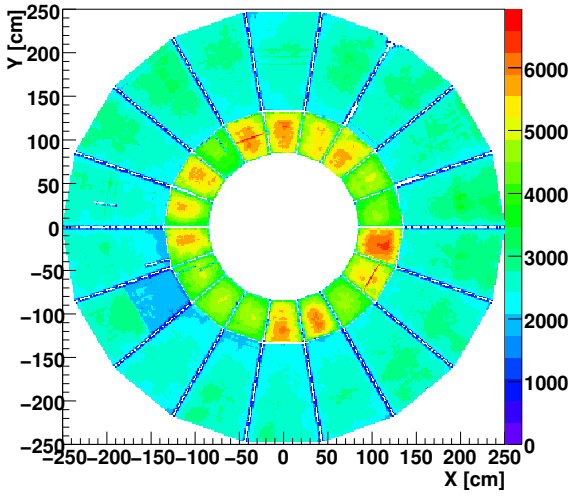

FIGURE IV-18: Gain topology on C-side for data taken in 2008.

a given pad-row. When a track passes over n pad-rows, it supposes to give n clusters. The krypton cluster is an object in a 3D space. Its projection to 2D pad plane forms more or less a circular shape which consists of several pad-rows. The 3D cluster finder collects the charge accumulated on pads belonging to neighbouring pad-rows and time slices and utilises all the methods to suppress the noise in the ALICE TPC. When all the clusters are reconstructed a separate **charge spectrum histogram** is produced for every pad in the chamber. The most important for the analysis is the largest peak which corresponds to the energy deposit of 41.6 keV. The main peak is **fitted with a Gaussian distribution**. The gain topology on the C-side of the TPC is shown in Fig. **IV-18**. The position of mean of the Gaussian is proportional to the total gain (the electronic response and the gas gain) of the pad. The other peaks have also been fitted in order to check non-linearity and as a cross-check of the calibration performed with the main peak.

There are several types of effects when looking at a different area of interests. One can consider a local gain variation within one sector or a global sector-by-sector gain variation.

Gain variation within sector. The crown of the krypton calibration is to produce pad-by-pad calibration constants which reflects gain topology. The investigation of systematic trends in TPC gain allows one to look for various mechanical distortions and imperfections in construction of the detector. The global structure of the sector is visible in radial and azimuthal projections. The average gain systematics in the radial (row) and azimuthal (pad) direction is shown in Fig. **IV-19**. There is a sizeable systematics reaching typically up to 18 %, 23 % and 11 % for IROCs, OROCs' medium pads and OROCs' long pads, respectively, in a radial direction within sector. An irregular curve describes the projection in this direction. There is also a visible systematics in azimuthal direction within sector which reflects probably catenarity of wires as well as a mechanical deformation of chamber. On top of that an edge effect is superimposed. There is an attenuation of gain on the edges visible specially in azimuthal direction. It is related to the range of electrons

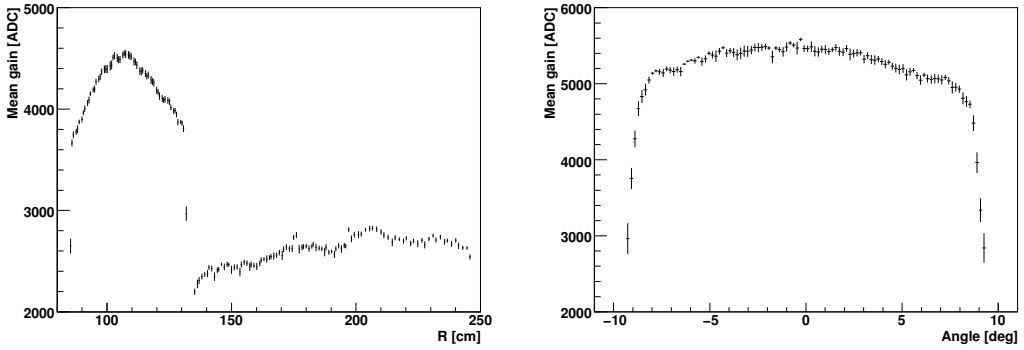

FIGURE IV-19: Radial (left) and azimuthal (right) systematics of gain variation within one sector. The step observed in the radial variation is due to the IROC-OROC transition.

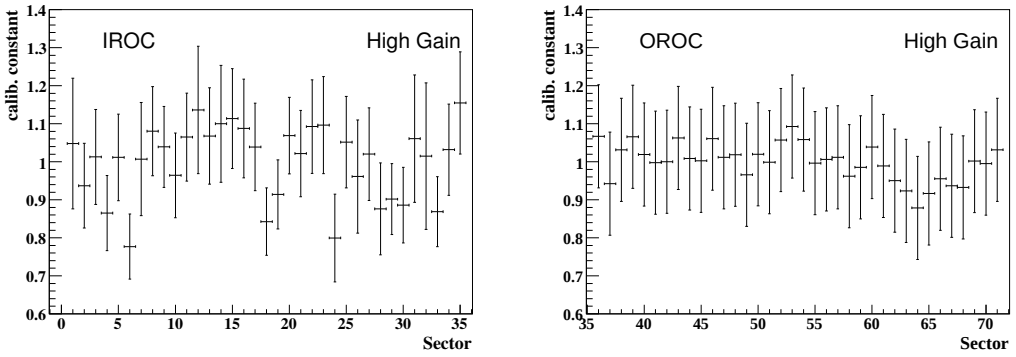

FIGURE IV-20: Sector-by-sector gain variation for IROC (left) and OROC (right).

from krypton decays and pad size. It is manifested by the leak of charge and touches 2-3 edge pads. Moreover, krypton calibration allows localizing not properly working cards, floating wires or noise regions. All the problematic regions are taken into account in a **correction routine** based on krypton gain maps and maximum charge $Q_{\max}$ on a pad maps. Based on that the **final gain map** is done.

Sector-by-sector gain variation. The magnitude of gain differences between sectors has been investigated. Fig. **IV-20** shows the gain computed for each inner and outer sector. Due to differences between inner and outer sectors, these two groups are not directly comparable. IROCs and OROCs differ by nominal HV settings, pad size, etc. Presented calibration constants have been normalized for inner and outer parts separately. The vertical bars correspond to typical gain variation inside the given sector.

One can observe larger maximal gain variation for inner chambers (39.1 %) than for outer chambers (21.7 %). When consider A- and C-side separately it bears out 37 %, 36 % for IROCs and 14.8 %, 18.6 % for OROCs, respectively. The mentioned values are presented for nominal gain. For lower ROC voltages variations are smaller, i.e. 28 % for IROCs and 13 % for OROCs at

low gain.

The aim of the krypton calibration is to take out the relative rather than absolute gain variation inside TPC sectors and between sectors. This is the reason why all calibration constants are rescaled to give an average equal to one.

The error on the mean obtained from the fit is of the order 0.2% on the single pad level (required is 1.5%). The calibrated spectrum of Kr decays for all OROCs is shown in Fig. **IV-17**. The resolution of the main peak is 4.0% for IROCs and 4.3% for OROCs.

IV.15 EMCal calibration

Although the EMCal is a different detector than the TPC the calibration steps are similar. In order to obtain the best energy resolution one needs to calibrate or equalize electronic response, monitor temperature or adjust timing. For all these purposes the EMCal calibration can be divided into the following steps:

- Energy calibration,
- Bad channels determination,
- Time calibration,
- Temperature calibration.

The energy calibration [315] follows several steps. The APDs which are attached to preamplifier and finally mounted to EMCal towers had been tested with a Light Emitting Diode (LED) system in a lab at first. The tests allowed measuring noise and voltage gain for each APD with accuracy of 20%. Then each SM was calibrated using energy deposit of cosmic ray muons at the Minimum Ionizing Particle (MIP) peak as they pass through a single tower. Typical MIP energy is $\sim$ 280 MeV. It allowed for a relative calibration and set the initial absolute energy scale. The accuracy achieved with the MIP method is $\sim$ 10%. After the installation of EMCal super modules in the cavern every tower was calibrated with MIPs using experimental data with an accuracy of $\sim$ 7%. Finally, with the high statistics pp collisions, each tower was calibrated via two photon invariant mass spectra. The π^0 peak observed in each tower was used in the calibration. The π^0 mass peak before and after the energy calibration with π^0 is shown in Fig. **IV-21**. The achieved accuracy is better than 3%.

In addition to calibration with cosmic MIPs, MIPs coming from pp collisions and π^0 peak mass calibration SMs were exposed on electron and hadron test beam with given energies. The linearity of the response was found to be better than 1% in the energy range $20-100$ GeV. Below the incidental energy of 20 GeV the reconstructed energy is lower. A drop of 10% is observed at 5 GeV. The non-linearity correction has been parameterized and applied during the analyses.

Bad channel map determination is based on the typical energy spectrum within one tower. We can distinguish dead, bad, warm and noisy channels beside good channels. The bad channel map is prepared per period of the data taking a posteriori. However, the good knowledge of bad channels is crucial for any kind of data analysis and triggering purposes. EMCal provides L0 and L1 triggers and bad or noisy channels are masked almost immediately when they are detected in the online data taking.

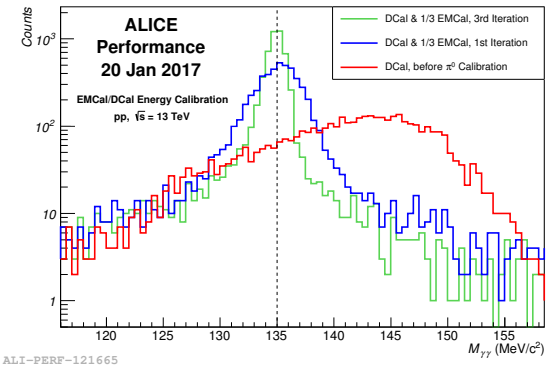

FIGURE IV-21: Iterative procedure of the energy calibration with π^0 mass peak using pp collision data at center-of-mass energy $\sqrt{s} = 13$ TeV. Two photon invariant mass distribution before π^0 calibration, after the first iteration and after the third iteration are shown in red, blue and green line, respectively. Dashed line shows the nominal π^0 mass.

The main goal of the **time calibration** is to correct cell time information by the average cell time over a period of data taking. The calibration corrects for a cable length (the signal propagation in the cables takes ~ 600 ns) and the electronic response. The period can be as long as one ALICE data taking period or the whole year. In principle time calibration should be the same for at least one year. However, all the electronic changes and different trigger setups impact the calibration. The bunch crossing (BC) in pp collisions during LHC Run II phase occurred every 25 ns[8]. The EMCal clock works with the other frequency than LHC clock, and samples every 100 ns. The time calibration also correct for that effect. Moreover, all the SMs should start recording data at the same time. However, during LHC Run II data taking the new firmware uploaded into electronics has a feature which causes lost of the synchronization between different Super Modules. The time calibration includes offline calculation of so called L1-phases for each SM and run. Figure **IV-22** shows time distribution before (on the left hand side) and after (on the right hand side) the time calibration, respectively. The cell time distribution is aligned at zero on the right hand side plot. The resolution of the main peak is below 3 ns. Well visible neighbouring peaks are comming from the out-of-bunch pile-up. The time calibration, crucial in the EMCal calibration allows removing clusters coming from pile-up, is necessary in the energy calibration with π^0 peak mass and helps to identify bad channels.

Temperature dependence of APD gain was tested in the test beam. It was found that LED amplitude changes by -2.1% per $^{\circ}C$ for a typical EMCal tower. The EMCal temperature has been monitored during data taking. The change of the π^0 peak mass position has been observed with temperature. There are two methods of temperature correction. In the first one the mean temperature is calculated per run to evaluate gain curves per tower. The second one uses the LED calibration system in the LED events recorded at the beginning of each run to quantify the gain variation from one reference run. Either the first or the second method is used in case of bad

[8]During LHC Run I phase pp collisions occurred every 50 ns. During Pb-Pb and p-Pb data taking periods the bunch spacing was even larger, 150 ns or 75 ns.

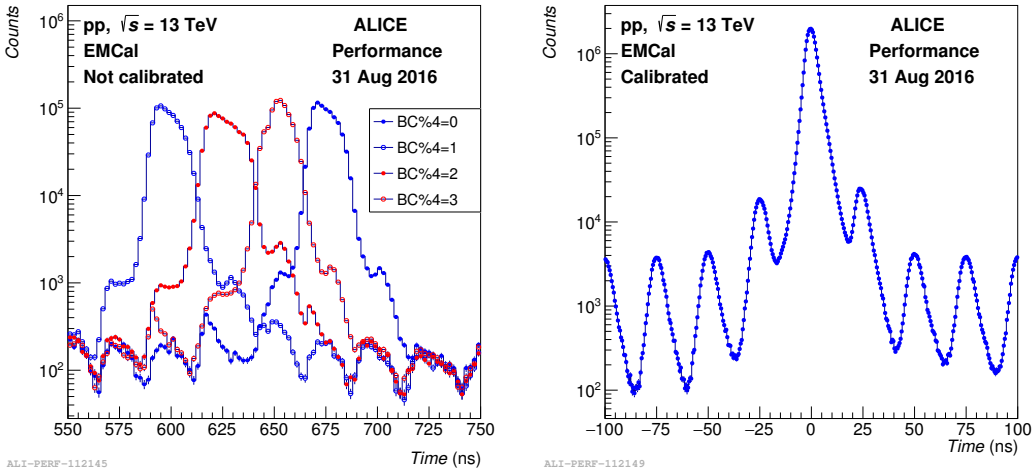

FIGURE IV-22: Left: Time distribution of EMCal cells for different bunch crossings before the time calibration. Right: Aligned time distribution after the time calibration.

performance of LED system or poor knowledge of the gain curves for some towers. Otherwise, both methods are used for a cross-check.

IV.16 Detector performance

The ALICE experiment has collected variety of data in pp, p-Pb and Pb-Pb collisions and spanning the energy range $\sqrt{s_{\mathrm{NN}}} = 0.9$ to 13 TeV. Calibration allowed reaching excellent performance [303] which is shown in this paper on just few chosen examples. The TPC detector provides information about particle identification in a wide momentum range via measurement of the specific energy loss ($\mathrm{d}E/\mathrm{d}x$), charge and momentum of each particle traversing the detector sensitive volume. The measured $\mathrm{d}E/\mathrm{d}x$ versus particle momentum in the TPC is shown in Fig. **IV-23**. The energy loss is described by the Bethe-Bloch formula with the ALEPH parameterization [316]. Data are very close to the analytical formulas, which are drawn as black lines. The clear separation between particle species is visible. Particles can be identified on a track-by-track basis at low momenta ($0.15 < p < 1$ GeV/c). A statistical basis separation is possible up to $p = 50$ GeV/c. The $\mathrm{d}E/\mathrm{d}x$ resolution is about 5.2% in pp collisions (designed value was 5.5%) and 6.5% in the $0-5$% most central Pb-Pb collisions. Figure **IV-24** shows combined ITS-TPC transverse momentum resolution. It takes value of ~ 1% at $p_{\mathrm{T}} = 1$ GeV/c and linearly rise to ~ 10% at $p_{\mathrm{T}} = 50$ GeV/c.

The energy E deposited in EMCal by electrons can be compared to the measured track momentum p that point to the cluster and E/p can be measured. Electrons deposit their entire energy in the calorimeter, while hadrons lose a small fraction. A clean electron sample was obtained from photon conversions in the detector material. Hadrons (protons and charged pions) have been identified from decays of neutral particles (Λ and K^0_S, respectively). The E/p ratio is shown in Fig. **IV-25** for electrons (a) and hadrons (b). There is very good agreement between data and PYTHIA Monte Carlo within uncertainties.

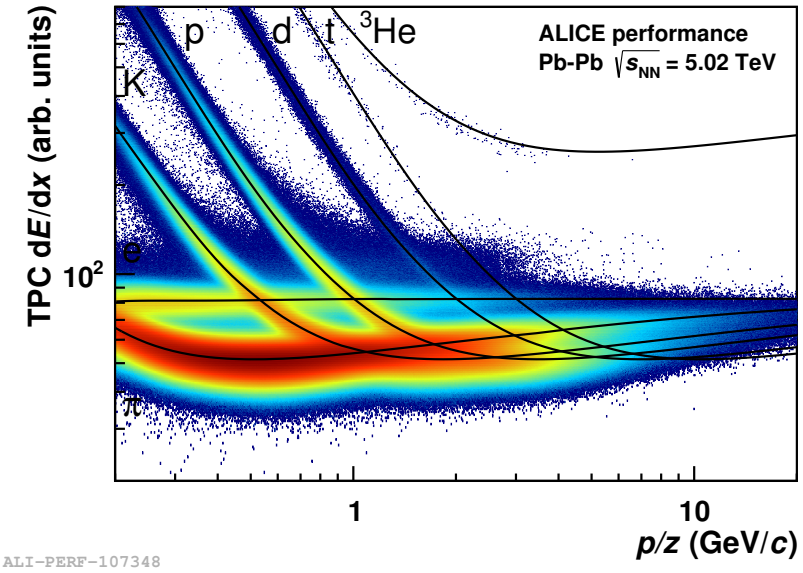

FIGURE IV-23: Specific energy loss ($\mathrm{d}E/\mathrm{d}x$) in the TPC versus particle momentum in Pb-Pb collisions at center-of-mass energy $\sqrt{s_{\mathrm{NN}}} = 5.02$ TeV. The lines show the parameterization of the expected mean energy loss.

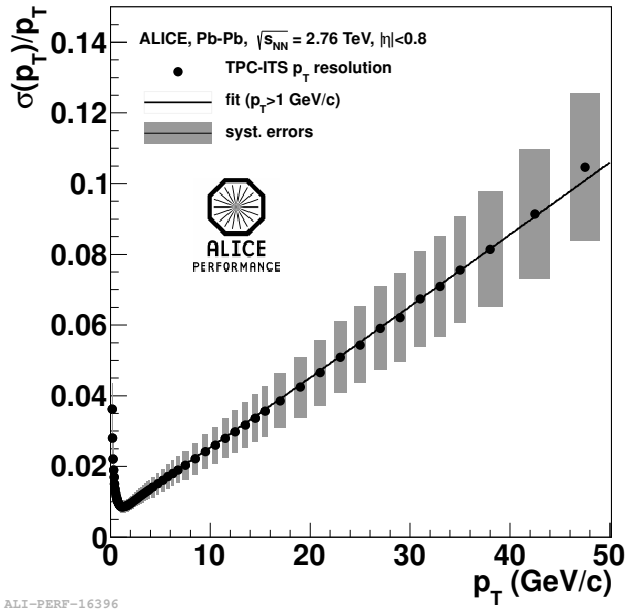

FIGURE IV-24: Transverse momentum resolution combined from TPC and ITS measured in Pb-Pb collisions at center-of-mass energy $\sqrt{s_{\mathrm{NN}}} = 2.76$ TeV.

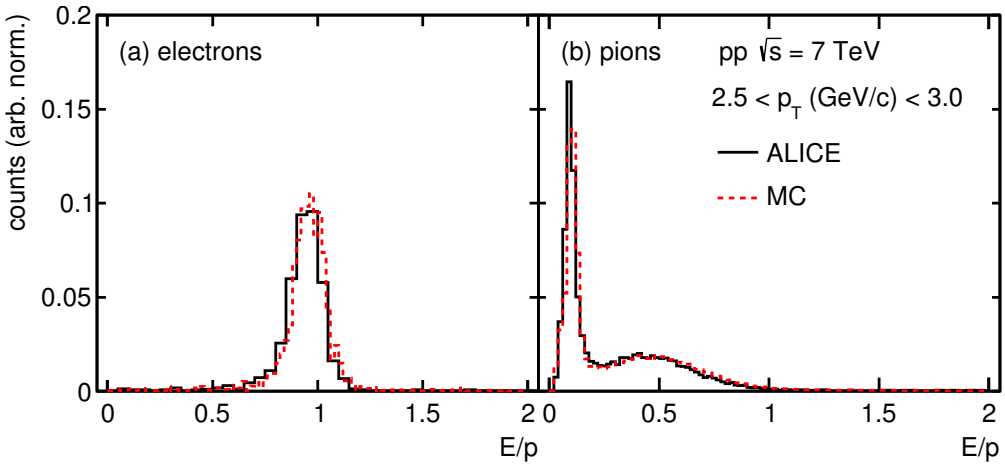

FIGURE IV-25: E/p distribution for (a) electrons and (b) pions in pp collisions at $\sqrt{s} = 7$ TeV. The red dotted line denotes PYTHIA MC simulations, solid black line denotes data [303].

The interaction of low p_{T} photons with detector material is dominated by electron-positron pair creation. The converted photon together with its conversion point can be measured. The photon conversion probability is very sensitive to the amount of material and its chemical composition. Due to that facts photon conversion method (PCM) is a great tool to measure the material budget of the ITS and the TPC detectors and their support structures like a tomograph. The distribution of the reconstructed photon conversion points on the X-Y plane is shown in Fig. **IV-26** and the radial distribution is shown in Fig. **IV-27**. Different layers of the ITS and the TPC are clearly visible. The integrated material budget for radius $R < 180$ cm and for $|\eta| < 0.9$ is $11.4 \pm 0.5\%$ X_0, and can be translated to the conversion probability of $\sim 8.5\%$. It is well described by MC simulations.

The detection of light neutral mesons is a benchmark for calorimeters. The π^0 mesons are identified through the invariant mass of photon pairs. The transverse momentum distribution of the π^0 peak width and the π^0 peak position in pp collisions at $\sqrt{s} = 7$ TeV are shown in Fig. **IV-28** on top and bottom panel, respectively. The very low p_{T} range can be accessed with PCM method, while higher p_{T} range is accessible with calorimeter measurements. The granularity of detectors is reflected in the hierarchy of the peak width. The rise of the peak position and width is driven by the overlapped photon clusters in EMCal. There is also a very good agreement between data and MC.

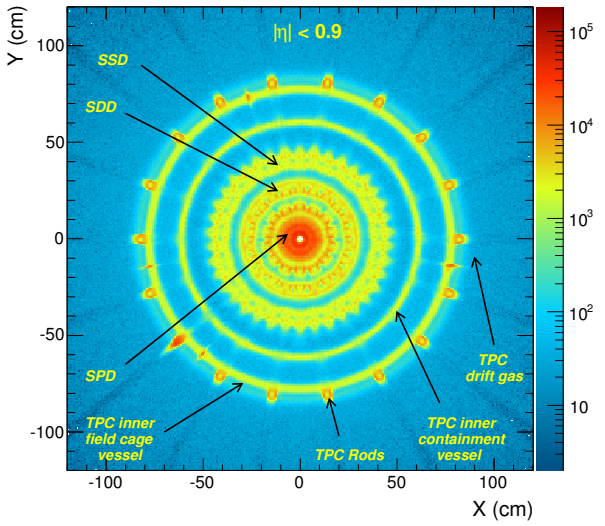

FIGURE IV-26: Distribution of the reconstructed photon conversion points for $|\eta| < 0.9$ in the plane transverse to the beam [303].

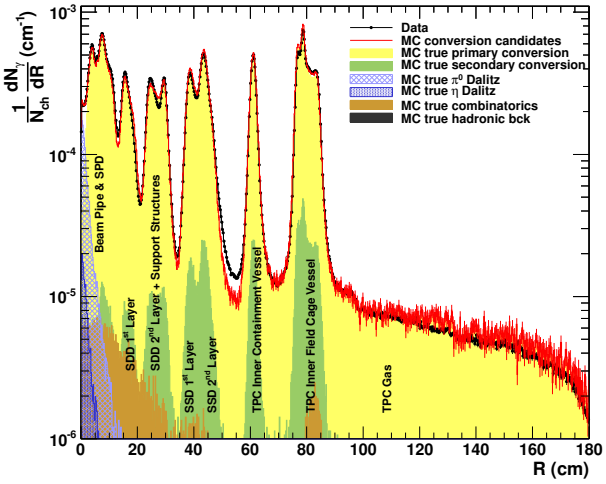

FIGURE IV-27: Radial distribution of the reconstructed photon conversion points for $|\eta| < 0.9$ (black) compared to MC simulations (red). Different contributions to MC are shown with different colors [303].

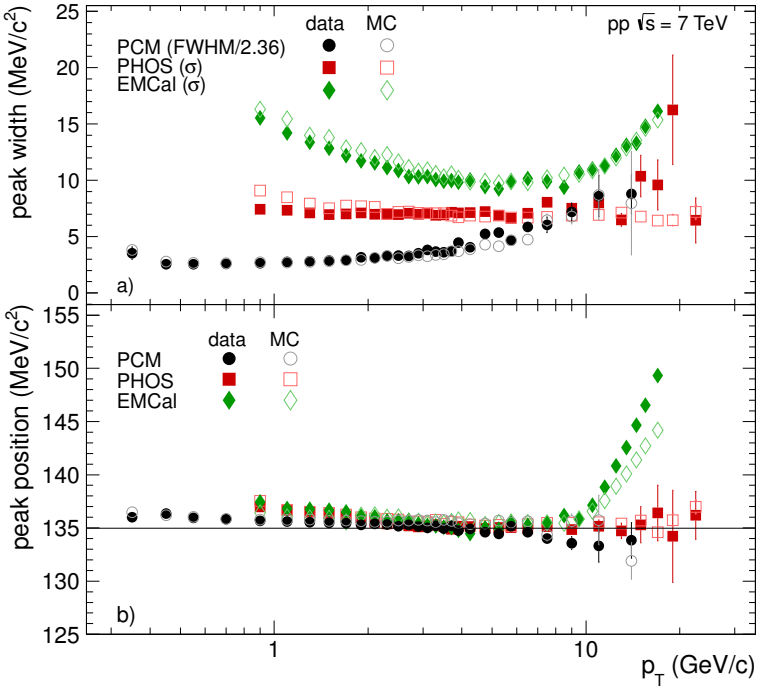

FIGURE IV-28: Reconstructed π^0 peak width (a) and position (b) in pp collisions at $\sqrt{s} = 7$ TeV for PCM method (black), PHOS (red) and EMCal (green). Data (full symbols) are compared to MC simulations (open symbols) (PYTHIA for PHOS and PCM, and π^0 clusters embedding in data for EMCal) [303].

CHAPTER V

NEUTRAL MESONS MEASURED WITH THE ALICE DETECTOR

During almost ten years of data taking, the ALICE experiment has performed many analyses with neutral mesons. The motivation for neutral meson analyses with ALICE is described in Sec. **V.1**. The basic work flow for the data analysis is briefly discussed below. It can be summarized in several steps. The corresponding sections have been provided in brackets.

1. Event selection (Sec. **V.2**),
2. Photon reconstruction/identification (Sec. **V.3**),
3. Neutral meson reconstruction (Sec. **V.4**),
4. Spectrum corrections (Sec. **V.5**),
5. Systematic uncertainties (Sec. **V.6**),
6. Merging results from different methods (Sec. **V.7**),
7. Results (Sec. **V.8**, **V.9**, **V.10**).

All these steps are explained in subsequent sections. There are two important quantities when considering production spectra. After a slight modification of Eq. **II.3**, the π^0 and η meson differential production cross-sections can be written in a form:

$$E\frac{\mathrm{d}^3\sigma}{\mathrm{d}p^3} = \frac{1}{2\pi p_{\mathrm{T}}}\frac{1}{\mathcal{L}}\frac{1}{BR}\frac{1}{\varepsilon\times A}\frac{N(\Delta p_{\mathrm{T}},\Delta y)-N_{\mathrm{s}}}{\Delta p_{\mathrm{T}}\Delta y}, \tag{V.1}$$

where the luminosity

$$\mathcal{L} = \frac{N_{\mathrm{evt}}}{\sigma_{\mathrm{MB}}}R_{\mathrm{trig}} \tag{V.2}$$

is expressed in terms of the trigger cross-section σ_{MB}, the number of events N_{evt} and R_{trig} is the trigger rejection factor, BR is the branching ratio of a meson in a given decay channel, $\varepsilon\times A$ is the efficiency and acceptance correction, $N(\Delta p_{\mathrm{T}},\Delta y)$ is the number of reconstructed mesons in a given Δp_{T} and Δy interval, and N_{s} is the strangeness correction. When the cross-section for a given trigger is not known, one can calculate the invariant yield:

$$E\frac{\mathrm{d}^3N}{\mathrm{d}p^3} = \frac{1}{2\pi N_{\mathrm{evt}}}\frac{\mathrm{d}^2N}{p_{\mathrm{T}}\mathrm{d}p_{\mathrm{T}}\mathrm{d}y} = \frac{1}{2\pi p_{\mathrm{T}}}\frac{1}{N_{\mathrm{evt}}}\frac{1}{R_{\mathrm{trig}}}\frac{1}{BR}\frac{1}{\varepsilon\times A}\frac{N(\Delta p_{\mathrm{T}},\Delta y)-N_{\mathrm{s}}}{\Delta p_{\mathrm{T}}\Delta y}. \tag{V.3}$$

V.1 Physics motivation for π^0 and η meson studies with ALICE

The ALICE experiment is one of the LHC experiments. The LHC accelerator provided pp beams with the center-of-mass energy of $\sqrt{s} = 0.9$ to 13 TeV, nuclear collisions at $\sqrt{s_{\rm NN}} = 2.76$ and 5.02 TeV as well as p-Pb collisions at $\sqrt{s_{\rm NN}} = 5.02$ and 8.16 TeV. Data were delivered during two long periods, LHC Run I (2008-2013) and LHC Run II (2015-2018) separated by the long maintenance period, Long Shutdown 1 (LS1), in 2013-2015. The center-of-mass collision energy reached at the LHC is $\sim$ 4-30 times larger than at RHIC. It implies a new energy regime which had not been explored before the LHC in collider experiments.

The ALICE experiment has been designed to study the Quark-Gluon Plasma (QGP) which is formed in heavy-ion collisions (HIC) at the LHC. However, it can also be used to investigate phenomena in pp and p-Pb collisions.

Production spectra of neutral mesons, such as π^0 or η, can be described by the convolution of hard parton cross-sections, which can be calculated within perturbative quantum chromodynamics and nonperturbative parton distribution functions or fragmentation functions. If PDFs or FFs are known from other experiments, such as hadron production or deep-inelastic scattering in clear e^+e^- annihilation, one can test pQCD. Alternatively, information about the fragmentation function can be obtained. e^+e^- collision experiments are mostly sensitive to the quark-to-hadron fragmentation function, whereas hadronic experiments provide information on the gluon fragmentation. Additionally, hadrons have the inner structure which also can be probed in pp collisions. In consequence, measurements of the meson production spectra in a wide kinematic range and for several colliding energies provide new constraints on PDF and FF parameterizations.

Meson production in HIC allows for studying several effects. The development of collective flow and test of the bulk properties can be examined at low-$p_{\rm T}$ ($p_{\rm T} < 3$ GeV/c). At higher $p_{\rm T}$, one can observe modification of the nucleon PDF in nuclei, energy loss by hard partons in interactions with the dense QGP medium, non-linear recombination effects caused by the dense matter [317], etc. The high-$p_{\rm T}$ ($p_{\rm T} > 5$ GeV/c) light meson production results from hadronization of partons produced in the hard scattering. At moderately high $p_{\rm T}$, the π^0 and η meson are mainly produced via gluon fragmentation at LHC energies. Due to the different color factor in the quark-gluon and gluon-gluon vertex, gluons will suffer a larger energy loss in the medium compared to quarks. Therefore, a comparison of the amount of suppression of the light neutral meson yield and heavier hadrons may provide input for comparison of the energy loss by different partons. In addition, a different relative contribution of quarks and gluons also impacts the light meson production and can lead to a difference in the suppression pattern for π^0 and η mesons.

Precise measurements of the η/π^0 ratio provide valuable information. The systematic uncertainties accompanying measurements in the same detector layout are decreased because of partial cancellations. The same occurs in case of theoretical predictions. The $m_{\rm T}$ scaling can be tested in the η/π^0 ratio. Only precise measurements can show the possible $m_{\rm T}$ scaling violation in the low-$p_{\rm T}$ regime. However, the high-$p_{\rm T}$ part of the ratio, which has a universal character, is necessary for a correct normalization.

Neutral mesons are source of the major background in direct photon, single electron and di-electron spectra analyses. The $m_{\rm T}$ scaling is important in this context, because it is used to estimate unknown contributions to the background.

Lastly, the advantage of studying well-identified particles in the final state (such as π^0 or η mesons) over studying unidentified particles (such as charged hadrons) is interpretation unaffected by contributions from baryons (protons) and other mesons.

V.2 Event selection

ALICE has measured neutral meson production spectra for five center-of-mass energies $\sqrt{s}$ = 0.9 [318], 2.76 [319, 320], 5.02 [19, 321], 7 [318] and 8 TeV [322] in pp collisions. ALICE has also measured non-single diffractive (NSD) π^0 and η meson spectra in p-Pb collisions at the center-of-mass energy of $\sqrt{s_{\rm NN}} = 5.02$ TeV [323] as well as in several centrality classes of Pb-Pb collisions at $\sqrt{s_{\rm NN}} = 2.76$ [319, 324] and 5.02 [321] TeV. Different minimum bias (MB) triggers are used in the ALICE experiment. The $\rm MB_{OR}$ trigger requires a hit in at least one of the two SPD layers or a signal in one of the V0 hodoscopes. The $\rm MB_{AND}$ trigger requires a time coincidence between hits in both V0 counters. The cross-section measurement for each system and energy relies on these two MB triggers performed in Van-der-Meer scans [325, 326, 327]. The summary of the trigger cross-sections ($\sigma_{\rm MB_{OR}}$ and $\sigma_{\rm MB_{AND}}$) and the inelastic cross-section ($\sigma_{\rm pp}^{\rm INEL}$) for pp collisions at different energies is shown in Table **V-1**. The cross-sections for pp collisions at $\sqrt{s} = 0.9$ TeV relies on the $\rm p\bar{p}$ measurement at UA5 [328]. The result for pp collisions at $\sqrt{s} = 5.02$ TeV has been updated and the new value is $\sigma_{\rm MB_{AND}} = 50.87 \pm 0.04$ mb [329]. For Pb-Pb collisions at $\sqrt{s_{\rm NN}} = 2.76$ TeV, the value estimated for centrality determination [309] was used.

System	$\sqrt{s_{\rm NN}}$ (TeV)	Cross-section (mb) $\sigma_{\rm MB_{OR}}$	$\sigma_{\rm pp}^{\rm INEL}$	$\sigma_{\rm MB_{AND}}$	Ref.
pp	0.9	$47.8^{+2.4}_{-1.9}$	52.5 ± 2		[328, 325]
pp	2.76	$\sigma_{\rm MB_{AND}}/0.8613 \pm 0.0006$	$62.8^{+2.4}_{-4.0} \pm 1.2^{\rm lumi}$	47.7 ± 0.9	[325]
pp	5.02		67.6 ± 0.6	51.2 ± 1.2	[326]
pp	7	62.2 ± 2.2	$73.2^{+2.0}_{-4.6} \pm 2.6^{\rm lumi}$		[325]
pp	8			55.80 ± 1.45	[327]
Pb-Pb	2.76			$(7.64 \pm 0.22) \times 10^3$	[309]

TABLE V-1: The minimum bias trigger cross-section ($\sigma_{\rm MB_{OR}}$ and $\sigma_{\rm MB_{AND}}$) and the inelastic cross-section for a given collision type at a given center-of-mass energy $\sqrt{s_{\rm NN}}$.

ALICE has also collected data with rare EMCal and PHOS triggers. There are EMC1 or EMC7 and PHI7 - L0 EMCal and PHOS triggers with different thresholds and EG1 or EG2 - EMCal L1 triggers with different thresholds. The energy threshold values for triggers are given in Table **V-2**. The L0 EMCal trigger checks the energy deposited in 2×2 adjacent cells evaluated with a sliding window algorithm within each Trigger Region Unit (TRU) spanning 4×24 cells in coincidence with an MB trigger. The L1 EMCal trigger extends the search with a sliding window across neighboring TRUs. The L0 PHOS trigger uses a window of 4×4 adjacent cells evaluated with the Weighted Sum algorithm in coincidence with an MB trigger. In order to properly normalize triggered events, the trigger rejection factor ($R_{\rm trig}$) is calculated. It is the ratio of calorimeter triggered

and MB cluster energy spectrum as a function of the cluster energy. The ratio should be constant above the trigger threshold provided that triggers do not change the reconstruction efficiency of clusters. The example trigger rejection factor curves are shown in Fig. **V-1**. If the trigger rejection factors are known, luminosities for different triggers can be calculated. Trigger rejection factors and corresponding luminosities for different analyses are given in Table **V-2**. For further analysis only the events with the z-coordinate of the vertex position in the global ALICE coordinate system, $|z| < 10$ cm, are used. The z-vertex distribution for pp and Pb-Pb collisions is shown in Fig. **V-2**.

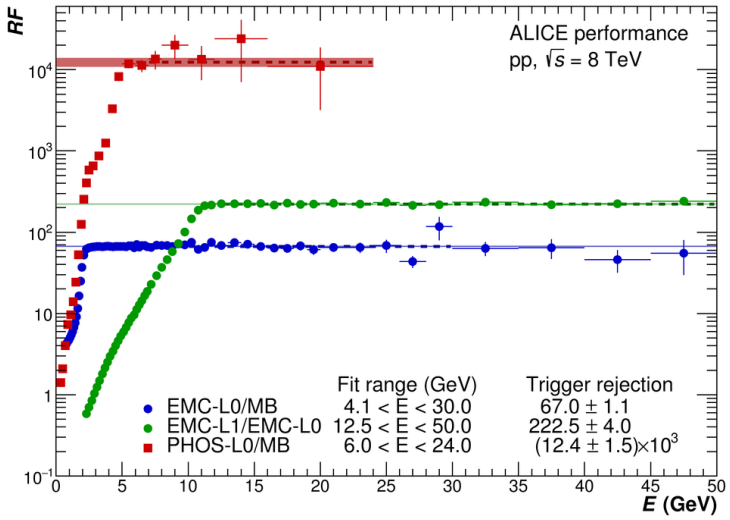

FIGURE V-1: Trigger rejection factor (*RF*) for PHOS-L0 and EMC-L0/L1 triggers. RFs are obtained by the constant fit in the fit range illustrated by dotted lines. The light-colored bands indicate uncertainties [322].

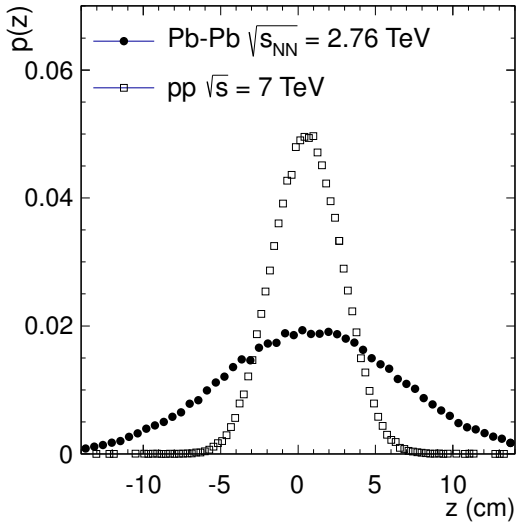

FIGURE V-2: z projections of the luminous region obtained from reconstructed vertices in pp and Pb-Pb collisions (folded with vertex resolution) [303].

System	$\sqrt{s_{\mathrm{NN}}}$ (TeV)	Method	Trigger	R_{trig}	$\mathcal{L}$ (nb^{-1})	Ref.
pp	0.9	PCM	INT1	1	0.14	[318]
pp	0.9	PHOS π^0	INT1	1	0.14	[318]
pp (2011)	2.76	PHOS	INT1	1	0.63	[319]
pp (2011)	2.76	PCM	INT1	1	1.05	[319]
pp (2011)	2.76	EMC, PCM, PCM-EMC	INT1	1	0.542 ± 0.010	[320]
pp (2011)	2.76	EMC, PCM-EMC, mEMC	EMC1	1217 ± 67	13.8 ± 0.806	[320]
pp (2013)	2.76	EMC, PCM, PCM-EMC	INT7	1	0.335 ± 0.013	[320]
pp (2013)	2.76	EMC, PCM-EMC	EMC7	126.0 ± 4.3	1.19 ± 0.062	[320]
pp (2013)	2.76	EMC, PCM-EMC, mEMC	EG2	1959 ± 131	6.98 ± 0.542	[320]
pp (2013)	2.76	EMC, PCM-EMC, mEMC	EG1	7743 ± 685	47.1 ± 4.57	[320]
pp	5.02	EMC, PCM	INT7	1	2	[19, 321]
pp	5.02	PHOS	INT7	1	20.8	[19, 321]
pp	5.02	PHOS	PHI7	$(23.99 \pm 0.12) \times 10^3$	470	[19, 321]
pp	7	PCM	INT1	1	5.6	[318]
pp	7	PHOS π^0	INT1	1	4.0	[318]
pp	7	PHOS η	INT1	1	5.7	[318]
pp	8	EMC, PCM-EMC	INT7	1	$1.94 \pm 0.05_{\mathrm{norm}}$	[322]
pp	8	PHOS	INT7	1	$1.25 \pm 0.04_{\mathrm{norm}}$	[322]
pp	8	PCM	INT7	1	$2.17 \pm 0.06_{\mathrm{norm}}$	[322]
pp	8	EMC, PCM-EMC	EMC7	67 ± 1.1	$40.9 \pm 0.7_{\mathrm{sys}} \pm 1.1_{\mathrm{norm}}$	[322]
pp	8	EMC, PCM-EMC	EG1	$(14.9 \pm 0.3) \times 10^3$	$615 \pm 15_{\mathrm{sys}} \pm 16_{\mathrm{norm}}$	[322]
pp	8	PHOS	PHI7	$(12.4 \pm 1.5) \times 10^3$	$135.6 \pm 16.8_{\mathrm{sys}} \pm 3.6_{\mathrm{norm}}$	[322]
p-Pb	5.02	EMC, PCM, Dalitz, PCM-EMC, PHOS	INT7	1	0.05	[323]
Pb-Pb (2010)	2.76	PHOS	INT1	1	16.1×10^6 events	[319]
Pb-Pb (2010)	2.76	PCM	INT1	1	13.2×10^6 events	[319]
Pb-Pb (2011)	2.76	PCM, EMC	INT7 (0 – 10%)	1	20.1×10^{-3}	[324]
Pb-Pb (2011)	2.76	PCM, EMC	INT7 (20 – 50%)	1	4.8×10^{-3}	[324]
Pb-Pb	5.02	PHOS	INT7 (0 – 90%)	1	12×10^{-3}	[321]

TABLE V-2: A collision system, a center-of-mass energy $\sqrt{s_{\mathrm{NN}}}$, an analysis method, a trigger name and corresponding trigger rejection factor (R_{trig}) and luminosity are given for each neutral meson analysis. $\mathrm{MB_{OR}}$/INT1 and $\mathrm{MB_{AND}}$/INT7 are Minimum Bias L0 triggers. EMC1 and EMC7 are EMCal L0 triggers, EG1, EG2 are EMCal L1 triggers, PHI7 is PHOS L0 trigger with the corresponding trigger thresholds: $E_{\mathrm{th}}^{\mathrm{EMC1}} \approx 3.4$ GeV, $E_{\mathrm{th}}^{\mathrm{EMC7}} \approx 2$ GeV, $E_{\mathrm{th,\ pp@2.76TeV}}^{\mathrm{EG1}} \approx 5.5$ GeV, $E_{\mathrm{th}}^{\mathrm{EG2}} \approx 3.5$ GeV, $E_{\mathrm{th,\ pp@8TeV}}^{\mathrm{EG1}} \approx 8.4$ GeV, $E_{\mathrm{th}}^{\mathrm{PHI7}} \approx 4$ GeV ($E_{\mathrm{th}}^{\mathrm{PHI7}} \approx 3$ GeV for pp@5TeV in 2015).

V.3 Photon reconstruction

There are two photon measurement methods used in the ALICE detector. The first is based on a measurement of energy deposited in the sensitive material of a calorimeter. This method is exploited by PHOS and EMCal. The second one is based on the external conversion of photons into e^+e^- pairs in the detector material and is called the photon conversion method (PCM). In that case the conversion pair is registered in the large volume gaseous Time Projection Chamber and in the Inner Tracking System. The two methods are described below.

A group of calorimeter cells somehow related to each other is called a cluster. There are four algorithms used for clusterization in ALICE calorimeters. They are briefly described below.

- **V1 clusterizer** associates all the adjacent cells (exceeding some minimum energy threshold E_{cell}) to a cluster initiated by the seed cell with the energy exceeding some threshold E_{seed}, unless they are neighbors. There can only be four neighboring cells (the distance on the discrete two-dimensional XY plane is $\Delta X + \Delta Y = 1$ for neighbors) for each cell. A cell can only be associated to one cluster. The cluster is formed when no other cell is a neighbor of any cell in the cluster. When a cluster is formed all its features (the total energy, the center of gravity, etc.) are calculated and the algorithm starts looking for a new cluster. A consequence of such an algorithm is that one cluster can contain all cells in the super module.

- **V1 clusterizer with unfolding** divides multi-maxima (a maximum or, to be more precise, a local maximum is a cell in a cluster surrounded by less energetic cells) clusters reconstructed with the V1 clusterizer into single-maxima clusters. The algorithm splits energy of clusters being unfolded by splitting energy in cells. When the number of local maxima in a V1 protocluster is found to be greater than one, the fraction energy profiles are fitted to the protocluster. A new set of unfolded clusters with a proper dustribution of energy in cells is created.

- At first, all cells are ranked by energy in the **V2 clusterizer**. The most energetic cell (with the energy above E_{seed}) is the seed. A scan over cells already associated to the cluster and check for neighbors is done in iterations. However, the energy of a neighboring cell should be smaller in order for it to become a neighbor. When a cluster is formed, the procedure is repeated but with a smaller pool of available cells.

- In the **NxN clusterizer**, the seed is found to have the energy above E_{seed}. Then the window of 3×3 cells with the seed cell in the middle is opened and all the eight cells are checked to ensure they have lower energy than the seed. If this requirement is satisfied, a new cluster is formed and the procedure is repeated.

Cells must fulfill the minimum energy threshold, except for the NxN clusterizer. The resulting sketch of the different clusterizers is shown in Fig. **V-3**. In case of EMCal every clusterizer has been used. In case of PHOS only two options, V1 and V1 with unfolding clusterizers, are available. From the perspective of a neutral meson analysis, clusterizers have different performance. Due to lower granularity of EMCal, photon clusters coming from π^0 tend to overlap already at $p_{\text{T}} \simeq 6$ GeV/c. It results in a π^0 spectrum range up to $p_{\text{T}} \simeq 12$ GeV/c with the V1 clusterizer. The range can be

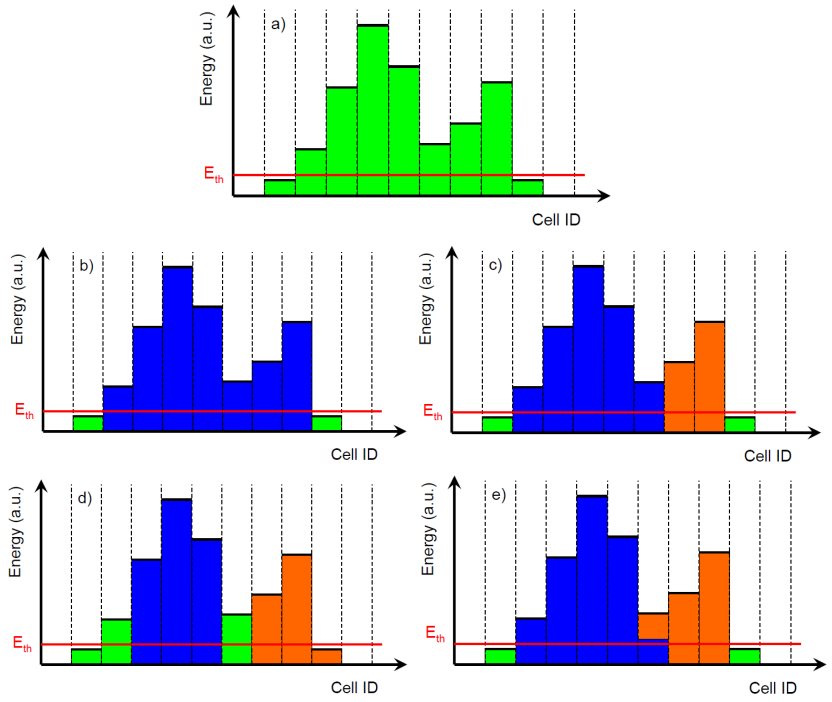

FIGURE V-3: a) An example of fired cells (green) in a calorimeter. The red line indicates the minimum energy threshold. b) Result of the V1 clusterizer: one big cluster (blue) is formed, cells below threshold (green) are not attached to cluster. c) Result of the V2 clusterizer: two clusters (blue and orange) are formed, cells below threshold (green) are not attached to any cluster. d) Result of the NxN clusterizer: two clusters (blue and orange) are formed, cells below threshold (green) are not attached to any cluster; note a cell below threshold attached to a cluster. d) Result of the V1 with unfolding clusterizer: two clusters (blue and orange) are formed, cells below threshold (green) are not attached to any cluster, one cell has energy shared among clusters.

extended with the other clusterizers. The NxN takes a maximum of 9 cells, which results in an artificial energy cut-off for higher-energy clusters. The V2 and V1 with unfolding give a similar performance extending the resolved clusters range to $p_{\mathrm{T}} \simeq 12$ GeV/c, which results in the π^0 spectrum range of up to $p_{\mathrm{T}} \simeq 20$ GeV/c. However, with smarter cell energy sharing the unfolding can go a bit further in p_{T} than V2.

Due to a much larger PHOS granularity, photon clusters are resolved up to $p_{\mathrm{T}} \simeq 20$ GeV/c and the range is only limited by available statistics. In case of η meson, its opening angle is so large that the clusterization method doesn't have a significant impact on the range and only statistics matters.

When the pool of clusters is prepared, the photon candidates are chosen based on selection criteria. These take into account a shower shape, cluster-track matching, timing and others. The cluster-track matching reduces contamination from charged particles (see Fig. **IV-25**), timing reduces clusters coming from a different bunch crossing (pile-up) (see Fig. **IV-22**, right-hand side).

A distinction between photons, electrons, neutrons and the so called merged neutral mesons is based on the shower shape. The shower shape can be characterized by a larger eigenvalue of the energy decomposition of clusters in the calorimeter pseudo-rapidity η and azimuth angle φ plane and expressed as:

$$\sigma^2_{\text{long}} = 0.5\left(\sigma^2_{\varphi\varphi} + \sigma^2_{\eta\eta} + \sqrt{(\sigma^2_{\varphi\varphi} - \sigma^2_{\eta\eta})^2 + 4\sigma^4_{\eta\varphi}}\right), \tag{V.4}$$

where

$$\sigma^2_{\alpha\beta} = <\alpha\beta> - <\alpha><\beta>, \tag{V.5}$$

and

$$<\alpha> = \frac{\sum w_i \alpha_i}{\sum w_i}, \tag{V.6}$$

with a weight $w_i = \max(0, 4.5 + \log(E_i/E))$, which logarithmically depends on the energy E_i of a given cell i to the cluster energy E. The different contributions to the shower shape spectrum are illustrated in Fig. **V-4**. Photonic clusters (direct or coming from the π^0 or η decay) are mostly located below $\sigma^2_{\text{long}} = 0.3$. The dominant contribution above $\sigma^2_{\text{long}} = 0.3$ is coming from merged π^0 showers.

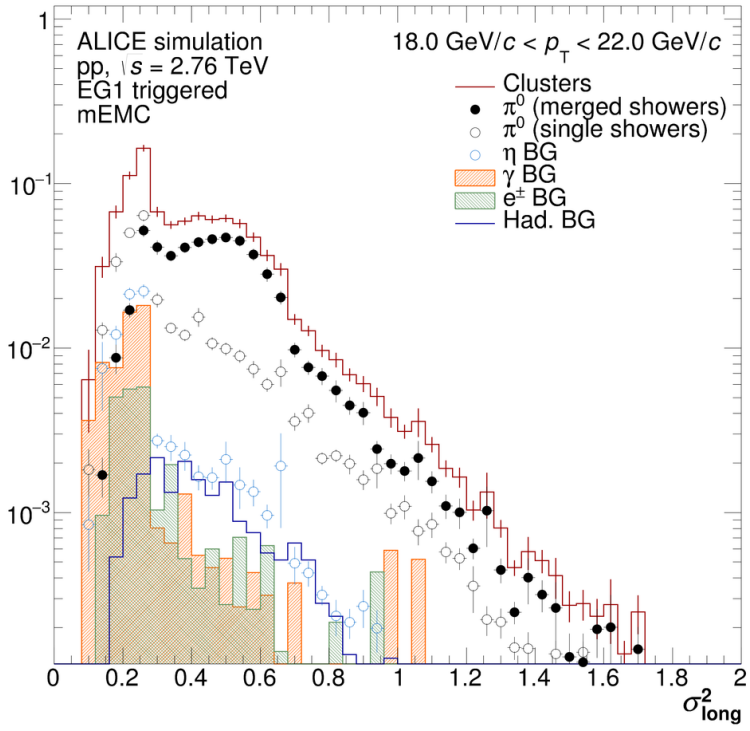

FIGURE V-4: Different contributions to the reconstructed clusters (red solid line) shower shape (σ^2_{long}) distribution for π^0 candidates with $18 < p_{\text{T}} < 22$ GeV/c in MC. Black dots denote π^0 clusters coming from merged showers, open black and blue circles - resolved photon showers from π^0 and η, respectively, orange shaded area is coming from direct photons, green shaded area from electrons and blue solid line indicates hadrons [320].

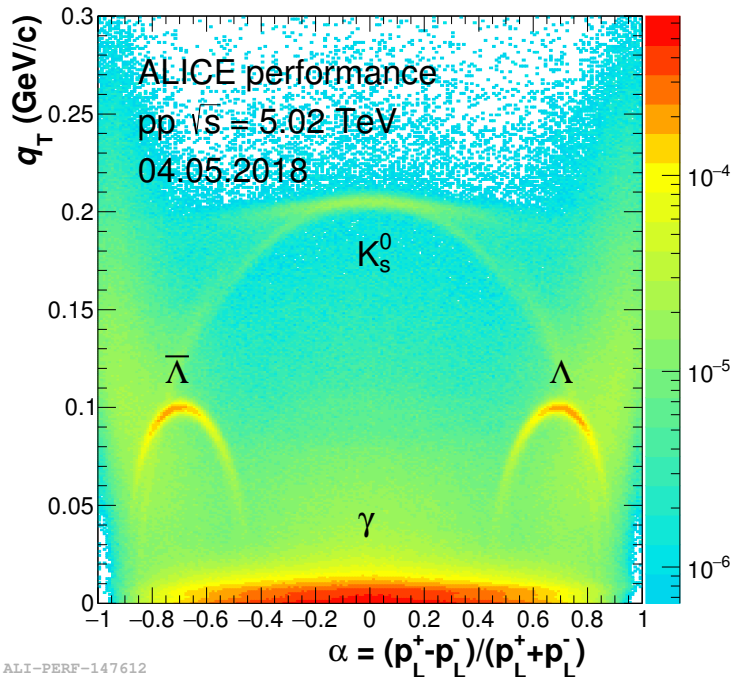

FIGURE V-5: Armanteros-Podolanski plot for photon candidates.

Photons are reconstructed from e^+e^- pairs using the secondary vertex (V0) finding algorithm [330] in the photon conversion method (PCM). Both electron legs are required to have tracks with a specific energy loss in the TPC in the proximity of the average electron $\mathrm{d}E/\mathrm{d}x$ and to fulfill the electron hypothesis in the TOF detector. Tracks are refitted with the photon mass constrained. Together with an opening angle between e^+ and e^- tracks requirement, they reduce combinatorial background. The Dalitz e^+e^- pairs are distinguished by a radial distance from the interaction point requirement. The K^0_S and Λ contamination is suppressed by the selection in the Armanteros-Podolanski (AP) variables; transverse momentum q_T - the transverse momentum of the daughter particle p_T with respect to the reconstructed mother particle $\overrightarrow{p_\mathrm{m}}$; and the longitudinal momentum asymmetry α, defined as follows:

$$q_\mathrm{T} = \frac{|\overrightarrow{p_\mathrm{T}} \times \overrightarrow{p_\mathrm{m}}|}{|\overrightarrow{p_\mathrm{m}}|}, \tag{V.7}$$

and

$$\alpha = \frac{p_\mathrm{L}^+ - p_\mathrm{L}^-}{p_\mathrm{L}^+ + p_\mathrm{L}^-}, \tag{V.8}$$

where p_L^+ and p_L^- are longitudinal momenta of positively and negatively charged daughter particles, respectively. The AP plot of photon candidates is shown in Fig. **V-5**.

V.4 Neutral meson reconstruction

Neutral mesons are mostly combined from photon pairs using the invariant mass technique. However, they can also be identified in a single cluster analysis via shower shapes. For the invariant mass analysis we consider cases where two photons are registered in the same calorimeter (either PHOS or EMCal), both photons are real and reconstructed via the PCM method, one photon is real and the other virtual (Dalitz decay) and both are reconstructed via the PCM method or the hybrid method where one photon is registered in EMCal and the other reconstructed in PCM. The invariant mass is calculated as follows:

$$M_{\gamma\gamma} = \sqrt{2E_1E_2(1-\cos\theta_{12})}, \tag{V.9}$$

where E_1 and E_2 are photon candidates energies and θ_{12} is an opening angle between them measured in the laboratory frame. Neutral mesons are visible as an excess yield at their respective rest mass, above background. In order to ensure the proper background description (in EMCal), a minimum separation distance is required. The uncorrelated background is determined by mixing photon pairs from different events in the same class of z-vertex position, photon candidate multiplicity as well as transverse momentum. Then, this background is normalized in proper side-band and further subtracted. The combinatorial background subtraction is particularly important in Pb-Pb and p-Pb collisions as well as in the low p_{T} range of the spectrum. The residual correlated background is parameterized as a linear or second order polynomial. The signal is parameterized by Gaussian, Crystal Ball [331] (CB) or Gaussian convoluted with exponent to account for bremsstrahlung [332], depending on the system and the method of the analysis. The Gaussian convoluted with the exponent has the following functional form:

$$f(x) = A\left(G(x) + \exp\left(\frac{x-M}{\lambda}\right)(1-G(x))\Theta(x-M)\right), \tag{V.10}$$

with

$$G(x) = \exp\left(-0.5\left(\frac{x-M}{\sigma}\right)^2\right), \tag{V.11}$$

where the $G(x)$ component represents Gaussian with a mean M, width σ and an amplitude A for a given meson, λ is an inverse slope parameter of exponent, $\Theta(x-M)$ is a Heaviside function which specifies when the exponential component is taken into account. The functional form of CB is as follows:

$$f(x) = \begin{cases} AG(x) & \text{for } \frac{x-M}{\sigma} < a, \\ A\left(\frac{n}{|a|}\right)^n \exp\left(-0.5a^2\right)\left(\frac{n}{|a|} - |a| - \frac{x-M}{\sigma}\right)^{-n} & \text{for } \frac{x-M}{\sigma} > a, \end{cases} \tag{V.12}$$

where a and n fit parameters control the left-hand side tail caused by bremsstrahlung. The methods of the analysis for each energy and system are summarized in Table **V-2**.

The neutral meson raw yields are extracted by integrating background subtracted invariant mass distributions in a defined window around a meson mass peak (usually it is an equivalent of ~ 3 standard deviations around the peak, but one needs to take into account a larger bremsthralung tail

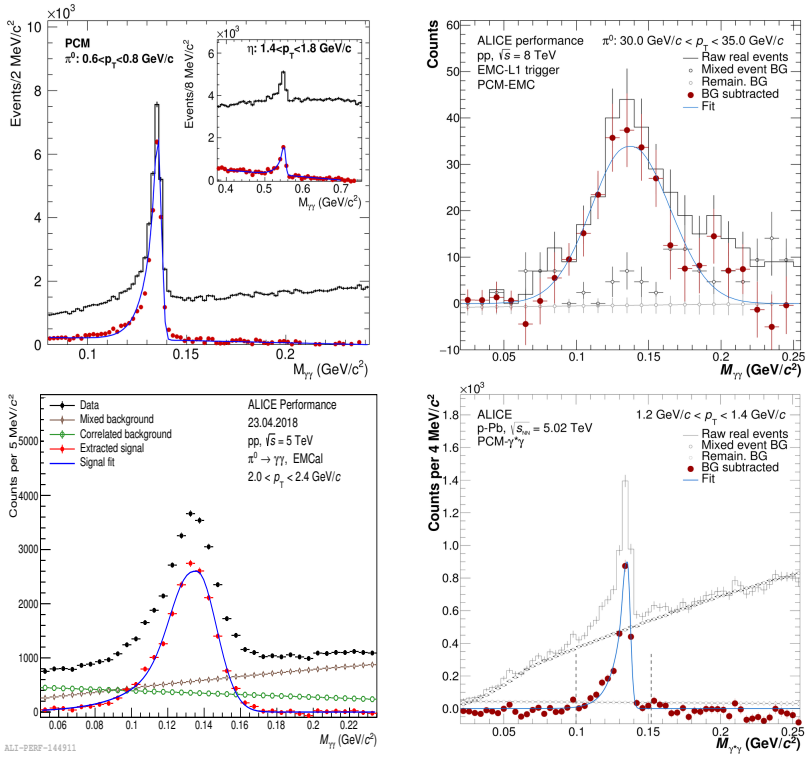

FIGURE V-6: The invariant mass of two photon candidates without (dark) and with background subtracted (red) together with the fit line (blue) around π^0 nominal mass reconstructed with the PCM in pp collisions at $\sqrt{s} = 7$ TeV [318] (top left), the PCM-EMC in pp collisions at $\sqrt{s} = 8$ TeV [322] (top right), the EMC in pp collisions at $\sqrt{s} = 5.02$ TeV (bottom left) and the Dalitz in p-Pb collisions at $\sqrt{s} = 5.02$ TeV [323] (bottom right). The p_{T} range is indicated in each figure. The inset in the top left figure shows the invariant mass of two photons around η nominal mass.

on the left-hand side of the peak in some methods). The example invariant mass distributions in the proximity of the nominal π^0 and η meson mass are shown in Fig. **V-6**, **V-7** and **V-8**, respectively.

A single cluster analysis has been used in a high p_{T} range in pp collisions at $\sqrt{s} = 2.76$ TeV with EMCal. Two photon showers from the π^0 decay tend to merge in high p_{T} and form a single EMCal cluster. For that reason it is not possible to use the invariant mass analysis. Merged clusters from π^0 decays look more elongated than clusters from electrons or photons. Thus, the shower shape variable σ^2_{long} defined in Eq. **V.4** can be used to distinguish them (see Fig. **V-4**). A comparison of the π^0 meson mass position and width, reconstructed in pp collisions at $\sqrt{s} = 7$ TeV, is shown in Fig. **IV-28**. A comparison of the π^0 and η meson mass position and width, reconstructed in p-Pb collisions at $\sqrt{s} = 5.02$ TeV, is shown in Fig. **V-9**. The reconstructed mass and width peak positions in data are well reproduced by MC simulations. For EMC and PCM-EMC methods the meson peak position was not calibrated to the nominal meson mass position, but the cluster energy in MC was corrected by a p_{T}-dependent factor to obtain π^0 mass peak agreement in data and MC well below 0.5%. For other methods the agreement is on the same level or even much better.

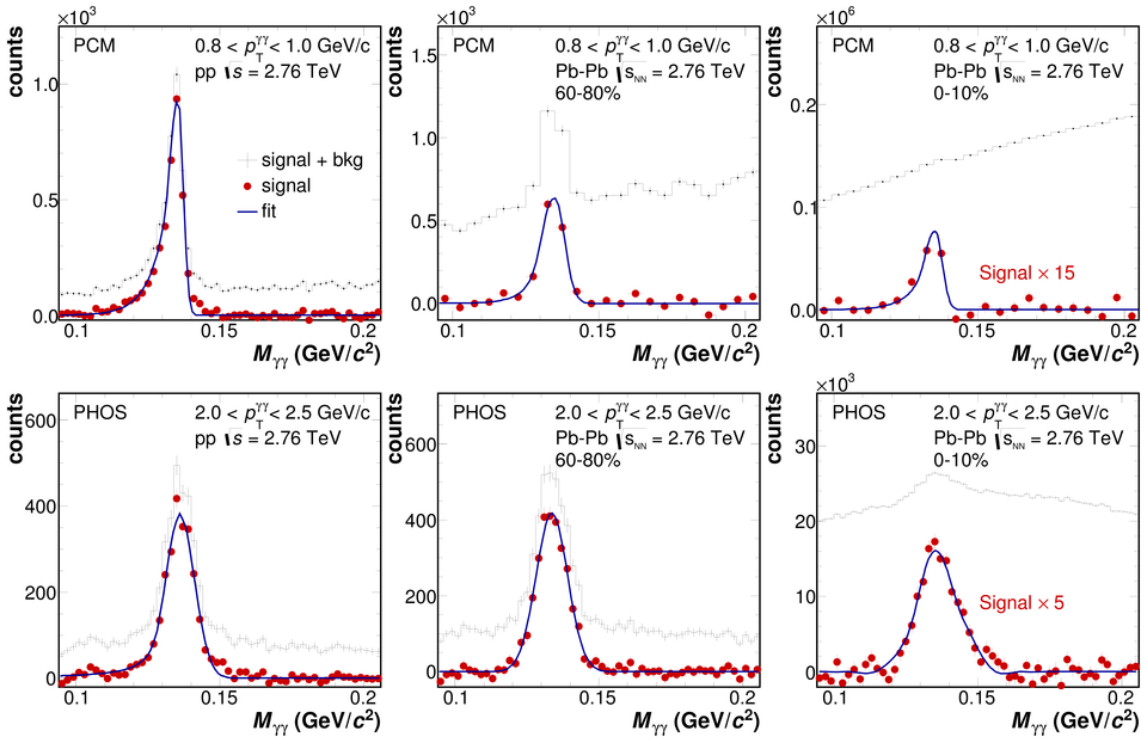

FIGURE V-7: Invariant mass before and after background subtraction in the π^0 mass region for pp (left column), 60-80% (middle column) and 0-10% (right column) Pb-Pb collisions at $\sqrt{s_{\rm NN}} = 2.76$ TeV reconstructed with the PCM (top row) and PHOS (bottom row) method. The $p_{\rm T}$ range is indicated in each figure [319].

V.5 Spectrum corrections

Based on the data or MC several corrections have been applied to obtain the final spectrum:

- Efficiency and acceptance correction, $\varepsilon \times A$,
- Feed-down correction, N_s,
- Vertex correction, $N_{\rm evt}$.

Due to the limited acceptance of detectors and different selection criteria applied for different methods, $\varepsilon \times$ **A correction** accounts for several effects such as cluster selection, meson reconstruction, the number of bad channels, interspace between super modules, etc. This correction affects the shape of the whole spectrum. The effective efficiencies $p_{\rm T}$ dependent normalized to the full azimuth and one rapidity unit ($|\Delta y| = 1$) are shown in Fig. **V-10** for π^0 and η mesons in pp collisions at $\sqrt{s} = 2.76$ TeV. The larger acceptance for EMCal compared to PHOS is reflected in curves. The drop-off at around $p_{\rm T} = 10$ GeV/c for EMCal is caused by merged showers. At $p_{\rm T} = 15$ GeV/c, the single shower analysis is more efficient. Due to a much larger granularity, the EMCal drop is not visible for PHOS, where it is shifted to much higher $p_{\rm T}$ values. A small conversion probability for PCM accounts for lower effective efficiency. The PCM-EMC method gains in reach and efficiency due to the hybrid technique. For all the methods except for mEMC, the purity $P = 1$. For the

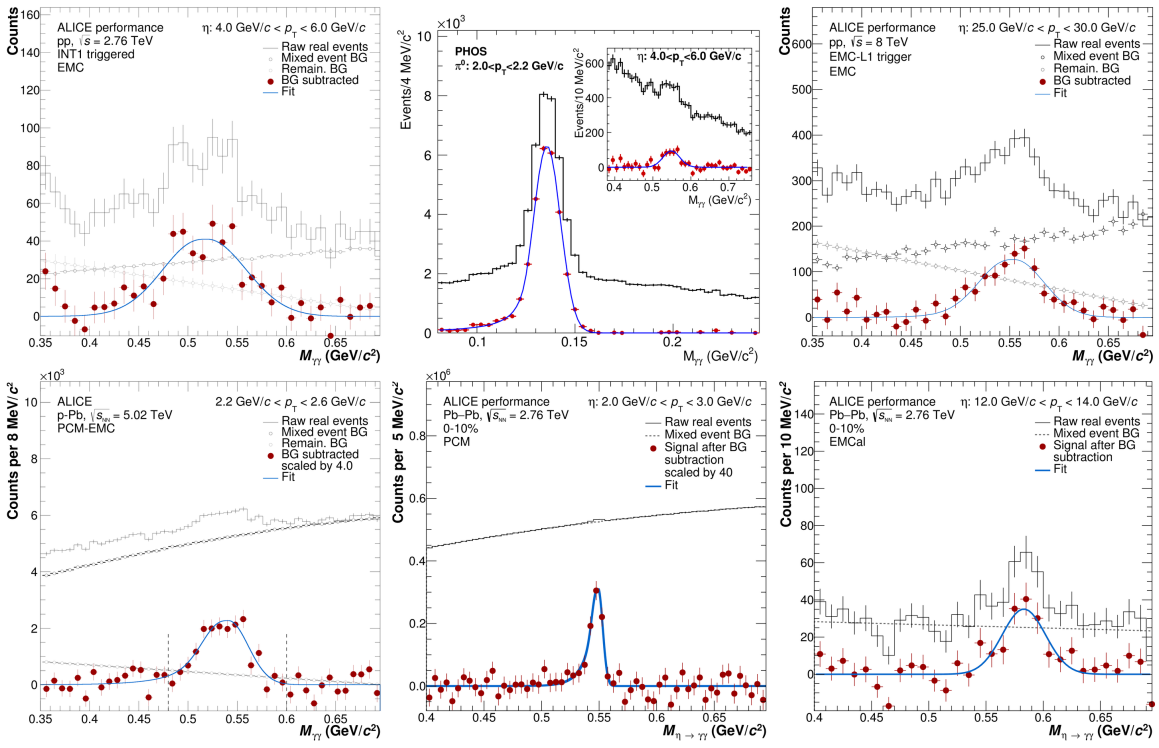

FIGURE V-8: Invariant mass without (dark) and with background subtracted (red) together with fit line (blue) around η nominal mass reconstructed with EMC in pp collisions at $\sqrt{s} = 2.76$ TeV [320] (top left), PHOS in pp collisions at $\sqrt{s} = 7$ TeV [318] (inset top middle), EMC in pp collisions at $\sqrt{s} = 8$ TeV [322] (top right), PCM-EMC in p-Pb collisions at $\sqrt{s} = 5.02$ TeV [323] (bottom left), 0-10% Pb-Pb collisions at $\sqrt{s_{\mathrm{NN}}} = 2.76$ TeV with PCM [324] (bottom middle) and 0-10% Pb-Pb collisions at $\sqrt{s_{\mathrm{NN}}} = 2.76$ TeV with EMC [324] (bottom right). The regular size figure in top middle shows invariant mass around π^0 nominal mass. The p_{T} range is indicated in each figure.

mEMC method, other than merged π^0 sources are taken into account. The correction is MC-based.

The **feed-down correction** is mostly related to the π^0 meson production. For η meson it is negligible. One needs to account for and subtract from the yield the mesons coming from long-lived particles which decay far away from the interaction point. These particles contain strange quark. The largest source of neutral mesons from strange particles are K^0_S particles. In addition, the strangeness production in MC simulations does not reproduce this from data. As an example, see the kaon-to-pion ratio in pp collisions at $\sqrt{s} = 7$ TeV [333] compared to various QCD-inspired models as shown in Fig. **V-11**. The $K^{\pm}/\pi^{\pm}$ ratio differs by 10% to 60% depending on the model and p_{T} range. Moreover, none of the models describes both the kaon-to-pion and the proton-to-pion ratio simultaneously. The feed-down correction is most important at low p_{T} and takes $\sim 10\%$ at $p_{\mathrm{T}} = 1$ GeV/c, then decreases to $\sim 5\%$ at $p_{\mathrm{T}} = 4$ GeV/c and remains constant. This correction affects the neutral meson yield and is important in the low-p_{T} region. The correction is MC-based. However, single particle spectra are corrected by results obtained from real data.

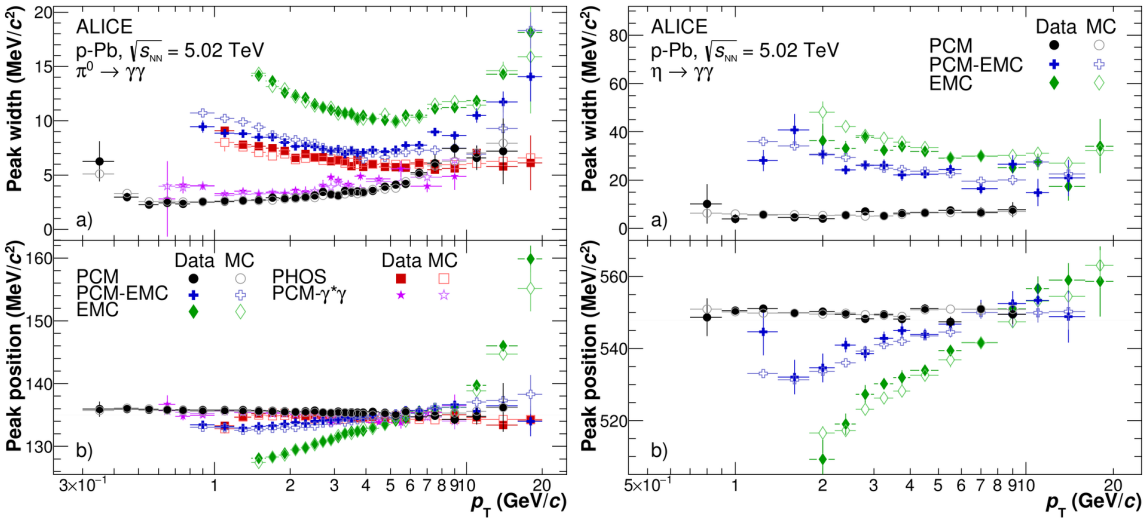

FIGURE V-9: Left: Reconstructed π^0 peak width (a) and position (b) in p-Pb collisions at $\sqrt{s} =$ 5.02 TeV for PCM method (black), PHOS (red), PCM-EMC (blue), Dalitz (violet) and EMCal (green). Right: Reconstructed η peak width (a) and position (b) in p-Pb collisions at $\sqrt{s} = 5.02$ TeV for PCM method (black), PCM-EMC (blue) and EMCal (green). Data (full symbols) are compared to MC simulations (open symbols) [323].

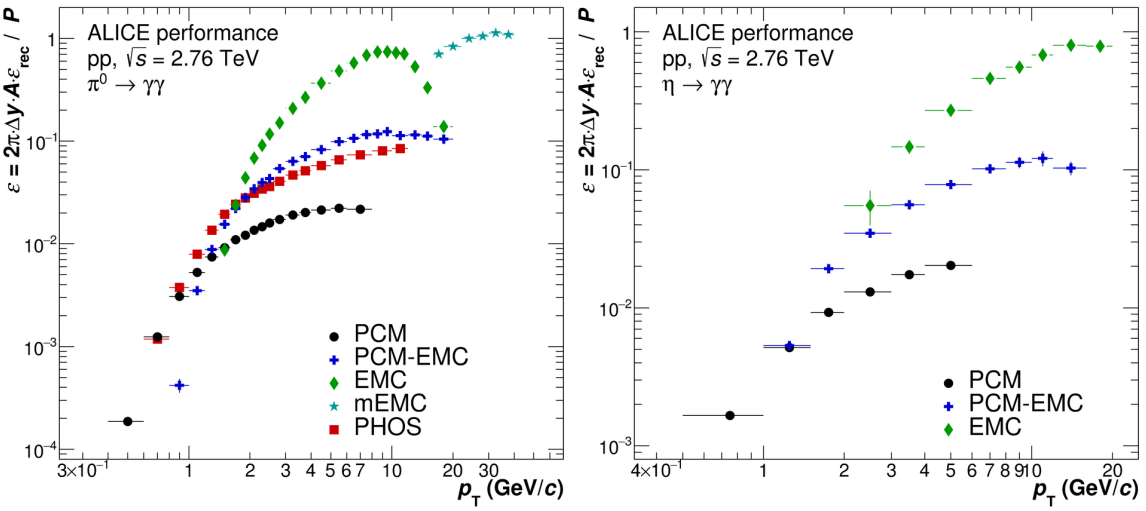

FIGURE V-10: Effective normalized efficiency p_T dependent correction for different methods of π^0 (left panel) and η (right panel) meson reconstruction in pp collisions at $\sqrt{s} = 2.76$ TeV [320].

The last and the smallest number is **vertex correction** which affects normalization, N_{evt}. It is $\sim 1\%$ and is due to the particle detection inefficiency causing the lack of vertex reconstruction.

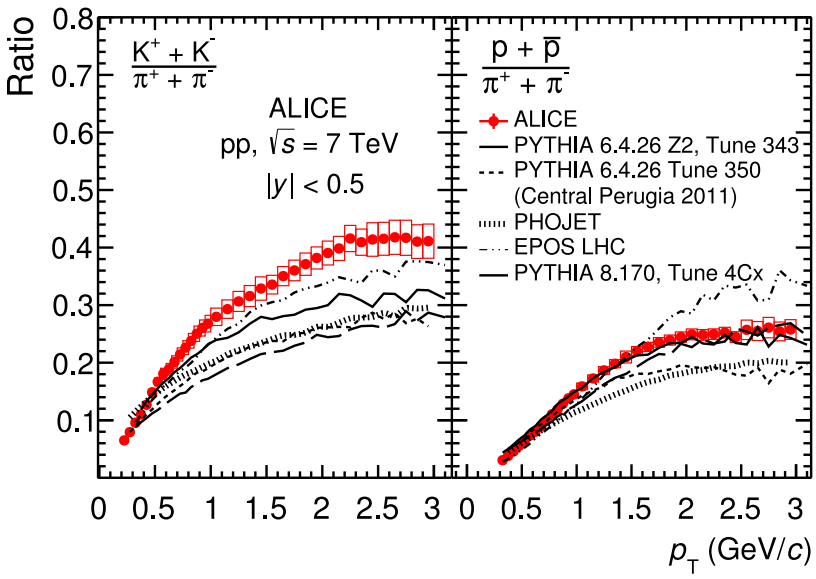

FIGURE V-11: Kaon-to-pion (left panel) and proton-to-pion (right panel) ratio compared to various QCD-inspired models in pp collisions at $\sqrt{s} = 7$ TeV [333].

V.6 Systematic uncertainties

The sources of systematic uncertainties vary from method to method. A typical trend looks as follows. It is as high as 15-20% at low-p_{T}, then rapidly falls down to a value $\sim$ 6-10% at $p_{\mathrm{T}} = 3-4$ GeV/c, and remains approximately flat to $p_{\mathrm{T}} \approx 10$ GeV/c. Then it rises again to a value of $\sim 20\%$ at $p_{\mathrm{T}} \approx 30$ GeV/c.

The largest uncertainty is coming from the material budget. It is constant at the level of 9% for the PCM method, 4.2% for EMC-based methods and 3.5% for PHOS.

The energy calibration for calorimeters is also burdened with non-negligible uncertainty. It varies depending on p_{T}, collision energy and the system as well as the meson type. It is $\sim$ 1-7% for PHOS or $\sim$ 2-5.5% for EMCal for pp or p-Pb collisions, and $\sim$ 4-8%for PHOS or 8.6% for EMCal in Pb-Pb collisions.

The signal yield extraction is also non-negligible. Usually, it is larger at low-p_{T} due to a larger combinatorial background. It is $\sim$ 3-7% at low-p_{T} ($p_{\mathrm{T}} \sim 1$ GeV/c), then falls down to the level of $\sim 2\%$ for PHOS. It remains at $\sim 2\%$ up to $p_{\mathrm{T}} \approx 10$ GeV/c and rises to $\sim 5\%$ at $p_{\mathrm{T}} = 15$ GeV/c due to cluster merging for EMCal. It is more difficult to extract a signal in central Pb-Pb collisions and at low p_{T}, which is reflected in 2 to 3 times larger uncertainty. For η meson, uncertainty on the signal yield extraction is larger $\sim$ 2-3 times due to the smaller available statistics and $\sim$ 2.5 times larger width than for the π^0 meson.

In particular cases, the efficiency extraction was a source of sizeable uncertainty of 4-9% (pp collisions at $\sqrt{s} = 8$ TeV) for almost all methods. It is also problematic in Pb-Pb collisions when an embedded meson sample is used for efficiency extraction.

For PCM method, a sizeable source is electron/positron identification, especially in Pb-Pb col-

lisions which can be as large as $\sim 10.5\%$ at $p_{\mathrm{T}} = 5$ GeV/c.

V.7 Merging results from different methods

Merging the methods allows not only for the extension of the measured p_{T} range, but also for the reduction of systematic uncertainties.

Different methods and different trigger types are analyzed for one collision type and energy. To combine them into one final result that takes into consideration statistical and systematic uncertainties as well as correlations between them, the Best Linear Unbiased Estimate (BLUE) algorithm [334, 335, 336] is used. At first, a spectrum is done for a given method merging all available triggers. Trigger samples have uncorrelated statistical uncertainties, since different triggers use non-overlapping data samples. Then, spectra from different methods can be merged. The PCM, EMC and PHOS methods are independent measurements and they are treated as uncorrelated. For other methods a proper correlation was found. A good agreement between different methods allows for merging the spectra.

When a spectrum is merged, the invariant cross-sections are corrected for the finite p_{T} bin width according to the prescription in [337]. The y values are kept to the bin averages and the p_{T} position is calculated at a point where the differential cross-section coincides with the bin average. Usually, the Tsallis function [338], the power function, the modified Hagedorn function [339] or the two component model (TCM) function [340] have been used for the correction in the ALICE experiment. All the mentioned functions are given below. The Tsallis function is as follows:

$$E\frac{\mathrm{d}^3\sigma}{\mathrm{d}p^3} = A\frac{C(n-1)(n-2)}{nC[nC+m(n-2)]}\left(1+\frac{m_{\mathrm{T}}-m}{nC}\right)^{-n}, \tag{V.13}$$

where A, C, n are free parameters, m is the meson rest mass and m_{T} is the transverse mass. The power law function is given by:

$$E\frac{\mathrm{d}^3\sigma}{\mathrm{d}p^3} = Ap_{\mathrm{T}}^{-n}, \tag{V.14}$$

where A and n are fit parameters. The modified Hagedorn function looks as follows:

$$E\frac{\mathrm{d}^3\sigma}{\mathrm{d}p^3} = A(\exp[-(ap_{\mathrm{T}}+bp_{\mathrm{T}}^2)]+p_{\mathrm{T}}/p_0)^{-n}, \tag{V.15}$$

where A, a, b, p_0 and n are free parameters. The TCM function is as follows:

$$E\frac{\mathrm{d}^3\sigma}{\mathrm{d}p^3} = A_{\mathrm{e}}\exp(-E_{\mathrm{T,kin}}/T_{\mathrm{e}}) + A\left(1+\frac{p_{\mathrm{T}}^2}{T^2n}\right)^{-n}, \tag{V.16}$$

where $E_{\mathrm{T,kin}} = \sqrt{p_{\mathrm{T}}^2+m^2} - m$ is the transverse kinematic energy with the meson rest mass m and a number of free parameters: A_{e}, A, T_{e}, T and n.

The ALICE experiment provided results in a very broad range. The Tsallis distribution can describe spectra at a low-p_{T} range, but deviates considerably at high-p_{T}. The power law works only

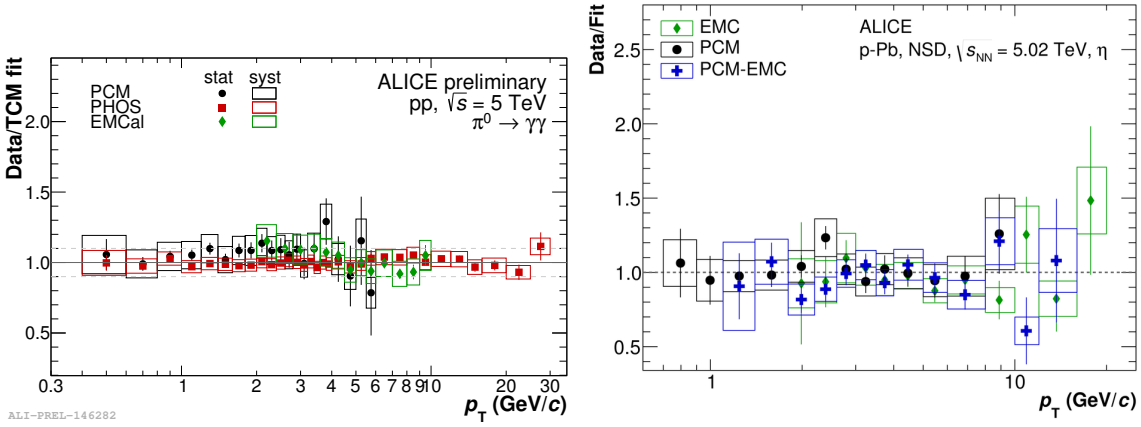

FIGURE V-12: Ratio between individual π^0 invariant cross-section measurements in pp collisions at $\sqrt{s} = 5.02$ TeV and TCM fit to the combined meson cross-section (left) and η invariant differential yield in p-Pb collisions at $\sqrt{s_{\rm NN}} = 5.02$ TeV and Tsallis fit to the combined meson yield (right) [323].

in the high-$p_{\rm T}$ region (above $p_{\rm T} \approx 3.5$ GeV/c) and cannot properly describe the low-$p_{\rm T}$ region. The TCM function describes reasonably well the whole spectrum with 10% agreement.

The agreement between individual methods can be visible on the ratio of data points coming from individual methods to the fit to the common spectrum. It is shown in Fig. **V-12** for π^0 spectrum in pp collisions at $\sqrt{s} = 5.02$ TeV (left panel) and for η spectrum in p-Pb collisions at $\sqrt{s_{\rm NN}} = 5.02$ TeV (right panel) [323]. The agreement between methods is within 15%.

V.8 Production spectra of π^0 and η meson

ALICE has measured π^0 production spectra for five center-of-mass energies $\sqrt{s} = 0.9$ [318], 2.76 [319, 320], 5.02 [19, 321], 7 [318] and 8 TeV [322] in pp collisions. All the spectra were measured by PHOS and PCM. EMCal was used for the measurement at energies $\sqrt{s} = 2.76$, 5 and 8 TeV. The hybrid method EMCal-PCM was additionally used at $\sqrt{s} = 2.76$ and 8 TeV. The use of different techniques allows for performing measurements in a very wide $p_{\rm T}$ range from 0.3 GeV/c to 40 GeV/c. The $p_{\rm T}$ distributions of π^0 meson and comparisons to the PYTHIA 8 [341] event generator or NLO pQCD calculations are presented in Fig. **V-13**. PYTHIA 8 describes reasonably well the results at all energies in the whole $p_{\rm T}$ range. However, it over predicts data in the intermediate $p_{\rm T}$ region for higher energies. Uncertainty bands of NLO pQCD calculations represent simultaneous variation of renormalization and factorization scales by a factor of 2. The MSTW PDF [56] (CT10 PDF [342] has been used for data at $\sqrt{s} = 5.02$ TeV) and DSS14 FF [84] used in predictions better describe the measured spectra compared to the previously used calculations [318]. However, the larger the center-of-mass energy and $p_{\rm T}$, the larger discrepancy between NLO pQCD and data is observed. It seems that higher order corrections are less important than parton distributions, particularly gluon distributions in this energy range. It needs to be stressed that $\sqrt{s} = 7$ TeV results on the π^0 meson production were taken into account as an input when DSS14 FF was calculated.

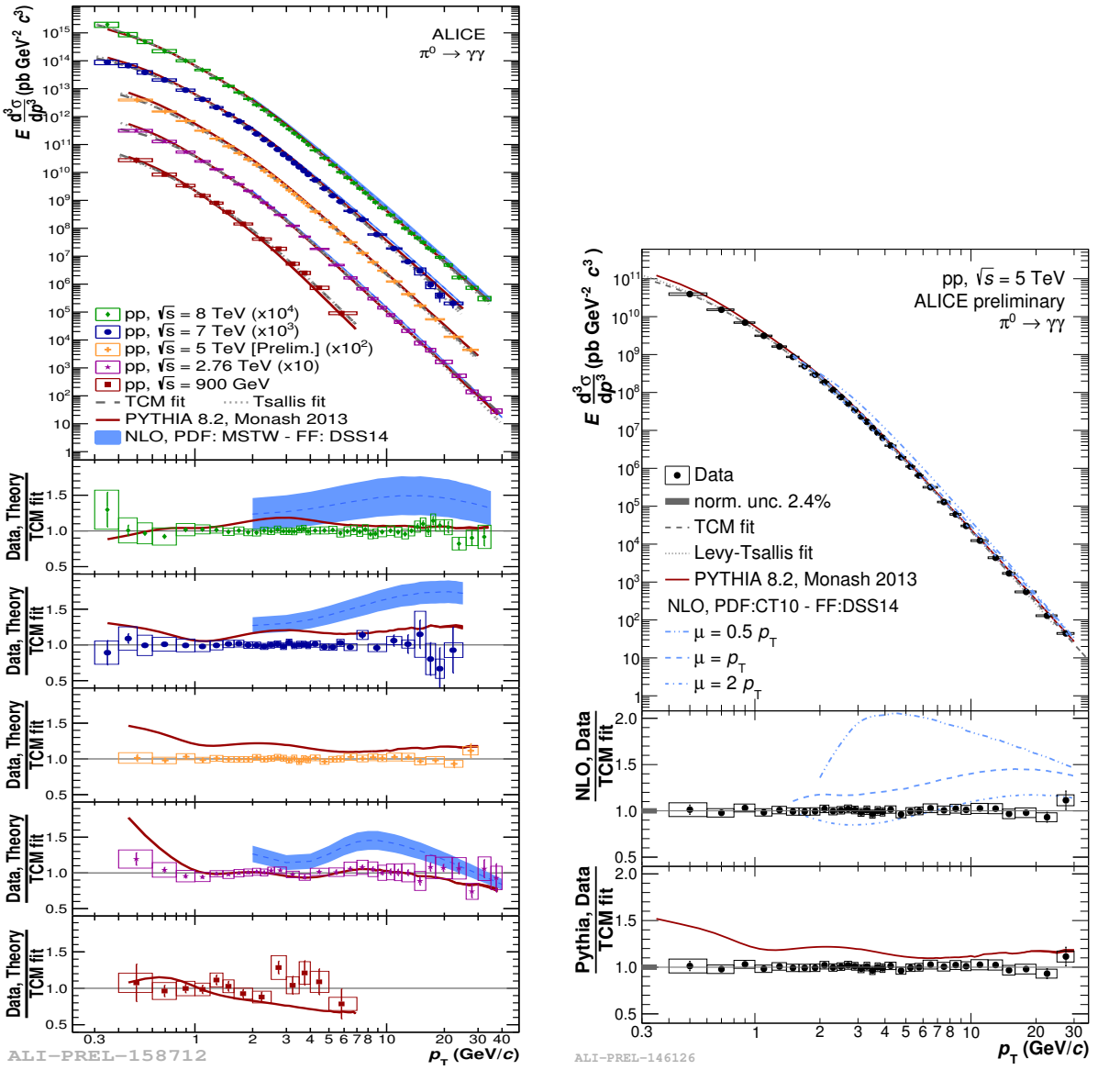

FIGURE V-13: Left: The π^0 production cross-section in pp collisions for the center-of-mass energy $\sqrt{s} = 0.9$ [318], 2.76 [319, 320], 5.02 [19, 321], 7 [318], 8 TeV [322] compared to the PYTHIA 8 [341] event generator and NLO pQCD calculations with MSTW PDF [56] and DSS14 FF [84] for different factorization and renormalization scale μ spanning $\mu = 0.5 p_T$ to $2 p_T$ as a band and parameterized by Tsallis [338] and TCM [340] function are shown in the top panel. The ratios of data and calculations to the TCM fit are shown in bottom panels for each energy separately. Right: The π^0 production cross-section in pp collisions at $\sqrt{s} = 5.02$ TeV [321] compared to the PYTHIA 8 event generator and NLO pQCD calculations with CT10 PDF [342] and DSS14 FF for different factorization and renormalization scale μ and parameterized by Tsallis or TCM function is shown in the top panel. The ratios of data and calculations to the TCM fit are shown in bottom panels.

Measurements of the η meson spectrum have been done at the four center-of-mass energies in pp collisions in ALICE, $\sqrt{s} = 0.9$ [343], 2.76 [320], 7 [318] and 8 TeV [322]. The PCM method was used to analyze every spectrum. The EMCal itself and the combination of EMCal and PCM was used to get results at $\sqrt{s} = 2.76$ and 8 TeV. In addition, PHOS was incorporated to analyze the results for $\sqrt{s} = 7$ TeV. The spectra span the range $0.4 < p_T < 35$ GeV/c. The p_T distributions of η meson and comparisons to PYTHIA 8 and NLO pQCD calculations are presented in Fig. **V-14**. PYTHIA 8 describes η meson spectra, although, for the two highest energies it over predicts the low-p_T region. It is also clearly visible that NLO pQCD calculations with CTEQ6M5 (PDF) [344] with AESSS (FF) [85] over predict data by 50-100%. Predictions with a higher scale ($\mu = 2p_T$) describe the data better than with a lower scale. This result indicates that the η meson fragmentation function should be updated as it was done for pions [84].

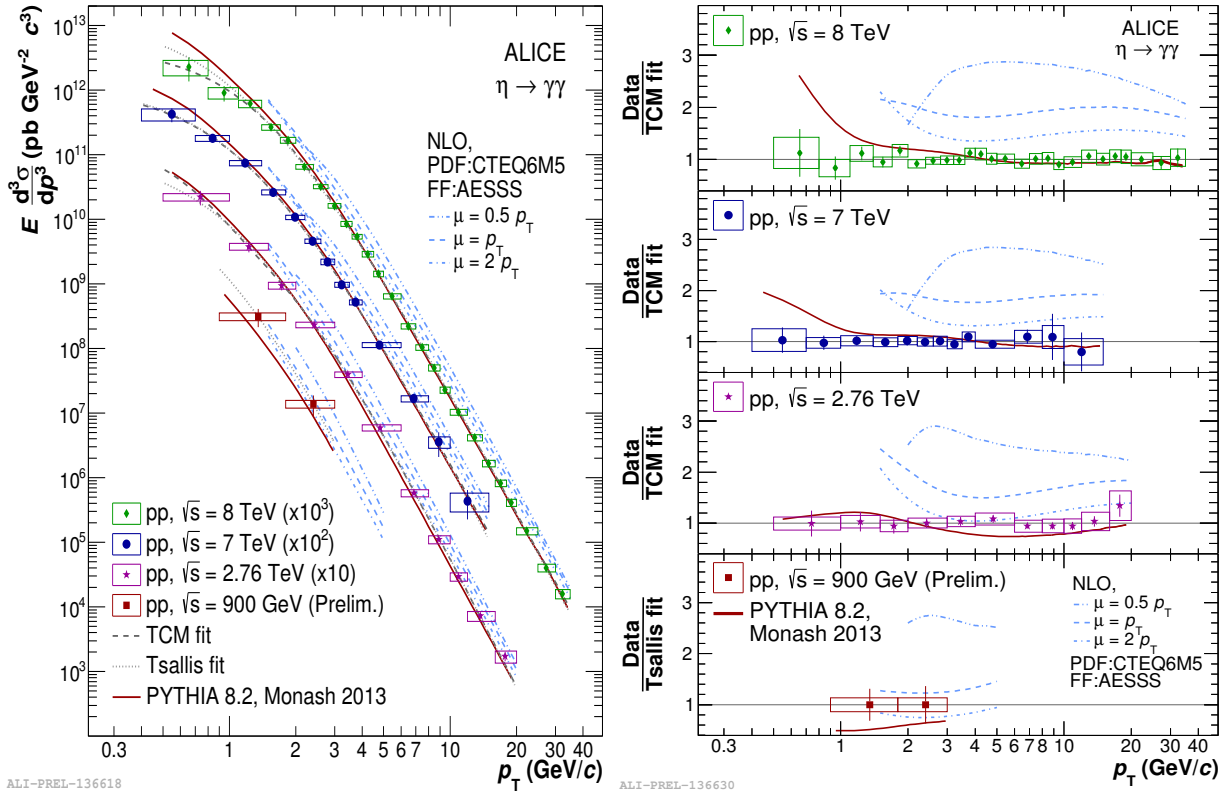

FIGURE V-14: Left: The η production cross-section in pp collisions for the center-of-mass energy $\sqrt{s} = 0.9$ [343], 2.76 [320], 7 [318], 8 TeV [322] compared to PYTHIA 8 [341] and NLO pQCD calculations using CTEQ6M5 (PDF) [344] and with AESSS (FF) [85]. The NLO pQCD calculations are shown for the factorization and renormalization scale $\mu = 0.5p_T$, p_T and $2p_T$. Right: The ratios of data and calculations to TCM fit [340] are shown for each energy separately.

ALICE has also measured π^0 and η meson spectra in non-single diffractive (NSD) p-Pb collisions at the center-of-mass energy $\sqrt{s_{NN}} = 5.02$ TeV [323]. The results compared to a variety of models and scaled NLO pQCD calculations are shown in Fig. **V-15**. The spectra are measured in the range $0.3 < p_T < 20$ GeV/c and $0.7 < p_T < 20$ GeV/c for π^0 and η mesons, respectively. Five

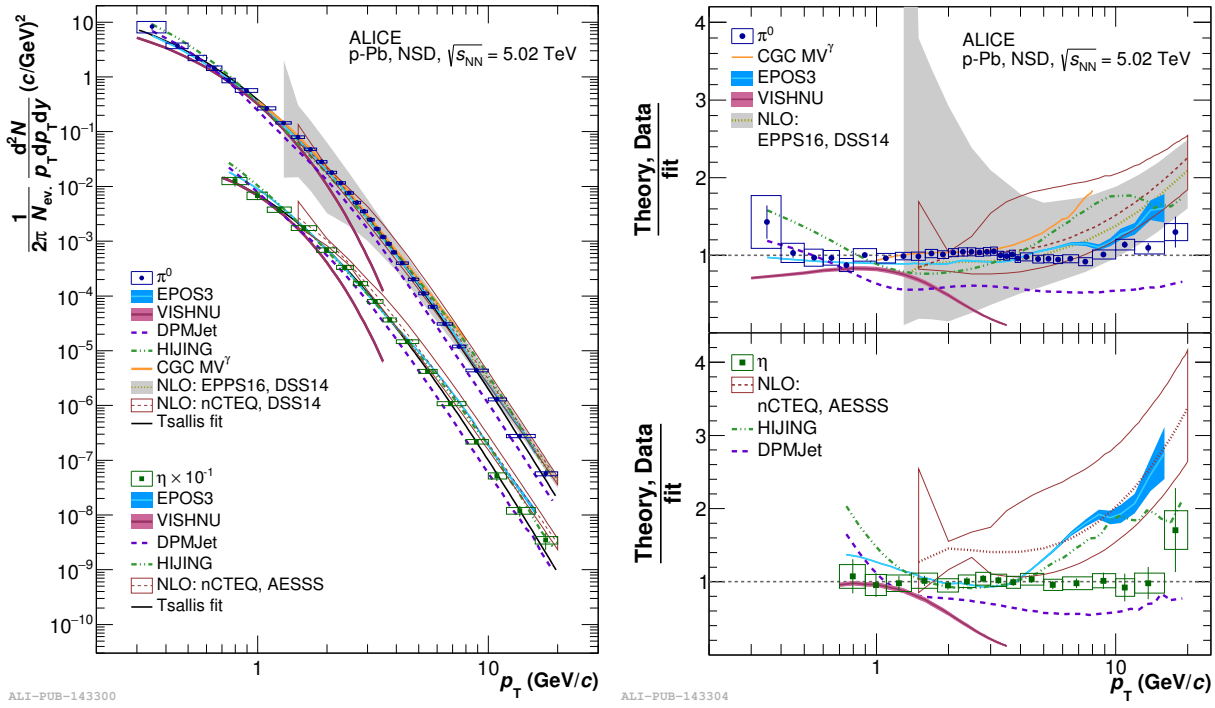

FIGURE V-15: Left: The π^0 and η meson production cross-section in p-Pb collisions for the center-of-mass energy $\sqrt{s_{NN}} = 5.02$ TeV [323] compared to various models (EPOS3 [348], VISHNU [349], HIJING [100], DPMJET [350], CGC [317]) and scaled NLO pQCD calculations [345, 67, 57, 65, 84, 85]. Right: The ratio of model prediction and scaled NLO pQCD calculations to Tsalis fit for π^0 (top panel) and η (bottom panel) meson spectra for p-Pb collisions at $\sqrt{s_{NN}} = 5.02$ TeV [323].

different methods (PHOS, EMCal, PCM, PCM-EMCal and Dalitz) were involved in the π^0 meson measurements, while for the η meson only three (EMCal, PCM, PCM-EMCal) were accessible.

The ratio of the model predictions and data to the Tsallis fit to the measured data is presented in Fig. **V-15**. It is clearly visible that scaled NLO pQCD predictions [345, 346, 347] using the EPPS16 nuclear PDF (nPDF) [67] with the CT14 PDF [57] or the nCTEQ nPDF [65] and the DSS14 FF [84] describe the π^0 spectrum well in the whole range while failing in the high-p_T region for η meson where the scaled NLO pQCD [345] with the nCTEQ nPDF [65] and the AESSS FF [85] is used. The same behavior can be observed for the EPOS3 model [348]. The VISHNU model [349] reproduces data at low-p_T. Both EPOS and VISHNU use the hydrodynamic description of hot matter evolution, which shows how important it is to include the hydrodynamic flow to achieve a good description of physics at low p_T. The high-p_T deviation of the VISHNU model is probably related to missing hard processes contributing in this model. Both HIJING [100] and DPMJET [350] models describe p-Pb data within 20-80% depending on the p_T. The CGC [317] model agrees with the π^0 meson spectrum below $p_T = 4$ GeV/c and tends to increasingly deviate above this value.

Based on Pb-Pb data collected in 2010, the π^0 production spectra have been measured in 6

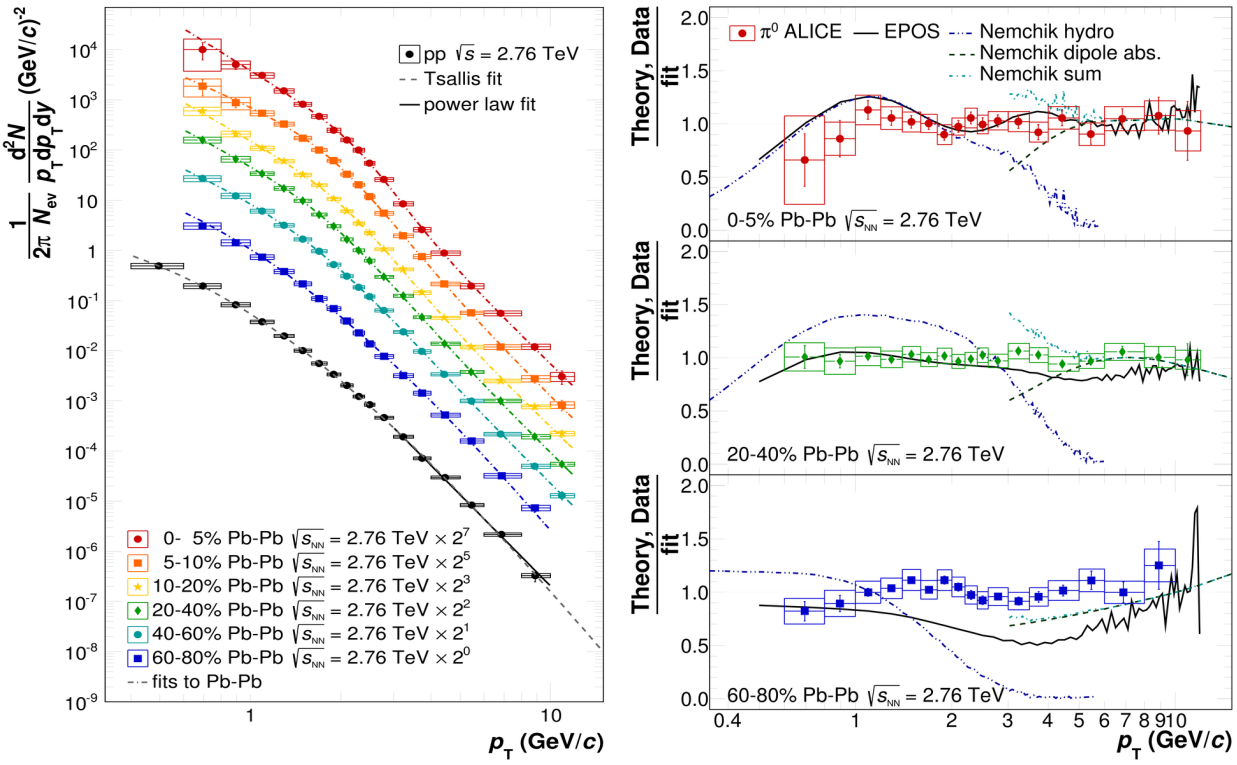

FIGURE V-16: Left: Invariant differential yields of π^0 mesons produced in six centrality classes in Pb-Pb and inelastic pp collisions at $\sqrt{s_{\rm NN}} = 2.76$ TeV [319]. Vertical lines show the statistical uncertainty, horizontal lines indicate the bin width, systematic uncertainties are shown as boxes. Dashed lines represent Tsallis fits, solid line represents the power law fit only in pp collisions. Right: The ratios of measured π^0 spectra for three centrality classes and theory predictions to the fit function. The solid line denotes the EPOS [351] event generator. Dashed, dot-dashed and double dot-dashed lines represent Nemchik calculations [352, 353] and its component parts.

centrality classes $(0-5-10-20-40-60-80\%)$ [319]. The results are shown in Fig. **V-16** on the left-hand side. The ratios of measured π^0 spectra for three centrality classes and theory predictions to the fit function are shown in Fig. **V-16** on the right-hand side. Data are compared to the EPOS [351] event generator and Nemchik calculations [352, 353]. The EPOS model describes rather well the central Pb-Pb collisions, but tends to underestimate $1 < p_{\rm T} < 5$ GeV/c region towards more peripheral collisions, probably due to the underestimation of hydrodynamic flow in peripheral collisions. The Nemchik model reproduces the most central Pb-Pb collisions quite well, except for the transition region between hydrodynamic and hard contribution. Semi-central (20-40%) collisions are over predicted in the low-$p_{\rm T}$ region, while the high-$p_{\rm T}$ region is relatively well described.

Thanks to an increase of the integrated luminosity, collected in 2011 Pb-Pb period, up to $L \approx 0.1$ nb^{-1}, ALICE could measure π^0 meson spectra in the extended range [324] up to $p_{\rm T} =$ 20 GeV/c (in comparison with [319]) and, for the first time, $p_{\rm T}$ spectra of the η meson [324] in Pb-Pb collisions at $\sqrt{s_{\rm NN}} = 2.76$ TeV. The neutral meson results coming from PCM and EM-

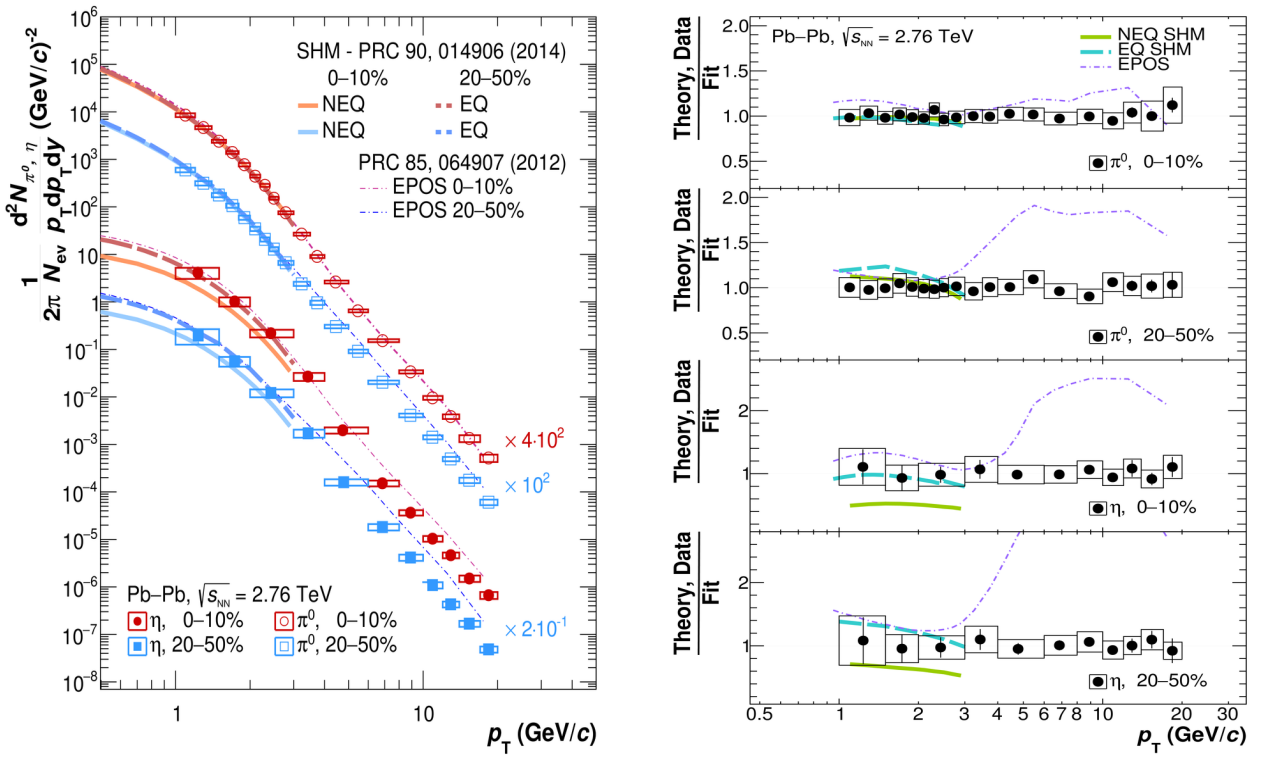

FIGURE V-17: Left: The π^0 (open symbols) and η (close symbols) meson production cross-section in 0-10% central (red) and 20-50% semi-peripheral (blue) Pb-Pb collisions for the center-of-mass energy $\sqrt{s_{\rm NN}} = 2.76$ TeV [324] compared to predictions of EPOS [351] (dash-dotted line) and two scenarios (EQ (dashed line) and NEQ (solid line)) in the SHM [354, 355, 356] model. Right: Ratio of data or theory calculations to the TCM fit to data for different centralities and neutral mesons on separate panels. The solid line denotes NEQ SHM, dashed line EQ SHM, and dash-dotted line EPOS predictions.

Cal for central (0-10%) and semi-central (20-50%) Pb-Pb collisions at $\sqrt{s_{\rm NN}} = 2.76$ TeV shown in Fig. **V-17** are compared to predictions of EPOS [351] and the statistical hadronization model (SHM) [354, 355, 356]. The equilibrium (EQ) and non-equilibrium (NEQ) versions of SHM model describe the shape of π^0 spectra. Only EQ SHM describes η measurements, while NEQ SHM underestimates them. It indicates the possibility of a different flow profile for the mesons in question. The EPOS model describes the spectrum in central collisions and only the low-$p_{\rm T}$ part in peripheral ones as in the previous measurement [319]. The η meson spectrum is described by EPOS only in the low-$p_{\rm T}$ range and deviates above $p_{\rm T} \approx 4$ GeV/c for both centrality classes.

ALICE has recently measured π^0 spectra in Pb-Pb collisions at $\sqrt{s_{\rm NN}} = 5.02$ TeV in three centrality classes in the range $0.4 < p_{\rm T} < 30$ GeV/c [321]. Spectra shown in Fig. **V-18** are compared to SHM model which describes them in the same way as for the lower energy. No EPOS predictions for this energy are yet available.

The π^0 and η meson production spectra measured at various energies and collision systems are summarized in Table **V-3**.

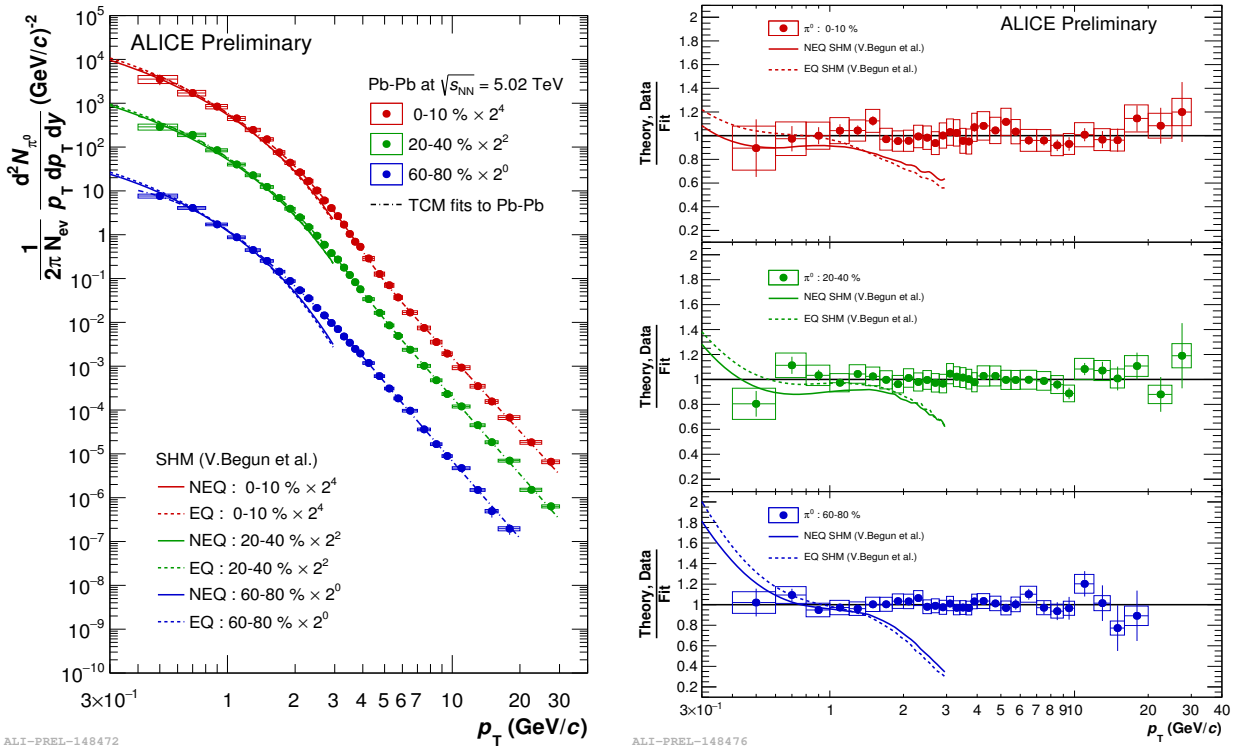

FIGURE V-18: Left: The π^0 production cross-section in three centrality classes ($0-10\%$ in red, $20-40\%$ in green and $60-80\%$ in blue) of Pb-Pb collisions for the center-of-mass energy $\sqrt{s_{\rm NN}} =$ 5.02 TeV [321] compared to SHM [354, 355, 356] model. Right: Ratio of data or theory prediction to the TCM fit to data. Solid line denotes NEQ SHM while dashed line EQ SHM model.

V.9 The η/π^0 ratio

ALICE has measured the η/π^0 ratio in pp collisions for $\sqrt{s} = 0.9$ [343], 2.76 [320], 7 [318], 8 TeV [322], in p-Pb collisions at $\sqrt{s_{\rm NN}} = 5.02$ TeV [323] and in Pb-Pb collisions at $\sqrt{s_{\rm NN}} =$ 2.76 TeV [324]. The ratios are shown in Figs. **V-19**, **V-20**, **V-21** in pp, p-Pb and Pb-Pb collisions, respectively. The construction of the ratio allows for a more precise measurement because of cancellation of large systematic uncertainties caused by the material budget in the PCM method or the absolute energy scale in calorimeters. The ratio is universal among collision energies and systems except for, probably the most central Pb-Pb collisions. It grows at low-$p_{\rm T}$ and then goes to the asymptotic value of ~ 0.45 at $p_{\rm T} > 4$ GeV/c. Systematic uncertainties cancel not only for the experimental data but also for the NLO pQCD calculation, where the influence of the PDF is reduced in the η/π^0 ratio. The η/π^0 ratio is well reproduced by NLO pQCD predictions, although they have difficulties in describing the single meson spectra. PYTHIA 8 describes well (within 20-30%) the η/π^0 ratio in pp collisions, although there are some tensions below $p_{\rm T} = 1.5$ GeV/c for collisions at $\sqrt{s} = 8$ TeV, where the shape and ratio cannot be fully reproduced. HIJING and DPMJET overestimate the low $p_{\rm T}$ part of the ratio in p-Pb collisions and agree for $p_{\rm T} > 4$ GeV/c. EPOS3 and VISHNU models follow data points at low-$p_{\rm T}$. However, EPOS3 tends to rise above

System	$\sqrt{s_{\rm NN}}$ (TeV)	Centrality	Meson	$p_{\rm T}$ range	η/π^0 ratio	Ref.
pp	0.9		π^0	$0.4-7$		[318]
pp	2.76		π^0	$0.4-40$		[319, 320]
pp	5.02		π^0	$0.4-30$		[19, 321]
pp	7		π^0	$0.3-25$		[318]
pp	8.16		π^0	$0.3-35$		[322]
pp	0.9		η	$0.9-3$	~ 0.5	[343]
pp	2.76		η	$0.5-20$	$0.474 \pm 0.015 \pm 0.024$ [322]	[320]
pp	7		η	$0.4-15$	$0.476 \pm 0.020 \pm 0.020$ [322]	[318]
pp	8.16		η	$0.5-35$	$0.455 \pm 0.006 \pm 0.014$	[322]
p-Pb	5.02		π^0	$0.3-20$		[323]
p-Pb	5.02		η	$0.7-20$	$0.483 \pm 0.015 \pm 0.015$	[323]
Pb-Pb	2.76	$0-5\%$	π^0	$0.6-12$		[319]
Pb-Pb	2.76	$5-10\%$	π^0	$0.6-12$		[319]
Pb-Pb	2.76	$10-20\%$	π^0	$0.6-12$		[319]
Pb-Pb	2.76	$20-40\%$	π^0	$0.6-12$		[319]
Pb-Pb	2.76	$40-60\%$	π^0	$0.6-12$		[319]
Pb-Pb	2.76	$60-80\%$	π^0	$0.6-10$		[319]
Pb-Pb	2.76	$0-10\%$	π^0	$1-20$		[324]
Pb-Pb	2.76	$20-50\%$	π^0	$1-20$		[324]
Pb-Pb	2.76	$0-10\%$	η	$1-20$	$0.457 \pm 0.013 \pm 0.018$	[324]
Pb-Pb	2.76	$20-50\%$	η	$1-20$	$0.457 \pm 0.013 \pm 0.018$	[324]
Pb-Pb	5.02	$0-10\%$	π^0	$0.4-30$		[321]
Pb-Pb	5.02	$20-40\%$	π^0	$0.4-30$		[321]
Pb-Pb	5.02	$60-80\%$	π^0	$0.4-30$		[321]

TABLE V-3: π^0 and η production cross-section in pp, p-Pb and Pb-Pb collisions at various center-of-mass energies measured with the ALICE experiment. For each collision system, the center-of-mass energy $\sqrt{s}$ and the $p_{\rm T}$ range is quoted. For the η meson measurement, also the constant value of η/π^0 ratio is given at high $p_{\rm T}$, where the first uncertainty is statistical and the second systematical. For Pb-Pb collisions, the centrality class is also given.

$p_{\rm T} = 4$ GeV/c and does not agree with data. The ratio in Pb-Pb collisions is described by EPOS up to $p_{\rm T} = 4$ GeV/c. Then it rises and does not follow the data similarly to the p-Pb case. The EQ SHM model also works in the low-$p_{\rm T}$ regime, while NEQ SHM under predicts data. The high-$p_{\rm T}$ part of the ratio is well-described within uncertainties by the NLO pQCD-inspired DCZW model [358] which includes a modification of fragmentation functions due to the parton energy loss. Models show the importance of hydrodynamical flow at low $p_{\rm T}$ in the collision. The discrepancy in the EPOS description of the ratio at high $p_{\rm T}$ reflects the disagreement in the single η spectra description.

The η/π^0 ratio is also compared to the $m_{\rm T}$ scaling prediction. The curve shown for pp collisions in bottom Fig. **V-19** and for p-Pb collisions in Fig. **V-20** follows data points at high-$p_{\rm T}$ (results for different energies agree between each other; they also agree with lower collision energy results, like

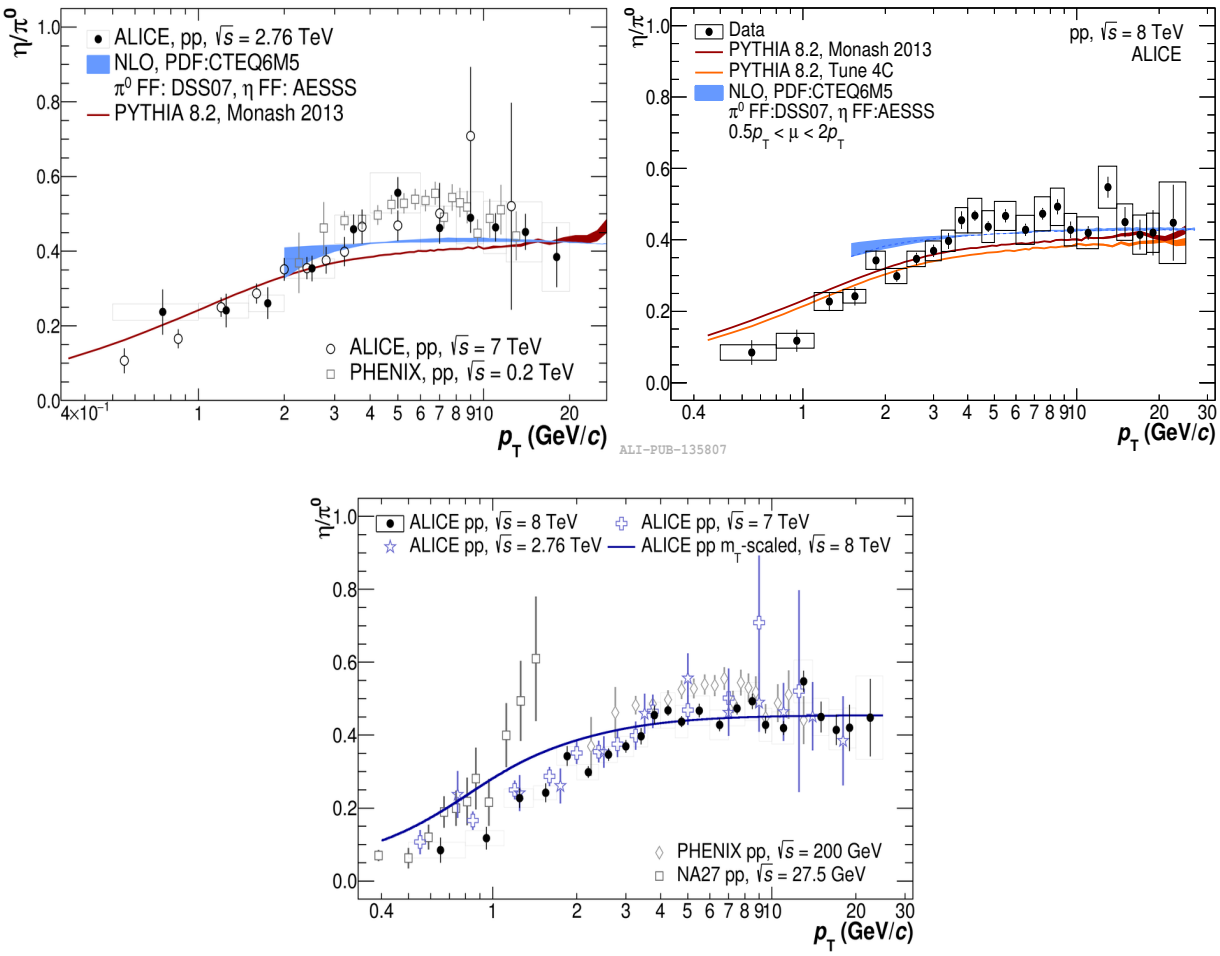

FIGURE V-19: Top left: The η/π^0 ratio in pp collisions at $\sqrt{s} = 2.76$ TeV [320] (full dots), $\sqrt{s} = 7$ TeV [318] (open dots) and $\sqrt{s} = 0.2$ TeV [187] (open squares) compared to NLO pQCD calculations [344, 84, 85] (blue band) and PYTHIA 8 [341] (red band). Top right: The η/π^0 ratio in pp collisions at $\sqrt{s_{\rm NN}} = 8$ TeV [322] compared to PYTHIA 8 Monash tune [341] (brown band) and 4C tune [357] (red band) as well as to NLO pQCD calculations (blue band) with CTEQ6M5 [344] as PDF and DSS07 [84] or AESSS [85] as FF for π^0 or η meson, respectively. Bottom: Comparison of the η/π^0 ratio in pp collisions at $\sqrt{s} = 2.76$ (stars), 7 (crosses) and 8 TeV (full dots) measured with ALICE as well as other experiments at lower energies at $\sqrt{s} = 27.5$ (NA27 [181], squares) and 200 GeV (PHENIX [187], diamonds). The blue line denotes the $m_{\rm T}$ scaling prediction.

for example from PHENIX [187]) and deviates from data in low-$p_{\rm T}$. The same pattern is present for every system and energy. The deviation of data from the $m_{\rm T}$ scaling is significant. It is 6.2 σ below $p_{\rm T} = 3.5$ GeV/c in pp collisions at $\sqrt{s} = 8$ TeV. A smaller, but still significant deviation from the $m_{\rm T}$ scaling, 5.7σ, can be observed at $\sqrt{s} = 7$ TeV. For pp collisions at $\sqrt{s} = 2.76$ TeV the deviation is on the level of 2.1σ. The deviation from $m_{\rm T}$ scaling has been observed in pp collisions at $\sqrt{s} = 27.5$ GeV in the low-$p_{\rm T}$ range by NA27 [181] measurement, where points below $p_{\rm T} = 1$ GeV/c were below the prediction curve and above this value - above the curve, burdened

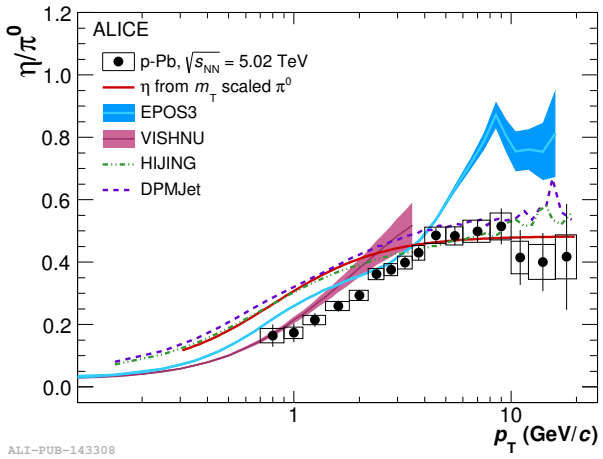

FIGURE V-20: The η/π^0 ratio in p-Pb collisions at $\sqrt{s_{NN}} = 5.02$ TeV [323] compared to EPOS3 [348] (blue band), VISHNU [349] (violet band), HIJING [100] (green dot-dashed line) and DPMJET [350] (dark blue dashed line) models as well as m_T scaling predictions (red solid line).

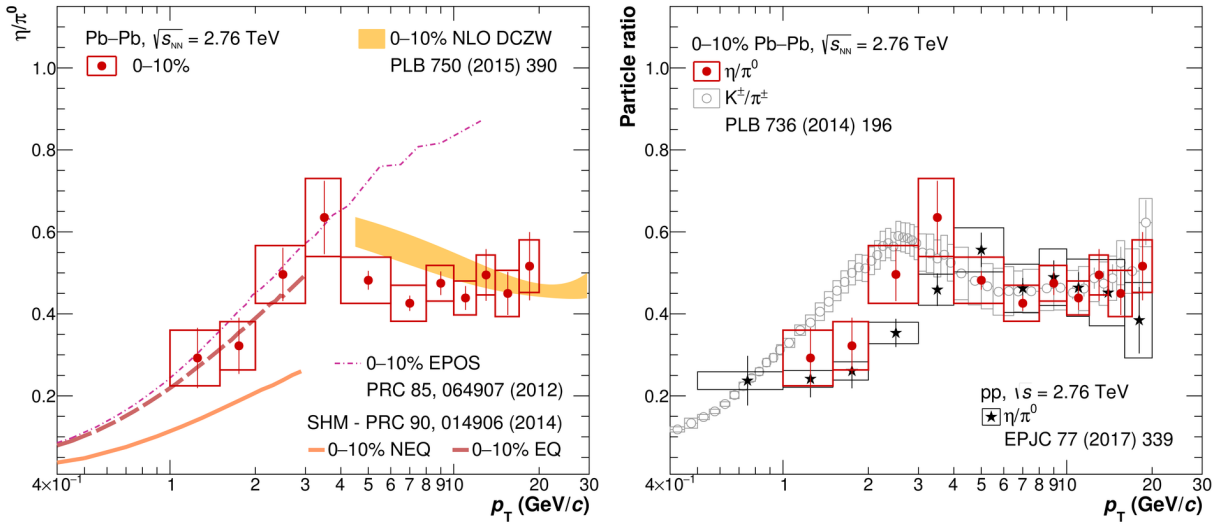

FIGURE V-21: Left: The η/π^0 ratio for the 0-10% most central Pb-Pb collisions at $\sqrt{s_{NN}} = 2.76$ TeV [324] compared to EPOS [351] (dot-dashed line), SHM [354, 355, 356] (EQ - dashed line, NEQ - solid line) models and NLO pQCD calculations [358] (orange band). Right: The same ratio (full circles) compared to a corresponding result in pp collisions (stars) and to the $K^{\pm}/\pi^{\pm}$ measurement in the same centrality class, system and energy [359] (open circles).

with large uncertainties and not so conclusive. In p-A collisions, the deviation from the m_T scaling was observed in $\sqrt{s_{NN}} = 29.1$ GeV (TAPS/CERES [205]). The presence of radial flow effects and contributions to the π^0 or η spectra coming from other resonances decays are possible candidates for the m_T scaling violation.

A comparison of results in the most central Pb-Pb collisions to pp collisions (see Fig. **V-21** on the right-hand side) indicates the possibility of deviation from pp-like behavior, which is visible between $2 < p_T < 4$ GeV/c. The η/π^0 ratio is compared with the $K^{\pm}/\pi^{\pm}$ ratio, both in the same centrality class (0-10%), collision system (Pb-Pb) and collision energy ($\sqrt{s_{NN}} = 2.76$ TeV). The relative mass difference between charged kaon and pions or η and neutral pion is approximately the same. Also, both kaon and η meson have strangeness content. The comparison is shown in Fig. **V-21** on the right-hand side. There is a relatively good agreement between these two ratios. However, due to large uncertainties in the η/π^0 ratio, the unambigous conclusion is not possible. More precise data are needed.

V.10 Nuclear modification factor R_{AA}

The nuclear modification factor was calculated according to Eq. **II.5**. Since R_{AA} is the result of combination of spectra in Pb-Pb collisions and in pp collisions, the corresponding spectra were taken for Pb-Pb and pp collisions at $\sqrt{s_{NN}} = 2.76$ TeV [319] and later extended to a larger p_T range [324, 320], and at $\sqrt{s_{NN}} = 5.02$ TeV [321]. The measured R_{AA} for π^0 and η mesons at $\sqrt{s_{NN}} = 2.76$ TeV are presented in Fig. **V-22**, while results for π^0 meson R_{AA} at $\sqrt{s_{NN}} = 5.02$ TeV are shown in Fig **V-23**. A clear p_T dependence is observed. For the most central collisions, the

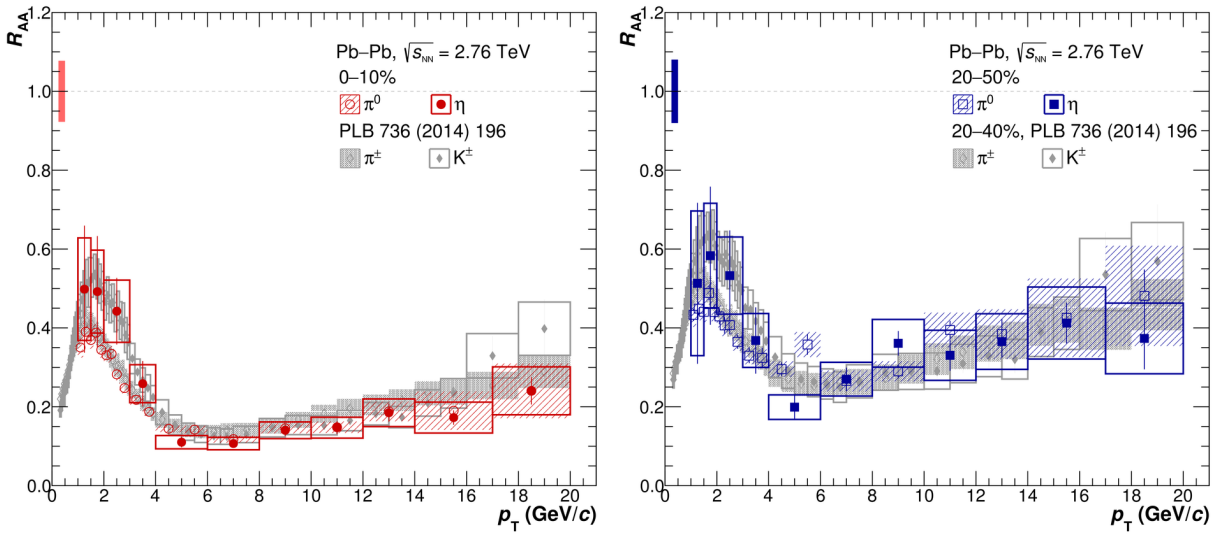

FIGURE V-22: The measured R_{AA} [324] for π^0 (open circles and squares) and η (full circles and squares) mesons in the 0-10% (left) and 20-50% (right) centrality classes at $\sqrt{s_{NN}} = 2.76$ TeV compared to $\pi^{\pm}$ (open diamonds) and $K^{\pm}$ [360] (full diamonds) in the same centrality classes, energy and system. The boxes around a unity represent the total uncertainty on the T_{AA} and pp spectrum normalization.

R_{AA} increases to the maximum value of around $p_T = 1.5$-2 GeV/c, then falls down reaching a minimum for $p_T \approx 7$ GeV/c, after which it slowly increases. The p_T-dependent relative gluon and quark contribution to the meson production could be responsible for the high-p_T increase, because

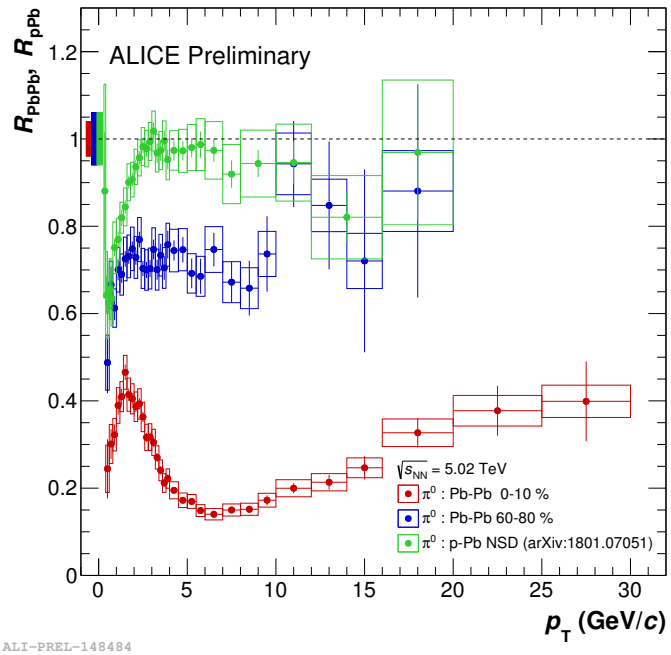

FIGURE V-23: The measured R_{AA} [321] for π^0 mesons in the 0-10% (red) and 60-80% (blue) centrality classes at $\sqrt{s_{NN}} = 5.02$ TeV compared to NSD p-Pb collisions at $\sqrt{s_{NN}} = 5.02$ TeV [323]. The boxes around a unity represent the total uncertainty on T_{AA} and pp spectrum normalization.

they suffer different energy loss. Gluons suffer more than quarks (by factor $\sim 9/4$) due to a larger Casimir factor [361]. A centrality dependence is also visible. A similar behavior is observed for central and semi-central collisions (although with a smaller suppression over the full p_T range), but different from peripheral ones. Moreover, despite the mass difference, the same suppression pattern and magnitude is expressed by π^0 and η mesons at higher $p_T > 4$ GeV/c. The present accuracy does not allow for distinguishing between differences in the suppression of two mesons in lower p_T. The nuclear modification factors of neutral mesons are compared to charged kaons and pions R_{AA} [360] measured at the same collision energy and in the same system, as shown in Fig. **V-22**. The η meson R_{AA} shows the same trend as the charged kaon R_{AA}. All the mentioned particles have a similar suppression pattern above $p_T > 4$ GeV/c. This result is consistent with baryon and strange meson R_{AA} and supports the idea that the energy loss in the medium is purely a partonic effect.

A comparison of the neutral pion R_{AA} evolution with a collision energy is very instructive. The R_{AA} in the most central collisions spanning the center-of-mass energy $\sqrt{s_{NN}} = 17.3$ GeV (WA98 [209]) through $\sqrt{s_{NN}} = 39$, 62.4 and 200 GeV (PHENIX [231, 236]) to $\sqrt{s_{NN}} = 2.76$ TeV (ALICE [324]) is shown in Fig. **V-24** (left). The R_{AA} of η meson measured with ALICE is compared to the PHENIX result at $\sqrt{s_{NN}} = 200$ GeV [228]. The systematic decrease of R_{AA} with increasing energy is clearly visible above $p_T \simeq 2$ GeV/c (although results above $p_T \approx 12$ GeV/c are inconclusive due to large uncertainties). R_{AA} for ALICE data is lower than for PHENIX, although spectra are flatter for ALICE. This fact indicates that the decrease of R_{AA} due to higher energy densities created at larger collision energies dominates over the increase of R_{AA} due to

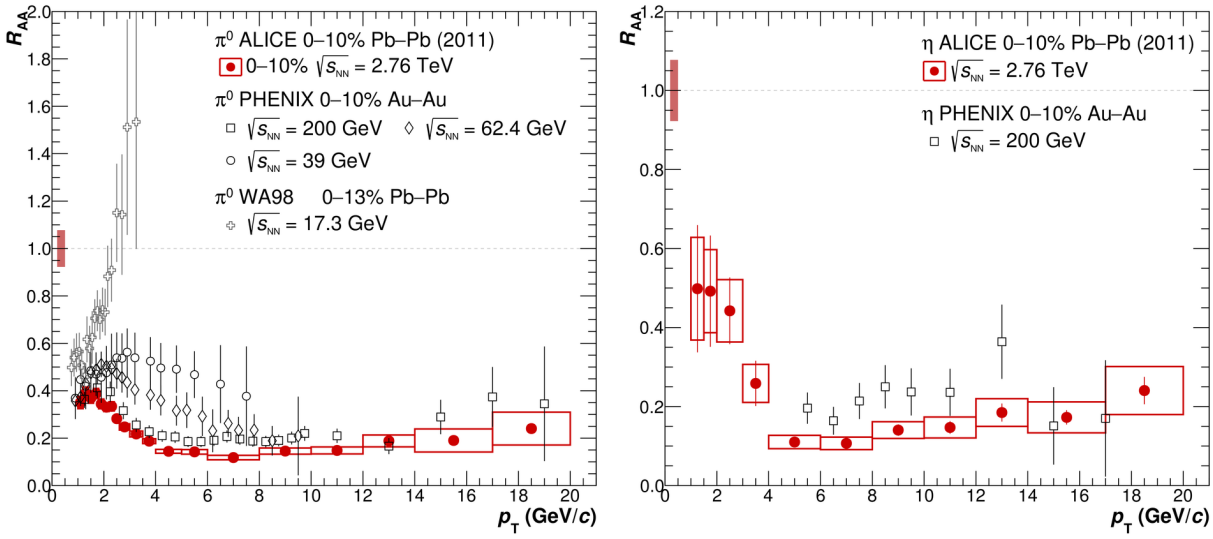

FIGURE V-24: The comparison of R_{AA} of π^0 (left) and η (right) mesons in the most central collisions measured in ALICE [324] with results from lower center-of-mass energy experiments (WA98 [209] and PHENIX [231, 236, 228]).

the hardening of initial parton spectra. An agreement of the neutral pion R_{AA} for two energies $\sqrt{s_{\mathrm{NN}}} = 2.76$ and 5.02 TeV can also be observed.

The R_{AA} measured in $\sqrt{s_{\mathrm{NN}}} = 2.76$ and 5.02 TeV with ALICE is compared to theoretical predictions in Figs. **V-25** and **V-26**, respectively. Each model, DCZW [358], WHDG [362] and Djordjevic [363], describes R_{AA} of π^0 meson in the most central event class in Pb-Pb collisions at $\sqrt{s_{\mathrm{NN}}} = 2.76$ TeV above $p_{\mathrm{T}} = 6$ GeV/c. The Djordjevic model describes well within uncertainties the other centrality class. The WHDG model has a tendency to a slightly larger suppression for both centralities and both mesons. The DCZW model overestimates the R_{AA} for η meson in the range $4 < p_{\mathrm{T}} < 8$ GeV/c, which can suggest incorrect relative quark and gluon contributions to the η meson production. The Djordjevic models [364, 365] and the Vitev model [366, 367] describe p_{T} and centrality dependence of R_{AA} at $\sqrt{s_{\mathrm{NN}}} = 5.02$ TeV reasonably well.

The nuclear modification factor, R_{pPb}, has been measured for p-Pb collisions at the center-of-mass energy $\sqrt{s_{\mathrm{NN}}} = 5.02$ TeV [323]. However, due to the lack of pp spectra at that time, the interpolation from spectra at $\sqrt{s} = 2.76$, 7 and 8 TeV was applied assuming a power law behavior for the evolution of the cross-section in each p_{T} interval as a function of $\sqrt{s}$ given by $\mathrm{d}^2\sigma(\sqrt{s})/\mathrm{d}y\mathrm{d}p_{\mathrm{T}} \sim \sqrt{s}^{\alpha(p_{\mathrm{T}})}$, where $\alpha(p_{\mathrm{T}})$ is the fit parameter. The R_{pPb} for both π^0 and η meson is shown in Fig. **V-27**. Both R_{pPb} values for π^0 and η are consistent with a unity within uncertainties above $p_{\mathrm{T}} = 2$ GeV/c. There is also a good agreement between charged [368] and neutral pions R_{pPb} over the full p_{T} range. Data are compared to the theory predictions. Central values of the NLO predictions using either EPPS16 or nCTEQ nPDF lie below the data points for $p_{\mathrm{T}} < 6$ GeV/c for both mesons. Uncertainties for calculations using nCTEQ are small and differ sizeably with data, while large EPPS16 uncertainties make the agreement with data. The CGC predictions reproduce the π^0 R_{pPb}.

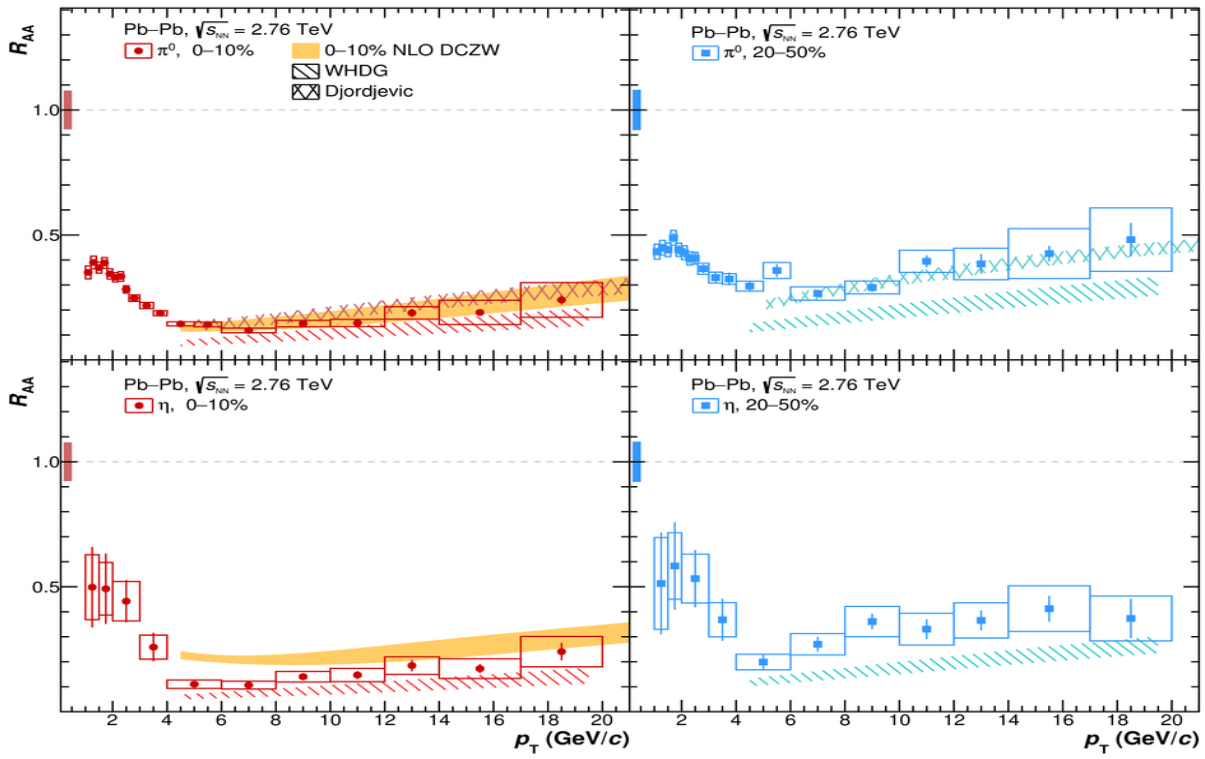

FIGURE V-25: R_{AA} of π^0 (top) and η (bottom) mesons as a function of p_T measured in Pb-Pb collisions at $\sqrt{s_{NN}} = 2.76$ TeV [324] in two centrality classes compared to NLO pQCD model predictions: DCZW [358] (solid bands), WHDG [362] (dashed bands) and Djordjevic [363] (crossed bands, π^0 only).

V.11 Summary

The measurements of the invariant π^0 yields in pp collisions at $\sqrt{s} = 0.9$, 2.76, 5.02, 7 and 8 TeV, the invariant η yields in pp collisions at $\sqrt{s} = 0.9$, 2.76, 7 and 8 TeV, π^0 and η yields for p-Pb collisions at $\sqrt{s_{NN}} = 5.02$ TeV as well as for Pb-Pb collisions at $\sqrt{s_{NN}} = 2.76$ TeV in a wide p_T range have been presented. Results for Pb-Pb collisions at $\sqrt{s_{NN}} = 5.02$ TeV in three centrality classes have also been shown.

The NLO pQCD predictions describe the pp results at lower colliding energies quite well, while there is an increasing discrepancy at large p_T for three highest energies, especially for the η meson. Models incorporating the hydrodynamic description of the hot matter evolution reproduce the low p_T end of the measured spectra in p-Pb and Pb-Pb collisions.

The η/π^0 ratio shows a universal behavior for small systems such as pp or p-Pb, and probably some deviations in central Pb-Pb collisions. The ratio is constant and consistent with m_T scaling at $p_T > 4$ GeV/c, but shows significant deviations from m_T scaling at low p_T in all collision systems and for each collision energy.

A strong suppression can be observed in the central Pb-Pb collisions, while the nuclear modification factor for p-Pb collisions is consistent with a unity at $p_T > 2$ GeV/c. Various models describe

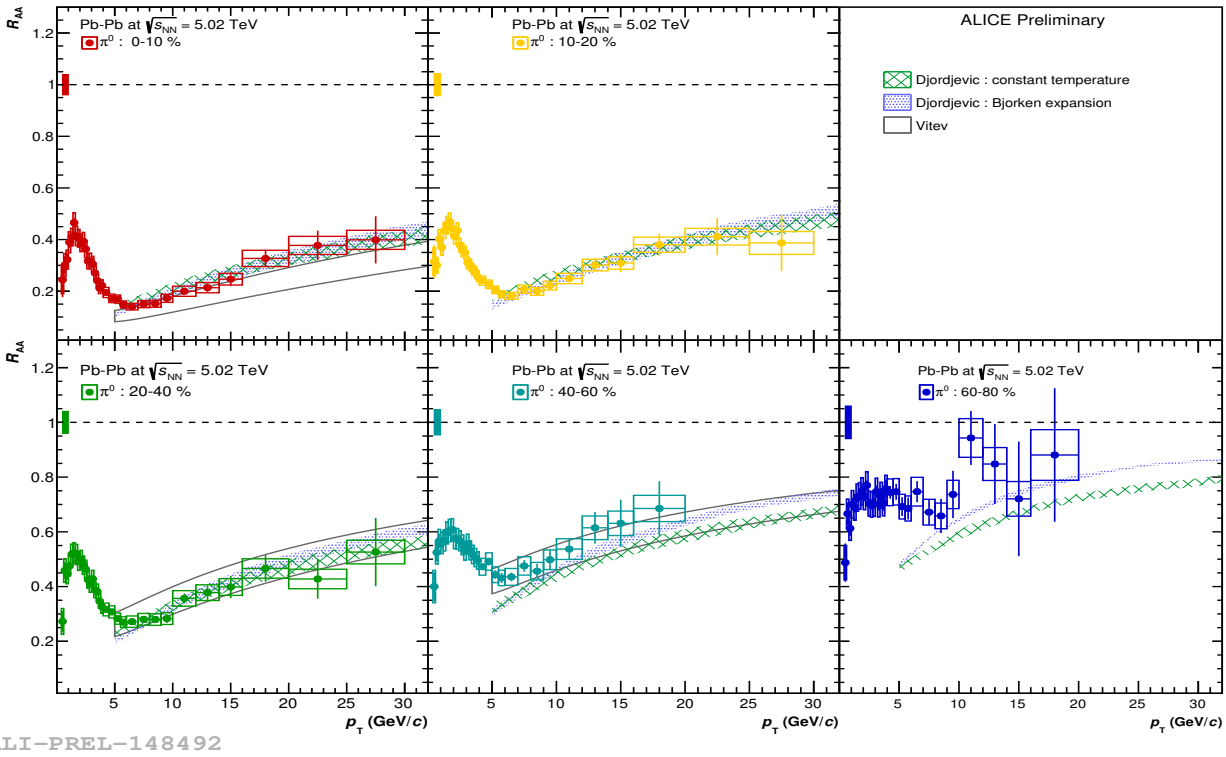

FIGURE V-26: R_{AA} of π^0 meson as a function of p_T measured in several centrality classes of Pb-Pb collisions at $\sqrt{s_{NN}} = 5.02$ TeV [321] compared to Djordjevic models [364, 365] and Vitev model [366, 367].

R_{AA} in Pb-Pb data with a different level of agreement. R_{pPb} is reasonably well reproduced by NLO pQCD calculations with the latest nPDFs or CGC models. All these results support the idea that the parton energy loss in the hot QCD medium is responsible for the neutral pion suppression in central Pb-Pb collisions.

The obtained results show the lack of uniform theoretical description of neutral meson production and are an important input for constraining models in small and large systems. The results also provide constraints on parton density functions inside the proton as well as in the nucleus and identified fragmentation functions.

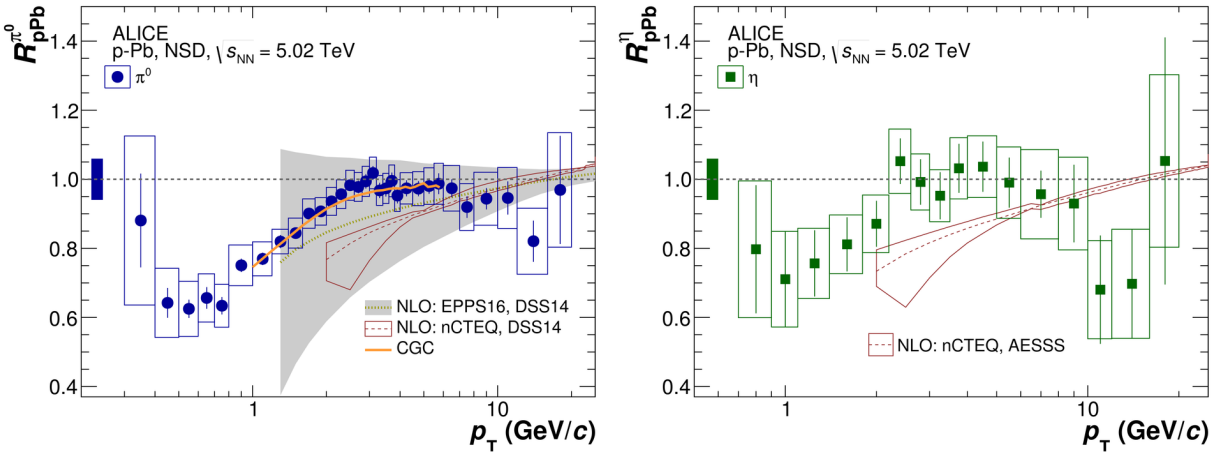

FIGURE V-27: The nuclear modification factor R_{pPb} for π^0 (left) and η (right) meson measured in NSD p-Pb collisions at $\sqrt{s_{\mathrm{NN}}} = 5.02$ TeV. The boxes around a unity denote the overall normalization uncertainty [323]. R_{pPb} are compared to theoretical models: NLO pQCD calculations using EPPS16 nPDF [67] with CT14 PDF [57] and DSS14 FF [84] (gray band), NLO pQCD using nCTEQ nPDF [65] and DSS14 FF (for π^0) or AESSS FF (for η) [85] (brown lines) and CGC [317] (orange line).

CHAPTER VI

PERSPECTIVES FOR RUN II DATA

The Alice experiment has collected data for different systems and energies. However, some full statistics analyses have not started yet due to ongoing calibrations or data processing (for example for pp collisions at $\sqrt{s} = 13$ TeV). There are just fractional results which are based on limited subsamples of data. As an example, the neutral meson analysis in pp collisions at $\sqrt{s} = 13$ TeV is very promising. This analysis is shortly discussed in Sec. **VI.1**.

The neutral mesons analyses are not so demanding in statistics. Moreover, analysis with preliminary calibration is possible to get a hint of the underlying possibilities. In particular, when considering any analysis with direct or/and isolated photons one needs to relay on the best possible calibration. Having analysed direct photon spectra, very good knowledge of background photon sources is crucial. The decay products coming from π^0 and η mesons are major sources of background and measurements of their spectra as first are necessary.

There are also analyses which are "statistics hungry". There are several reasons which cause needs for large statistics. We can consider rare processes, or frequent processes but measured with low efficiency or reduced acceptance of the detector. Such an example is the isolated photon-jet correlation analysis, where we have "suppression" due to photons in the final state and limited acceptance of detectors (like EMCal, which at the beginning consisted of 4 super modules and now consists of 20 SMs). It was checked that this analysis was not possible in LHC Run I in ALICE due to lack of statistics, while expectations for LHC Run II are discussed in Sec. **VI.2**.

There are several detector upgrades foreseen during LHC Long Shutdown 2 started in December 2018. The Inner Tracking System [369], the Time Projection Chamber [370] and Muon Tracking System [371] will be significantly modified. ALICE is going to upgrade detectors to gain both better resolution and faster readout. Then greater luminosity could be collected. The first tests of upgraded ALICE TPC based on GEM readout have been already performed, and excellent performance was demonstrated [372].

VI.1 Studies of neutral mesons in pp collisions at $\sqrt{s} = 13$ TeV

The neutral meson analysis in pp at $\sqrt{s} = 13$ TeV has been started on the small subsample of experimental data coming from the 2015 data taking period. π^0 and η mesons have been reconstructed in PCM, EMCal and PHOS. Invariant mass spectra of two photon cluster candidates around π^0

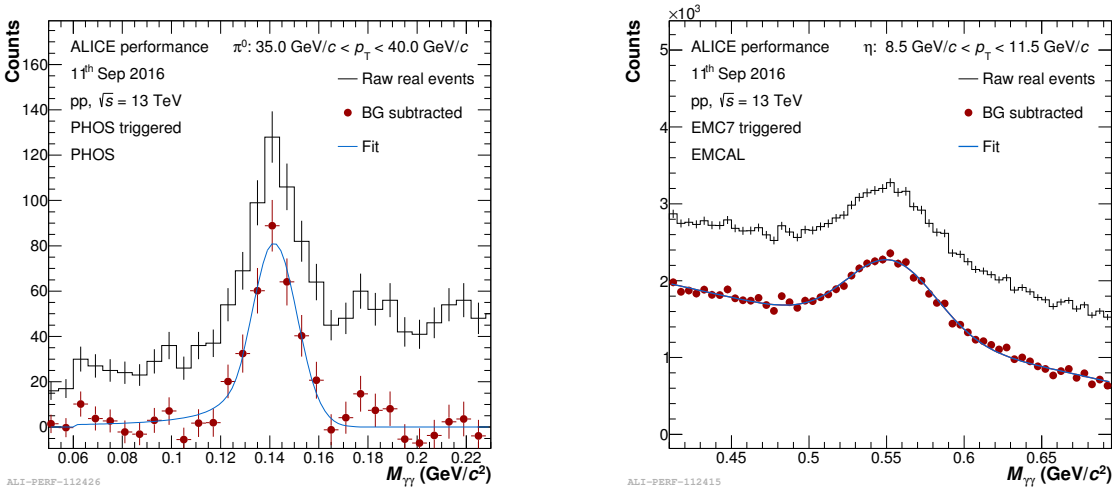

FIGURE VI-1: Invariant mass of two photon candidates around π^0 (left) and η (right) meson nominal mass measured by PHOS and EMCal in pp collisions at $\sqrt{s} = 13$ TeV. p_T range is indicated in the figures. Data are shown in black, mixed background subtracted data are shown in red, the blue curve denotes fit to signal and remaining residual background.

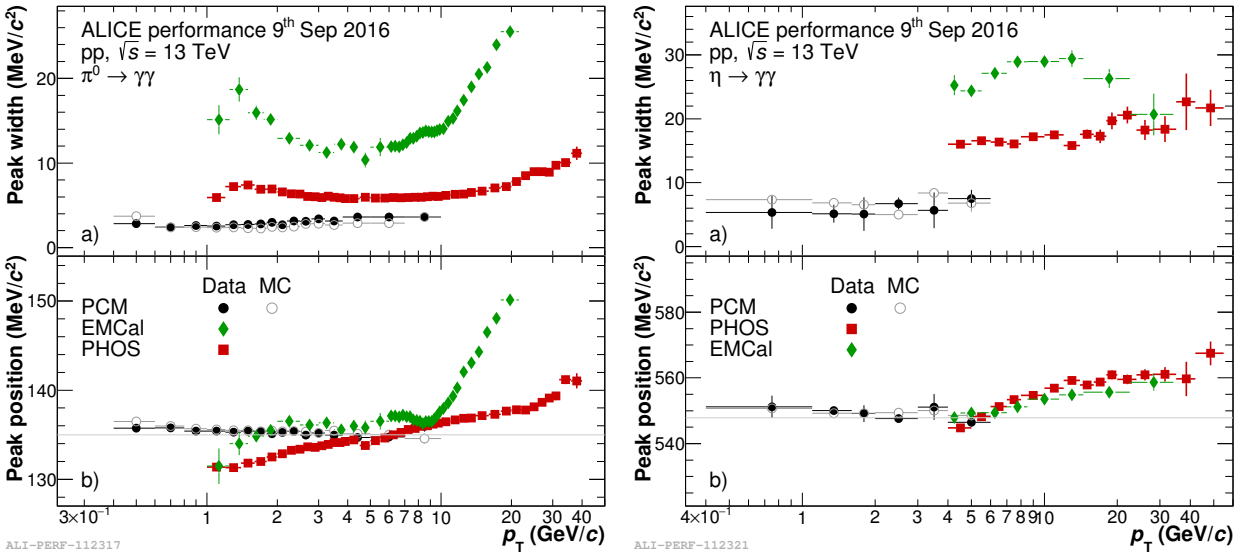

FIGURE VI-2: Left: Peak width (top panel) and position (bottom panel) of π^0 meson. Right: Peak width (top panel) and position (bottom panel) of η meson. Mesons are reconstructed via invariant mass technique in EMCal (green diamond), PHOS (red square) and PCM (black full dot) in pp collisions at $\sqrt{s} = 13$ TeV. Open black dots denote mesons reconstructed in MC.

and η mass peak are shown in Fig. **VI-1** for PHOS and EMCal, respectively. Distributions of peak width and position versus p_T for π^0 and η meson are shown in Fig. **VI-2**. ALICE has collected

much more data (factor ~ 20) in comparison to 2015. The full dataset will allow for very precise measurements.

VI.2 Feasibility studies of isolated photon-jet correlations

Direct photon searches have been performed in many experiments in parallel to the neutral meson analyses. As it was said before, it was very important to measure neutral meson spectra first because π^0 and η mesons are responsible for major background to the direct photon spectrum coming from decay photons. Direct photons have been measured also at the LHC in ATLAS (i.e. [373]) and CMS (i.e. [374]) up to very high-p_{T} (1 TeV/c) as well as in the ALICE experiment [375, 376] and the LHCb (i.e. [377]) at very low-p_{T} (1 GeV/c).

The other piece of the puzzle are jets, which were observed for the first time in 1975 in the e^+e^- collisions [378]. Since then, they have been studied in the e^+e^-, ep, pp, $\bar{\mathrm{p}}$p and nuclear collisions at various accelerators. A number of jet algorithms have been elaborated. The cone [379], k_{T} [380] and anti-k_{T} [381] algorithms can be distinguished among the others. The jet reconstruction algorithms let us determine the direction or the total transverse momentum of the jet.

The isolated photon-jet correlation analysis has been made in pp and Pb-Pb collisions at $\sqrt{s_{\mathrm{NN}}} = 2.76$ TeV for the first time at the LHC by CMS collaboration [382]. Since this measurement, γ-jet processes have been extensively studied in other systems and energies, and by different collaborations (see i.e. [383, 384, 385, 386, 387]).

To measure the parton to hadron fragmentation function (FF) with higher precision, photon correlated with jet events can be used. Photons do not interact via color exchange. They are produced as a result of the Compton scattering ($qg \to q\gamma$ - dominant mechanism at the LHC) or the annihilation ($q\bar{q} \to g\gamma$) in the leading order of the perturbative theory, like shown in Fig. **VI-3**. When

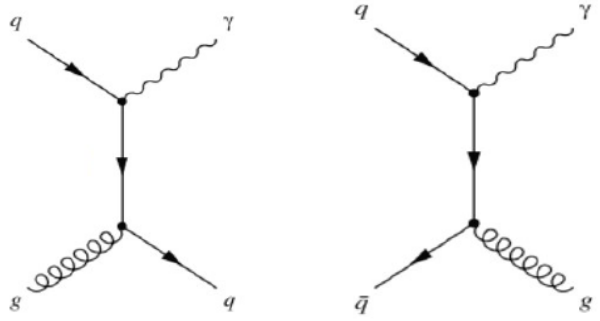

FIGURE VI-3: Example diagrams of direct photon production: Compton scattering (left) and annihilation (right).

produced in a hard scattering their energy is equal to the associated parton energy ($E^{\gamma} = E^{\mathrm{parton}}$) due to the energy conservation law. However, they can be scattered and their energy can be slightly modified. Photons are insensitive to the final state interactions, so they carry information about the parton hadronized to jet energy ($E^{\gamma} \approx E^{\mathrm{parton}} \approx E^{\mathrm{jet}}$). However, using photons has a disadvantage. The frequency of the photonic interaction is suppressed by factor of ~ 100 in comparison

to dijet production due to the presence of the electromagnetic coupling in the interaction vertex. It results in smaller available statistics. With sufficient statistics, the fragmentation function, defined as the normalized distribution of hadron momenta relative to that of the parent parton can be constructed [388] and measured:

$$F_{\mathrm{z}}(z^{\gamma}, p_{\mathrm{T}}^{\gamma}) = \frac{1}{N_{\mathrm{jet}}} \frac{\mathrm{d}N_{\mathrm{particle}}}{\mathrm{d}z^{\gamma}}, \tag{VI.1}$$

where

$$z^{\gamma} = p_{\mathrm{T}}^{\mathrm{particle}} / p_{\mathrm{T}}^{\gamma}. \tag{VI.2}$$

Sometimes the FF can be expressed in terms of $\xi = -\ln z^{\gamma}$. There are also two important variables when considering photon-jet correlations: the angular correlation ($\Delta\varphi^{\gamma-jet} = \varphi^{\gamma} - \varphi^{jet}$) and the transverse momentum balance ($r^{\gamma-jet} = p_{\mathrm{T}}^{jet} / p_{\mathrm{T}}^{\gamma}$) which can show a potential medium effect.

Due to the fact that pp data at $\sqrt{s} = 13$ TeV are currently being calibrated, at the present time one can only estimate the expected results. Although the collected luminosity for this data sample exceeds 16.5 pb^{-1} the simulations were done for 7 pb^{-1}. The difference accounts for possible inefficiencies in data quality.

Two scenarios were considered for photon-jet correlation studies. In the first case charged jets (jets which consist only of charged components) are considered in the TPC acceptance accompanied by a single photon in the EMCal acceptance. The second scenario assumes full jets (jets which consists both of charged and neutral components) reconstructed in the EMCal acceptance, and photons additionally in the DCal or PHOS acceptances.

Simulations were done with the Pythia 6 event generator, where prompt photon processes were generated with cross-sections: $\sigma(q + \bar{q} \to g + \gamma) = 2.5933 \times 10^{-1}$ μb and $\sigma(q + g \to q + \gamma) = 4.8913$ μb. Additional assumptions were imposed:

- number of bad channels (5%),
- photons reconstructed in the fiducial volume (50%),
- photon isolation (getting rid of fragmentation photons) with cone radius $R = 0.3$ efficiency (75%)
- jets reconstructed with anti-k_{T} algorithm with the resolution parameter $R^{jet} = 0.3$.

One third of charged jets were found in the TPC acceptance and one fifth of full jets were found in the EMCal acceptance, what results in ~ 10 k and ~ 4 k counts for $p_{\mathrm{T}}^{\gamma} > 20$ GeV/c for the first and second scenario, respectively. This is illustrated in Fig. **VI-4**.

The correlations between photon and jet transverse momentum for charged and full jets are shown in Fig. **VI-5**. (The calorimeter energy linearity in the considered region for photons is well known, within 2%.) The region with $p_{\mathrm{T}}^{\mathrm{jet}} < 10$ GeV/c is dominated by fake jets (combinatorial jets are a feature of the jet-clustering algorithm: all the particles are clustered into jets) or jets "half reconstructed" in detector acceptance (this happens when only a fraction of a jet is falling into the acceptance of the detector). A background jet correlated with photon results in a structure in the

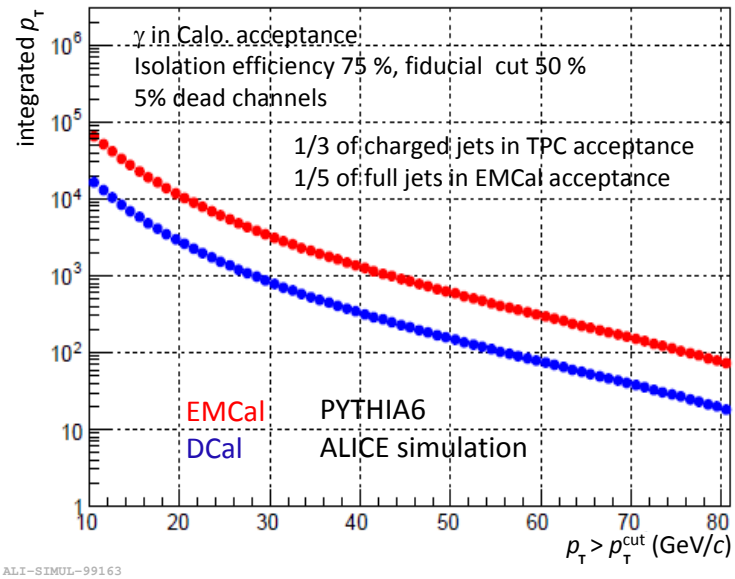

FIGURE VI-4: Expected isolated photon-jet pairs yield above the threshold p_T^{cut}, for reconstructed charged jets in the TPC acceptance and photons in the EMCal acceptance (red), or full jets in the EMCal acceptance and photon in the DCal and PHOS acceptances (blue).

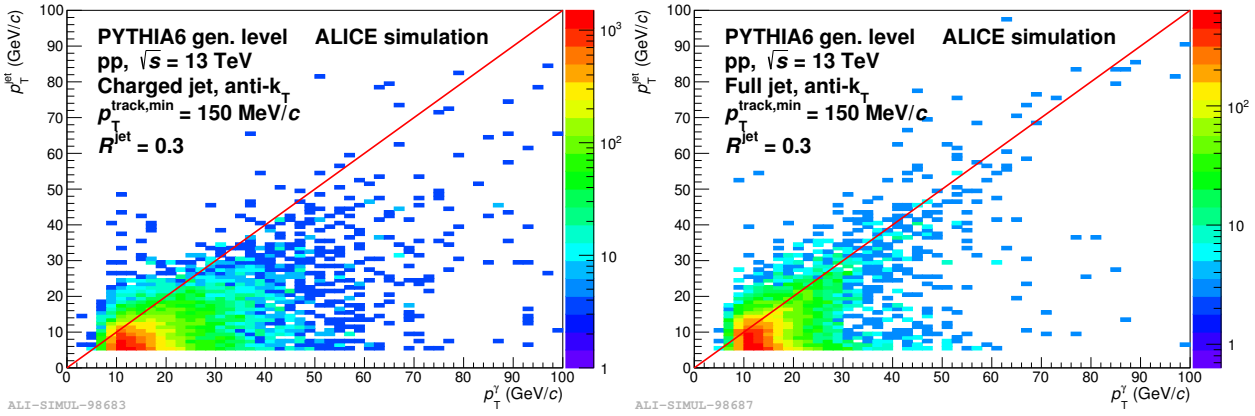

FIGURE VI-5: Correlation between reconstructed jet and photon transverse momentum at generator level for charged (left) and full jets (right). The red line shows the 1:1 correlation and is drawn to guide an eye.

momentum balance $r^{\gamma-jet} \approx 0.2$. It is well visible for full jets but merged with the main distribution for charged jets, as shown in Fig. **VI-6**.

To reduce the fake jet contribution some requirements on jets are imposed on the jet area (A^{jet}), location of the jet cone (fully in the detector acceptance) and photon-jet correlation (back-to-back

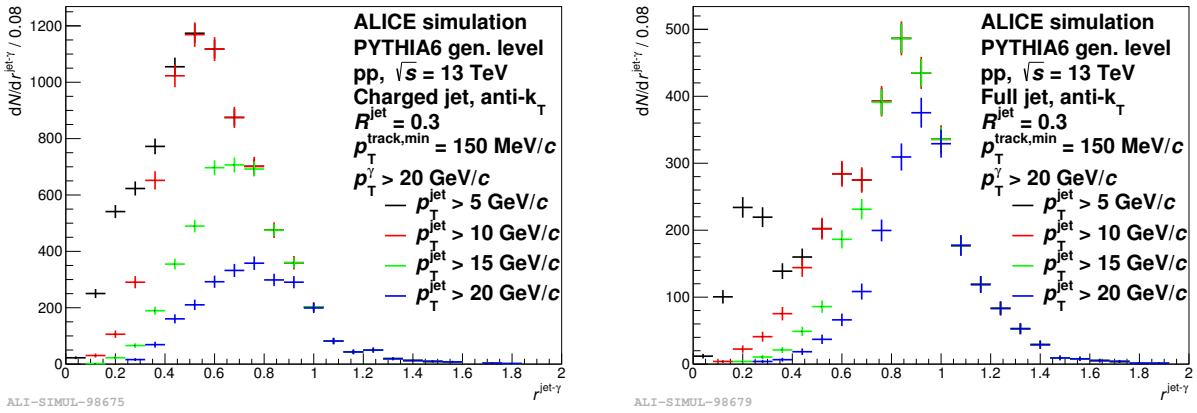

FIGURE VI-6: Charged (left) and full (right) jet-photon transverse momentum balance for different minimum $p_{\mathrm{T}}^{\mathrm{jet}}$.

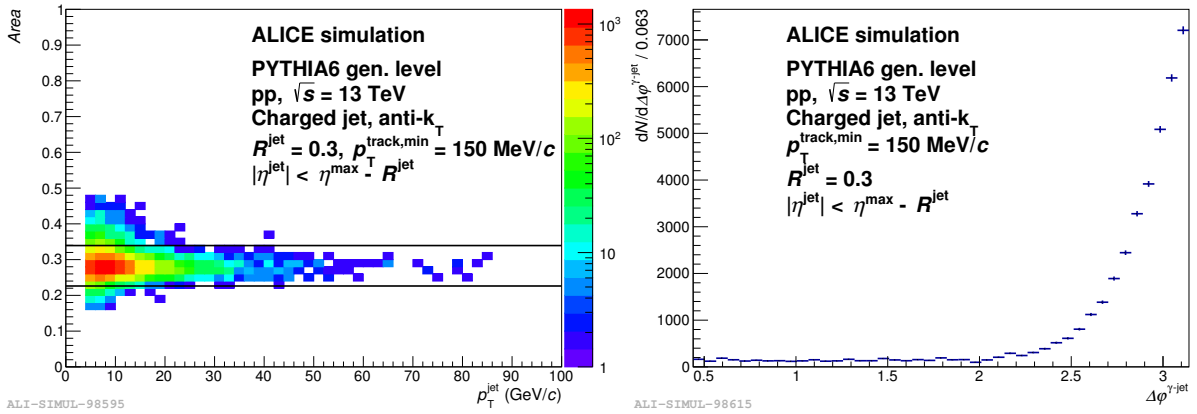

FIGURE VI-7: Left: The area of charged jet versus $p_{\mathrm{T}}^{\mathrm{jet}}$. Right: The azimuth distance between photon and reconstructed charged jet axis.

configuration). The jet area versus jet transverse momentum distribution and angular correlation of photon and jet are shown in Fig. **VI-7** for charged jets. For full jets these distributions look very similar.

Both the photon and jet p_{T} thresholds ($p_{\mathrm{T}}^{\gamma} > 20$ GeV/c and $p_{\mathrm{T}}^{\mathrm{jet}} > 10$ GeV/c, respectively) reduce the fake jet contribution. The fake jet contribution can also be reduced by requirements on the minimum p_{T} value of jet constituents. A requirement of $p_{\mathrm{T}}^{\mathrm{min}} = 1$ GeV/c is sufficient, however we loose the possibility to study softer fragmentation. One can consider different jet resolution parameters to study different fragmentations. The larger jet resolution parameter the softer is the fragmentation process, because more constituents are caught and associated to a jet. The scan of photon-jet balance for three jet resolution parameters $R^{\mathrm{jet}} = 0.2$, 0.3 and 0.4 is shown in Fig. **VI-8**.

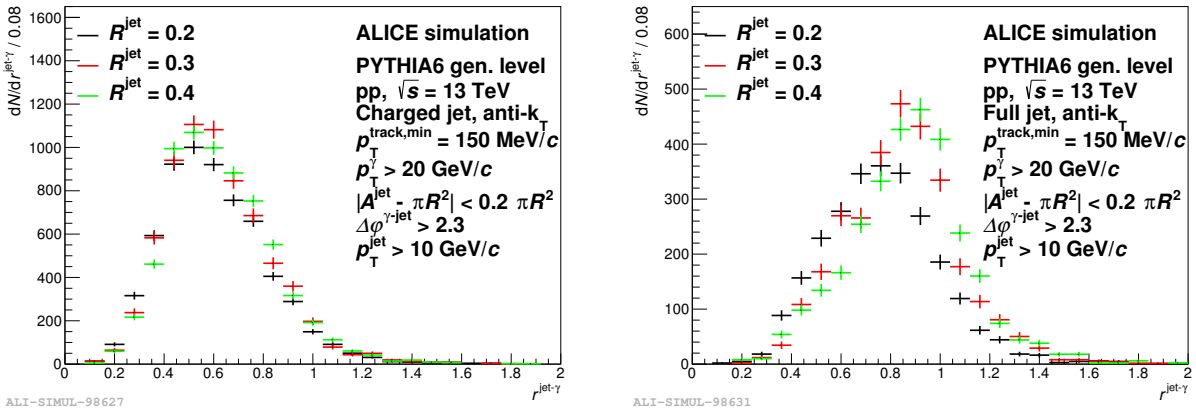

FIGURE VI-8: Photon-jet transverse momentum balance for jets reconstructed with different resolution parameter $R^{\mathrm{jet}} = 0.2$, 0.3 and 0.4 for charged (left) and full (right) jets.

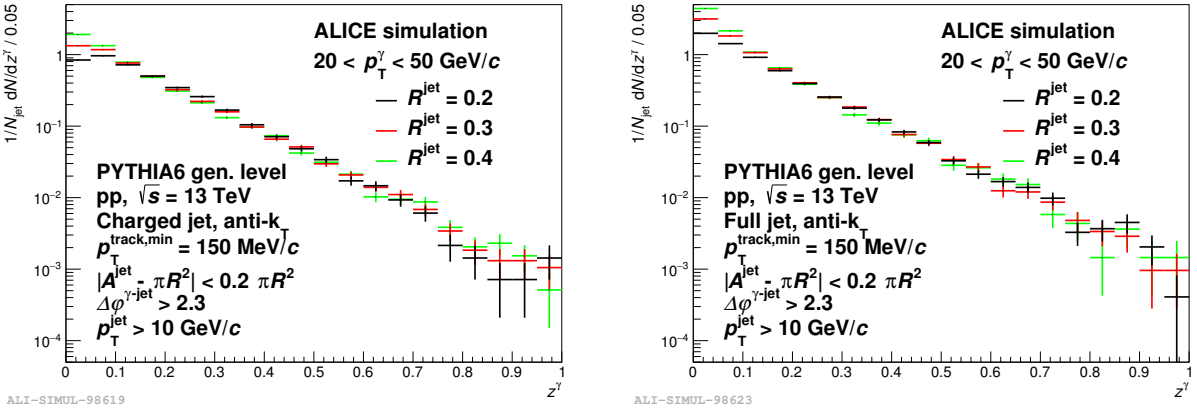

FIGURE VI-9: Charged (left) and full (right) jet fragmentation function in terms of z^{γ} for resolution parameters $R^{\mathrm{jet}} = 0.2$, 0.3 and 0.4.

The maximum of $r^{\mathrm{jet}-\gamma}$ distribution is shifted towards larger values for full jets and slightly wider for charged jets. The fragmentation function in terms of z^{γ} or ξ is shown in Fig. **VI-9** and **VI-10**, respectively.

The isolated photon-jet correlation analysis is feasible for pp collisions at $\sqrt{s} = 13$ TeV for $20 < p_{\mathrm{T}}^{\gamma} < 60$ GeV/c. A clear angular correlation between photon and jet is expected in the azimuthal angle. However, this correlation is more clearly visible for full jets than for charged jets. The transverse momentum balance is a good variable for background discrimination studies. The higher track p_{T} the harder the fragmentation process, but background jets are removed. Greater jet momentum threshold also removes background.

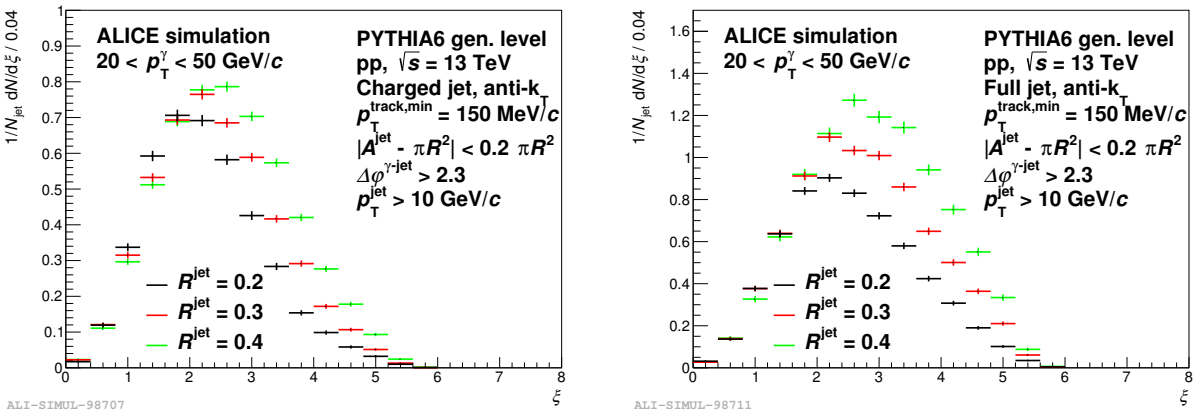

FIGURE VI-10: Charged (left) and full (right) jet fragmentation function in terms of ξ for resolution parameters $R^{\text{jet}} = 0.2$, 0.3 and 0.4.

CHAPTER VII

CONCLUSIONS

The aim of this paper was to give an overview of inclusive production of neutral mesons and show several aspects of detectors which are crucial for measurements but very often hidden behind the great results or discoveries. Neutral mesons like π^0 or η are reconstructed via their photonic decays. Since there are two abstract classes of photon identification/reconstruction, calorimetric measurement of energy deposit by photon and identification and combination of e^+e^- pairs coming from photon conversions, the proper calibration of calorimeters or tracking devices, respectively, is required. Therefore, the calibration of EMCal and TPC was discussed and excellent performance was achieved.

The summary of neutral meson production results in hadron-hadron, nucleus-nucleus and hadron-nucleus system was presented. It provides the great reference for future studies and comparisons among different energies and systems. It is very frequent in the high energy physics that results for some energy do not exist and one needs to interpolate. Having look-up tables helps to do the job properly and achieve approximation of desired spectrum before it is measured. However, at the expense of increased systematic uncertainty. From the other hand, there are different ways that observables scales with a collision energy and precision measurements at multiple energies test that.

The measurement of η/π^0 production cross-section ratio was emphasized. The results from decades of measurement show the universal pattern of this ratio among systems and energies. There was a hint of m_{T} scaling. However, the previous results were not accurate enough to show any kind of deviation or m_{T} scaling violation. Results from cosmic experiments, low energy FNAL or ISR, SPS experiments and RHIC experiments showed universality. The LHC accelerator had opened the possibility of measurement of neutral meson production in unknown energy regime that time.

The ALICE experiment was able to measure π^0 and η meson inclusive production cross-section in pp collisions spanning the center-of-mass collision energy $\sqrt{s} = 0.9$ to 8 TeV, p-Pb collisions at $\sqrt{s_{\mathrm{NN}}} = 5.02$ TeV and Pb-Pb collisions at $\sqrt{s_{\mathrm{NN}}} = 2.76$ and 5.02 TeV. The spectra are measured in a very wide p_{T} range and show the monotonic behaviour over several orders of magnitude. From the other side the measured η/π^0 ratio shows a significant deviation from m_{T} scaling in the very low-p_{T} range. In particular, it shows how important is η meson spectrum measurement in context of direct photons or low mass dielectron analyses. The η meson together with the π^0 meson are

responsible for $\sim 98\%$ background coming from decay products.

The status of the quark-gluon plasma searches seen by neutral meson eyes has also been discussed. The existence of the same type of matter - strongly interacting quark-gluon plasma - probed by neutral mesons has been confirmed in the ALICE experiment. It was confirmed that suppression seen in central Pb-Pb collisions is a final state effect rather than initial state effect.

The π^0 and η meson spectra, η/π^0 ratio, and nuclear modification factors helped constrain on theoretical models in both perturbative and non-perturbative regimes and we learned more about hadron physics and nuclear physics.

With new data samples which have just been collected and will be collected after the long shutdown 2 we hope to get new precise results which will help to achieve better understanding of nature. The pp collision data at $\sqrt{s} = 13$ TeV can provide very precise measurement of neutral mesons spectra (not only π^0 or η mesons but also ω or $\eta^{'}$) or help to constrain better jet fragmentation functions. The new $\sim 10\times$ larger sample of Pb-Pb collision data at $\sqrt{s_{\mathrm{NN}}} = 5.02$ TeV will allow access to both precision scans and constrain models with higher precision.

ACKNOWLEDGEMENTS

I wish to thank all the people who helped me with realization of this manuscript by they patience, encouraging conversations, constructive inspiration and advices. Most of all, I wish to thank Dr. Andrzej Bożek, Dr. Eryk Czerwiński, Prof. Jan Figiel, Prof. Lidia Görlich, Prof. Marek Kowalski, Dr. Aleksander Kusina, Dr. Paweł Malecki, Dr. Ewa Markiewicz, Dr. Chistoph Mayer, Dr. Christine Nattrass, Dr. Jacek Otwinowski, Dr. Radosław Ryblewski, Dr. Sabastian Sapeta, Dr. Andrzej Siódmok, Prof. Soren Sorensen and Dr. Iwona Sputowska. I want to thank all my colleagues for their understanding and support.

I would like to thank the ALICE collaboration for the possibility to use data as well as for the pleasure I had while working with collaborators during shifts, meetings and in the spare time. I am grateful to the members of working groups I am involved in for their inspiring and conclusive remarks and discussions.

I am indebted to Prof. Jack Steinberger for very inspiring conversation during breakfast at CERN after which his words fell into my mind.

I would like to thank librarians from the Institute of Nuclear Physics PAN and from CERN for their help, friendly attitude and tremendous work.

Finally, I wish to thank my family: my parents, for their support and unfinite love, my kids Emil and Milena for their patience, understanding, joy and optimism. Most of all, I wish to thank my wife Justyna for her peace of mind, patience, understanding and infinite encouragement.

BIBLIOGRAPHY

[1] A. A. Logunov *et al.* *"High-energy behaviour of inelastic cross sections"*, *Phys. Lett.* **B25** (1967) 611-614; DOI:10.1016/0370-2693(67)90130-X.

[2] D. J. Gross and F. Wilczek, *"Asymptotically Free Gauge Theories - I"*, *Phys. Rev.* **D8** (1973) 3633-3652; DOI:10.1103/PhysRevD.8.3633.

[3] K. G. Wilson, *"Confinement of Quarks"*, *Phys. Rev.* **D10** (1974) 2445-2459; DOI:10.1103/PhysRevD.10.2445.

[4] J. C. Collins, M. J. Perry, *"Superdense Matter: Neutrons Or Asymptotically Free Quarks?"*, *Phys. Rev. Lett.* **34** (1975) 1353; DOI:10.1103/PhysRevLett.34.1353.

[5] N. Cabibbo, G. Parisi, *"Exponential Hadronic Spectrum and Quark Liberation"*, *Phys. Lett.* **B59** (1975) 67-69; DOI:10.1016/0370-2693(75)90158-6.

[6] E. V. Shuryak, *"Quark-Gluon Plasma and Hadronic Production of Leptons, Photons and Psions"*, *Phys. Lett.* **B78** (1978) 150; *Sov. J. Nucl. Phys.* **28** (1978) 408; *Yad. Fiz.* **28** (1978) 796-808; DOI:10.1016/0370-2693(78)90370-2.

[7] M. Gyulassy, M. Plumer, *"Jet Quenching in Dense Matter"*, *Phys. Lett.* **B243** (1990) 432-438; DOI:10.1016/0370-2693(90)91409-5.

[8] X.-N. Wang, M. Gyulassy, *"Gluon shadowing and jet quenching in A + A collisions at* $\sqrt{s} = 200$ *GeV"*, *Phys. Rev. Lett.* **68** (1992) 1480-1483; DOI:10.1103/PhysRevLett.68.1480.

[9] J. Adams *et al.* (STAR Collaboration) *"Experimental and theoretical challenges in the search for the quark gluon plasma: The STAR Collaboration's critical assessment of the evidence from RHIC collisions"*, *Nucl. Phys.* **A757** (2005) 102-183; DOI:10.1016/j.nuclphysa.2005.03.085.

[10] K. Adcox *et al.* (PHENIX Collaboration), *"Formation of dense partonic matter in relativistic nucleus-nucleus collisions at RHIC: Experimental evaluation by the PHENIX collaboration"*, *Nucl. Phys.* **A757** (2005) 184-283; DOI:10.1016/j.nuclphysa.2005.03.086.

[11] B. B. Back *et al.* (PHOBOS Collaboration), *"The PHOBOS perspective on discoveries at RHIC"*, *Nucl. Phys.* **A757** (2005) 28-101; DOI:10.1016/j.nuclphysa.2005.03.084.

[12] I. Arsene *et al.* (BRAHMS Collaboration), *"Quark gluon plasma and color glass condensate at RHIC? The Perspective from the BRAHMS experiment"*, *Nucl. Phys.* **A757** (2005) 1-27; DOI:10.1016/j.nuclphysa.2005.02.130.

[13] R. Baier, Y. L. Dokshitzer, A. H. Mueller , S. Peigne, D. Schiff, *"Radiative energy loss and p(T) broadening of high-energy partons in nuclei"*, *Nucl. Phys.* **B484** (1997) 265-282; DOI:10.1016/S0550-3213(96)00581-0.

[14] M. Gyulassy, P. Levai, I. Vitev, *"NonAbelian energy loss at finite opacity"*, *Phys. Rev. Lett.* **85** (2000) 5535-5538; DOI:10.1103/PhysRevLett.85.5535.

[15] J. Alme *et al.*, *"The ALICE TPC, a large 3-dimensional tracking device with fast readout for ultra-high multiplicity events"*, *Nucl. Instrum. Meth.* **A622** (2010) 316-367; DOI:10.1016/j.nima.2010.04.042.

[16] A. Matyja *et al.* (ALICE TPC Collaboration), *"ALICE TPC: Design and performance"*, *PoS EPS-HEP2009* (2009) 128; DOI:10.22323/1.084.0128.

[17] A. Rybicki, *"Charged hadron production in elementary and nuclear collisions at 158 GeV/c"*, Ph.D. Dissertation, H. Niewodniczanski Institute of Nuclear Physics, Polish Academy of Sciences, Krakow, 2002, CERN-THESIS-2003-005.

[18] A. Matyja (ALICE Collaboration), *"Inclusive production of neutral mesons in ALICE"*, *Acta Phys. Polon.* **B42** (2011) 1517-1529; DOI:10.5506/APhysPolB.42.1517.

[19] A. Matyja (ALICE Collaboration), *"Neutral meson and photon production at the LHC measured with the ALICE experiment"*, *Nucl. Part. Phys. Proc.* **300-302** (2018) 99-106; DOI:10.1016/j.nuclphysbps.2018.12.018.

[20] A. Matyja (ALICE Collaboration), *"Perspectives of gamma-jet correlation analysis in Run2 in ALICE"*, poster at Quark Matter 2015, XXV International Conference on Ultrarelativistic Nucleus-Nucleus Collisions, September 27 - October 3, 2015, Kobe Fashion Mart, Kobe, Japan.

[21] D. de Florian and W. Vogelsang, *"Threshold resummation for the inclusive-hadron cross-section in pp collisions"*, *Phys. Rev.* **D71** (2005) 114004; DOI:10.1103/PhysRevD.71.114004.

[22] R. Brock *et al.* (CTEQ Collaboration), *"Handbook of perturbative QCD: Version 1.0"*, *Rev. Mod. Phys.* **67** (1995) 157-248; DOI:10.1103/RevModPhys.67.157.

[23] B. Andersson *et al.*, *"A Model for the Reaction Mechanism and the Baryon Fragmentation Distributions in Low $p_\perp$ Hadronic Interactions"*, *Nucl. Phys.* **B178** (1981) 242-262; DOI:10.1016/0550-3213(81)90408-9.

[24] P. D. B. Collins, *"An Introduction to Regge Theory and High-Energy Physics"* (1977); DOI:10.1017/CBO9780511897603.

[25] R. S. Bhalerao, *"Relativistic heavy-ion collisions"*, arXiv:1404.3294 [nucl-th] (2014); DOI:10.5170/CERN-2014-001.219 and references therein.

[26] Z. Fodor, S. D. Katz, *"Critical point of QCD at finite T and μ, lattice results for physical quark masses"*, *JHEP* **0404** (2004) 050; DOI:10.1088/1126-6708/2004/04/050.

[27] F. Karsch, *"Lattice results on QCD thermodynamics"*, *Nucl. Phys.* **A698** (2002) 199-208; DOI:10.1016/S0375-9474(01)01365-3.

[28] J. D. Bjorken, *"Highly Relativistic Nucleus-Nucleus Collisions: The Central Rapidity Region"*, *Phys. Rev.* **D27** (1983) 140-151; DOI:10.1103/PhysRevD.27.140.

[29] A. K. Chaudhuri, *"Viscous Hydrodynamic Model for Relativistic Heavy Ion Collisions"*, *Advances in High Energy Physics* **2013** (2013) 693180; DOI:10.1155/2013/693180.

[30] J. D. Bjorken, *"Hadron Final States in Deep Inelastic Processes"*, *Lect. Notes Phys.* **56** (1976) 93.

[31] M. L. Miller, K. Reygers, S. J. Sanders and P. Steinberg, *"Glauber Modeling in High Energy Nuclear Collisions"*, *Ann. Rev. Nucl. Part. Sci.* **57** (2007) 205; DOI: 10.1146/annurev.nucl.57.090506.123020.

[32] F. Gelis, E. Iancu, J. Jalilian-Marian, R. Venugopalan, *"The Color Glass Condensate"*, *Ann. Rev. Nucl. Part. Sci.* **60** (2010) 463-489; DOI:10.1146/annurev.nucl.010909.083629.

[33] R. Raitio, *"Hydrodynamics of hadronic matter in heavy ion collisions"*, *Nucl. Phys.* **A418** (1984) 539-548; DOI:10.1016/0375-9474(84)90574-8.

[34] E. Shuryak, *"Strongly coupled quark-gluon plasma in heavy ion collisions"*, *Rev. Mod. Phys.* **89** (2015) 035001; DOI:10.1103/RevModPhys.89.035001.

[35] W. Florkowski, *"Hydrodynamic description of ultrarelativistic heavy-ion collisions"*, arXiv:1712.05162 [nucl-th] (2017).

[36] M. Ploskon, *"Heavy-ion collisions - hot QCD in a lab"*, arXiv:1808.01411 (2018).

[37] J. Schukraft, R. Stock, *"Toward the Limits of Matter: Ultra-relativistic nuclear collisions at CERN"*, arXiv:1505.06853 [nucl-ex] (2015); DOI:10.1142/9789814644150_0003.

[38] E. Shuryak, *"Physics of Strongly coupled Quark-Gluon Plasma"*, *Prog. Part. Nucl. Phys.* **62** (2009) 48-101; DOI:10.1016/j.ppnp.2008.09.001.

[39] M. Gyulassy, L. McLerran, *"New Forms of QCD Matter Discovered at RHIC"*, *Nucl. Phys.* **A750** (2005) 30-63; DOI:10.1016/j.nuclphysa.2004.10.034.

[40] M. H. Thoma, *"The Quark-Gluon-Plasma Liquid"*, *J. Phys.* **G31** (2005) L7, Erratum-ibid. **G31** (2005) 539; DOI: 10.1088/0954-3899/31/1/L02, 10.1088/0594-3899/31/5/c01.

[41] G. Hanson *et al.*, *"Evidence for Jet Structure in Hadron Production by e^+e^- Annihilation"*, *Phys. Rev. Lett.* **35** (1975) 1609-1612; DOI:10.1103/PhysRevLett.35.1609.

[42] J. Adams *et al.* (STAR Collaboration), *"Evidence from d+Au measurements for final-state suppression of high-p_T hadrons in Au+Au collisions at RHIC"*, *Phys. Rev. Lett.* **91** (2003) 072304; DOI:10.1103/PhysRevLett.91.072304.

[43] J. Adams *et al.* (STAR Collaboration), *"Direct observation of dijets in central Au+Au collisions at $\sqrt{s_{NN}} = 200$ GeV"*, *Phys. Rev. Lett.* **97** (2006) 162301; DOI:10.1103/PhysRevLett.97.162301.

[44] C. Marquet, T. Renk, *"Jet quenching in the strongly-interacting quark-gluon plasma"*, *Phys. Lett.* **B685** (2010) 270-276; DOI:10.1016/j.physletb.2010.01.076.

[45] M. Gyulassy, I. Vitev, X.-N. Wang, B.-W. Zhang, *"Jet Quenching and Radiative Energy Loss in Dense Nuclear Matter"*, Quark-Gluon Plasma 3, pp. 123-191 (2004), arXiv:nucl-th/0302077; DOI:10.1142/9789812795533_0003.

[46] D. d'Enterria, *"Jet quenching"*, *Landolt-Bornstein* **23** (2010) 471; DOI:10.1007/978-3-642-01539-7_16.

[47] S. A. Bass *et al.*, *"Systematic Comparison of Jet Energy-Loss Schemes in a realistic hydrodynamic medium"*, *Phys. Rev.* **C79** (2009) 024901; DOI:10.1103/PhysRevC.79.024901.

[48] N. Armesto *et al.*, *"Comparison of Jet Quenching Formalisms for a Quark-Gluon Plasma 'Brick'"*, *Phys. Rev.* **C86** (2012) 064904; DOI:10.1103/PhysRevC.86.064904.

[49] G.-Y. Qin, X.-N. Wang, *"Jet quenching in high-energy heavy-ion collisions"*, *Int. J. Mod. Phys.* **E24** (2015) 1530014; DOI:10.1142/S0218301315300143, 10.1142/9789814663717_0007.

[50] S. S. Adler *et al.* (PHENIX Collaboration), *"High transverse momentum η production in p+p, d+Au and Au+Au collisions at $\sqrt{s_{NN}} = 200$ GeV"*, *Phys. Rev.* **C75** (2007) 024909; DOI:10.1103/PhysRevC.75.024909.

[51] B. Abelev *et al.* (ALICE Collaboration), *"Transverse Momentum Distribution and Nuclear Modification Factor of Charged Particles in p-Pb Collisions at $\sqrt{s_{NN}} = 5.02$ TeV"*, *Phys. Rev. Lett.* **110** (2013) 082302; DOI:10.1103/PhysRevLett.110.082302.

[52] G. Altarelli, G. Parisi, *"Asymptotic Freedom in Parton Language"*, *Nucl. Phys.* **B126** (1977) 298-318; DOI:10.1016/0550-3213(77)90384-4.

[53] V. N. Gribov, L. N. Lipatov, *Deep inelastic ep scattering in perturbation theory"*, *Sov. J. Nucl. Phys.* **15** (1972) 438-450.

[54] Y. L. Dokshitzer, *"Calculation of the structure functions for deep inelastic scattering and e^+e^- annihilation by perturbation theory in quantum chromodynamics"*, (in russian), *Sov. Phys. JETP* **46** (1977) 641-653.

[55] L. N. Lipatov, *"The parton model and perturbation theory"*, *Sov. J. Nucl. Phys.* **20** (1975) 94-102, [Yad. Fiz.20,181(1974)].

[56] A. D. Martin, W. J. Stirling, R. S. Thorne, G. Watt, *"Parton distributions for the LHC"*, *Eur. Phys. J.* **C63** (2009) 189-285; DOI:10.1140/epjc/s10052-009-1072-5.

[57] S. Dulat *et al.*, *"New parton distribution functions from a global analysis of quantum chromodynamics"*, *Phys. Rev.* **D93** 3, (2016) 033006; DOI:10.1103/PhysRevD.93.033006.

[58] L. A. Harland-Lang, A. D. Martin, P. Motylinski, R. S. Thorne, *"Parton distributions in the LHC era: MMHT 2014 PDFs"*, *Eur. Phys. J.* **C75** (5) (2015) 204; DOI:10.1140/epjc/s10052-015-3397-6.

[59] R. D. Ball, *et al.*, *"Parton distributions for the LHC Run II"*, *JHEP* **1504** (2015) 040; DOI:10.1007/JHEP04(2015)040.

[60] S. Alekhin, J. Bl umlein, S. Moch, R. Placakyte, *"Parton distribution functions, s, and heavy-quark masses for LHC Run II"*, *Phys. Rev.* **D96** (2017) 014011; DOI:10.1103/PhysRevD.96.014011.

[61] A. Accardi, L. T. Brady, W. Melnitchouk, J. F. Owens, N. Sato, *"Constraints on large-x parton distributions from new weak boson production and deep-inelastic scattering data"*, *Phys. Rev.* **D93** (2016) 114017; DOI:10.1103/PhysRevD.93.114017.

[62] H. Abramowicz, *et al.*, *"Combination of measurements of inclusive deep inelastic ep scattering cross sections and QCD analysis of HERA data"*, *Eur. Phys. J.* **C75** (2015) 580; DOI:10.1140/epjc/s10052-015-3710-4.

[63] J. Gao, L. Harland-Lang, J. Rojo, *"The Structure of the Proton in the LHC Precision Era"*, *Phys. Rept.* **742** (2018) 1-121; DOI:10.1016/j.physrep.2018.03.002.

[64] M. Arneodo, *"Nuclear effects in structure functions"*, *Phys. Rept.* **240** (1994) 301; DOI:10.1016/0370-1573(94)90048-5.

[65] K. Kovarik *et al.*, *"nCTEQ15 - Global analysis of nuclear parton distributions with uncertainties in the CTEQ framework"*, *Phys. Rev.* **D93** 8, (2016) 085037; DOI:10.1103/PhysRevD.93.085037.

[66] K. J. Eskola, H. Paukkunen and C. A. Salgado, *"EPS09: A New Generation of NLO and LO Nuclear Parton Distribution Functions"*, *JHEP* **0904** (2009) 065; DOI:10.1088/1126-6708/2009/04/065.

[67] K. J. Eskola, P. Paakkinen, H. Paukkunen, and C. A. Salgado, *"EPPS16: Nuclear parton distributions with LHC data"*, *Eur. Phys. J.* **C77** 3, (2017) 163; DOI:10.1140/epjc/s10052-017-4725-9.

[68] M. Hirai, S. Kumano, T.-H. Nagai, *"Determination of nuclear parton distribution functions and their uncertainties in next-to-leading order"*, *Phys. Rev.* **C76** (2007) 065207; DOI:10.1103/PhysRevC.76.065207.

[69] D. de Florian, R. Sassot, P. Zurita, M. Stratmann, *"Global Analysis of Nuclear Parton Distributions"*, *Phys. Rev.* **D85** (2012) 074028; DOI:10.1103/PhysRevD.85.074028.

[70] H. Khanpour, S. A. Tehrani, *"Global Analysis of Nuclear Parton Distribution Functions and Their Uncertainties at Next-to-Next-to-Leading Order"*, *Phys. Rev.* **D93** (2016) 014026; DOI:10.1103/PhysRevD.93.014026.

[71] G. Curci, W. Furmanski, R. Petronzio, *"Evolution of parton densities beyond leading order: The non-singlet case"*, *Nucl. Phys.* **B175** 27-92; DOI:10.1016/0550-3213(80)90003-6.

[72] W. Furmanski, R. Petronzio, *"Singlet parton densities beyond leading order"*, *Phys. Lett.* **B97** (1980) 437-442; DOI:10.1016/0370-2693(80)90636-X.

[73] L. Baulieu, E. G. Floratos, C. Kounnas, *"Parton model interpretation of the cut vertex formalism"*, *Nucl. Phys.* **B166** (1980) 321-339; DOI:10.1016/0550-3213(80)90230-8.

[74] M. Stratmann, W. Vogelsang, *"Next-to-leading order evolution of polarized and unpolarized fragmentation functions"*, *Nucl. Phys.* **B496** (1997) 41-65; DOI:10.1016/S0550-3213(97)00182-X.

[75] S. Kretzer, *"Fragmentation functions from flavor inclusive and flavor tagged e^+e^- annihilations"*, *Phys. Rev.* **D62** (2000) 054001; DOI:10.1103/PhysRevD.62.054001.

[76] B. A. Kniehl, G. Kramer, and B. Potter, *"Fragmentation functions for pions, kaons, and protons at next-to-leading order"*, *Nucl. Phys.* **B582** (2000) 514; DOI:10.1016/S0550-3213(00)00303-5.

[77] L. Bourhis, M. Fontannaz, J.-Ph. Guillet, M. Werlen, *"Next-to-leading order determination of fragmentation functions"*, *Eur. Phys. J.* **C19** (2001) 89-98; DOI:10.1007/s100520100579.

[78] M. Hirai, S. Kumano, T.-H. Nagai, K. Sudoh, *"Determination of fragmentation functions and their uncertainties"*, *Phys. Rev.* **D75** (2007) 094009; DOI:10.1103/PhysRevD.75.094009.

[79] S. Albino, B. A. Kniehl, G. Kramer, *"Fragmentation functions for light charged hadrons with complete quark flavor separation"*, *Nucl. Phys.* **B725** (2005) 181-206; DOI:10.1016/j.nuclphysb.2005.07.010.

[80] D. de Florian, R. Sassot, M. Stratmann, *"Global analysis of fragmentation functions for pions and kaons and their uncertainties"*, *Phys. Rev.* **D75** (2007) 114010; DOI:10.1103/PhysRevD.75.114010.

[81] D. de Florian, R. Sassot, M. Stratmann, *"Global analysis of fragmentation functions for protons and charged hadrons"*, *Phys. Rev.* **D76** (2007) 074033; DOI:10.1103/PhysRevD.76.074033.

[82] S. Albino, B. A. Kniehl, G. Kramer, *"AKK Update: Improvements from New Theoretical Input and Experimental Data"*, *Nucl. Phys.* **B803** (2008) 42-104; DOI:10.1016/j.nuclphysb.2008.05.017.

[83] D. d'Enterria, K. J. Eskola, I. Helenius, H. Paukkunen, *"Confronting current NLO parton fragmentation functions with inclusive charged-particle spectra at hadron colliders"*, *Nucl. Phys.* **B883** (2014) 615-628; DOI:10.1016/j.nuclphysb.2014.04.006.

[84] D. de Florian, R. Sassot, M. Epele, R.J. Hernández-Pinto and M. Stratmann, *"Parton-to-Pion Fragmentation Reloaded"*, *Phys. Rev. D* **91** (2015) 1, 014035; DOI:10.1103/PhysRevD.91.014035.

[85] C. A. Aidala, F. Ellinghaus, R. Sassot, J. P. Seele, and M. Stratmann, *"Global Analysis of Fragmentation Functions for Eta Mesons"*, *Phys. Rev.* **D83** (2011) 034002; DOI:10.1103/PhysRevD.83.034002.

[86] S. Gieseke, *"Monte Carlo event generators"*, *Nucl. Phys. Proc. Suppl.* **222-224** (2012) 174-186; DOI:10.1016/j.nuclphysbps.2012.03.018.

[87] A. Buckley *et al.*, *"General-purpose event generators for LHC physics"*, *Phys. Rept.* **504** (2011) 145-233; DOI:10.1016/j.physrep.2011.03.005.

[88] A. Siódmok, *"LHC Event Generation with General-purpose Monte Carlo Tools"*, *Acta Phys. Polon.* **B44** (2013) 1587-1601; DOI:10.5506/APhysPolB.44.1587.

[89] T. Sjöstrand, S. Mrenna, P. Z. Skands, *"PYTHIA 6.4 Physics and Manual"*, *JHEP* **0605** (2006) 026; DOI:10.1088/1126-6708/2006/05/026.

[90] T. Sjöstrand, S. Mrenna, P. Z. Skands, *"A Brief Introduction to PYTHIA 8.1"*, *Comput. Phys .Commun.* **178** (2008) 852-867; DOI:10.1016/j.cpc.2008.01.036.

[91] G. Corcella *et al.*, *"HERWIG 6.5 release note"*, e-Print: hep-ph/0210213 (2002).

[92] M. Bahr *et al.*, *"Herwig++ Physics and Manual"*, *Eur. Phys. J.* **C58** (2008) 639-707; DOI:10.1140/epjc/s10052-008-0798-9.

[93] T. Gleisberg *et al.*, *"SHERPA 1. alpha: A Proof of concept version"*, *JHEP* **0402** (2004) 056; DOI:10.1088/1126-6708/2004/02/056.

[94] T. Gleisberg *et al.*, *"Event generation with SHERPA 1.1"*, *JHEP* **0902** (2009) 007; DOI:10.1088/1126-6708/2009/02/007.

[95] B. Andersson *et al.*, *"Parton Fragmentation and String Dynamics"*, *Phys. Rept.* **97** (1983) 31-145; DOI:10.1016/0370-1573(83)90080-7.

[96] B. R. Webber, *"A QCD Model for Jet Fragmentation Including Soft Gluon Interference"*, *Nucl. Phys.* **B238** (1984) 492-528; DOI:10.1016/0550-3213(84)90333-X.

[97] S. Gieseke, C. Rohr, A. Siodmok, *"Colour reconnections in Herwig++"*, *Eur. Phys. J.* **C72** (2012) 2225; DOI:10.1140/epjc/s10052-012-2225-5.

[98] H. J. Drescher *et al.*, *"Parton based Gribov-Regge theory"*, *Phys. Rept.* **350** (2001) 93-289; DOI:10.1016/S0370-1573(00)00122-8.

[99] K. Werner *et al.*, *"Event-by-Event Simulation of the Three-Dimensional Hydrodynamic Evolution from Flux Tube Initial Conditions in Ultrarelativistic Heavy Ion Collisions"*, *Phys. Rev.* **C82** (2010) 044904; DOI:10.1103/PhysRevC.82.044904.

[100] M. Gyulassy and X. N. Wang, *"HIJING 1.0: A Monte Carlo program for parton and particle production in high-energy hadronic and nuclear collisions"*, *Comput. Phys. Commun.* **83** (1994) 307; DOI:10.1016/0010-4655(94)90057-4.

[101] H. Yukawa *"On the Interaction of Elementary Particles"*, *Proc. Phys. Math. Soc. Jap.* **17** (1935) 48-57, *Prog.Theor.Phys.Suppl.* **1** 1-10; DOI:10.1143/PTPS.1.1.

[102] C. M. G. Lattes, H. Muirhead, G. P. S. Occhialini and C. F. Powell, *"Processes Involving Charged Mesons"*, *Nature* **159** (1947) 694-697; DOI:10.1038/159694a0.

[103] R. Bjorklund, W. E. Crandall, B. J. Moyer, H. F. York, *"High Energy Photons from Proton-Nucleon Collisions"*, *Phys. Rev.* **77** 2 (1950) 213-218; DOI:10.1103/PhysRev.77.213.

[104] M. Tanabashi *et al.* (Particle Data Group), *Phys. Rev. D* **98**, 030001 (2018).

[105] A. Pevsner *et al.*, *"Evidence for a Three-Pion Resonance Near 550 MeV"*, *Phys. Rev. Lett.* **7** (1961) 421; DOI:10.1103/PhysRevLett.7.421.

[106] E. J. Lofgren, *"Experiences with the Bevatron"*, United States, (1958) https://www.osti.gov/servlets/purl/877349; DOI:10.2172/877349.

[107] M. Gell-Mann, *"The Eightfold Way: A Theory of strong interaction symmetry*, United States (1961); https://www.osti.gov/servlets/purl/4008239; DOI:10.2172/4008239.

[108] M. Gell-Mann, *"Symmetries of Baryons and Mesons" Phys. Rev.* **125** 3 (1962) 1067; DOI:10.1103/PhysRev.125.1067.

[109] M. Gell-Mann, *"A Schematic Model of Baryons and Mesons"*, *Phys. Lett.* **8** 3 (1964) 214-215; DOI:10.1016/S0031-9163(64)92001-3.

[110] G. Zweig, *"An SU(3) Model for Strong Interaction Symmetry and its Breaking"*, (1964) *CERN Report* No.8182/TH.401; http://cds.cern.ch/record/352337/files/CERN-TH-401.pdf.

[111] G. Zweig, *"An SU(3) Model for Strong Interaction Symmetry and its Breaking: II"*, (1964) *CERN Report* No.8419/TH.412; http://cds.cern.ch/record/570209/files/CERN-TH-412.pdf.

[112] F. W. Büsser, *et al.*, *"Observation of π^0 mesons with large transverse momentum in high-energy proton proton collisions"*, *Phys. Lett.* **46B** (1973) 471-476; DOI:10.1016/0370-2693(73)90169-X.

[113] F. W. Büsser, *et al.*, *"A study of high transverse momentum η and π^0 mesons at the CERN ISR"*, *Phys. Lett.* **B55** (1975) 232-236; DOI:10.1016/0370-2693(75)90450-5.

[114] F. W. Büsser, *et al.*, *"A study of inclusive spectra and two-particle correlations at large transverse momentum"*, *Nucl. Phys.* **B106** (1976) 1-30; DOI:10.1016/0550-3213(76)90366-7;

[115] M. Banner *et al.*, *"Large transverse momentum particle production at* 90° *in proton-proton collisions at the ISR"*, *Phys. Lett.* **44B**, (1973) 537; DOI:10.1016/0370-2693(73)90017-8.

[116] J. A. Appel *et al.*, *"Hadron Production at Large Transverse Momentum"*, *Phys. Rev. Lett.* **33** (1974) 719; DOI:10.1103/PhysRevLett.33.719.

[117] D. C. Carey *et al.*, *"Production of Large-Transverse-Momentum Gamma Rays in pp Collisions from 50 to 400 GeV"*, *Phys. Rev. Lett.* **32** (1974) 24; DOI:/10.1103/PhysRevLett.32.24.

[118] D. C. Carey *et al.*, *"Inclusive π^0 Production in pp Collisions at 50-400 GeV/c"*, *Phys. Rev. Lett.* **33** (1974) 327; DOI:10.1103/PhysRevLett.33.327.

[119] K. Eggert *et al.*, *"A study of high transverse momentum π^0's at ISR energies"*, *Nucl. Phys.* **B98** (1975) 49-72; DOI:10.1016/0550-3213(75)90199-6.

[120] H. Campbell *et al.*, *"Study of Inclusive γ and π^0 Production in 12.4 GeV/c pp Interactions"*, *Phys. Rev.* **D8** (1973) 3824; DOI:10.1103/PhysRevD.8.3824.

[121] D. Swanson *et al.*, *"Study of inclusive π^0 spectra and correlations in 12.4 GeV/c proton-proton interactions"*, *Phys. Lett.* **B48** (1974) 479; DOI:10.1016/0370-2693(74)90383-9.

[122] K. Jaeger *et al.*, *"Inclusive γ, π^0, K^0, and Λ production in 12.4 GeV/c pp interactions"*, *Phys. Rev.* **D11** (1975) 1756; DOI:10.1103/PhysRevD.11.1756.

[123] G. Levman *et al.*, *"Study of prompt e^+e^-, η^0, and ω^0 production in low-energy $\bar{p}p$ annihilations"*, *Phys. Rev.* **D21** (1980) 1; DOI:10.1103/PhysRevD.21.1.

[124] P. Darriulat *et al.*, *"Structure of Final States with a High Transverse Momentum π^0 in Proton Proton Collisions"*, *Nucl. Phys.* **B107** (1976) 429-456; DOI: 10.1016/0550-3213(76)90146-2.

[125] P. Darriulat *et al.*, *"Large Transverse Momentum Photons from High-Energy Proton Proton Collisions"*, *Nucl. Phys.* **B110** (1976) 365; DOI: 10.1016/0550-3213(76)90227-3.

[126] A. G. Clark *et al.*, *"Inclusive π^0 production from high-energy p-p collisions at very large transverse momenta"*, *Phys. Lett.* **74B** (1978) 267-272; DOI:10.1016/0370-2693(78)90570-1.

[127] A. L. S. Angelis *et al.*, *"A measurement of inclusive π^0 production at large p_T from p-p collisions at the CERN ISR"*, *Phys. Lett.* **B79** (1978) 505-510; DOI:10.1016/0370-2693(78)90416-1.

[128] E. Amaldi *et al.*, *"Single Direct Photon Production In pp Collisions At $\sqrt{s} = 53.2$ GeV In The P_T Interval 2.3 To 5.7 GeV/c" Nucl. Phys.* **B150** (1979) 326-344; DOI: 10.1016/0550-3213(79)90305-5.

[129] E. Amaldi *et al.*, *"Inclusive η Production In p+p Collision At Isr Energies"*, *Nucl. Phys.* **B158** (1979) 1-10; DOI: 10.1016/0550-3213(79)90183-4.

[130] C. Kourkoumelis *et al.*, *"Study of resolved high-p_T neutral pions at the CERN ISR"*, *Phys. Lett.* **B83** (1979) 257-260; DOI:10.1016/0370-2693(79)90698-1.

[131] C. Kourkoumelis *et al.*, *"Inclusive π^0 production at very large p_T at the ISR"*, *Phys. Lett.* **B84** (1979) 271-276; DOI:10.1016/0370-2693(79)90301-0.

[132] C. Kourkoumelis *et al.*, *"Inclusive η Production at High p_T at the ISR"*, *Phys. Lett.* **B84** (1979) 277-280; DOI:10.1016/0370-2693(79)90302-2.

[133] C. Kourkoumelis *et al.*, *"A Study of the Production of High-p_T π^0's at the CERN Intersecting Storage Rings"*, *Z. Phys.* **C5** (1980) 95-104; DOI:10.1007/BF01576190.

[134] D. Lloyd Owen *et al.*, *"Angular dependence of high-p_T π^0 production"*, *Phys. Rev. Lett.* **45** (1980) 89; DOI:10.1103/PhysRevLett.45.89.

[135] E. Anassontzis *et al.*, *"High-p_T Direct Photon Production in pp Collisions"*, *Z. Phys.* **C13** (1982) 277-289; DOI:10.1007/BF01572345.

[136] A. L. S. Angelis *et al.*, *"A comparison of the production of π^0-mesons in $p\bar{p}$ and pp interactions at the CERN ISR"*, *Phys. Lett.* **B118** (1982) 217-220; DOI:10.1016/0370-2693(82)90631-1.

[137] A. L. S. Angelis *et al.* (BCMOR Collaboration), *"Large Transverse Momentum π^0 Production in $\alpha\alpha$, dd and pp Collisions at the CERN ISR"*, *Phys. Lett.* **B185** (1987) 213-217; DOI:10.1016/0370-2693(87)91557-7.

[138] T. Akesson *et al.* (AFS Collaboration), *"Production of π^0 and η^0 at 11° in pp Collisions at $\sqrt{s} = 63$ GeV" Z. Phys.* **C18** (1983) 5-11; DOI: 10.1007/BF01571698.

[139] T. Akesson *et al.* (AFS Collaboration), *"A comparison of direct photon, π^0 and η in $p\bar{p}$ and pp interactions at the CERN ISR"*, *Phys. Lett.* **B158** (1985) 282-288; DOI:10.1016/0370-2693(85)90971-2.

[140] T. Akesson *et al.* (AFS Collaboration), *"Inclusive η Production at Low Transverse Momentum in 63 GeV pp Collisions at the CERN Intersecting Storage Rings"*, *Phys. Lett.* **B178** (1986) 447-451; DOI: 10.1016/0370-2693(86)91409-7.

[141] T. Akesson *et al.* (AFS Collaboration), *"High p_T γ and π^0 Production, Inclusive and With a Recoil Hadronic Jet, in pp Collisions at $\sqrt{s} = 63$ GeV"*, *Sov. J. Nucl. Phys.* **51** (1990) 836-845; *Yad. Fiz.* **51** (1990) 1314-1331.

[142] A. L. S. Angelis *et al.*, *"High transverse energy and high transverse momentum events in $p\bar{p}$ and pp interactions at the CERN intersecting storage rings"*, *Nucl. Phys.* **B263** (1986) 228-244; DOI:10.1016/0550-3213(86)90036-2.

[143] D. C. Carey *et al.*, *"A Unified Description of Single - Particle Production in pp Collisions"*, *Phys. Rev. Lett.* **33** (1974) 330; DOI:10.1103/PhysRevLett.33.330.

[144] D. C. Carey *et al.*, *"Inclusive π^0 production by high-energy protons"*, *Phys. Rev.* **D14** (1976) 1196; DOI:10.1103/PhysRevD.14.1196.

[145] G. Donaldson *et al.*, *"Inclusive π^0 Production at Large Transverse Momentum from $\pi^{\pm}p$ and pp Interactions at 100 and 200 GeV/c"*, *Phys. Rev. Lett.* **36** (1976) 1110; DOI:10.1103/PhysRevLett.36.1110.

[146] G. Donaldson *et al.*, *"Inclusive η Production at Large Transverse Momenta"*, *Phys. Rev. Lett.* **40** (1978) 684; DOI:10.1103/PhysRevLett.40.684.

[147] G. Donaldson *et al.*, *"Comparison of High-Transverse-Momentum π^0 Production from π^-, K^-, p, and $\bar{p}$ Beams"*, *Phys. Rev. Lett.* **40** (1978) 917; DOI:10.1103/PhysRevLett.40.917.

[148] G. Donaldson *et al.*, *"Angular dependence of high-transverse-momentum inclusive π^0 production in $\pi^{\pm}p$ and pp interactions"*, *Phys. Lett.* **B73** (1978) 375-379; DOI:10.1016/0370-2693(78)90537-3.

[149] A. V. Barnes *et al.*, *"Inclusive π^0 and η Production From 100 GeV/c $\pi^{\pm}p$ Collisions in the Triple Regge Region"*, *Nucl. Phys.* **B145** (1978) 45-66; DOI:10.1016/0550-3213(78)90412-1.

[150] A. V. Barnes *et al.*, *"Inclusive π^0 And η Production In The All Neutral Mode From 100 GeV/c π^- P Collisions"*, *Nucl. Phys.* **B145** (1978) 67-84; DOI:10.1016/0550-3213(78)90413-3.

[151] A. V. Barnes *et al.*, *"Precise Tests of Triple Regge Theory From π^0 and η Inclusive Production in 100 GeV/c $\pi^{\pm}p$ Collisions"*, *Phys. Rev. Lett.* **41** (1978) 1260; DOI:10.1103/PhysRevLett.41.1260.

[152] R. G. Kennett *et al.*, *"Inclusive π^0 and η Production From Kaon, Proton and Anti-proton Beams in the Triple Regge Region"*, *Nucl. Phys.* **B177** (1981) 1-20; DOI:10.1016/0550-3213(81)90264-9.

[153] R. G. Kennett *et al.*, *"The Production of Neutral Pions From 200 GeV π^-p Collisions in the High x Region"*, *Nucl. Phys.* **B284** (1987) 653-673; DOI:10.1016/0550-3213(87)90055-1.

[154] R. D. Kass *et al.*, *"Charged And Neutral Particle Production From 400 Gev/c PP Collisions"*, *Phys. Rev.* **D20** (1979) 605-614; DOI:10.1103/PhysRevD.20.605.

[155] D. L. Adams *et al.* (FNAL E704 Collaboration), *"Single spin asymmetries and invariant cross-sections of the high transverse momentum inclusive π^0 production in 200 GeV/c pp and $\bar{p}p$ interactions"*, *Phys. Rev.* **D53** (1996) 4747-4755; DOI: 10.1103/PhysRevD.53.4747.

[156] G. Alverson *et al.* (E706 Collaboration), *"Production of π^0 mesons at high p_T in π^- Be and p Be collisions at 500 GeV/c"*, *Phys. Rev.* **D45** (1992) R3899-R3902; DOI:10.1103/PhysRevD.45.R3899.

[157] G. Alverson *et al.* (E706 Collaboration), *"Production of direct photons and neutral mesons at large transverse momenta by π^- and p beams at 500 GeV/c"*, *Phys. Rev.* **D48** (1993) 5-28; DOI:10.1103/PhysRevD.48.5.

[158] L. Apanasevich *et al.* (FNAL E706 Collaboration), *"Evidence for parton k_T effects in high-p_T particle production"*, *Phys. Rev. Lett.* **81** (1998) 2642-2645; DOI:10.1103/PhysRevLett.81.2642.

[159] L. Apanasevich *et al.* (FNAL E706 Collaboration), *"Production of π^0 and η mesons at large transverse momenta in pp and pBe Interactions at 530 and 800 GeV/c"*, *Phys. Rev.* **D68** (2003) 052001; DOI:10.1103/PhysRevD.68.052001.

[160] L. Apanasevich *et al.* (FNAL E706 Collaboration), *"Production of π^0 and η Mesons at Large Transverse Momenta in π^-p and π^-Be Interactions at 515 GeV/c"*, *Phys. Rev.* **D69** (2004) 032003; DOI:10.1103/PhysRevD.69.032003.

[161] A. C. Borg *et al.*, *"Inclusive Pion and eta Production in K^-p Interactions at 14.3 GeV/c"*, *Nucl. Phys.* **B106** (1976) 430-450; DOI: 10.1016/0550-3213(76)90388-6.

[162] J. Bartke *et al.*, *"Eta and omega Meson Production in Medium-Energy $\pi^\pm p$ and K^-p Interactions"*, *Nucl. Phys.* **B118** (1977) 360-370; DOI: 10.1016/0550-3213(77)90232-2.

[163] I. V. Ajinenko *et al.*, *"Neutral Pion Production in K^+p Interactions at 32 GeV/c"*, *Nucl. Phys.* **B162** (1980) 61-78; DOI:10.1016/0550-3213(80)90431-9.

[164] C. Poiret *et al.*, *"Inclusive γ and pi^0 production in $\bar{p}p$ interactions at 32 GeV/c"*, *Z. Phys.* **C7** (1981) 283-287; DOI:10.1007/BF01431560.

[165] M. Barth *et al.*, *"Inclusive Photon And π^0 Production In K^+p Interactions At 70 GeV/c"*, *Z. Phys.* **C22** (1984) 23-31; DOI: 10.1007/BF01577560.

[166] J. L. Bailly *et al.* (EHS-RCBC Collaboration), *"Inclusive π^0 Production in 360 GeV pp Interactions Using the European Hybrid Spectrometer"*, *Z. Phys.* **C22** (1984) 119; DOI: 10.1007/BF01572158.

[167] S. Chakrabarti *et al.*, *"Inclusive γ-production in $\bar{p}p$ interactions at 12 GeV/c"*, *Z. Phys.* **C27** (1985) 1; DOI: 10.1007/BF01642474.

[168] I. V. Ajinenko *et al.* (NA22 Collaboration), *"Inclusive π^0 Production in π^+p, ^+p and pp Interactions at 250 GeV/c"*, *Z. Phys.* **C35** (1987) 7; DOI:10.1007/BF01561049.

[169] C. De Marzo *et al.* (NA24Collaboration), *"A Measurement of* π^0 *Production at Large Transverse Momentum in* $\pi^- p$, $\pi^+ p$ *and* pp *Collisions at 300 GeV/c"* *Phys. Rev.* **D36** (1987) 16-20; DOI:10.1103/PhysRevD.36.16.

[170] M. Banner *et al.* (UA2 Collaboration), *"Inclusive* π^0 *production at the CERN* p-$\bar{p}$ *collider"*, *Phys. Lett.* **B115** (1982) 59-64; DOI:10.1016/0370-2693(82)90514-7.

[171] M. Banner *et al.* (UA2 Collaboration), *"Inclusive particle production in the transverse momentum range between 0.25 and 40 GeV/c at the CERN Sp*$\bar{p}$*S collider"*, *Z. Phys.* **C27** (1985) 329; DOI:10.1007/BF01548636.

[172] F. Pauss *et al.* (ACCMOR Collaboration), *"Forward Particle Production in* $\pi^- p$ *and* $K^- p$ *Collisions at 58 GeV/c and Comparison With Quark Models"*, *Z. Phys.* **C27** (1985) 211; DOI:10.1007/BF01556611.

[173] R. J. Apsimon *et al.* (WA69 [Omega Photon] Collaboration) *"Inclusive production of* π^0 *mesons in* πp, Kp *and* γp *collisions at energies around 100 GeV"*, *Z. Phys.* **C52** (1991) 397-405; DOI:10.1007/BF01559433.

[174] R. J. Apsimon *et al.* (WA69 [Omega Photon] Collaboration) *"Inclusive production of* η *mesons in* πp, Kp *and* γp *collisions at energies around 100 GeV"*, *Z. Phys.* **C54** (1992) 185-191; DOI:10.1007/BF01566647.

[175] M. Bonesini *et al.* (WA70 Collaboration), *"High Transverse Momentum* π^0 *Production by* π^- *and* $\pi+$ *on Protons at 280 GeV/c"*, *Z. Phys.* **C37** (1987) 39-50; DOI: 10.1007/BF01442066.

[176] M. Bonesini *et al.* (WA70 Collaboration), *"Production of High Transverse Momentum Prompt Photons and Neutral Pions in Proton Proton Interactions at 280 GeV/c",Z. Phys.* **C38** (1988) 371-382; DOI: 10.1007/BF01584385.

[177] M. Bonesini *et al.* (WA70 Collaboration), *"High Transverse Momentum* η *Production in* $\pi^- p$, $\pi+p$ *and* pp *Interactions at 280 GeV/c"*, *Z. Phys.* **C42** (1989) 527; DOI: 10.1007/BF01557657.

[178] J. Antille *et al.* (UA6 Collaboration), *"A measurement of the inclusive* π^0 *and* η *production cross-sections at high* p_{T} *in* $p\bar{p}$ *and* pp *collisions at* $\sqrt{s} = 24.3$ *GeV"*, *Phys. Lett.* **B194** (1987) 568-572; DOI:10.1016/0370-2693(87)90236-X.

[179] G. Ballocchi *et al.* (UA6 Collaboration), *"Direct photon cross sections in proton-proton and antiproton-proton interactions at* $\sqrt{s} = 24.3$ *GeV"*, *Phys. Lett.* **B436** (1998) 222-230; DOI:10.1016/S0370-2693(98)01001-6.

[180] M. Aguilar-Benitez *et al.* (NA27 Collaboration), *"Inclusive* π^0 *and* η^0 *Production in* $\pi^- p$ *Interactions at 360 GeV/c"*, *Z. Phys.* **C34** (1987) 419; DOI: 10.1007/BF01679860.

[181] M. Aguilar-Benitez *et al.* (NA27 Collaboration), *"Inclusive particle production in 400 GeV/c pp-interactions"*, *Z. Phys.* **C50** (1991) 405-426; DOI: 10.1007/BF01551452.

[182] F. Abe *et al.* (CDF Collaboration), *"A Prompt photon cross-section measurement in $\bar{p}p$ collisions at $\sqrt{s} = 1.8$ TeV"*, *Phys. Rev.* **D48** (1993) 2998-3025; DOI:10.1103/PhysRevD.48.2998.

[183] S. S. Adler *et al.* (PHENIX Collaboration), *"Mid-rapidity neutral pion production in proton proton collisions at $\sqrt{s} = 200$ GeV"*, *Phys. Rev. Lett.* **91** (2003) 241803; DOI:10.1103/PhysRevLett.91.241803.

[184] A. Adare *et al.* (PHENIX Collaboration), *"Inclusive cross-section and double helicity asymmetry for π^0 production in p + p collisions at $\sqrt{s} = 200$ GeV: Implications for the polarized gluon distribution in the proton"*, *Phys. Rev.* **D76** (2007) 051106; DOI:10.1103/PhysRevD.76.051106.

[185] S. S. Adler *et al.* (PHENIX Collaboration), *"Centrality dependence of π^0 and η production at large transverse momentum in $\sqrt{s_{\rm NN}} = 200$ GeV d+Au collisions"*, *Phys. Rev. Lett.* **98** (2007) 172302; DOI:10.1103/PhysRevLett.98.172302.

[186] A. Adare *et al.* (PHENIX Collaboration), *"Inclusive cross section and double helicity asymmetry for π^0 production in p+p collisions at $\sqrt{s} = 62.4$ GeV"*, *Phys. Rev.* **D79** (2009) 012003; DOI: 10.1103/PhysRevD.79.012003.

[187] A. Adare *et al.* (PHENIX Collaboration), *"Cross section and double helicity asymmetry for η mesons and their comparison to π^0 production in p+p collisions at $\sqrt{(s)} = 200$ GeV"*, *Phys. Rev.* **D83** (2011) 032001; DOI:10.1103/PhysRevD.83.032001.

[188] A. Adare *et al.* (PHENIX Collaboration), *"Cross section and transverse single-spin asymmetry of η mesons in $p^{\uparrow} + p$ collisions at $\sqrt{s} = 200$ GeV at forward rapidity"*, *Phys. Rev.* **D90** (2014) 072008; DOI:10.1103/PhysRevD.90.072008.

[189] A. Adare *et al.* (PHENIX Collaboration), *"Inclusive cross section and double-helicity asymmetry for π^0 production at midrapidity in p+p collisions at $\sqrt{s} = 510$ GeV"*, *Phys. Rev.* **D93** (2016) 011501; DOI:10.1103/PhysRevD.93.011501.

[190] J. Adams *et al.* (STAR Collaboration), *"Cross-sections and transverse single spin asymmetries in forward neutral pion production from proton collisions at $\sqrt{s} = 200$ GeV"*, *Phys. Rev. Lett.* **92** (2004) 171801; DOI:10.1103/PhysRevLett.92.171801.

[191] J. Adams *et al.* (STAR Collaboration), *"Forward neutral pion production in p+p and d+Au collisions at $\sqrt{s_{\rm NN}} = 200$ GeV"*, *Phys. Rev. Lett.* **97** (2006) 152302; DOI:10.1103/PhysRevLett.97.152302.

Phys. Rev. **D80** (2009) 111108; DOI:10.1103/PhysRevD.80.111108.

[192] B. I. Abelev *et al.* (STAR Collaboration), *"Inclusive π^0, η, and direct photon production at high transverse momentum in p+p and d+Au collisions at $\sqrt{s_{\rm NN}} = 200$ GeV"*, *Phys. Rev.* **C81** (2010) 064904; DOI:10.1103/PhysRevC.81.064904.

[193] L. Adamczyk *et al.* (STAR Collaboration), *"Transverse Single-Spin Asymmetry and Cross-Section for π^0 and η Mesons at Large Feynman-x in Polarized p+p Collisions at $\sqrt{s} =$ 200 GeV"*, *Phys. Rev.* **D86** (2012) 051101; DOI:10.1103/PhysRevD.86.051101.

[194] L. Adamczyk *et al.* (STAR Collaboration), *"Neutral pion cross section and spin asymmetries at intermediate pseudorapidity in polarized proton collisions at $\sqrt{s} = 200$ GeV"*, *Phys. Rev.* **D89** (2014) 012001; DOI:10.1103/PhysRevD.89.012001.

[195] D. Antreasyan *et al.*, *"Production of Kaons, Protons, and Antiprotons with Large Transverse Momentum in p-p and p-d Collisions at 200, 300, and 400 GeV"*, *Phys. Rev. Lett.* **38** (1977) 115; DOI:10.1103/PhysRevLett.38.115.

[196] A. G. Clark *et al. "Large Transverse Momentum π^0 Production in Proton-Proton, Deuteron-Proton, and Deuteron-deuteron Collisions at the CERN ISR"*, *Nucl. Phys.* **B142** (1978) 189-204; DOI: 10.1016/0550-3213(78)90196-7.

[197] R. M. Baltrusaitis *et al.*, *"Inclusive π^0 Production over Large X_T and X_F Ranges in 200-, 300-, and 400-GeV/c Proton-Beryllium Interactions"*, *Phys. Rev. Lett.* **44** (1980) 122-125; DOI:10.1103/PhysRevLett.44.122.

[198] R. M. Baltrusaitis *et al.*, *"A Search for Direct Photon Production in 200 and 300 GeV/c Proton-Beryllium Interactions"*, *Phys. Lett.* **B88** (1979) 372-378; DOI:10.1016/0370-2693(79)90489-1.

[199] J. Povlis *et al.* (E629 Fermilab Collaboration), *"Nuclear Enhancement of π^0 and η mesons Produced at Large Transverse Momenta"*, *Phys. Rev. Lett.* **51** (1983) 967; DOI:10.1103/PhysRevLett.51.967.

[200] S. W. Delchamps, *"Inclusive π^0 and η^0 Meson Production at Large Transverse Momentum in 300 GeV/c p - Be Collisions"*, FERMILAB-THESIS-1985-35, UMI-86-00863 (1985).

[201] J. Kanzaki *et al.*, *"Inclusive Production Of π^0 And η^0 In 12 GeV p-Be Collisions"*, *J. Phys. Soc. Jap.* **50** (1981) 3849-3858; DOI: 10.1143/JPSJ.50.3849.

[202] A. Karabarbounis *et al.*, *"Production of π^0 at large transverse momentum in $\alpha\alpha$ and αp collisions at the CERN intersecting storage rings"*, *Phys. Lett.* **B104** (1981) 75-78; DOI:10.1016/0370-2693(81)90858-3.

[203] J. Badier *et al.* (NA3 Collaboration), *"Inclusive High p_T π^0 Production From $\pi^\pm$ and Protons at 200 GeV/c"*, *Z. Phys.* **C30** (1986) 45; DOI: 10.1007/BF01560676.

[204] V. Tikhmirov (HELIOS Collaboration), *"Low-p_T π^0 and η production in p-Be interactions at 450 GeV"*, HADRON 95, Proceedings of the 6th International Conference on Hadron Spectroscopy (World Scientific Publishing, 1995).

[205] G. Agakishiev *et al.* (TAPS and CERES Collaboration), *"Neutral meson production in p-Be and p-Au collisions at 450-GeV beam energy"*, *Eur. Phys. J.* **C4** (1998) 249-257; DOI:10.1007/s100529800804.

[206] R. Albrecht *et al.* (WA80 Collaboration), *"Photon and Neutral Pion Distributions in 60 and 200 A GeV* ^{16}O *+ Nucleus and Proton + Nucleus Reactions"* *Phys. Lett.* **B201** (1988) 390-396; DOI:10.1016/0370-2693(88)91161-6.

[207] R. Albrecht *et al.* (WA80 Collaboration), *"Transverse Momentum Distributions of Neutral Pions From Central and Peripheral* ^{16}O *+ Au Collisions at 200 AGeV"*, *Z. Phys.* **C47** (1990) 367-376; DOI:10.1007/BF01565859.

[208] R. Albrecht *et al.* (WA80 Collaboration), *"Upper limit for thermal direct photon production in heavy ion collisions at 60 A/GeV and 200 A/GeV"*, *Z. Phys.* **C51** (1991) 1-10; DOI:10.1007/BF01579555.

[209] M. M. Aggarwal *et al.* (WA98 Collaboration), *"Suppression of High-*p_{T} *Neutral Pions in Central Pb+Pb Collisions at* $\sqrt{s_{\mathrm{NN}}} = 17.3$ *GeV Relative to p+C and p+Pb Collisions"*, *Phys. Rev. Lett.* **100** (2008) 242301; DOI:10.1103/PhysRevLett.100.242301.

[210] E. Chiavassa *et al. "The reaction* $p^{12}C \rightarrow \eta$ *X from* $T_{\mathrm{p}} = 800$ *MeV to* $T_{\mathrm{p}} = 1500$ *MeV"*, *Europhys. Lett.* **41** (1998) 365-369; DOI:10.1209/epl/i1998-00158-3.

[211] S. S. Adler *et al.* (PHENIX Collaboration), *"Absence of suppression in particle production at large transverse momentum in* $\sqrt{s_{\mathrm{NN}}} = 200$ *GeV d + Au collisions"*, *Phys. Rev. Lett.* **91** (2003) 072303; DOI:10.1103/PhysRevLett.91.072303.

[212] G. Agakishiev *et al.* (HADES Collaboration), *"Inclusive pion and* η *production in p+Nb collisions at 3.5 GeV beam energy"*, *Phys. Rev.* **C88** (2013) 024904; DOI:10.1103/PhysRevC.88.024904.

[213] R. Santo *et al.* (WA80 Collaboration), *"Single photon and neutral meson production from WA80"*, *Nucl. Phys.* **A566** (1994) 61C-68C; DOI:10.1016/0375-9474(94)90609-2.

[214] R. Albrecht *et al.* (WA80 Collaboration), *"Production of* η *Meson in* 200*AGeV/c S+S and S+Au Reactions"*, *Phys. Lett.* **B361** (1995) 14-20; DOI:10.1016/0370-2693(95)01166-N.

[215] R. Albrecht *et al.* (WA80 Collaboration), *"Transverse momentum distributions of neutral pions from nuclear collisions at 200 AGeV"*, *Eur. Phys. J.* **C5** (1998) 255-267; DOI:10.1007/s100520050267.

[216] M. Aggarwal *et al.* (WA98 Collaboration), *"Photon and neutral meson production in 158 A GeV* ^{208}Pb *+ Pb collisions"*, *Nucl. Phys.* **A610** (1996) 200C-212C; DOI:10.1016/S0375-9474(96)00355-7.

[217] M. M. Aggarwal *et al.* (WA98 Collaboration), *"Centrality Dependence of Neutral Pion Production in* 158*A GeV* ^{208}Pb *+* ^{208}Pb *Collisions"*, *Phys. Rev. Lett.* **81** (1998) 4087-4091; DOI:10.1103/PhysRevLett.81.4087. Erratum: *Phys. Rev. Lett.* **84** (2000) 578-579.

[218] M. M. Aggarwal *et al.* (WA98 Collaboration), *"Direct photon production in* 158*A GeV* ^{208}Pb *+* ^{208}Pb*"*, nucl-ex/0006007 (2000).

[219] M. M. Aggarwal *et al.* (WA98 Collaboration), *"Transverse mass distributions of neutral pions from Pb-208 induced reactions at* 158 *A GeV"*, *Eur. Phys. J.* **C23** (2002) 225-236; DOI:10.1007/s100520100886.

[220] F. D. Berg *et al.* (TAPS Collaboration), *"Neutral meson production in relativistic heavy ion collisions"*, *Z. Phys.* **A340** (1991) 297-302; DOI:10.1007/BF01294678.

[221] R. S. Mayer *et al.* (TAPS Collaboration), *"Investigation of pion absorption in heavy ion induced subthreshold* π^0 *production"*, *Phys. Rev. Lett.* **70** (1993) 904-907; DOI:10.1103/PhysRevLett.70.904.

[222] O. Schwalb *et al.* (TAPS Collaboration), *"Mass dependence of* π^0 *production in heavy ion collisions at 1 A/GeV"*, *Phys. Lett.* **B321** (1994) 20-25; DOI:10.1016/0370-2693(94)90322-0.

[223] F. D. Berg *et al.* (TAPS Collaboration), *"Transverse momentum distributions of* η *mesons in near threshold relativistic heavy ion reactions"*, *Phys. Rev. Lett.* **72** (1994) 977-980; DOI:10.1103/PhysRevLett.72.977.

[224] R. Averbeck *et al.* (TAPS Collaboration), *"Production of* π^0 *and* η *mesons in carbon-induced relativistic heavy ion collisions"*, *Z. Phys.* **A359** (1997) 65-73; DOI:10.1007/s002180050368.

[225] R. Averbeck *et al.* (TAPS Collaboration), *"Neutral pions and* η *mesons as probes of the hadronic fireball in nucleus-nucleus collisions around 1A GeV"*, *Phys. Rev.* **C67** (2003) 024903; DOI:10.1103/PhysRevC.67.024903.

[226] K. Adcox *et al.* (PHENIX Collaboration), *"Suppression of hadrons with large transverse momentum in central Au+Au collisions at* $\sqrt{s_{\rm NN}} = 130$ *GeV"*, *Phys. Rev. Lett.* **88** (2002) 022301; DOI:10.1103/PhysRevLett.88.022301.

[227] S. S. Adler *et al.* (PHENIX Collaboration), *"Suppressed* π^0 *production at large transverse momentum in central Au+ Au collisions at* $\sqrt{s_{\rm NN}} = 200$ *GeV"*, *Phys. Rev. Lett.* **91** (2003) 072301; DOI:10.1103/PhysRevLett.91.072301.

[228] S. S. Adler *et al.* (PHENIX Collaboration), *"Common Suppression Pattern of* η *and* π^0 *Mesons at High Transverse Momentum in Au+Au Collisions at* $\sqrt{s_{\rm NN}} = 200$ *GeV"*, *Phys. Rev. Lett.* **96** (2006) 202301; DOI:10.1103/PhysRevLett.96.202301.

[229] S. S. Adler *et al.* (PHENIX Collaboration), *"A Detailed Study of High-*$p_{\rm T}$ *Neutral Pion Suppression and Azimuthal Anisotropy in Au+Au Collisions at* $\sqrt{s_{\rm NN}} = 200$ *GeV"*, *Phys. Rev.* **C76** (2007) 034904; DOI:10.1103/PhysRevC.76.034904.

[230] A. Adare *et al.* (PHENIX Collaboration), *"Onset of* π^0 *Suppression Studied in Cu+Cu Collisions at* $\sqrt{s_{\rm NN}} = 22.4$*,* 62.4*, and* 200 *GeV"*, *Phys. Rev. Lett.* **101** (2008) 162301; DOI:10.1103/PhysRevLett.101.162301.

[231] A. Adare *et al.* (PHENIX Collaboration), *"Suppression pattern of neutral pions at high transverse momentum in Au + Au collisions at $\sqrt{s_{\rm NN}} = 200$ GeV and constraints on medium transport coefficients"*, *Phys. Rev. Lett.* **101** (2008) 232301; DOI:10.1103/PhysRevLett.101.232301.

[232] A. Adare *et al.* (PHENIX Collaboration), *"Quantitative Constraints on the Opacity of Hot Partonic Matter from Semi-Inclusive Single High Transverse Momentum Pion Suppression in Au+Au collisions at $\sqrt{s_{\rm NN}} = 200$ GeV"*, *Phys. Rev.* **C77** (2008) 064907; DOI:10.1103/PhysRevC.77.064907.

[233] S. Afanasiev *et al.* (PHENIX Collaboration), *"High-$p_{\rm T}$ π^0 Production with Respect to the Reaction Plane in Au + Au Collisions at $\sqrt{s_{\rm NN}} = 200$ GeV"*, *Phys. Rev.* **C80** (2009) 054907; DOI:10.1103/PhysRevC.80.054907.

[234] A. Adare *et al.* (PHENIX Collaboration), *"Transverse momentum dependence of η meson suppression in Au+Au collisions at $\sqrt{s_{\rm NN}} = 200$ GeV"*, *Phys. Rev.* **C82** (2010) 011902; DOI:10.1103/PhysRevC.82.011902.

[235] A. Adare *et al.* (PHENIX Collaboration), *"Azimuthal anisotropy of neutral pion production in Au+Au collisions at $\sqrt{s_{\rm NN}} = 200$ GeV: Path-length dependence of jet quenching and the role of initial geometry"*, *Phys. Rev. Lett.* **105** (2010) 142301; DOI:10.1103/PhysRevLett.105.142301.

[236] A. Adare *et al.* (PHENIX Collaboration), *"Evolution of π^0 suppression in Au+Au collisions from $\sqrt{s_{\rm NN}} = 39$ to 200 GeV"*, *Phys. Rev. Lett.* **109** (2012) 152301; DOI:10.1103/PhysRevLett.109.152301.

[237] A. Adare *et al.* (PHENIX Collaboration), *"Neutral pion production with respect to centrality and reaction plane in Au+Au collisions at $\sqrt{s_{\rm NN}} = 200$ GeV"*, *Phys. Rev.* **C87** (2013) 034911; DOI:10.1103/PhysRevC.87.034911.

[238] C. Aidala *et al.* (PHENIX Collaboration), *"Production of π^0 and η mesons in Cu+Au collisions at $\sqrt{s_{\rm NN}} = 200$ GeV"*, *Phys. Rev.* **C98** (2018) 054903; DOI:10.1103/PhysRevC.98.054903.

[239] M. Sarsour *et al.* (PHENIX Collaboration), *"Recent PHENIX Results on High-$p_{\rm T}$ π^0 and η Production in Cu+Au and U+U Collisions"*, *J. Phys. Conf. Ser.* **1070** (2018) 012011; DOI:10.1088/1742-6596/1070/1/012011.

[240] J. Adams *et al.* (STAR Collaboration), *"Photon and neutral pion production in Au + Au collisions at $\sqrt{s_{\rm NN}} = 130$ GeV"*, *Phys. Rev.* **C70** (2004) 044902; DOI:10.1103/PhysRevC.70.044902.

[241] B. I. Abelev *et al.* (STAR Collaboration), *"Neutral Pion Production in Au+Au Collisions at $\sqrt{s_{\rm NN}} = 200$ GeV"*, *Phys. Rev.* **C80** (2009) 044905; DOI:10.1103/PhysRevC.80.044905.

[242] J. K. Storrow, *"Photoproduction at HERA: A Summary of the discussions of the working group on photoproduction"*, *J. Phys.* **G19** (1993) 1641-1670; DOI:10.1088/0954-3899/19/10/025.

[243] M. Dittmar *et al.*, *"Working Group I: Parton distributions: Summary report for the HERA LHC Workshop Proceedings"*, hep-ph/0511119 (2005).

[244] A. Bacchetta *et al.*, *"Summary of Workshop on Future Physics with HERA Data"*, arXiv:1601.01499 [hep-ex] (2016).

[245] H. J. Lipkin and H. J. Peshkin, *"Internal Symmetries and Model-Independent Relations for Inclusive Processes"*, *Phys. Rev. Lett.* **28** (1972) 862; DOI:10.1103/PhysRevLett.28.862.

[246] D. Antreasyan *et al.*, *"Production of Hadrons at Large Transverse Momentum in 200, 300 and 400 GeV pp and pn Collisions"*, *Phys. Rev.* **D19** (1979) 764-778; DOI:10.1103/PhysRevD.19.764.

[247] H. J. Frisch *et al.*, *"The Inclusive Production of Hadrons at High p_{T} in 200 and 300 GeV $\pi^- p$ and $\pi^- N$ Collisions"*, *Phys. Rev.* **D27** (1983) 1001; DOI:10.1103/PhysRevD.27.1001.

[248] R. Horgan and M. Jacob, *"Jet production at collider energy"*, *Nucl. Phys.* **B179** (1981) 441-460; DOI:10.1016/0550-3213(81)90013-4.

[249] R. D. Field and R. P. Feynman, *"Quark elastic scattering as a source of high-transverse-momentum mesons"*, *Phys. Rev.* **D15** (1977) 2590; DOI:10.1103/PhysRevD.15.2590.

[250] M. Benayoun *et al.*, *"Prompt Meson Production At Large p_{T}"*, *Nucl. Phys.* **B282** (1987) 653, Erratum: *Nucl. Phys.* **B303** (1988) 751; DOI:10.1016/0550-3213(87)90703-6.

[251] S. M. Berman, J. D. Bjorken and J. B. Kogut, *"Inclusive Processes at High Transverse Momentum"*, *Phys. Rev.* **D4** (1971) 3388; DOI:10.1103/PhysRevD.4.3388.

[252] J. F. Gunion, S. J. Brodsky and R. Blankenbecler, *"Composite Theory of Inclusive Scattering at Large Transverse Momenta" Phys. Rev.* **D6** (1972) 2652; DOI:10.1103/PhysRevD.6.2652.

[253] R. Blankenbecler, S. J. Brodsky and J. F. Gunion, *"Inclusive Processes at High Transverse Momentum"*, *Phys. Lett.* **B42** (1972) 461-465; DOI:10.1016/0370-2693(72)90107-4.

[254] V. V. Anisovich and V. M. Shekhter, *"Quark model for multiparticle and inclusive reactions"*, *Nucl. Phys.* **B55** (1973) 455-473; DOI:10.1016/0550-3213(73)90391-X.

[255] J. D. Bjorken and G. R. Farrar, *"Particle ratios in energetic hadron collisions"*, *Phys. Rev.* **D9** (1974) 1449; DOI:10.1103/PhysRevD.9.1449.

[256] R. Blankenbecler, S. J. Brodsky and J. F. Gunion, *"Analysis of Particle Production at Large Transverse Momentum"*, *Phys. Rev.* **D12** (1975) 3469-3487; DOI: 10.1103/PhysRevD.12.3469.

[257] D. W. Sivers, S. J. Brodsky and R. Blankenbecler, *"Large Transverse Momentum Processes"*, *Phys. Rept.* **23** (1976) 1-121; DOI: 10.1016/0370-1573(76)90015-6.

[258] M. K. Chase, W. J. Stirling, *"A Comparison of Models for Large Transverse Momentum Meson Production"*, *Nucl. Phys.* **B133** (1978) 157-188; DOI: 10.1016/0550-3213(78)90173-6.

[259] E. Fischbach, G. W. Look, *"Phenomenological Description of the Parton Parton Interaction in High Transverse Momentum Collisions"*, *Phys. Rev.* **D15** (1977) 2576; DOI: 10.1103/PhysRevD.15.2576.

[260] R. D. Field, *"Can Existing High Transverse Momentum Hadron Experiments Be Interpreted by Contemporary Quantum Chromodynamic Ideas?"*, *Phys. Rev. Lett.* **40** (1978) 997; DOI: 10.1103/PhysRevLett.40.997.

[261] R. P. Feynman, R. D. Field, G. C. Fox, *"A Quantum Chromodynamic Approach for the Large Transverse Momentum Production of Particles and Jets"*, *Phys. Rev.* **D18** (1978) 3320; DOI: 10.1103/PhysRevD.18.3320.

[262] A. P. Contogouris, R. Gaskell and S. Papadopoulos, *"Parton transverse momenta and quantum-chromodynamic effects in large-p_{T} hadron production"*, *Phys. Rev.* **D17** (1978) 2314; DOI:10.1103/PhysRevD.17.2314.

[263] E. Yen *"New Scaling Variable and Early Scaling in Single Particle Inclusive Distributions for Hadron-Hadron Collisions"*, *Phys. Rev.* **D10** (1974)836; 10.1103/PhysRevD.10.836.

[264] R. Hagedorn, *"Multiplicities, p_{T} Distributions and the Expected Hadron $\rightarrow$ Quark - Gluon Phase Transition"*, *Riv. Nuovo Cim.* **6N10** (1983) 1-50; DOI:10.1007/BF02740917.

[265] M. Bourquin and J.-M. Gaillard, *"A simple phenomenological description of hadron production"*, *Nucl. Phys.* **B114** (1976) 334-364; DOI: 10.1016/0550-3213(76)90592-7.

[266] T. Sjostrand *et al.*, *"High-energy physics event generation with PYTHIA 6.1"*, *Comput. Phys. Commun.* **135** (2001) 238-259; DOI:10.1016/S0010-4655(00)00236-8.

[267] P. K. Khandai, P. Shukla, V. Singh, *"Meson spectra and m_{T} scaling in p + p, d+Au, and Au + Au collisions at $\sqrt{s_{\mathrm{NN}}} = 200$ GeV"*, *Phys. Rev.* **C84** (2011) 054904; DOI:10.1103/PhysRevC.84.054904.

[268] K. Adcox *et al.*, *"Formation of dense partonic matter in relativistic nucleus-nucleus collisions at RHIC: Experimental evaluation by the PHENIX collaboration"*, *Nucl. Phys.* **A757** (2005) 184-283; DOI:10.1016/j.nuclphysa.2005.03.086.

[269] R. Witt (STAR Collaboration), *"$< p_{\mathrm{t}} >$ systematics and m_{t} scaling"*, nucl-ex/0403021 (2004).

[270] T. Peitzmann, *"Mass generation in coalescence: Effects on hadron spectra"*, *Acta Phys. Hung.* **A27** (2006) 363-366; DOI:10.1556/APH.27.2006.2-3.41.

[271] B. L. Combridge, J. Kripfganz and J. Ranft, *"Hadron Production at Large Transverse Momentum and QCD"*, *Phys. Lett.* **70B** (1977) 234; DOI:10.1016/0370-2693(77)90528-7.

[272] J. F. Owens, E. Reya and M. Gluck, *"Detailed Quantum Chromodynamic Predictions for High-p_T Processes"*, *Phys. Rev.* **D18** (1978) 1501; DOI:10.1103/PhysRevD.18.1501.

[273] F. Aversa, P. Chiappetta, M. Greco and J. P. Guillet, *"QCD Corrections to Parton-Parton Scattering Processes"*, *Nucl. Phys.* **B327** (1989) 105; DOI:10.1016/0550-3213(89)90288-5.

[274] D. de Florian, *"Next-to-leading order QCD corrections to one hadron production in polarized pp collisions at RHIC"*, *Phys. Rev.* **D67** (2003) 054004; DOI:10.1103/PhysRevD.67.054004.

[275] B. Jager, A. Schafer, M. Stratmann and W. Vogelsang, *" Next-to-leading order QCD corrections to high-p_T pion production in longitudinally polarized pp collisions*, *Phys. Rev.* **D67** (2003) 054005; DOI:10.1103/PhysRevD.67.054005.

[276] P. Aurenche *et al.*, *"Large p_T inclusive π^0 cross-sections and next-to-leading-order QCD predictions"*, *Eur. Phys. J.* **C13** (2000) 347-355; DOI:10.1007/s100520000309.

[277] U. Baur *et al.*, *"Report of the working group on photon and weak boson production"*, FERMILAB-CONF-00-411-AE, hep-ph/0005226 (2000).

[278] C. Bourrely, J. Soffer, *"Do we understand the single spin asymmetry for π^0 inclusive production in pp collisions?"*, *Eur. Phys. J.* **C36** (2004) 371-374; DOI:10.1140/epjc/s2004-01956-4.

[279] D. d'Enterria, *"Indications of suppressed high p_T hadron production in nucleus - nucleus collisions at CERN-SPS"*, *Phys. Lett.* **B596** (2004) 32-43; DOI:10.1016/j.physletb.2004.06.071.

[280] A. Adare *et al.* (PHENIX Collaboration), *"The Polarized gluon contribution to the proton spin from the double helicity asymmetry in inclusive pi^0 production in polarized p + p collisions at $\sqrt{s} = 200$ GeV"*, *Phys. Rev. Lett.* **103** (2009) 012003; DOI:10.1103/PhysRevLett.103.012003.

[281] A. Adare *et al.* (PHENIX Collaboration), *"Inclusive double-helicity asymmetries in neutral-pion and eta-meson production in $\vec{p} + \vec{p}$ collisions at $\sqrt{s} = 200$ GeV"*, *Phys. Rev.* **D90** (2014) 012007; DOI:10.1103/PhysRevD.90.012007.

[282] B. I. Abelev *et al.* (STAR Collaboration), *"Forward Neutral Pion Transverse Single Spin Asymmetries in p+p Collisions at $\sqrt{s} = 200$ GeV"*, *Phys. Rev. Lett.* **101** (2008) 222001; DOI:10.1103/PhysRevLett.101.222001.

[283] B. I. Abelev *et al.* (STAR Collaboration), *"Longitudinal double-spin asymmetry and cross section for inclusive neutral pion production at midrapidity in polarized proton collisions at $\sqrt{s} = 200$ GeV"*,

[284] J. Adam *et al.* (STAR Collaboration), *"Longitudinal Double-Spin Asymmetries for π^0s in the Forward Direction for 510 GeV Polarized pp Collisions"*, *Phys. Rev.* **D98** (2018) 032013; DOI:10.1103/PhysRevD.98.032013.

[285] R. Sharma, I. Vitev, and B.-W. Zhang, *"Light-cone wave function approach to open heavy flavor dynamics in QCD matter" Phys. Rev.* **C80** (2009) 054902; DOI:10.1103/PhysRevC.80.054902.

[286] I. Vitev, *"Testing the mechanism of QGP-induced energy loss"*, *Phys. Lett.* **B639** (2006) 38-45; DOI:10.1016/j.physletb.2006.05.083.

[287] W. A. Horowitz, M. Gyulassy, *"The Surprising Transparency of the sQGP at LHC"*, *Nucl. Phys.* **A872** (2011) 265-285; DOI:10.1016/j.nuclphysa.2011.09.018.

[288] A. Majumder, C. Shen, *"Suppression of the High $p_{\rm T}$ Charged Hadron $R_{\rm AA}$ at the LHC"*, *Phys. Rev. Lett.* **109** (2012) 202301; DOI:10.1103/PhysRevLett.109.202301.

[289] A. Dainese, C. Loizides, G. Paic, *"Leading-particle suppression in high energy nucleus-nucleus collisions"*, *Eur. Phys. J.* **C38** (2005) 461-474; DOI:10.1140/epjc/s2004-02077-x.

[290] C. Loizides, *"High transverse momentum suppression and surface effects in Cu+Cu and Au+Au collisions within the PQM model"*, *"Eur. Phys. J.* **C49** (2007) 339-345; DOI:10.1140/epjc/s10052-006-0059-8.

[291] M. Gyulassy, P. Levai, I. Vitev, *"Jet quenching in thin quark gluon plasmas. 1. Formalism"*, *Nucl. Phys.* **B571** (2000) 197-233; DOI:10.1016/S0550-3213(99)00713-0.

[292] S. Wicks, W. Horowitz, M. Djordjevic, M. Gyulassy, *"Heavy quark jet quenching with collisional plus radiative energy loss and path length fluctuations"*, *Nucl. Phys.* **A783** (2007) 493-496; DOI:10.1016/j.nuclphysa.2006.11.102.

[293] S. Wicks, W. Horowitz, M. Djordjevic, M. Gyulassy, *"Heavy quark jet quenching with collisional plus radiative energy loss and path length fluctuations"*, *Nucl. Phys.* **A784** (2007) 426-442; DOI:10.1016/j.nuclphysa.2006.12.048.

[294] H. Zhang, J. F. Owens, E. Wang, X.-N. Wang, *"Dihadron tomography of high-energy nuclear collisions in NLO pQCD"*, *Phys. Rev. Lett.* **98** (2007) 212301; DOI:10.1103/PhysRevLett.98.212301.

[295] P. B. Arnold, G. D. Moore, L. G. Yaffe, *"Photon emission from ultrarelativistic plasmas"*, *JHEP* **0111** (2001) 057; DOI:10.1088/1126-6708/2001/11/057.

[296] P. B. Arnold, G. D. Moore, L. G. Yaffe, *"Photon and gluon emission in relativistic plasmas"*, *JHEP* **0206** (2002) 030; DOI:10.1088/1126-6708/2002/06/030.

[297] X.-N. Wang, X. Guo, *"Multiple parton scattering in nuclei: Parton energy loss"*, *Nucl. Phys.* **A696** (2001) 788-832; DOI:10.1016/S0375-9474(01)01130-7.

[298] C. A. Salgado, U. A. Wiedemann, *"Calculating quenching weights"*, *Phys. Rev.* **D68** (2003) 014008; DOI:10.1103/PhysRevD.68.014008.

[299] A. Drees, H. Feng, J. Jia, *"Medium induced jet absorption at RHIC"*, *Phys. Rev.* **C71** (2005) 034909; DOI:10.1103/PhysRevC.71.034909.

[300] J. Jia, R. Wei, *"Dissecting the role of initial collision geometry for jet quenching observables in relativistic heavy ion collisions"*, *Phys. Rev.* **C82** (2010) 024902; DOI:10.1103/PhysRevC.82.024902.

[301] K. Aamodt *et al.* (ALICE Collaboration), *"The ALICE experiment at the CERN LHC"*, *JINST* **3** (2008) S08002; DOI:10.1088/1748-0221/3/08/S08002.

[302] L. Evans *et al.*, *"LHC Machine"*, *JINST* **3** (2008) S08001; DOI:10.1088/1748-0221/3/08/S08001.

[303] B. Abelev *et al.* (ALICE Collaboration), *"Performance of the ALICE Experiment at the CERN LHC"*, *Int. J. Mod. Phys.* **A29** (2014) 1430044; DOI:10.1142/S0217751X14300440.

[304] G. Dellacasa *et al.* (ALICE Collaboration), *"ALICE technical design report of the photon spectrometer (PHOS)"*, *CERN-LHCC-99-04* (1999).

[305] Y. Kharlov (ALICE Collaboration), *"Performance of Calorimetry in ALICE"*, **PoS** (LHCP2018) 231, arXiv:1809.08183.

[306] T. Cormier *et al.*, *"ALICE electromagnetic calorimeter : addendum to the ALICE technical proposal" CERN-LHCC-2006-014*, *CERN/LHCC*, 96-32-Add3 (2006).

[307] T. Cormier *et al.*, *"ALICE DCal: An Addendum to the EMCal Technical Design Report Di-Jet and Hadron-Jet correlation measurements in ALICE"*, *CERN-LHCC-2010-011*, *ALICE-TDR-14-add-1* (2010).

[308] U. Abeysekara *et al.*, *"ALICE EMCal Physics Performance Report"*, arXiv:1008.0413 [physics.ins-det] (2010).

[309] B. Abelev *et al.* (ALICE Collaboration), *"Centrality determination of Pb-Pb collisions at* $\sqrt{s_{\rm NN}} = 2.76$ *TeV with ALICE"*, *Phys. Rev.* **C88** 044909; DOI:10.1103/PhysRevC.88.044909.

[310] J. Adam *et al.* (ALICE Collaboration), *"Centrality dependence of particle production in p-Pb collisions at* $\sqrt{s_{\rm NN}} = 5.02$ *TeV"*, *Phys. Rev.* **C91** (2015) 064905; DOI:10.1103/PhysRevC.91.064905.

[311] D. Decamp *et al.* (ALEPH Collaboration), *"ALEPH: A detector for electron-positron annnihilations at LEP"*, *Nucl. Instrum. Meth.* **A294** (1990) 121-178, *Erratum: Nucl. Instrum. Meth.* **A303** (1991) 393; DOI:10.1016/0168-9002(90)91831-U.

[312] A. De Min *et al.* (DELPHI Collaboration), *"Performance of the HPC calorimeter in DELPHI"*, *IEEE Trans. Nucl. Sci.* 42 (1995) 491-498; DOI:10.1109/23.467923.

[313] S. Afanasev *et al.* (NA49 Collaboration), *"The NA49 large acceptance hadron detector"*, *Nucl. Instrum. Meth.* **A430** (1999) 210-244; DOI:10.1016/S0168-9002(99)00239-9.

[314] V. Eckardt *et al.*, *"Calibration of the STAR forward time projection chamber with krypton-83m"*, e-Print: nucl-ex/0101013 (2001).

[315] J. Allen *et al.*, *"Performance of prototypes for the ALICE electromagnetic calorimeter"*, *Nucl. Instrum. Meth.* **A615** (2010) 6-13; DOI:10.1016/j.nima.2009.12.061.

[316] W. Blum, W. Riegler and L. Rolandi, *"Particle Detection with Drift Chambers"*, 2nd edn. (Springer-Verlag, 2008), http://www.springer.com/physics/elementary/book/978-3-540-76683-4.

[317] T. Lappi, H. Mäntysaari, *"Single inclusive particle production at high energy from HERA data to proton-nucleus collisions"*, *Phys. Rev.* **D88** (2013) 114020; DOI:10.1103/PhysRevD.88.114020.

[318] B. Abelev *et al.* (ALICE Collaboration), *"Neutral pion and* η *meson production in proton-proton collisions at* $\sqrt{s} = 0.9$ *TeV and* $\sqrt{s} = 7$ *TeV"*, *Phys. Lett.* **B717** (2012) 162-172; DOI:10.1016/j.physletb.2012.09.015.

[319] B. Abelev *et al.* (ALICE Collaboration), *"Neutral pion production at midrapidity in pp and Pb-Pb collisions at* $\sqrt{s_{\rm NN}} = 2.76$ *TeV"*, *Eur. Phys. J.* **C74** (2014) 3108; DOI:10.1140/epjc/s10052-014-3108-8.

[320] S. Acharya *et al.* (ALICE Collaboration), *"Production of* π^0 *and* η *mesons up to high transverse momentum in pp collisions at 2.76 TeV"*, *Eur. Phys. J.* **C77** (2017) 339; DOI: 10.1140/epjc/s10052-017-4890-x.

[321] D. Sekihata (ALICE Collaboration), *"Energy and system dependence of nuclear modification factors of inclusive charged particles and identified light hadrons measured in p-Pb, Xe-Xe and Pb-Pb collisions with ALICE"*, arXiv:1807.11240 [hep-ex] (2018).

[322] S. Acharya *et al.* (ALICE Collaboration), *"*π^0 *and* η *meson production in proton-proton collisions at* $\sqrt{s} = 8$ *TeV"*,*Eur. Phys. J.* **C78** (2018) 263; DOI:10.1140/epjc/s10052-018-5612-8.

[323] S. Acharya *et al.* (ALICE Collaboration), *"Neutral pion and* η *meson production in p-Pb collisions at* $\sqrt{s_{\rm NN}} = 5.02$ *TeV"*,arXiv:1801.07051v1 [nucl-ex] (2018).

[324] S. Acharya *et al.* (ALICE Collaboration), *"Neutral pion and* η *meson production at midrapidity in Pb-Pb collisions at* $\sqrt{s_{\rm NN}} = 2.76$ *TeV"*, *Phys. Rev.* **C98** (2018) 044901; DOI: 10.1103/PhysRevC.98.044901.

[325] B. Abelev *et al.* (ALICE Collaboration), *"Measurement of inelastic, single- and double-diffraction cross sections in proton-proton collisions at the LHC with ALICE"*, *Eur. Phys. J.* **C73** (2013) 2456; DOI:10.1140/epjc/s10052-013-2456-0.

[326] S. Acharya *et al.* (ALICE Collaboration), *" ALICE luminosity determination for pp collisions at* $\sqrt{s} = 5$ *TeV"*, ALICE-PUBLIC-2016-005 (2016), http://cds.cern.ch/record/2202638.

[327] S. Acharya *et al.* (ALICE Collaboration), *"ALICE luminosity determination for pp collisions at* $\sqrt{s} = 8$ *TeV"*, ALICE-PUBLIC-2017-002 (2017), http://cds.cern.ch/record/2255216.

[328] G. J. Alner *et al.* (UA5 Collaboration), *"Antiproton-proton cross sections at 200 and 900 GeV c.m. energy"*, *Z. Phys.* **C32** (1986) 153-161; DOI:10.1007/BF01552491.

[329] S. Acharya *et al.* (ALICE Collaboration), *"ALICE 2017 luminosity determination for pp collisions at* $\sqrt{s} = 5$ *TeV"*, ALICE-PUBLIC-2018-014 (2018), http://cds.cern.ch/record/2648933.

[330] B. Alessandro (ed.)*et al.*, *"ALICE Collaboration, ALICE: Physics Performance Report, Volume II"*, *J. Phys.* **G32** (2006) 1295-2040; DOI:10.1088/0954-3899/32/10/001.

[331] T. Skwarnicki, Ph.D. Thesis, Institute of Nuclear Physics, Krakow 1986; *"A study of the radiative cascade transitions between the upsilon-prime and upsilon resonances"*, DESY Internal Report, DESY F31-86-02 (1986).

[332] K. Koch, *"*π^0 *and* η *measurement with photon conversions in ALICE in proton-proton collisions at* $\sqrt{s} = 7$ *TeV"*, *Nucl. Phys.* **A855** (2011) 281; DOI:10.1016/j.nuclphysa.2011.02.059.

[333] J. Adam *et al.* (ALICE Collaboration), *"Measurement of pion, kaon and proton production in proton-proton collisions at* $\sqrt{s} = 7$ *TeV"*, *Eur. Phys. J.* **C75** (2015) 226; DOI:10.1140/epjc/s10052-015-3422-9.

[334] L. Lyons, D. Gibaut, P. Clifford, *"How to combine correlated estimates of a single physical quantity"*, *Nucl. Instrum. Methods* **A270** (1988) 110; DOI:10.1016/0168-9002(88)90018-6.

[335] A. Valassi, *"Combining correlated measurements of several different physical quantities"*, *Nucl. Instrum. Meth.* **A500** (2003) 391-405; DOI:10.1016/S0168-9002(03)00329-2.

[336] A. Valassi, R. Chierici, *"Information and treatment of unknown correlations in the combination of measurements using the BLUE method" Eur. Phys. J.* **C74** (2014) 2717; DOI:10.1051/epjconf/201713711006.

[337] G. D. Lafferty, T. R. Wyatt, *"Where to stick your data points : the treatment of measurements within wide bins"*, *Nucl. Instrum. Meth.* **A355** (1995) 541; DOI:10.1016/0168-9002(94)01112-5.

[338] C. Tsallis, *"Possible generalization of Boltzmann-Gibbs statistics"*, *J. Statist. Phys.* **52** (1988) 479; DOI:10.1007/BF01016429.

[339] A. Adare *et al.* (PHENIX Collaboration), *"Detailed measurement of the e^+e^- pair continuum in p + p and Au + Au collisions at $\sqrt{s_{\rm NN}} = 200$ GeV and implications for direct photon production"*, *Phys. Rev.* **C81** (2010) 034911 (2010); DOI:10.1103/PhysRevC.81.034911.

[340] A. Bylinkin, N. S. Chernyavskaya and A. A Rostovtsev, *"Predictions on the transverse momentum spectra for charged particle production at LHC-energies from a two component model"*, *Eur. Phys. J.* **C75** (2015) 166; DOI:10.1140/epjc/s10052-015-3392-y.

[341] P. Skands, S. Carrazza, and J. Rojo, *"Tuning PYTHIA 8.1: the Monash 2013 Tune"*, *Eur. Phys. J.* **C74** (2014) 3024; DOI:10.1140/epjc/s10052-014-3024-y.

[342] M. Guzzi *et al.* (CTEQ Collaboration) *"CT10 parton distributions and other developments in the global QCD analysis"*, *SMU-HEP-10-11* (2011); e-Print: arXiv:1101.0561 [hep-ph].

[343] K. Reygers (ALICE Collaboration), *"Production of Neutral Pions and Eta-mesons in pp Collisions Measured with ALICE"*, *J. Phys.* **G38** (2011) 124076; DOI:10.1088/0954-3899/38/12/124076.

[344] W. Tung, H. Lai, A. Belyaev, J. Pumplin, D. Stump, and C.-P. Yuan, *"Heavy Quark Mass Effects in Deep Inelastic Scattering and Global QCD Analysis"*, *JHEP* **0702** (2007) 053; DOI:10.1088/1126-6708/2007/02/053.

[345] B. Jager, A. Schafer, M. Stratmann, and W. Vogelsang, *Phys. Rev.* **D67** (2003) 054005.

[346] I. Helenius, K. J. Eskola, H. Honkanen, and C. A. Salgado, *"Impact-Parameter Dependent Nuclear Parton Distribution Functions: EPS09s and EKS98s and Their Applications in Nuclear Hard Processes"*, *JHEP* **07** (2012) 073; DOI:10.1007/JHEP07(2012)073.

[347] D. d'Enterria, K. J. Eskola, I. Helenius, H. Paukkunen, *"Confronting current NLO parton fragmentation functions with inclusive charged-particle spectra at hadron colliders"*, *Nucl. Phys.* **B883** (2014) 615-628; DOI:10.1016/j.nuclphysb.2014.04.006.

[348] K. Werner *et al.*, *"Analysing radial flow features in p-Pb and p-p collisions at several TeV by studying identified particle production in EPOS3"*, *Phys. Rev. C* **89** (2014) 064903; DOI:10.1103/PhysRevC.89.064903.

[349] C. Shen *et al.*, *"Collectivity and electromagnetic radiation in small systems"*, *Phys. Rev. C* **95** (2017) 014906; DOI:10.1103/PhysRevC.95.014906.

[350] S. Roesler, R. Engel and J. Ranft, *"The Monte Carlo event generator DPMJET-III"*, SLAC-PUB-8740, hep-ph/0012252(2010); DOI:10.1007/978-3-642-18211-2_166.

[351] K. Werner *et al.*, *"Jets, Bulk Matter, and their Interaction in Heavy Ion Collisions at Several TeV"*, *Phys. Rev. C* **85** (2012) 064907; DOI:10.1103/PhysRevC.85.064907.

[352] B. Kopeliovich, J. Nemchik, I. Potashnikova, I. Schmidt, *"Quenching of high-pT hadrons: Energy Loss vs Color Transparency"*, *Phys. Rev.* **C86** (2012) 054904; DOI:10.1103/PhysRevC.86.054904.

[353] J. Nemchik, I. A. Karpenko, B. Kopeliovich, I. Potashnikova, Y. M. Sinyukov, *"High-pT hadrons from nuclear collisions: Unifying pQCD with hydrodynamics"*, arXiv:1310.3455 (2013).

[354] W. Broniowski and W. Florkowski, *"Explanation of the RHIC p_{T}-spectra in a thermal model with expansion"*, *Phys. Rev. Lett.* **87** (2001) 272302; DOI:10.1103/PhysRevLett.87.272302.

[355] V. Begun, W. Florkowski and M. Rybczynski, *"Explanation of hadron transverse-momentum spectra in heavy-ion collisions at $\sqrt{s_{\mathrm{NN}}} = 2.76$ TeV within chemical non-equilibrium statistical hadronization model"*, *Phys. Rev. C* **90** (2014) 014906; DOI:10.1103/PhysRevC.90.014906.

[356] V. Begun, *"Resonances in a sudden chemical freeze-out model"*, arXiv:1710.05934 [hep-ph]; DOI:10.1051/epjconf/201817115002.

[357] R. Corke and T. Sjöstrand, *"Interleaved Parton Showers and Tuning Prospects"*, *JHEP* **1103** (2011) 032; DOI:10.1007/JHEP03(2011)032.

[358] W. Dai, X.-F. Chen, B.-W. Zhang, E. Wang, *"η meson production of high-energy nuclear collisions at NLO"*, *Phys. Lett.* **B750** (2015) 390; DOI:10.1016/j.physletb.2015.09.053.

[359] B. Abelev, *et al.* (ALICE Collaboration), *"Centrality dependence of π, K, p production in Pb-Pb collisions at $\sqrt{s_{\mathrm{NN}}} = 2.76$ TeV"*, *Phys. Rev.* **C88** (2013) 044910; DOI:10.1103/PhysRevC.88.044910.

[360] B. Abelev, *et al.* (ALICE Collaboration), *"Production of charged pions, kaons and protons at large transverse momenta in pp and Pb-Pb collisions at $\sqrt{s_{\mathrm{NN}}} = 2.76$ TeV"*, *Phys. Lett.* **B736** (2014) 196-207; DOI:10.1016/j.physletb.2014.07.011.

[361] S. Sarkar, H. Satz, and B. Sinha, *"The physics of the Quark-Gluon Plasma"*, *Lect. Notes Phys.* **785** (2010) 1-369; DOI:10.1007/978-3-642-02286-9.

[362] W. A. Horowitz, *"LHC predictions from an extended theory with elastic, inelastic, and path length fluctuating energy loss"*, *Int. J. Mod. Phys.* **E16** (2007) 2193-2199; DOI: 10.1142/S0218301307007672.

[363] M. Djordjevic and M. Djordjevic, *"LHC jet suppression of light and heavy flavor observables"*, *Phys. Lett.* **B734** (2014) 286-289; DOI:10.1016/j.physletb.2014.05.053.

[364] D. Zigic, I. Salom, J. Auvinen, M. Djordjevic, M. Djordjevic, *"Joint R_{AA} and v_2 predictions for Pb+Pb collisions at the LHC within DREENA-C framework"*, arXiv:1805.03494 [nucl-th] (2018).

[365] D. Zigic, I. Salom, M. Djordjevic, M. Djordjevic, *"DREENA-B framework: first predictions of R_{AA} and v_2 within dynamical energy loss formalism in evolving QCD medium"*, arXiv:1805.04786 [nucl-th] (2018).

[366] Z.-B. Kang, R. Lashof-Regas, G. Ovanesyan, P. Saad, I. Vitev, *"Jet quenching phenomenology from soft-collinear effective theory with Glauber gluons"*, *Phys. Rev. Lett.* **114** (2015) 092002; DOI:10.1103/PhysRevLett.114.092002.

[367] Y.-T. Chien, A. Emerman, Z.-B. Kang, G. Ovanesyan, I. Vitev, *"Jet Quenching from QCD Evolution"*, *Phys. Rev.* **D93** (2016) 074030; DOI: 10.1103/PhysRevD.93.074030.

[368] J. Adam *et al.* (ALICE Collaboration), *"Multiplicity dependence of charged pion, kaon, and (anti)proton production at large transverse momentum in p-Pb collisions at* $\sqrt{s_{\rm NN}} =$ 5.02 *TeV"*, *Phys. Lett.* **B760** (2016) 720-735; DOI:10.1016/j.physletb.2016.07.050.

[369] L. Musa *et al.* (ALICE Collaboration), *"Upgrade of the Inner Tracking System Conceptual Design Report"*, CERN-LHCC-2012-013 ; LHCC-P-005 (2012).

[370] H. Appelshaeuser *et al.* (ALICE Collaboration), *"Title Upgrade of the ALICE Time Projection Chamber"*, CERN-LHCC-2013-020 ; ALICE-TDR-016 (2013).

[371] G. Martinez-Garcia *et al.* (ALICE Collaboration), *"Technical Design Report for the Muon Forward Tracker"*, CERN-LHCC-2015-001 ; ALICE-TDR-018 (2015).

[372] M. M. Aggarwal *et al.* (ALICE TPC Collaboration), *"Particle identification studies with a full-size 4-GEM prototype for the ALICE TPC upgrade"*, *Nucl. Instrum. Meth.* **A903** (2018) 215-223; DOI:10.1016/j.nima.2018.06.084.

[373] M. Aaboud *et al.* (ATLAS Collaboration), *"Measurement of the cross section for inclusive isolated-photon production in pp collisions at* $\sqrt{s} = 13$ *TeV using the ATLAS detector"*, *Phys. Lett.* **B770** (2017) 473-493; DOI:10.1016/j.physletb.2017.04.072.

[374] A. M. Sirunyan *et al.* (CMS Collaboration), *" Measurement of differential cross sections for inclusive isolated-photon and photon+jets production in proton-proton collisions at* $\sqrt{s} =$ 13 *TeV"*, *Eur. Phys. J.* **C79** (2019) 20; DOI:10.1140/epjc/s10052-018-6482-9.

[375] J. Adam *et al.* (ALICE Collaboration), *"Direct photon production in Pb-Pb collisions at* $\sqrt{s_{\rm NN}} = 2.76$ *TeV"*, *Phys. Lett.* **B754** (2016) 235-248; DOI:10.1016/j.physletb.2016.01.020.

[376] M. Germain (ALICE Collaboration), *"Direct photon measurements in pp and Pb-Pb collisions with the ALICE experiment"*, *Nucl. Phys.* **A967** (2017) 696-699; DOI:10.1016/j.nuclphysa.2017.05.094.

[377] T. Boettcher (LHCb Collaboration), *"Direct photon production at LHCb"*, *Nucl. Phys.* **A982** (2019) 251-254; DOI:10.1016/j.nuclphysa.2018.10.046.

[378] G. Hanson *et al.*, *"Evidence for Jet Structure in Hadron Production by* e^+e^- *Annihilation"*, *Phys. Rev. Lett.* **35** (1975) 1609-1612; DOI:10.1103/PhysRevLett.35.1609.

[379] S-L. Blyth *et al.*, *"A Cone jet-finding algorithm for heavy-ion collisions at LHC energies"*, *J. Phys.* **G34** (2007) 271-281; DOI:10.1088/0954-3899/34/2/008.

[380] M. Cacciari, G. P. Salam, *"Pileup subtraction using jet areas"*, *Phys. Lett.* **B659** (2008) 119-126; DOI:10.1016/j.physletb.2007.09.077.

[381] M. Cacciari, G. P. Salam, G. Soyez, *"The anti-k_t jet clustering algorithm"*, *JHEP* **0804** (2008) 063; DOI:10.1088/1126-6708/2008/04/063.

[382] S. Chatrchyan *et al.* (CMS Collaboration), *"Studies of jet quenching using isolated-photon+jet correlations in PbPb and pp collisions at $\sqrt{s_{\mathrm{NN}}} = 2.76$ TeV"*, *Phys. Lett.* **B718** (2013) 773-794; DOI:10.1016/j.physletb.2012.11.003.

[383] S. Chatrchyan *et al.* (CMS Collaboration), *"Rapidity distributions in exclusive Z + jet and γ + jet events in pp collisions at $\sqrt{s} = 7$ TeV"*, *Phys. Rev.* **D88** (2013) 112009; DOI:10.1103/PhysRevD.88.112009.

[384] S. Chatrchyan *et al.* (CMS Collaboration), *"Measurement of the triple-differential cross section for photon+jets production in proton-proton collisions at $\sqrt{s} = 7$ TeV"*, *JHEP* **1406** (2014) 009; DOI:10.1007/JHEP06(2014)009.

[385] A. M. Sirunyan *et al.* (CMS Collaboration), *"Study of jet quenching with isolated-photon+jet correlations in PbPb and pp collisions at $\sqrt{s_{\mathrm{NN}}} = 5.02$ TeV"*, *Phys. Lett.* **B785** (2018) 14-39; DOI:10.1016/j.physletb.2018.07.061.

[386] M. Aaboud *et al.* (ATLAS Collaboration), *"Measurement of photon-jet transverse momentum correlations in 5.02 TeV Pb + Pb and pp collisions with ATLAS"*, *Phys. Lett.* **B789** (2019) 167-190; DOI:10.1016/j.physletb.2018.12.023.

[387] M. Aaboud *et al.* (ATLAS Collaboration), *"Measurement of the cross section for isolated-photon plus jet production in pp collisions at $\sqrt{s} = 13$ TeV using the ATLAS detector"*, *Phys. Lett.* **B780** (2018) 578-602; DOI:10.1016/j.physletb.2018.03.035.

[388] M. Cacciari *et al.*, *"Jet Fragmentation Function Moments in Heavy Ion Collisions"*, *Eur. Phys. J.* **C73** (2013) 2319; DOI:10.1140/epjc/s10052-013-2319-8.